Nature-Inspired Polymers: Promising Materials for OTFT-Based Sensors

by

Jesse Thomas Ernest Quinn

A thesis
presented to the University of Waterloo
in fulfillment of the
thesis requirement for the degree of
Doctor of Philosophy
in
Chemical Engineering (Nanotechnology)

Waterloo, Ontario, Canada, 2017

Examining Committee Membership

The following served on the Examining Committee for this thesis. The decision of the Examining Committee is by majority vote.

External Examiner	Prof. Jean-François Morin (Laval University, Associate Professor)
Supervisor(s)	Prof. Yuning Li (Associate Professor)
Internal Member	Prof. Michael Pope (Assistant Professor)
	Prof. Nasser Mohieddin Abukhdeir (Assistant Professor)
Internal-external Member	Dr. Hany Aziz (Professor)

AUTHOR'S DECLARATION

This thesis consists of material all of which I authored or co-authored: see Statement of Contributions included in the thesis. This is a true copy of the thesis, including any required final revisions, as accepted by my examiners.

I understand that my thesis may be made electronically available to the public.

Statement of Contribution

This thesis has incorporated several published papers whereby I, Jesse Quinn, was listed as principle author or shared principle author. However, the following published papers could not be accomplished without collaboration with my colleagues within our group or externally.

The contents of Chapter 3 have been published in:

L. Guo, J. Quinn, J. Wang, C. Guo, X. Li, J. Wang, Y. Li, *Dyes Pigm.* **2016**, *132*, 329–335.

The contents of Chapter 4 have been published in:

J. Quinn, C. Guo, L. Ko, B. Sun, Y. He, Y. Li, *RSC Adv.* **2016**, *6*, 22043–22051.

The contents of Chapter 5 have been published in:

J. Quinn, E. Jin, Y. Li, *Tetrahedron Lett.* **2015**, *56*, 2280–2282.

J. Quinn, C. Guo, B. Sun, A. Chan, Y. He, E. Jin, Y. Li, *J. Mater. Chem. C* **2015**, *3*, 11937–11944.

J. Quinn, Y. He, D. A. Khan, J. Rasmussen, H. Patel, F. Haider, W. Kapadia, Y. Li, *RSC Adv.* **2016**, *6*, 78477–78485.

5.4.5.3 is not yet published and in near-verbatim state to what is intended for submission. The following is the authorship order:

J. Quinn, F. Haider, H. Patel, D. A. Khan, Z. Y. Wang, Y. Li.

Abstract

The concept of an organic thin film transistor was first introduced in the late 1980s and research was directed toward two key merits of performance, field-effect mobility and current ON/OFF ratio. Today these two key merits of performance are still highly sought after; however, a shortcoming associated with most organic semiconductors is their susceptibility to chemical interactions and photo-excitation; to name but a few of their caveats. Consequently, the development of organic semiconductors with high charge carrier transport as well as good air stability is still desired.

Nature provides a vast diversity of materials and looking for natural or nature inspired semiconductors appears to be a promising route towards interesting and pertinent materials. Organic thin film transistors based on natural or natural-inspired semiconductors such as indigo, β-carotene, indanthrene, and perylene diimide have demonstrated good charge carrier transport and some cases demonstrated equally good stability in ambient conditions.

In this work, a number of moderately to excellent air stable polymeric semiconductors were designed and synthesized that were nature inspired. Chapter 3 describes the synthetic account and elaborates on a broad spectrum of properties pertaining to the novel fluorene-fused triphenodioxazine based polymer (**PFTPDOBT**). **PFTPDOBT** exhibited excellent charge transport performance in ambient conditions reaching hole mobilities as high as ~10^{-2} cm^2 V^{-1} s^{-1} and modest hole mobilities in water-gated transistors (~10^{-3} cm^2 V^{-1} s^{-1}). In Chapter 4, a series of pyrazino[2,3-g]quinoxaline-2,7-dione (PQx) based polymers were developed and characterized. These PQx based polymers displayed exciting UV-Vis-NIR spectra when in the presence of an organic acid or Lewis acid. Their electrical characteristics in OTFTs were typical of ambipolar charge transport. Hole mobilities reached as high as ~10^{-2} cm^2 V^{-1} s^{-1} with corresponding electron mobilities as high as ~10^{-3} cm^2 V^{-1} s^{-1}. Lastly, Chapter 5 gives accounts on significant research pertaining to novel polymeric semiconductors based on the pyrimido[4,5-*g*]quinazoline-4,9-dione (PQ) moiety. A systematic study of PQ-based polymeric semiconductors is presented in both nitrogen, ambient, and aqueous environments. Typical hole charge transport was obtained between ~10^{-2} and ~10^{-3} cm^2 V^{-1} s^{-1}. Both **PPQ2T-BT-24** and **PPQ2T-TT-24** demonstrated moderate to excellent stability in these environments. To exploit the photo-excitation of organic semiconductors, a series of PQ-based polymeric semiconductors were incorporated in phototransistors and also blended with $PC_{61}BM$. The **PPQ2T-BT-24**:**PC61BM** blend reached ultrafast response times as low as 1 ms for rise and 8 ms for fall with photoresponsivity as high as 0.88% and EQE of 189%.

Lastly, **PPQ2T-BT-24** and **PPQ2T-TT-24** were incorporated into OTFT gas sensors where they demonstrated low detection limits with fast recovery times for a particular analyte.

Acknowledgements

I would like to express my sincerest gratitude to my advisor, Dr. Yuning Li. His expertise and insights have helped me greatly during the course of this research work. Moreover, his patience and continuous encouragement allowed me to develop my research skills and gain more poise.

I am thankful for the Nuclear Magnetic Resonance (NMR) facility, and the manager Janet Venne, where all NMR analysis took place to confirm the identity of my synthetic intermediates and products. I am also grateful for the Mass Spectrometry (MS) facility where I received valuable training from Richard Smith and performed numerous analyses. I am indebted to the Giga-to Nano (G2N) centre where device fabrication and characterization took place. It was not without the excellent support and guidance of Richard Barber and Dr. Czang-Ho Lee that I was able to attain my goal of device fabrication and characterization. Lastly, I would like to thank Bert Habicher, Ronald Neill, and Ralph Dickhout for their time, support, and assistance.

I am indebted to my colleagues Yinghui He, Dr. Mylène LeBorgne, Dr. Chang Guo, Dr. Bin Sun, Dr. Yun-Feng Deng, and Dr. Wei Hong for their training, support, and kind friendship. Moreover, I would like to recognize all my hard-working co-operative students especially Daid A. Khan, Fezza Haider, and Haritosh Patel. I would also like to thank all my committee members, Dr. Michael Pope, Dr. Nasser Mohieddin Abukhdeir, Dr. John Yeow, Dr. Hany Aziz, and Dr. Jean-François Morin.

Finally, I would like to acknowledge the unequivocal support from my family, especially my father Paul Quinn and wife Stephanie Ruediger Quinn, and friends. I thank them for giving me the inner strength, perseverance, and conviction that guides me to my goals.

Dedication

In memory of Jane Quinn. You left fingerprints of grace on our lives. You shan't be forgotten.

Table of Contents

List of Figures

List of Schemes

List of Tables

List of Symbols

A proportionality constant, channel area

B proportionality constant

c speed of light in vacuum, charge concentration (hole or electron)

D depth of absorption region

e (1.60218×10^{-19} C) elementary charge

ε dielectric constant

E electric field in the channel

E_g^{opt} optical band gap

EQE, η external quantum efficiency

g_{DS} channel conductance

g_m transconductance

h (6.6207×10^{-34} m^2 kg s^{-1}) Planck's constant

I_{DS} drain-source current

$I_{DS,dark}$ dark current

$I_{DS,ph}$ illuminated current

I_{GS} gate-source current

I_{ON}/I_{OFF} current ON/OFF ration

λ_{peak} wavelength of incident light with maximum intensity

L length

M_o molecular weight of the repeating monomer unit

M_n number-average molar mass

M_w weight-average molar mass

η hardness

π pi electrons, pi bond

P_{opt} incident optical power

R photoresponsivity

σ sigma bond

S subthreshold swing

μ charge carrier mobility

μm microns

ΔV_{TH} threshold voltage shift

V_{TH} threshold voltage

V_{DS} drain-source voltage

V_{GS} gate-source voltage

V_{ON} on voltage

W width, gate width

X_n number average degree of polymerization

X_w weight average degree of polymerization

List of Abbreviations

AcOH: acetic acid
AFM: atomic force microscopy
Al: aluminum
AO: atomic orbit
Au: gold
BGBC: bottom-gate bottom-contact
Cr: chromium
CV: cyclic voltammetry
DCM: dichloromethane
DDFTTF: 5,5'-bis-(7-dodecyl-9H-fluoren-2-yl)-2,2'-bithiophene
DDTS: dodecyltrichlorosilane
DMF: dimethylformamide
DSC: differential scanning calorimetry
EA: electron affinity
EGOFET: electrolyte-gated OFET
EIS: electrochemical impedance spectroscopy
FBIOFET: functional bio-interlayer OFET
FET: field-effect transistor
GaN: gallium nitride
HOMO: highest occupied molecular orbital
hr: hour(s)
InGaAs: indium gallium arsenide
IP: ionization potential
IR: infrared
ISOFET: ion-sensitive OFET
LCD: liquid crystal display
LUMO: lowest unoccupied molecular orbital
min: minute(s)
MO: molecular orbit
MOF: metal organic framework
MOS: metal-oxide semiconductor
MOSFET: metal-oxide semiconductor field-effect transistor
NBS: *n*-bromosuccinimde
NIR: near-infrared
OECT: organic electrochemical transistor
OFET: organic field-effect transistor
OLED: organic light emitting diode
OPT: organic phototransistor
OSC: organic semiconductor
OTFT: organic thin film transistor
P3HT: regioregular poly(3-hexylthiophene)
$PC_{61}BM$: [6,6]-Phenyl-C_{61}-butyric acid methyl ester
PDI: polydispersity index
PSC: polymer semiconductor
RFID: radio frequency identification card
rt: room temperature
Si: silicon
SiC: silicon carbide
TCE: 1,1,2,2-tetrachloroethane
TFA: trifluoroacetic acid
TGA: thermogravimetric analysis
TGBC: top-gate bottom-contact
TFT: thin film transistor
UV: ultraviolet
XRD: x-ray diffraction

Chapter 1
Introduction

1.1 Introduction to Organic Electronics

The organic electronic devices field can be considered a fast-paced world that has significant progress concerning both efficiency and device function. In addition to the archetypal devices, namely organic light-emitting diodes (OLEDs), thin-film transistors (OTFTs), and solar cells, auxiliary functions of said devices have been recognized. For example, smart pixels (display switches) [1], display drivers based on liquid crystal displays (LCDs) or OLEDs [2–7], electronic paper [4,8,9], memory devices that contain radio frequency identification cards (RFIDs) [10–16], electrophoretic cells [8,9,17], and sensors [18–27]. A significant number of these device types can already be realized as "all-organic", without inorganic constituents, thus a completely new realm is envisioned by the integration of said functional components on one common stage. An independent market research company known as IDTechEx that conducts detailed examinations of emerging technologies has reported that the organic electronics market will double by 2025. Furthermore, there are at least 3000 organizations currently pursuing organic electronics with a total market of $29.80 billion, as of 2015, that is expected to reach $73.69 billion by 2025. The forecast for the next three years suggests that majority of growth will be within the non-printed OLEDs, conductive inks, and sensors while other technologies are just in their infancies and are expected to grow exponentially as they emerge from research and development [28]. The most exciting benefits from implementing organic materials in electronic devices involves aspects like mechanical flexibility and light weight [29,30]. Such properties are attractive for mobile applications and wearable devices. Moreover, entirely new design concepts for consumer electronics are emerging, as organic electronic devices can conform to complex surface shapes [29,31,32].

The active organic materials of these devices can be divided into two classes, namely, small-molecules and polymers. Although the fundamental properties of both materials are effectively the same, the separation mainly relates to the way thin films are prepared. Small-molecules are usually thermally evaporated under vacuum whereas polymers are processed from solution. However, this is not entirely true as most small-molecules can be soluble, or solubility may be improved by the addition of side chains. Nonetheless, organic materials in principle have many advantages over conventional materials such as their fabrication process, which can avoid high temperature and high vacuum deposition processes by simply depositing from solution. For preparation from solution, several techniques are available such as the standard spin-coating method, inkjet printing [33], screen printing

[34], and flexographic printing [35] that allow large-volume/large-area roll-to-roll fabrication giving way to low production costs.

Both polymers and small-molecules have many common properties such as ionization potential (IP), electron affinity (EA), hardness (η), band-gap energy, solubility, tendency for crystal formation in solid state, and stability in ambient conditions, which all can be tuned by altering the chemical composition. Furthermore, such materials have demonstrated versatile functionalities such as optical, electrical, magnetic, and sensing properties in various types of organic electronics [29,31,32]. With the aforesaid merits, there have been numerous reports since the 1970s incorporating organic materials into conventional electronic devices that have led to performance properties that are comparable to or better than their inorganic counterparts, thereby increasing their practical commercial application interest and value [36–38].

1.2 Motivation for this Thesis

For the latter half of the 20th century, the major focus of inorganic chemistry was focused on semiconductors, metallic conductors, superconductors, and magnets. It was in the 1950s when the first organic small-molecule semiconductor was reported [39]. In the mid-1960s, William Little proposed that organic superconductors were possible and at room temperature [40,41]. This sparked the creation of what is known as the organic electronics field and generations of chemists to create novel organic semiconductive materials. In 1977 and 1978, the synthesis of highly conducting films of polyacetylene were reported [42,43], which lead to Alan J. Heeger, Hideki Shirakawa, and Alan MacDiarmid receiving the Nobel Prize in Chemistry in 2000 [44]. The field-effect phenomenon of organic semiconductors (OSCs) was described around 1970; however, the first example of a device (*i.e.* transistor) was not reported until the late 1980s [45,46]. The first examples were based on polyacetylene and polythiophenes where the latter is still actively studied today [46].

Transistors are ubiquitous electronic building blocks that have dominated the electronics industry since 1950s when first commercialized [47]. Inorganic field-effect transistors (FETs) have been utilized in all facets of electronics such as amplifiers, adders, shifters, inverters, modern memory devices, integrated circuits, and microprocessors [29]. They are used to amplify an electronic signal or divert current (switch) electrical power. There have been numerous inorganic FET architectures reported [48]; however, the thin film transistor (TFT) is the most relevant architecture to this thesis. TFTs are insulated gate FETs that operate on the same basic principle as metal-oxide semiconductor FETs (MOSFETs)

[49]. In other words, TFTs have an insulating substrate in contrast to MOSFETs that have a semiconductor material as a substrate that contains the opposite polarity to the source/drain diffusions. Furthermore, the source/drain contacts in TFTs are injecting contacts [50] to the semiconducting channel rather than to a p-n junction found in a MOSFET. Transistors consisting of OSCs as the active channel layer, typically, follow the TFT architecture and are commonly referred to as OTFTs.

Although the concept of an OTFT was first introduced in the late 1980s [45,46] the two key parameters of performance values, field-effect mobility (μ) and current ON/OFF ratio (I_{ON}/I_{OFF}), obtained from the initial organic materials were considered impractical and continued to be for many years [51]. With several decades of academic and industrial interest numerous materials have now appeared that have not only met but surpassed amorphous silicon in charge carrier transport (~0.1 to 1 $cm^2 V^{-1} s^{-1}$) [52–55]. However, a shortcoming associated with most OSCs is their sensitivity to air when used as the active channel layer in OTFTs. It is commonly believed that OSCs are susceptible to doping or trapping by interaction with ambient oxygen, moisture, and carbon dioxide resulting in larger off-currents and thus lower I_{ON}/I_{OFF} values. In addition, a positive shift in the threshold voltage (V_{TH}) is observed. Therefore, rigorous precautions are taken during material processing and device fabrication to exclude environmental elements that may alter the OTFT performance. These precautionary measures increase cost of manufacturing and off-set the appeal of OTFTs as inexpensive alternatives to conventional technology. Consequently, the development of OSCs with high charge carrier transport as well as air stability is still needed. On that note, it is also fair that a new material be assessed in a multitude of ways to demonstrate potential application in other fields.

To achieve air-stable charge carrier transport in OTFTs we looked towards natural-origin/derived chromophores and components therein and commercial dyes that are analogues of natural-origin chromophores. Such beliefs in natural-inspired materials for greater stability is supported by recent development surrounding indigoid dyes. Although indigo and derivatives (*e.g.* Tyrian purple) are not present in nature, their immediate natural precursors are. Dissimilar to many natural-origin dyes, indigoids have demonstrated extreme stability with respect to degradation, resulting in their continuous use throughout centuries [56]. From a more applicable view, they have been reported with modest to good air-stability in OTFTs [57–59]. An alternative natural-inspired chromophore is perylene diimide (PDI). PDI has also demonstrated high charge carrier transport and good air stability in OTFTs [60–62]. Several other nature-inspired/derived materials exists such as β-carotene, indanthrene yellow G, and indanthrene brilliant orange RF and have been reported in OTFTs [63].

As previously stated, it is also important to assess the potential of new materials. As such, one specific application related to this thesis is the use OSCs in light detection. OSCs by their very nature can be tuned for narrow (monochromatic) or broad (panchromatic) spectral sensitivity in the ultraviolet (UV) to the infrared (IR) region. As stated previously, the low-temperature processability, large-area surfaces, that can be virtually any type of substrate, allows for innovative applications and/or the realization of novel optoelectronic devices or complex systems such as large-area imagers and scanners that are rigid or conformable to a multitude of surface geometries. Organic light sensors represent a niche in organic electronics, but clearly offer many advantages that make them suitable for implementation in real applications [64]. However, initial reports of organic phototransistors (OPTs) based on small-molecules [65] or polymers [66–68] semiconductors had received limited attention due to their lower performances than that observed of their inorganic counterparts [69]. Although, several OPTs have achieved greater performance in key merits in recent times [70–76]. Thus, this niche field is in its infancy and offers an interesting outlet for novel OSCs. Likewise, OSCs are bestowed with inherent chemical and biological recognition capabilities or such properties can be achieved with proper functionalization and/or integration of bio-compatible elements (*i.e.* DNA, antibodies, enzymes or proteins) giving advantage over other sensing technologies (*e.g.* electrochemical or optical) allowing for a label-free responses using simple electronic read-outs that can be effortlessly miniaturized and potentially printed [77]. Numerous chemical and biological sensor technologies exist and some have been successfully commercialized [78]. Broadly speaking, commercialized sensor selectivity is achieved by sensor arrays coined electronic noses (*i.e.* measuring gaseous analytes) [79–81] and electronic tongues (*i.e.* measuring aqueous analytes) [82–84]. Each sensor within the array measures the change in a single parameter such as resistance, current, voltage, or conductivity. The resulting pattern obtained from the array of data is used for the recognition of chemical or biological species. For instance, the metal-oxide semiconductor (MOS) (*e.g.* tin dioxide) gas sensor (chemiresistor type sensor) has been commercially successful and operates with the basic principle that the MOS electric resistance changes when gas molecules are adsorbed on its surface [85]. Such devices have been incorporated into arrays to form electronic noses [21]. Because the combination of single parameter sensors in an array appears restrictive, it has been proposed that OTFTs may be used and that they may measure up to four parameters at room temperature when exposed to desire analytes [21,38]. Therefore, the utilization of OTFTs as aqueous and gas sensing devices offers another interesting practical application to pursue. In this thesis, we report several novel nature-inspired OSCs and their properties along with their characterization as active channel layers in OTFTs. In some cases, the OTFT

operational stability in ambient and aqueous conditions were characterized. Select OSCs were also characterized as OPTs and gas sensors.

1.3 Research Objectives

The objective of this study was to explore the potential use of several novel natural and nature-inspired π-conjugated moieties by incorporation into polymer backbones and evaluation through use as active channel layers in OTFT-based chemo and photo-sensors. The research accounts within consisted of the following tasks:

1) To synthesize and characterize several novel π-conjugated polymers based on nature or nature-inspired moieties.
2) To examine the aforementioned materials as active channel layers in OTFTs under practical conditions such as ambient or aqueous environments.
3) To examine the performance of the aforementioned materials as active channel layers in OTFT-based chemo and photo-sensors.

The realization and findings acquired from this work may be useful for the discovery of the next generation high performance printed electronic and sensing materials.

1.4 Thesis Structure

This thesis consists of six chapters and they are organized as follows:

The objective of the opening of this thesis is to provide the necessary background information that is crucial to understand the scientific results presented in the latter part of the thesis. In Chapter 2, a brief review of organic semiconductors and coupled applications based on organic thin film transistors are given. Chapter 3 presents a novel polymeric semiconductor based on fluorene-fused triphenodioxazine that exhibits excellent air stability and modest aqueous stability in OTFTs. Chapter 4 presents a series of novel polymeric semiconductors with interesting acid affinity along with modest OTFT performance. Chapter 5 details the accountants of a novel series of polymeric semiconductors, isomers of materials discussed in Chapter 4, as an active channel layer in phototransistors, with preliminary findings in water-gated transistors, and gas sensors. Finally, conclusions and a future outlook are presented in Chapter 6.

Chapter 2
Background

2.1 Organic Semiconductors

OSCs are often divided into two groups: π-conjugated polymers and π-conjugated small-molecules. π-Conjugation in these materials refers to a backbone chain of alternating double and single carbon–carbon bonds. Although, hydrogen and other heteroatoms such as sulfur, oxygen, and nitrogen are or can be present in the conjugated backbone. They also show properties typically associated with a semiconductor such as absorption and emission of visible light and a sufficient degree of conductivity for operation of traditional semiconductor devices. Since OSCs combine the electronic advantages of semiconductors along with the tunability and robustness of organic compounds they have received significant attention from both academia and industry [86]. Furthermore, if soluble or made soluble they can be processed from solution into thin films by various methods [33–35] adding further advantage over conventional semiconductors. An extensively studied π-conjugated polymer is regioregular poly(3-hexylthiophene) (P3HT) [87–91] while pentacene represents an equally well-studied π-conjugated small-molecule (Figure 2-1) [15,92–94].

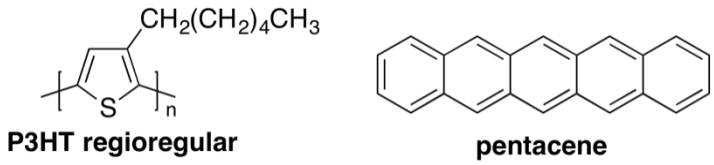

Figure 2-1. Structure of regioregular P3HT and pentacene.

2.2 Molecular Structure and Electronic Transport

To discuss covalent bonding one must consider the valence shell atomic orbitals of an element. For second period elements, such as carbon, nitrogen and oxygen, the valence shell atomic orbitals are designated as 2_s, $2p_x$, $2p_y$ and $2p_z$. The spatial distribution of electrons occupying each of these orbitals is shown in Figure 2-2. The valence shell electron configuration of carbon is 2_s^2, $2p_x^1$, $2p_y^1$ and $2p_z^0$. However, with this configuration only two covalent bonds would form and the octet rule would be broken. Yet, tetrahedral structures with carbon exist such as methane where four equivalent bonds lead to the desired octet (eight electrons in the valence shell). A simple explanation for this phenomenon was proposed by Linus Pauling. He suggested an orbital hybridization model in which all the valence

shell electrons of carbon are reorganized (Figure 2-2). In order to explain the structure of methane, the 2s and three 2p orbitals are transformed to four corresponding hybrid atomic orbitals, each having 25% s and 75% p character, and designated as sp^3. These hybrid orbitals have a specific orientation, and the four are positioned in a tetrahedral fashion. Thus, the four covalent bonds of methane consist of shared electron pairs with four hydrogen atoms in a tetrahedral configuration as predicted by VSEPR theory [95].

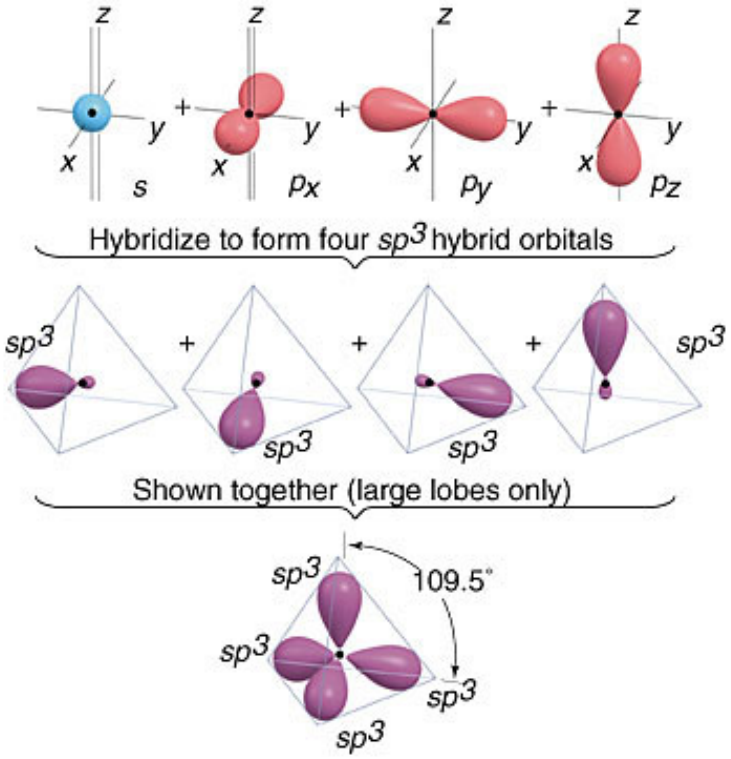

Figure 2-2. Type of atomic orbital and corresponding shape with formation of four sp^3 hybrid orbitals [95].

What we described above refers to molecules with only sigma (σ) bonds, but a different type of hybrid orbital exists for molecules with pi (π) bonds. The hybrid orbital designated as sp^2 is the mixing of 2s and two of the 2p orbitals where one of the 2p orbitals remains unhybridized (Figure 2-3). The sideways overlap of the unhybridized 2p orbital (perpendicular to the internuclear axis) produces a pi (π) bond. Simply put, a π bond is a covalent bond in which the overlap regions lie above and below the internuclear axis. In opposite fashion to σ bond, in a π bond there is zero probability of the electron on

the internuclear axis. Because the total overlap in the π bonds tends to be less than that in a σ bond, π bonds are weaker than σ bonds. A double bond, like that found in a π-conjugated molecule, consists of one σ bond and one π bond [95].

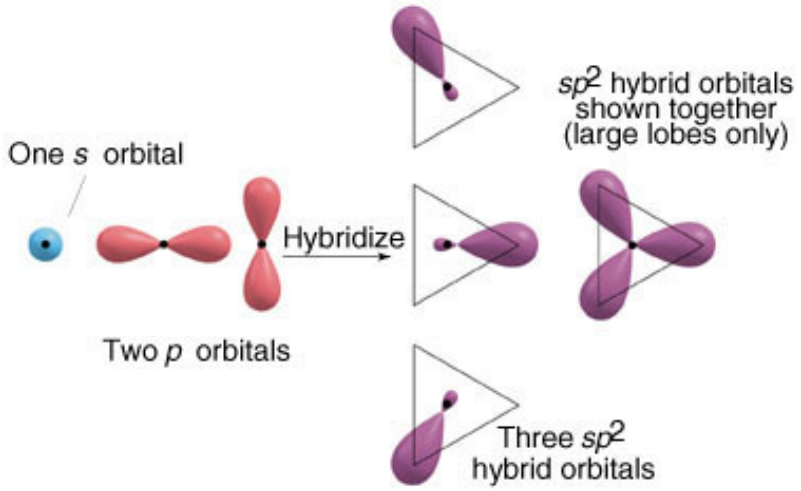

Figure 2-3. Formation of sp^2 hybrid orbitals [95].

As previously mentioned π-conjugation exists through a backbone chain of alternating double and single carbon-carbon bonds. This backbone, made of atoms, simply reflects the interaction of valence electrons of individual atoms leading to the formation of molecule orbitals (MOs). In other words, these MOs arise from the linear combination of atomic orbitals to form bonding and antibonding orbitals. The type of interaction between atomic orbitals, previously denoted as σ and π bonds, may be used as molecular-orbital symmetry labels representing bonding orbitals while σ* and π* reflect the antibonding orbitals. Electrons that spend most of their time between the nuclei of two atoms are what stabilize the molecule while electrons that spend most of their time outside the nuclei of two atoms destabilize the molecule. This holds true as the electron density increases between the nuclei when placing an electron in the bonding orbital whereas electron density decreases when an electron is placed in the antibonding orbital. Thus, placing an electron in the bonding orbital will stabilize the molecule whilst placing electrons into the antibonding orbitals will decrease the stability of the molecule. Electrons will fill according to the energy levels of the orbitals and populate the lower energy orbitals prior to the higher energy orbitals (Figure 2-4). Bond order gives an indication of the stability of a bond and if a bond order of zero is obtained the molecule is too unstable and such cannot exist [95]. The highest energy orbital that is occupied with electrons is called highest occupied molecular orbital

(HOMO) and the lowest energy orbital that is unoccupied by electrons is called lowest unoccupied molecular orbital (LUMO).

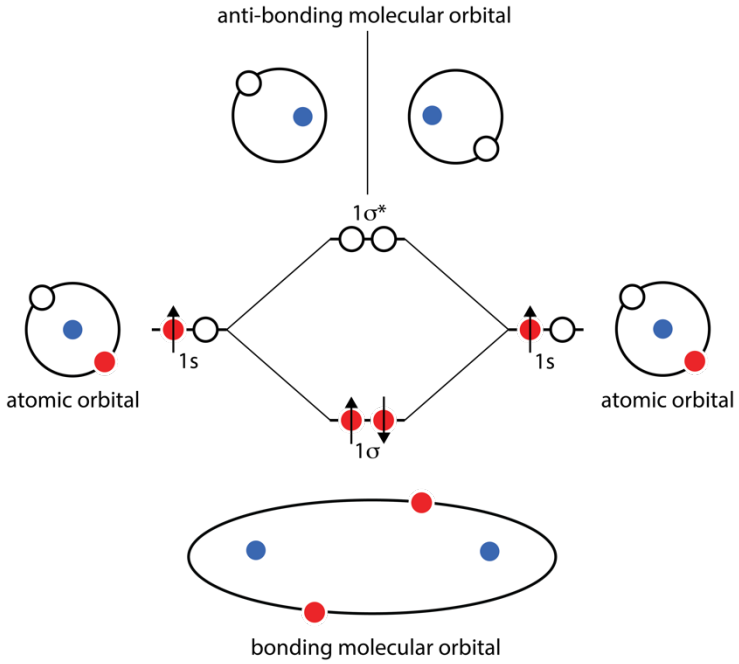

Figure 2-4. Energy level diagram for H_2 molecule.

The electrical conductivity of organic materials can range from insulating to conducting. This characteristic depends on the electronic states formed along the backbone which is based on the electrons of the carbon atoms and the means by which they interact with each other. Insulating materials are sp^3 hybridized while semiconducting materials are sp^2 hybridized. Thus, the localized electrons in the σ bonds form the backbone and dominate the mechanical properties whereas the electrons in the π bonds are delocalized along the backbone and are responsible for the electrical and optical properties. In the electronic ground state, the π bonding MOs will be filled with electrons and the higher energy π* MOs will remain empty (Figure 2-5). The number of discrete energy levels as bonding and antibonding orbitals (*i.e.* π and π*) are proportional to the number of carbon atoms in the backbone. For infinitely long π-conjugated backbones, such as some polymers, the discrete energy levels become so closely spaced that they form continuous bands. The filled band is known as the valence band and the empty band is known as the conducting band and the space between is known as the band gap (E_g) [96].

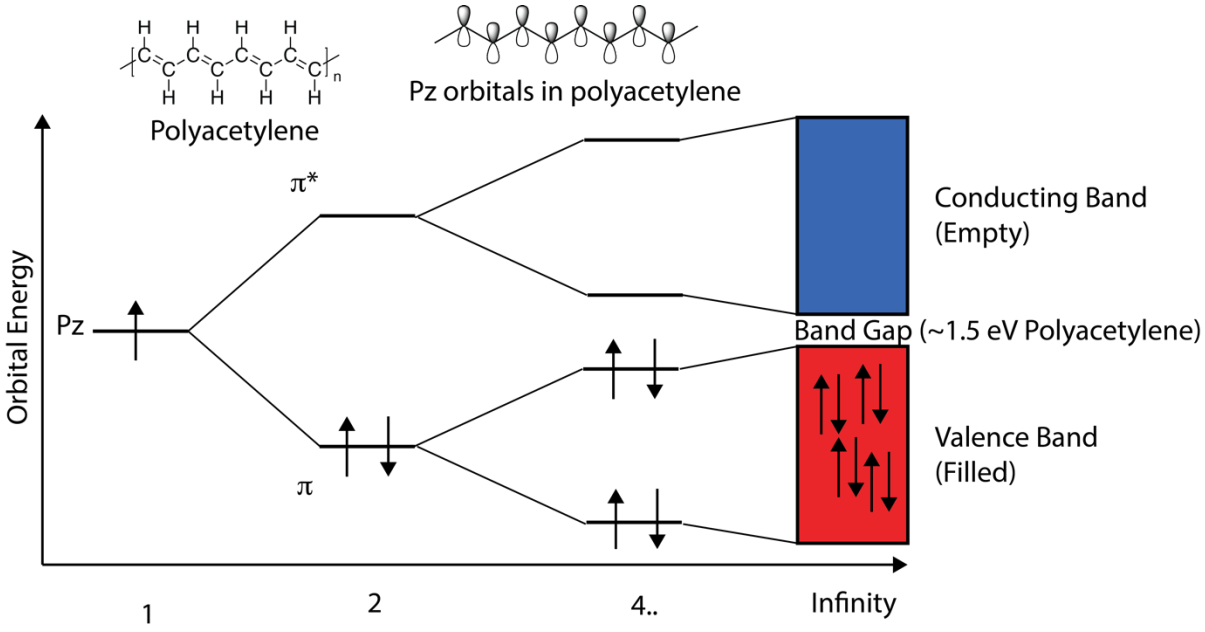

Figure 2-5. An orbital diagram of the π-conjugated polymer polyacetylene.

In the electronic ground state, all bonding orbitals are filled to the HOMO with two antiparallel spin paired electrons. For charge transport to take place, a charge on the molecule unit must exist. A charge can be made by the addition of an electron to the LUMO or by the removal of an electron from the HOMO. A charged molecular state can occur by several methods: (1) through injection or extraction of an electron at a metal contact and molecular interface. (2) Through reduction or oxidation by doping. (3) Through exothermic dissociation of a charge state by electron transfer to an adjacent molecule. In the event that an electron is given or taken, from a corresponding antibonding or bonding orbital, change in the spatial distribution of electrons occurs shifting bond lengths in the molecule. The energy associated with this change in molecular geometry is denoted as geometric reorganization energy, and the charge and geometric distortion of the molecule is denoted as a polaron. These effects are an inarguable characteristic of OSCs due to their low dielectric constant ($\varepsilon \approx 3–4$). Charge carriers, holes or electrons, generated by injection from contacts, doping, or optical excitation, may move coherently within the π-conjugated backbone while hopping will take place between different π-conjugated segments or molecules [96].

2.3 Organic Thin Film Transistors

FETs were first proposed by Lilienfield in 1930. In 1960, Kahng and Atalla fabricated the first MOSFET based on silicon. It was not until 1970 that organic FETs (OFETs) were proposed. OFETs consist of a thin OSC layer rather than a metal-oxide. The OSC can be a small molecule, oligomer, or polymer that is comprised of π-conjugated bonds exhibiting delocalized filled and empty π-orbitals [32,45,97]. Typically, OFETs adopt the TFT architecture oppose to MOSFET architectures [45,97]. Thus, OFETS have been commonly referred to as OTFTs. Figure 2-6 shows a schematic of a top-gate bottom-contact (TGBC) and bottom-gate bottom-contact (BGBC) OTFT. It must be noted that several other device architectures can be made depending on the relative position of the contacts and the dielectric/semiconductor layers as discussed later within this chapter.

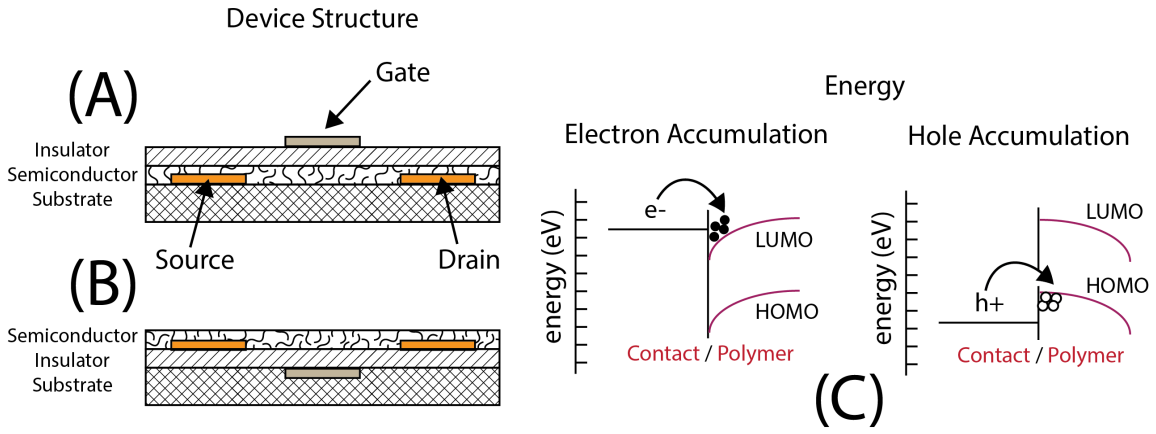

Figure 2-6. Schematic and materials of a TGBC (A) and BGBC (B) OTFT along with the energy levels of the contact-semiconductor material interface where charge accumulation takes place (C).

2.3.1 Device Operation

An OTFT is composed of three contacts (source, drain, and gate), a dielectric, and an OSC layer. Ideally, at slight source-drain current (I_{DS} = 0 A) flows when the gate voltage is zero (V_{GS} = 0 V) autonomously of the applied bias between the source-drain contacts (V_{DS}). The device turns ($I_{DS} \neq 0$ A) on when a gate field is applied ($V_{GS} \neq 0$ V), which induces charge carriers at the semiconductor/dielectric interface. The type of charge carrier induced is reflected by the polarity, be it positive or negative, of the applied biases (V_{DS} and V_{GS}). The charge carriers may be electrons (n-type material) or holes (p-type material) (Figure 2-6C) [22,26]. The transistor performances are evaluated from I-V plots (Figure 2-7), known as output and transfer curves, where key parameters such as the

field-effect mobility (μ), current on/off ratio (I_{ON}/I_{OFF}), threshold voltage (V_{TH}), on voltage (V_{ON}), and subthreshold swing (S) are taken [98].

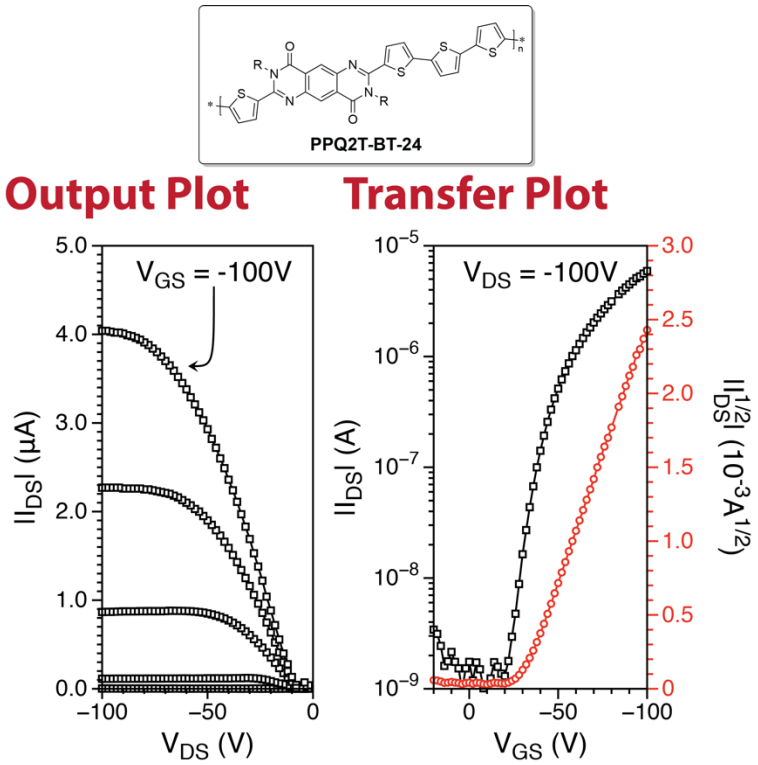

Figure 2-7. The output (left) and transfer (right) curves of a BGBC OTFT with a thin film of **PPQ2T-BT-24** annealed at 250 °C. Output curves are measured from 0 to -100 V at -20 V increments. Device dimensions L = 30 µm; W = 1000 µm.

As V_{DS} and V_{GS} magnitudes increase, a linear regime at low V_{DS} (*i.e.* $V_{GS} > V_{DS}$) is observed. The linear regime has three important parameters, channel conductance (g_{DS}), transconductance (g_m), and I_{DS}, which are given by Equations 2.1, 2.2, and 2.3, respectively [45]:

$$|V_{GS} - V_{TH}| > |V_{DS}| \begin{cases} g_{DS} = \left|\frac{\partial I_{DS}}{\partial V_{DS}}\right|_{V_{GS}=const} = \frac{W}{L}\mu C_i(V_{GS} - V_{TH}) & 2.1 \\ g_m = \left|\frac{\partial I_{DS}}{\partial V_{GS}}\right|_{V_{DS}=const} = \frac{W}{L}\mu C_i V_{DS} & 2.2 \\ I_{DS,lin} = \frac{W}{L}\mu C_i[(V_{GS} - V_{TH})V_{DS} - \frac{V_{DS}^2}{2}] & 2.3 \end{cases}$$

In the saturated regime the I_{DS} and g_m are given by Equations 2.4 and 2.5, respectively [45]:

$$|V_{DS}| > |V_{GS} - V_{TH}| \begin{cases} I_{DS,sat} = \frac{W}{2L}\mu C_i[(V_{GS} - V_{TH})^2 & 2.4 \\ g_m = \frac{W}{L}\mu C_i(V_{GS} - V_{TH}) & 2.5 \end{cases}$$

where W is channel width, L is channel length, C_i is the capacitance per unit area of the insulator layer, and μ is stated above [32,45].

The I_{ON}/I_{OFF} is also an important parameter and is measured from the transfer characteristics curve (I_{DS} plotted against V_{GS}). The I_{ON}/I_{OFF} is determined by the I_{DS} while the device is saturated for a given applied V_{GS} to that of the value with no V_{GS}. A large I_{ON}/I_{OFF} is considered ideal.

2.3.2 Organic Thin Film Transistors Used as Light Detectors

In order to make effective phototransistors, the material is required to detect specific wavelengths, ranging from the ultraviolet (UV) to infrared (IR) region, for use in medical imaging, biological/chemical sensing, communication, environmental monitoring and security [69,99,100]. Currently, most commercially available phototransistors are based on inorganic materials such as silicon carbide (SiC), silicon (Si), gallium nitride (GaN), and indium gallium arsenide (InGaAs), which are individually known to have relatively narrow response spectra [101,102]. Furthermore, inorganic phototransistors are limited to a small size detector due to the their complicated fabrication [103]. The deficiency of tunability and suitability for converging technology of aforesaid materials has shifted the focus to organic phototransistors (OPTs), which in contrast can be readily tuned for various band gaps, while providing facile device fabrication [69,104,105]. OPTs can also offer superior photoresponsivity (R); anthra[2,3-*b*]benzo[*d*]thiophene based devices displayed R values as high as 10^3 A W^{-1} [106], in comparison to the value of ~300 A W^{-1} for silicon single-crystal phototransistors [107]. In addition to exhibiting higher responsivity than their inorganic counterparts, OPTs based on small molecules are beginning to excel in response times too. [6,6]-Phenyl-C_{61}-butyric acid methyl ester ($PC_{61}BM$) incorporation is known to enhance OPT performance, especially response times, as it enlarges the difference between hole and electron transport, resulting in a higher photocurrent [108]. Based on these desirable characteristics, OPTs developed from a blend of $PC_{61}BM$ and poly[2-methoxy-5-(3',7'-dimethyloctyloxy-*p*-phenylene vinylene)] ($OC_1C_{10}PPV$) in a 15:1 ratio to achieve incredibly low response times in the microsecond range. Although the use of $PC_{61}BM$ provided significantly lower response times, the spectral bandwidth of the material is quite narrow and can only be obtained by using a light source with a wavelength of ~469 nm [109]. Meanwhile, *Xu et al.* proposed blending $PC_{61}BM$ with DPP-DTT polymer; however, a more balanced ratio of 1:1 was used, displaying a rise time of ~29

ms [108], which is comparable to those of inorganic photodetectors based on ZnO and In_2Te_3 nanowire, and GaTe nanosheets [110–112]. Several recent review papers provide a much deeper example base for OPTs [113,64,114].

Photoresponsivity and response times are only a few of the variety of parameters used to test OPT and photodiode performance in literature. Although mobility is occasionally used as a parameter, it is not one of the main figure of merits, which include *R*, photocurrent/dark current ratio, external quantum efficiency (*EQE*), response time, spectral bandwidth and dark current [102,115,116]. *R* can be defined as [117]:

$$\mathrm{R} = \frac{(I_{DS,ph} - I_{DS,dark})}{AP_{opt}} \qquad 2.6$$

where, A is the channel area, P_{opt} the incident optical power, and $I_{DS,ph}$ and $I_{DS,dark}$ are the drain current under illumination and in dark, respectively. The EQE values can be modelled by the equation [117]:

$$\mathrm{EQE} = \frac{(I_{DS,ph} - I_{DS,dark})hc}{PA_{opt}\lambda_{peak}e} \qquad 2.7$$

where $I_{DS,ph}$, $I_{DS,dark}$, P_{opt}, and A are defined previously, h (6.6207×10^{-34} m^2 kg s^{-1}) is Planck's constant, c is the speed of light in vacuum, e (1.60218×10^{-19} C) is the elementary charge, and λ_{peak} is the wavelength of incident light with maximum intensity.

It has been proposed that two different effects can occur in the active channel layer of inorganic semiconductors as the result of the illumination of the transistor and such it is believed that organic semiconductors follow suit [118,119]. The first effect, known as the photovoltaic effect, is dominant when the transistor operates in accumulation mode ($V_{GS} < V_{TH}$ for a p-channel device). In contrast, the second effect, known as the photoconductive effect, is dominant when the transistor operates in the depletion mode ($V_{GS} > V_{TH}$) and such the I_{DS} increases with the optical power or density of the light source [64].

2.3.2.1 The Photovoltaic Effect

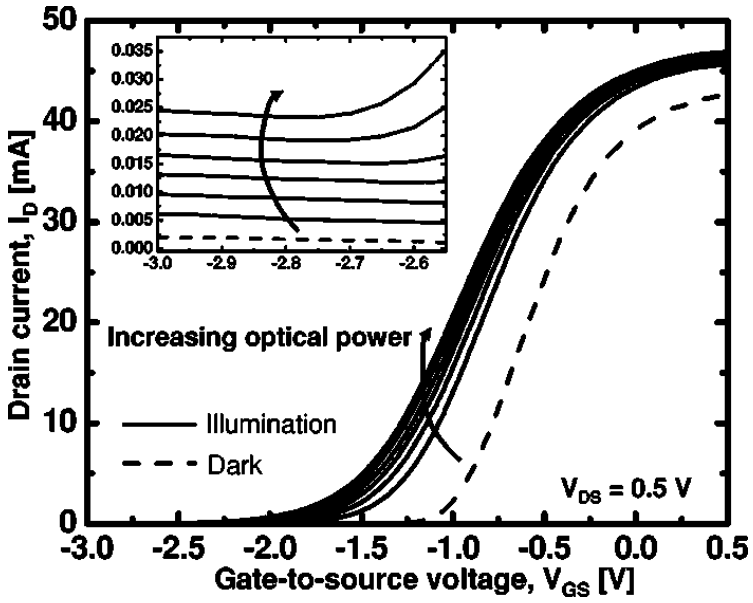

Figure 2-8. I-V plot demonstrating the photovoltaic effect. The inset is a magnified area of the plot where the photoconductive effect can be observed [120].

The photovoltaic effect, Figure 2-8, results in a photo-induced shift of V_{TH} towards more positive values for p-channel devices whereas for n-channel devices the opposite is true. The photo-induced shift of V_{TH} can be explained in p-channel devices by the accumulation of electrons at the source electrode whereas the photo-generated holes' flow unencumbered to the drain electrode when light absorption occurs. With the accumulation of electrons at the source electrode, the holes' injection barrier between the source and semiconductor channel is effectively lowered. Simultaneously, with the lowered injection barrier there is an effective decrease in contact resistance with a significant increase in I_{DS} [64]. The photocurrent caused by this effect can be expressed as [120]:

$$\mathrm{I_{ph,pv}} = g_m \Delta \mathrm{V_{TH}} = \frac{AkT}{e} \ln\left(1 + \frac{\eta q \lambda P_{opt}}{I_{DS,dark} hc}\right) \qquad 2.8$$

Where e is previously stated, η is the quantum efficiency, P_{opt} as previously stated, $I_{DS,dark}$ stated previously, hc/λ the photon energy, g_m stated previously, ΔV_{TH} the threshold voltage shift, and A is a proportionality parameter [120].

2.3.2.2 The Photoconductive Effect

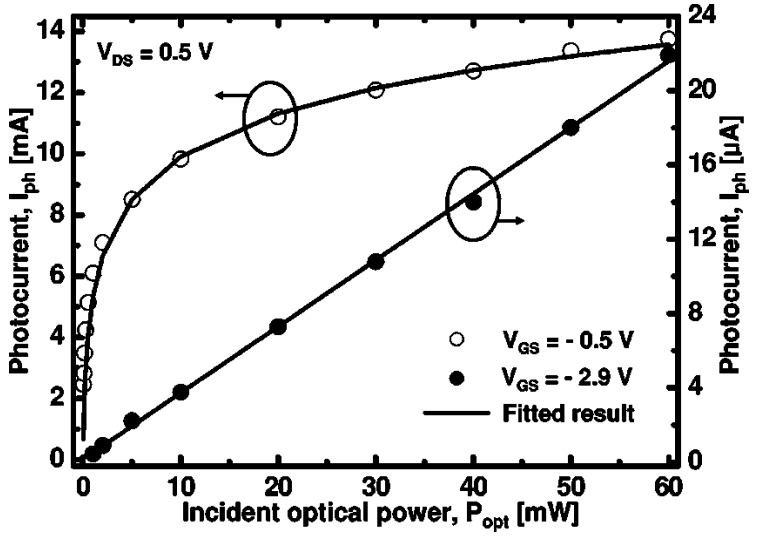

Figure 2-9. The photoconductive response in the on-state (V_{GS} = -0.5 V) and off-state (V_{GS} = -2.9 V) [120].

When the device is in the off-state ($V_{GS} > V_{TH}$ for *p*-channel), the photo-generated I_{DS} shows a linear response in correlation to the optical power of the light source due to the photoconductive effect, Figure 2-8 inset and Figure 2-9. The current can be modeled as:

$$\mathrm{I_{ph,pc}} = (e\mu cE)\mathrm{WD} = \mathrm{BP_{opt}} \qquad 2.9$$

where *e* is previously stated, μ as previously stated, *c* is the charge concentration (hole or electron), *E* the electric field in the channel, *W* the gate width, *D* the depth of absorption region, and *B* is a proportionality factor [120]. The photoconductive effect, in the simplest case, assumes contact ohmicity, which implies a charge neutrality exists in the device, thus for every injected electron there is a collected electron, unless an electron/hole recombination occurs. Because more than one electron can flow despite recombination, an efficiency higher than 100% is obtainable, supported by the ratio between recombination time and the electron transit time, consequently, a photoconductive gain is observed [64]. Further explanation and cases can be found in the following reference [121].

2.3.3 Organic Thin Film Transistors Used as Gas and Aqueous Sensors

Transistor based sensors can be loosely classified into several categories, namely, OTFTs or OFETs, and organic electrochemical transistors (OECTs) [26]. OTFT based sensors determine target analytes by physical or chemical changes in the semiconducting layers induced by the target analytes (Figure

2-10) [122]. These changes are considerably influenced by the grain boundary properties of OSC films and by the dielectric/insulator interface [26]. Therefore, OTFT based sensors are usually tuned *via* surface engineering [123–125]. In comparison, OECT based sensors have very different properties. The structural differences will be discussed later. First, the operating voltages (*ca.* 1 V) of OECTs are much lower than OTFTs, which inhibits hydrolysis during operation. Secondly, they can operate in aqueous environments that are essential for real-time chemo- and bio-sensing applications. Lastly, they have very simple architectures that allow for fabrication of channels and gate electrodes independently [26]. However, for a more detailed analysis of the topic refer to the following review papers [77,126–128].

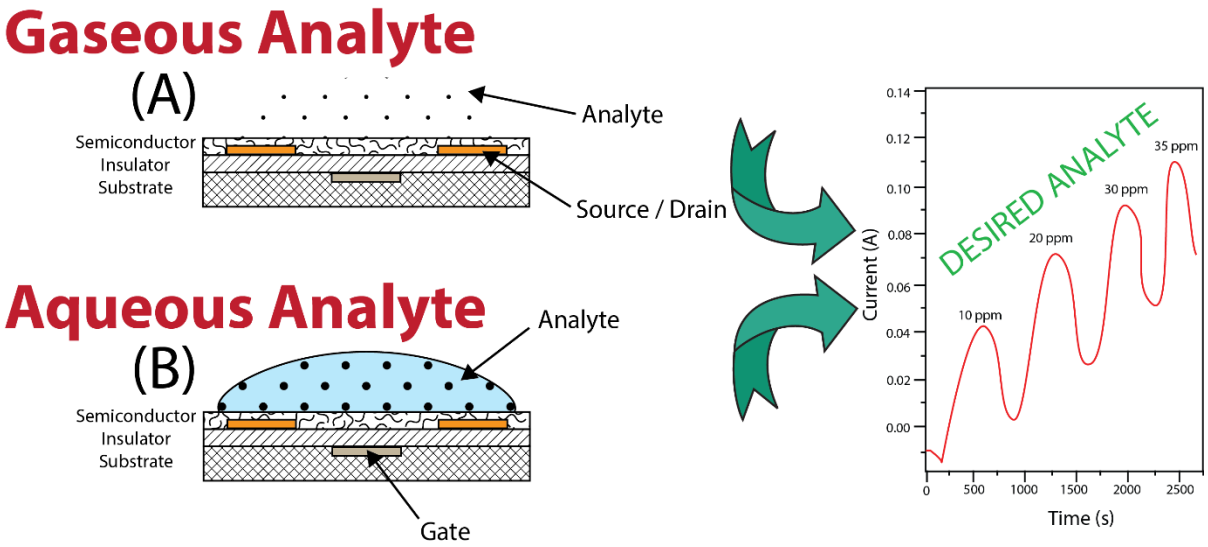

Figure 2-10. Schematic of BGBC OTFT based sensor with gaseous analyte (A) and aqueous analyte (B).

2.3.3.1 OTFT Sensor Architectures and Examples

In past, OTFT-based sensors normally adopted the TGBC and BGBC architectures (Figure 2-6) where I_{DS} is mainly modulated by the two parameters (*i.e.* V_{TH} and μ) from Equations 2.3 and 2.4. These equations are applicable to all FET based transistors [26]. It must be noted that the field-effect mobility of an OSC has little impact on the sensor performance [124]. As examples, Roberts *et al.* reported that sensing is achieved by analytes diffusing to the semiconductor-dielectric interface through the semiconductor grain boundaries inevitably influencing the field-effect carrier mobility [129]. Stoliar *et al.* reported the use of a BGBC OTFT immobilizing DNA on pentacene film [130]. Zhang *et al.* reported that the V_{TH} was positively shifted as DNA molecules were immobilized onto pentacene films

suggesting a doping mechanism [131,132]. To demonstrate real-time interaction of the analyte or rather the affinity/selectivity/detection of a target analyte with the OTFT, plots of I_{DS} as function of time are commonly reported in literature (Figure 2-11).

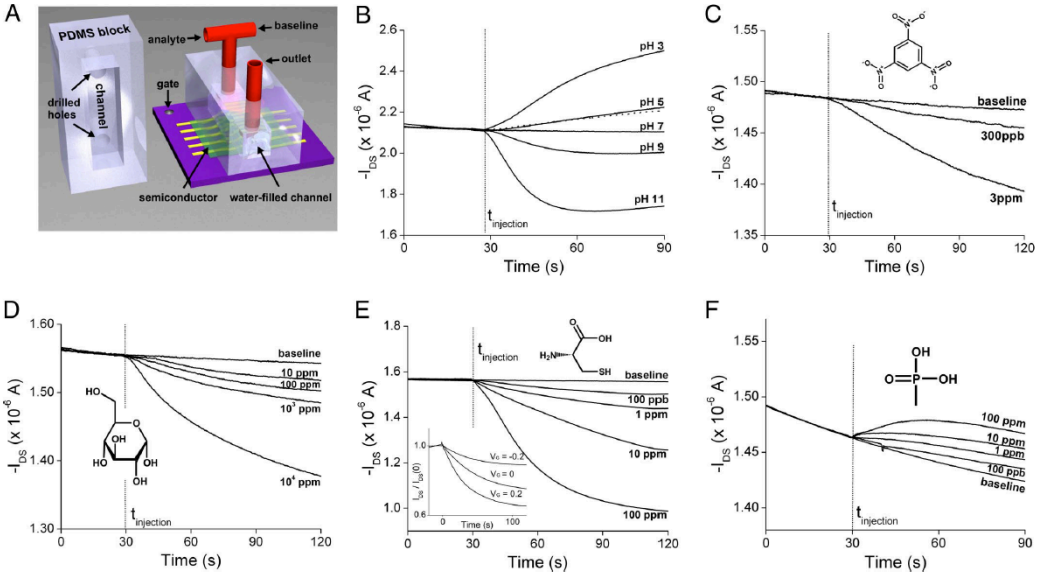

Figure 2-11. A) Schematic of encapsulated OTFT device. B-F) 5,5'-bis-(7-dodecyl-9H-fluoren-2-yl)-2,2'-bithiophene (DDFTTF) based OTFTs and their responses to various analytes and pH [129].

Several recent OTFT architectures have been employed for the study of biological/chemical analytes. The first architecture (Figure 2-12A) relies on bilayer structure with biological receptors anchored to the OSC surface. An aqueous sample with target analytes are then placed on the bio-receptor layer. Ultra-thin (22 nm) polymer gate dielectric is used for sub-volt operations [125]. Khan *et al.* reported 5,5'-bis-(7-dodecyl-9H-fluoren-2-yl)-2,2'-bithiophene (DDFTTF) modified with a thin poly-maleic anhydride layer that covalently linked peptide nucleic acid strands. Ultra-thin cross-linked poly(vinyl phenyl) polymer with 4,4'-(hexafluoroisopropylidene)dipthalic anhydride (HDA) was used as the dielectric. Their devices could detect as low as 100 nM for target DNA complements [133]. Hammock *et al.* demonstrated the addition of an ordered array of AuNPs (gold nanoparticles) on the surface of DDFTTF to functionalize the surface. Thrombin-specific aptamers were attached to the AuNPs. To prevent protein adsorption bovine serum albumin (BSA) was used. Detection of various analytes was possible by controlling the amount of thrombin on the surface [134].

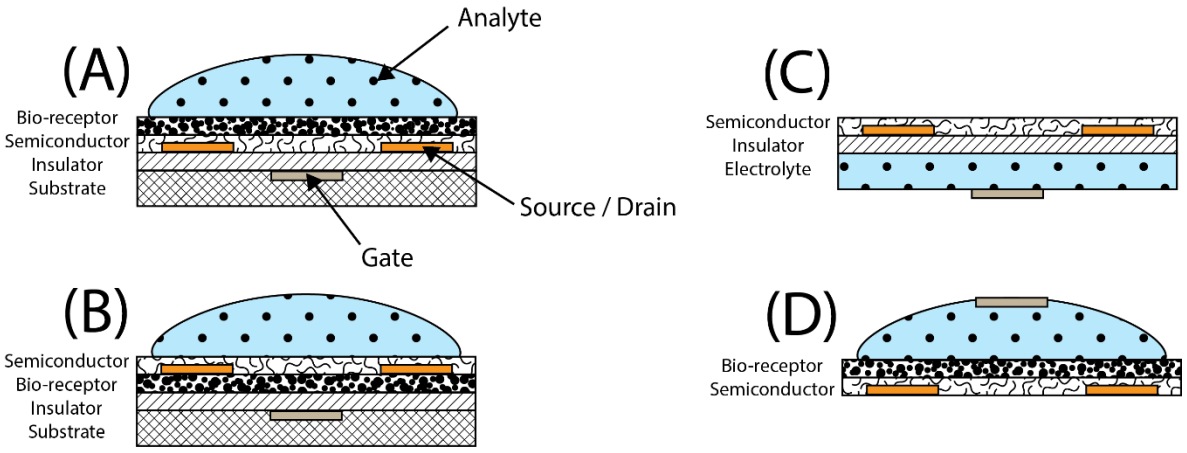

Figure 2-12. Several schematics of biosensors based on OTFT architectures; (A) top-contact bottom-gate with bilayer structure with biological receptors anchored to the semiconductor surface; (B) top-contact bottom-gate with functional bio-interlayer between semiconductor and insulator; (C) ion-sensitive OFET that has the gate separated from the insulator by an electrolyte; (D) electrolyte-gated OFET where the gate is separated from the bio-interlayer by an electrolyte.

The second architecture (Figure 2-12B) is known as the functional bio-interlayer (FBI) OFET. In this case, the bio-receptor layer is placed between the OSC and the gate dielectric. FBI-OFETs have demonstrated extreme sensitivity detecting as low as a few parts per trillion concentrations of anesthetics [123]. Likewise, Magliulo *et al.* reported ultra-sensitive (parts-per-trillion concentrations) FBI-OFETs based on a 20 nm thick poly(3-hexylthiophene) (P3HT) layer using streptavidin as the functional bio-interlayer.[135] Unfortunately, the target analyte needs to percolate/diffuse through the OSC to reach the bio-receptor layer. Therefore, large molecules are hindered and detection is limited [123,125].

The third architecture (Figure 2-12C) is known as an ion-sensitive OFET (ISOFET), which has the gate dielectric exposed to an electrolyte containing the target analyte. The gate electrode is separated from the insulator by the electrolyte. Field-effect doping modulates the I_{DS}, but the electric field across the gate dielectric is controlled by ions at the electrolyte/dielectric interface [22,136]. Bartric *et al.* demonstrated the use of ISOFETs to detect glucose and pH [137].

Lastly, the electrolyte-gated OFET (EGOFET) (Figure 2-12D) has the gate electrode separated from the bio-receptor layer by an aqueous solution of target analyte. By some authors EGOFET has been also labelled as an ISOFET as it has been reportedly used as an ion-selective sensor and that the mechanism of doping is similar to that of an ISOFET [138]. Recently, White *et al.* reported an EGOFET

based on P3HT as a DNA sensing platform with low voltage. The floating-gate electrode was functionalized with ssDNA strands [139].

In conclusion, in recent years there have been numerous architectures and most were mentioned here. However, there are some that have not been commonly employed or studied. For instance, Lai *et al.* proposed a new architecture labelled as an organic charge-modulated FET (OCMFET) as a direct replacement for ISOFET due to the limitations of miniaturizing certain components [124].

2.3.3.2 OECT Sensor Principles and Architecture

OECTs operate in a liquid or solid electrolyte at low voltages (Figure 2-13) [140]. When a V_{GS} is applied, cations (or anions) in the electrolyte are injected into the semiconducting layer causing doping and de-doping, resulting in a change of I_{DS}. Like OTFTs/OFETs, the I_{DS} of an OECT at a low V_{DS} is proportional to the μ in the channel when an effective gate voltage (V_{GS}^{eff}) is applied. So the I_{DS} is given by:

$$|V_{DS}| < |V_p - V_{GS}^{eff}| \quad I_{DS} = \frac{q\mu p_0 tW}{LV_p}\left(V_p - V_{GS}^{eff} + \frac{V_{DS}}{2}\right)V_{DS} \tag{2.10}$$

$$V_p = \frac{qp_0 t}{C_i^{eff}} \tag{2.11}$$

$$V_{GS}^{eff} = V_{GS} + V_{offset} \tag{2.12}$$

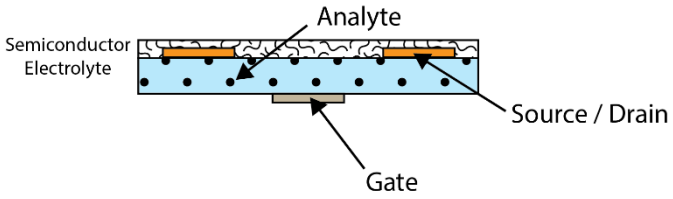

Figure 2-13. OECT sensor schematic. Similar to ISOFET but the insulator layer has been removed.

where V_P is the pinch-off voltage, q is the electric charge, and p_0 is the initial hole density in the active layer without any applied V_{GS}, t is the thickness of the active layer, C_i^{eff} is the effective gate capacitance of the transistor, and V_{offset} is determined by the potential changes at the gate/electrolyte interface and the electrolyte/channel interface [22,26].

OECTs have been praised as low-cost devices with high current modulations, fast responses, high stability in aqueous environments, and demonstrate reliable performance for long durations [26,141].

However, there are only a limited number of OSCs that can function in an OECT as most OSCs are not stable under aqueous environments. Nonetheless, OECTs have been integrated with microfluidic systems providing a new area of study with great opportunities for microfluidic-based chemical and biological sensors for real time analysis [26].

2.4 State-of-the-Art Air Stable Organic Semiconductors

The primary issue facing OTFTs for practical use is the enhancement of field-effect mobility (μ). With that said, a number of other caveats should not be neglected such as stability and durability under ambient conditions. Although intensive research efforts have significantly improved field-effect mobility reaching record numbers over 1 $cm^2 V^{-1} s^{-1}$ [142–145], in most cases, these enhancements are only achieved in inert conditions [146,147]. Among the reported state-of-the-art OSCs, benzo[b]benzo[4,5]thieno[2,3-d]thiophene (BTBT) and naphtho[2,3-b]naphtho[2',3':4,5]thieno[2,3-d]thiophene (DNTT) (Figure 2-14), have shown some of the highest hole field-effect mobilities reported to date along with moderate to excellent air stability [146,148,149].

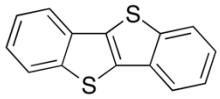

benzo[*b*]benzo[4,5]thieno[2,3-*d*]thiophene (**BTBT**)

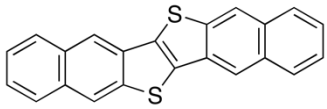

naphtho[2,3-*b*]naphtho[2',3':4,5]thieno[2,3-*d*]thiophene (**DNTT**)

Figure 2-14. Chemical structure of BTBT and DNTT.

From the structural point of view, OSCs that contain expanded π-frameworks enabling strong intermolecular overlap that in turn enhances the carrier transport in the solid state appears to be desirable. Moreover, a strong tendency to take on herringbone packing, which is suitable to construct two-dimensional electronic structure on the substrate when fabricated in OTFTs, is also considered ideal. However, such packing effects are more pertinent to small molecules than polymers. Electronically, high-lying HOMO energy levels and narrow band gaps may not be ideal and makes the OSC susceptible to air-oxidation in ambient conditions whereas narrow band gaps will readily cause photo-induced excitation that may lead to subsequent chemical reactions [150]. In order to circumvent the instability of OSCs as active channel layers in OTFTS, new OSCs employing low-lying HOMO

and LUMO energy levels with larger π-conjugated backbones have been recently developed [53,151,152]. For instance, recent reports of naphthalene-1,4,5,8-tetracarboxylic acid diimide (NDI) derivatives have demonstrated excellent air stability with modest electron field-effect mobilities approaching and in some cases surpassing 1 $cm^2 v^{-1} s^{-1}$, which have incorporated principles discussed prior (Figure 2-15) [153–155]. The small molecules, *N*,*N*′-bis(4-trifluoromethoxybenzyl) naphthalene-1,4,5,8-tetracarboxylic acid diimide (**NDI-BOCF$_3$**) and *N*,*N*′-bis(4-trifluoromethylthiobenzyl)naphthalene-1,4,5,8-tetracarboxylic acid diimide (**NDI-BSCF$_3$**), exhibit electron field-effect mobilities from 0.17 up to 0.73 $cm^2 V^{-1} s^{-1}$ in ambient conditions [153,155] whereas record-high electron field-effect mobilities (~8.5 $cm^2 V^{-1} s^{-1}$) were achieved with NDI and selenophene-containing polymer **PNBS** [156], which was also achieved under ambient conditions. Although slightly lower in field-effect mobility, but still notable, are two additional NDI-containing polymers (**PNDIF-T2** and **PNDIF-TVT**) that exhibit stable OTFT operation in ambient conditions with electron field-effect mobilities approaching 4 $cm^2 V^{-1} s^{-1}$ [154].

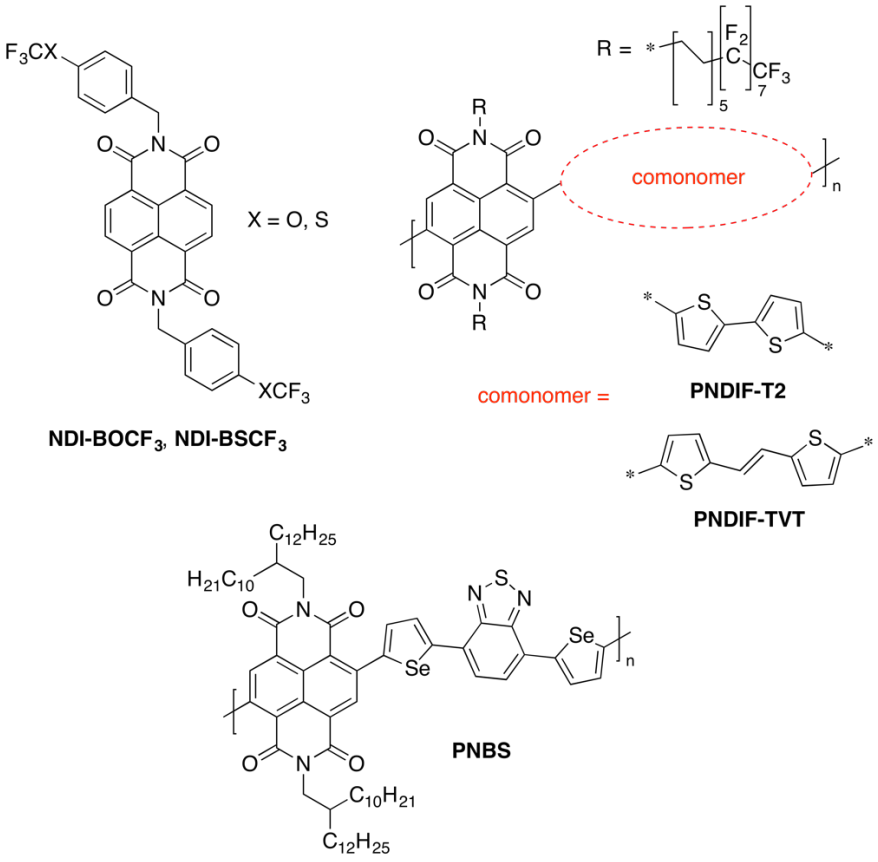

Figure 2-15. Chemical structure of NDI derivatives.

2.5 State-of-the-Art Organic Semiconductors for OTFT-Based Sensors

Incredible efforts in terms of the design and synthesis of novel OSCs, new device fabrication protocols, the establishment of suitable gate insulator layers, and interface engineering, have led to pronounced developments in high-performance OTFT-based sensors [157–159]. As previously discussed, some of the most detrimental issues always encountered in OTFTs is that their performances are susceptible to chemical interactions, photo-induced excitation, and dimensional deformation, disfavouring their use in modern circuits. From another standpoint, these unwanted problems could be simply exploited to detect external chemical and physical stimuli. The intrinsic capability of OTFTs to directly transform chemical or physical events to electrical signals renders them potentially applicable for numerous niche applications [160].

For an OTFT-based sensor, sensitivity and specificity are dominated by stimuli-electrical signal transduction and electrical signal amplification. These two fundamental processes are typically determined by the stimuli/active OSC layer interaction and the overall performance of the transistor, respectively. Although high field-effect mobility is not an essential requirement for an OTFT sensor, it may/can facilitate a greater signal amplification and response speed [157]. Nonetheless, stability and durability is required to maintain the practicality of the transistor. Certainly, compared to OTFT-based sensors, those using inorganic metal oxides as active layer materials are more stable. However, these inorganic transistors can only exhibit limited selectivity, and require high temperature for their operation. On one hand, these caveats disfavours their widespread application, on the other hand, their high-power requirements and consumption render them difficult to portabilization, thereby limiting their use in portable and real-time sensing [160].

Several different OSCs have been used in transistors for sensing applications and some have been mentioned in previous sections. The most notable OSCs used in such devices and applications have been pentacene, P3HT, poly(9,9-dioctylfluorene-co-bithiophene) (F8T2), poly(para-phenylene ethynylene)s with thioacetyl end groups (TA-PPE), 2,5-bis(dibutylaminostyryl)-1,4-phenylene-b-alkyne-b-1,4-bis(2-ethylhexyl)benzene terpolymer (BAS-PPE), α,ω-dihexylsexithiophene (DHα6T), and DDFTTF (Figure 2-1 and Figure 2-16). While polyaniline (PANI) and poly(3,4-ethylenedioxythiophene):poly(styrene sulfonic acid) (PEDOT:PSS) are quite common as well, they represent a class of semiconductors that are typically employed in OECT-based sensors only. In either case, the resulting devices can be used in various chemical sensors (humidity, ions, and pH), biosensors

(enzyme, antibody-antigen, glucose, dopamine, DNA, nicotinamide adenine dinucleotide (NADH) and cell), and photodetectors [77,127,160–162].

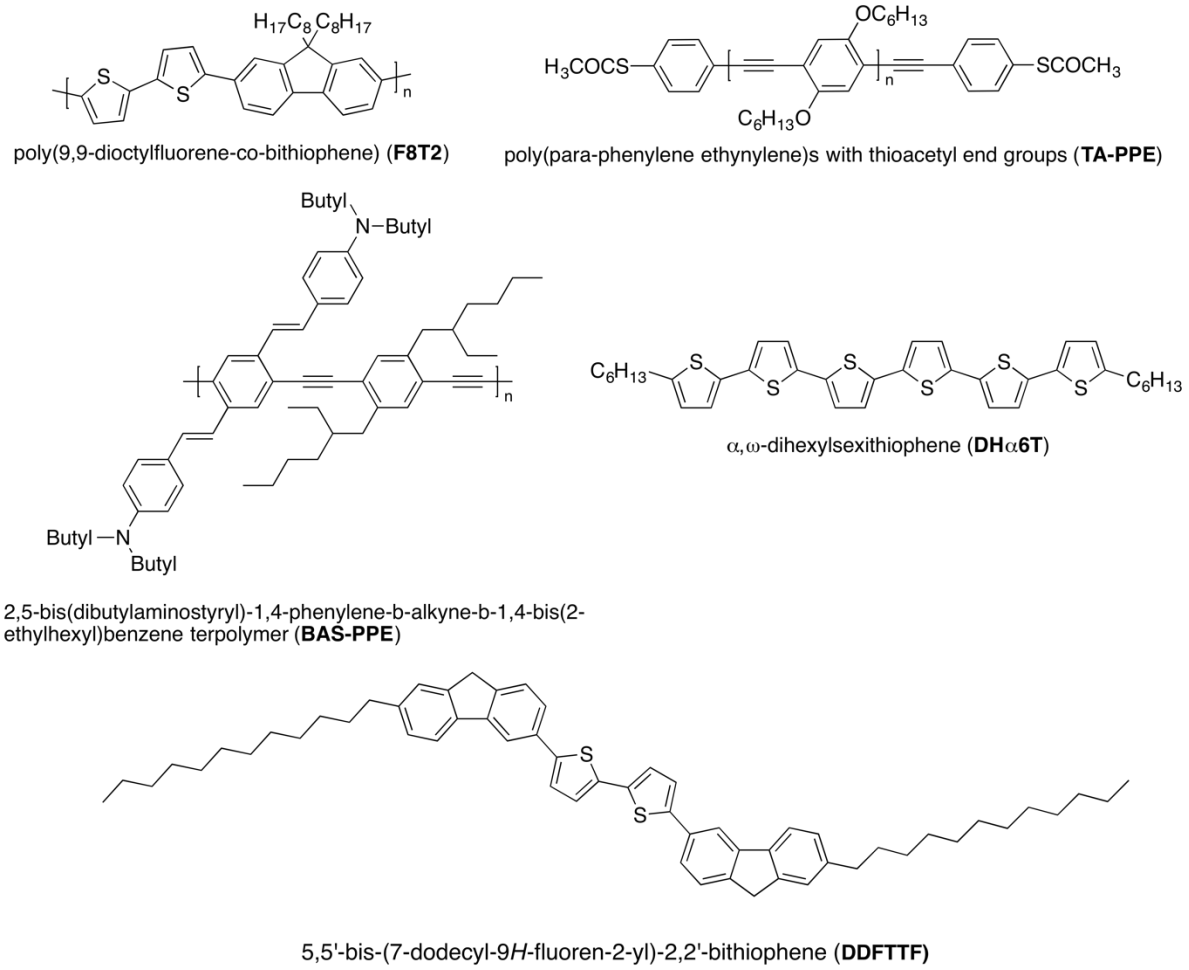

Figure 2-16. Chemical structures of several common active OSC layers for sensors.

In more recent years, a large number of novel OSCs with modest field-effect mobilities and significant improvements in stability have been synthesized, which will enable the fabrication of high performance OTFT-based sensors for real applications (Figure 2-17) [161]. For instance, PEDOT:PSS, although commonly used in OECT-based sensors, still has some drawbacks such as poor device lifetime induced by its acidity, structural, and electronic inhomogeneity. Recently, Liang *et al*. prepared polydopamine:polystyrenesulfonate (PDA:PSS) *via* the self-polymerization of dopamine in aqueous PSS. Based on their results, DA:PSS exhibited stable and quasireversible electrochemical oxidation behavior, excellent film formation, and lower acidity than that of PEDOT:PSS, demonstrating a viable alternative material to PEDOT:PSS [163]. Alternatively, highly sensitive and selective OTFT-based

humidity sensors comprising of porous pentacene films have been reported [164,165]. An extension of this work based on a porous-induced π-conjugated polymer (PBIBDF-BT), which demonstrated an enhancement in both sensitivity and selectivity towards humidity surpassing that achieved by the aforementioned material and others [166]. Following suit, a porous composite made of PDPP-TVT, a diketopyrrolopyrrole based π-conjugated polymer, and a metal organic framework (MOF) is reported as a receptor and pre-concentrator site for sensing explosive analytes. Surya *et al.* established that this above-mentioned material is efficient for the detection of explosive vapors with stable operation in ambient conditions with good selectivity as several explosive analytes were tested. Although, several other recent reports on the detection of explosives in vapor phase using alternative materials have been made [167], novel materials with greater sensitivity, stability, and selectivity are still highly sought after with biocompatibility and ease of fabrication in mind.

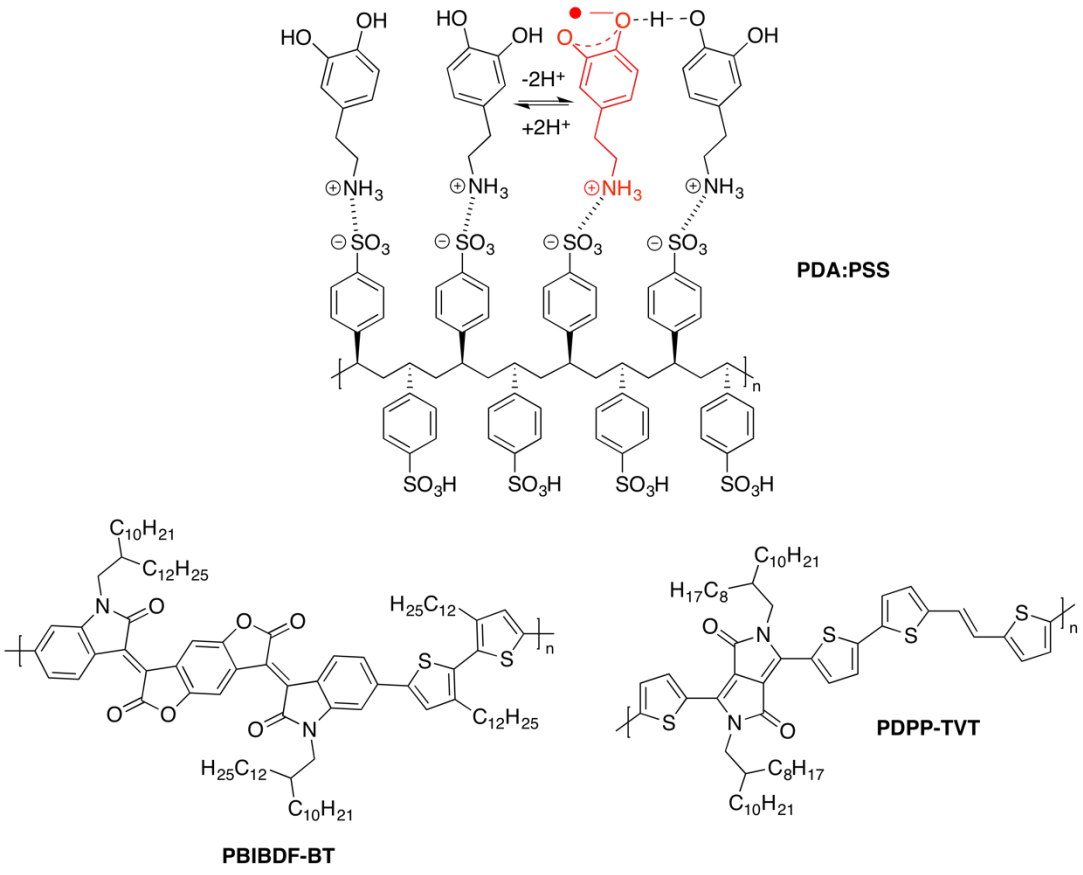

Figure 2-17. Chemical structures of novel OSCs as potential active channel layers for OTFT-based sensors.

Chapter 3

Fluorene-Fused Triphenodioxazine Based Polymer

This chapter is based on the following publication:

L. Guo, J. Quinn, J. Wang, C. Guo, X. Li, J. Wang, Y. Li, *Dyes Pigm.* **2016**, *132*, 329–335.

3.1 Introduction

Although, triphenodioxazine (TPDO), Figure 3-1, is the core structure of several commercial dyes and pigments including Pigment Violet 23, 35, 37, and 54 and Direct Blue 104, 106-109, and 190 [168], it is not a naturally occurring chromophore. TPDO falls into a general glass of compounds known as dioxazines which was first discovered in 1879 [169]. The conjugated quinoidal structure, which is symmetrically planar, is a very efficient chromophore with an intense coloration. The sulfonated derivatives of the parent structure yield colorants for direct usage on cotton; however, the parent triphenodioxazine has no practical importance as a colorant. It was not until 1952, that a strong violet pigment derived from a 9,10-dichlorotriphenodioxazine, was patented as Pigment Violet 23. While, not naturally derived, TPDO core reflects upon the long-term research aim of dyes that combine brightness and fastness properties that are superior to those chromophores that were natural obtained such as some anthraquinone dyes [170,171].

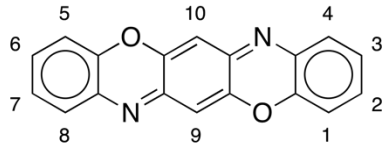

Figure 3-1. Parent structure of triphenodioxazine (TPDO).

Recently, several small molecule TPDO derivatives have been used as semiconductors in OPVs [172,173], dye-sensitized solar cells [174], and OTFTs [175–177], showing promising power conversion efficiencies as high as 6.3 % [174] and electron mobilities approaching 0.11 $cm^2V^{-1}s^{-1}$ [177]. Thus, we believe it is worthwhile to incorporate the TPDO moiety into polymer semiconductors to explore the optoelectronic properties of the resulting polymers.

3.2 Theoretical Study of Proposed Polymer

The calculated frontier energy levels for the isomeric **FTPDO-a**, **b** and **c** monomer units display similar characteristics and have energies within a narrow range of -3.04 to -3.08 eV for LUMO and -5.20 to -

5.28 eV for HOMO (Figure 3-2; Appendix, Figure A-1). Interestingly, both the LUMO and HOMO energy levels decrease by intervals of 0.02 and 0.04 eV, respectively, from **FTPDO-a** to **FTPDO-c**, suggesting that the LUMO and HOMO energy levels are only slightly affected by the different placement of the fluorene moiety fused to the TPDO core. Compared with the **FTPDO-a**, **b** and **c** monomer units, the calculated frontier energy levels for **FTPDOBT-a**, **b** and **c** dimers displayed only a minor increase in LUMO energy levels ranging from -2.95 to -2.97 eV, while the HOMO energy levels increased notably as expected with the addition of the bithiophene donor, ranging from -4.90 to -4.95 eV. For each dimer, the LUMO wavefunction localizes onto the **FTPDO** moiety and is more influenced by the electron-accepting nature of the acceptor, whereas the HOMO wavefunction is more delocalized along the dimer backbone and only marginally affected by the acceptor characteristics (Appendix, Figure A-2, Figure A-3 and Figure A-4).

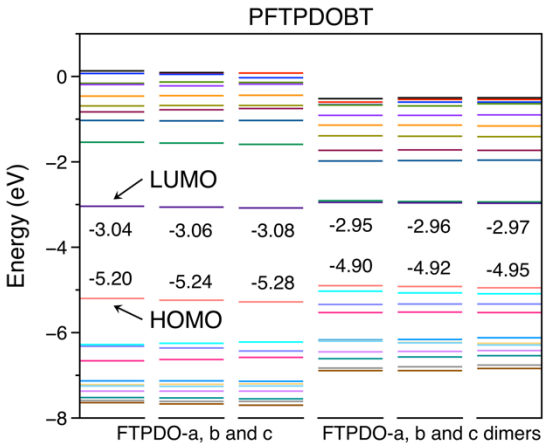

Figure 3-2. The molecular orbital energies (+/-10 from LUMO and HOMO) for **FTPDO-a**, **b** and **c** and **FTPDOBT-a**, **b** and **c** dimers.

3.3 Synthesis of FTPDO

The new fluorene-fused TPDO compound, **FTPDO**, and its polymer **PFTPDOBT** were prepared according to the synthetic route outlined in Scheme 3-1. Although, it must be noted that the **FTPDO** monomer was prepared by our collaborators. 2-Bromofluorene was first disubstituted at the 9-position with hexadecyl groups, followed by nitration at the 5-position, producing compound **2**. Reduction of **2** with hydrazine hydrate in the presence of iron (III) acetylacetonate ($Fe(acac)_3$) as a catalyst in ethylene glycol at 155 °C afforded the key amino fluorene compound **3**, which was reacted with chloranil to form the target **FTPDO**. Because the ring closure could occur at the 6- or 8-position of a fluorene unit,

three possible isomers, **FTPTO-a**, **b**, and **c**, might form (shown in the insert of Scheme 3-1). Thin layer chromatography (TLC) analysis indeed showed three overlapped spots, but the separation of these three compounds was not successful due to their very similar polarity. Nonetheless, since all three isomers of **FTPDO** have fully π-conjugated pathways between the two C-Br groups, they would form extended main chain conjugation if they are incorporated in the polymer backbone. Therefore, the mixture of **FTPTO-a**, **b**, and **c** was used as a comonomer to 5,5-bis(trimethylstannyl)-2,2'-bithiophene to form the polymer **PFTPDOBT** under typical Stille coupling polymerization conditions in the presence of $Pd_2(dba)_3$/P(*o*-tolyl)$_3$ as a catalyst in chlorobenzene at 130 °C for 72 h. The resulting polymer was precipitated from methanol and further purified by Soxhlet extraction using acetone, hexane, and chloroform. The polymer fraction dissolved by chloroform was dried to give the final polymer product in 82% yield.

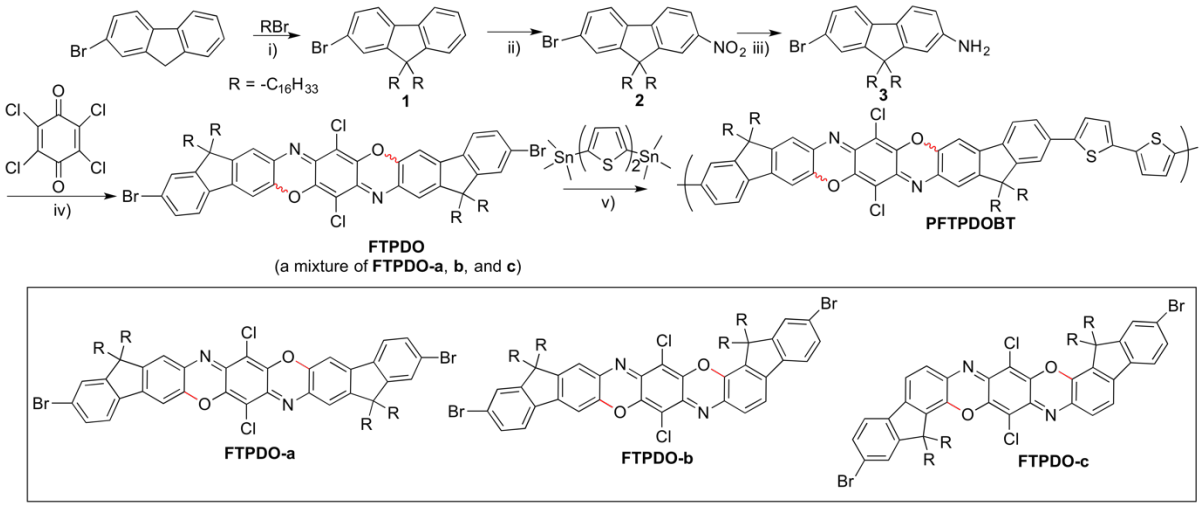

Scheme 3-1. Synthetic route to **FTPDO** and its polymer **PFTPDOBT**. i) *t*-BuOK, THF, r. t., 80%; ii) 90% HNO_3, 1, 2-dichloroethane, reflux, 94%; iii) $NH_2NH_2.H_2O$ (3.0 mL), $Fe(acac)_3$, ethylene glycol, 152 °C, 52%; iv) 4-toluenesulfonylchloride, nitrobenzene, 40 °C, 6%; v) $Pd_2(dba)_3$/P(*o*-tolyl)$_3$), chlorobenzene, 130 °C, 82%.

3.4 Characterization of Aforementioned Polymer

3.4.1 Molecular Weight Analysis

The proposed step growth mechanism by which π-conjugated copolymers are synthesized intrinsically makes molecular weight control difficult to achieve, although, alternative mechanisms for polymer

growth have been proposed [178]. Whilst molecular weight effects on π-conjugated copolymer properties have been observed anecdotally [179], more recently, pseudo-control over π-conjugated copolymers has been established by invoking the Carothers equation (number average degree of polymerization, X_n) [180]:

$$X_n = \frac{1+r}{1+r-2rp}, (0 < r \leq 1, p \leq 1) \quad 3.1$$

$$X_n = \frac{1+r}{1-r}, (0 < r \leq 1, p = 1) \quad 3.2$$

To use the Carothers equation to control the molecular weight in a predicative manner, the facile methodology is to vary the stoichiometric ratio of two monomers (r in Equation 3.1) while assuming the degree of reaction (p) is at unity or approaching unity. With this assumption, Equation 3.1 is simplified into Equation 3.2. Nonetheless, to effectively use Equation 3.2, one would have to optimize the reaction to promote completion (p = 1). This may be achieved by having pure monomers, whereby a precisely tuned stoichiometric ratio, r, is obtained in conjunction with high purity palladium catalyst. However, it is considered very difficult to obtain polymers of high molecular weight *via* palladium catalyzed polycondensation for any new π-conjugated copolymers not to mention accurately controlling molecular weight [181]. With that said, a stoichiometric ratio of monomers (1:1) was maintained for the aforementioned and latter Stille coupling reactions in thought of achieving high molecular weight; thus the X_n and number average molecular weight (M_n) simplify to [182]:

$$X_n = \frac{1}{1-p}, (r = 1) \quad 3.3$$

$$M_n = M_o X_n = \frac{M_o}{1-p} \quad 3.4$$

whereby the weight average degree of polymerization (X_w) and weight average molecular weight (M_w) are then define as [182]:

$$X_w = \frac{1+p}{1-p}, (r = 1) \quad 3.5$$

$$M_w = M_o X_w = \frac{M_0(1+p)}{1-p} \quad 3.6$$

hence, the polydispersity index (PDI) can be defined as [182]:

$$PDI = \frac{M_w}{M_n} = 1 + p \quad 3.7$$

therefore, if p = 1, the narrowest PDI that can be achieved in theory is 2 for step growth/polycondensation polymerization.

To elucidate the molecular weight properties, gel permeation chromatography (GPC) was used to characterize **PFTPDOBT**. Using 1,2,4-trichlorobenzene as an eluent at a column temperature of 140 °C, the M_n and *PDI* were determined to be 15.4 kDa and 2.64, respectively, relative to the polystyrene standards (Figure 3-3A). As explained above, the resulting PDI is expected to be greater than two, and such, the results establish a narrow PDI for **PFTPDOBT**. Moreover, a monomodal distribution was observed supporting the linear growth of **PFTPDOBT** rather than branching or crosslinking through the chlorine substituents on the **FTPDO** core.

The thermogravimetric analysis (TGA) thermogram of **PFTPDOBT** under nitrogen showed the 5% weight loss at a temperature of 354 °C (Figure 3-3B), indicating that this polymer is quite thermally stable. The differential scanning calorimetry (DSC) measurement did not show any obvious thermal transition in a temperature range between 25 °C and 300 °C (Figure 3-3C).

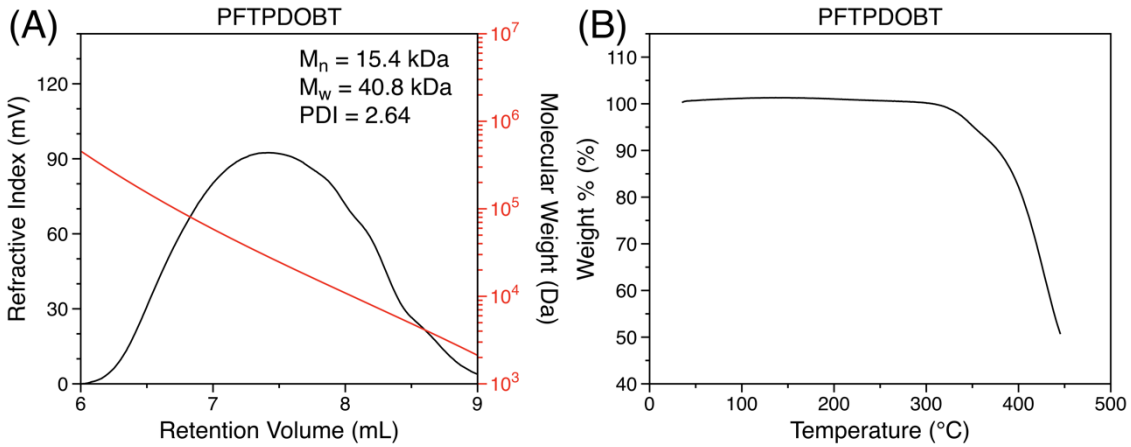

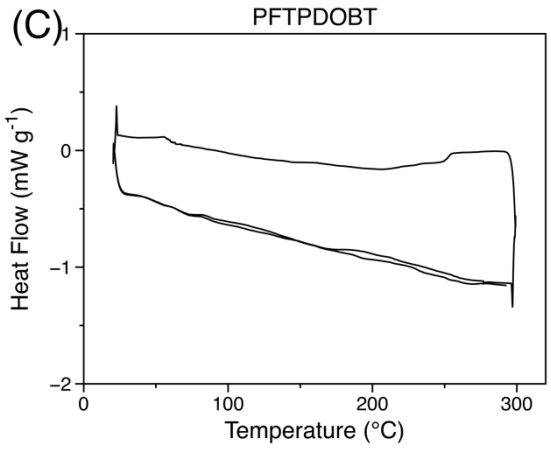

Figure 3-3. High temperature GPC trace of **PFTPDOBT** with refractive index detector measured at 140 °C using 1,2,4-trichlorobenzene as eluent and polystyrene as standards (A), the TGA (B) and DSC thermogram (C) of **PFTPDOBT** measured at a heating rate of 10 and 20 °C min^{-1} under nitrogen, respectively.

3.4.2 Optical and Electrochemical Analysis

PFTPDOBT showed a λ_{max} at 649 nm and a shoulder at ~670 nm in a chloroform solution. The polymer thin film spin-coated on a glass substrate showed a λ_{max} at 673 nm and a minor peak at ~620 nm (Figure 3-4A). The E_g^{opt} calculated from the onset absorption of the polymer film is 1.66 eV. The CV curves of the polymer film showed strong oxidation peaks, but no obvious reduction peaks (Figure 3-4B). The HOMO energy level of **PFTPDOBT** is obtained from its oxidation onset potential using ferrocene (Fc) ($E_{HOMO, Fc}$ = -4.8 eV) as a reference to be -5.61 eV. The lowest unoccupied molecular orbital (LUMO) energy level is estimated from the HOMO and the optical band gap to be -3.95 eV. The rather low HOMO and LUMO energy levels of **PFTPDOBT** suggest that **FTPDO** is a strong electron withdrawing building block. The narrow band gap of this polymer can be attributed to the intramolecular charge transfer from the donor (bithiophene) to the acceptor (the TPDO core).

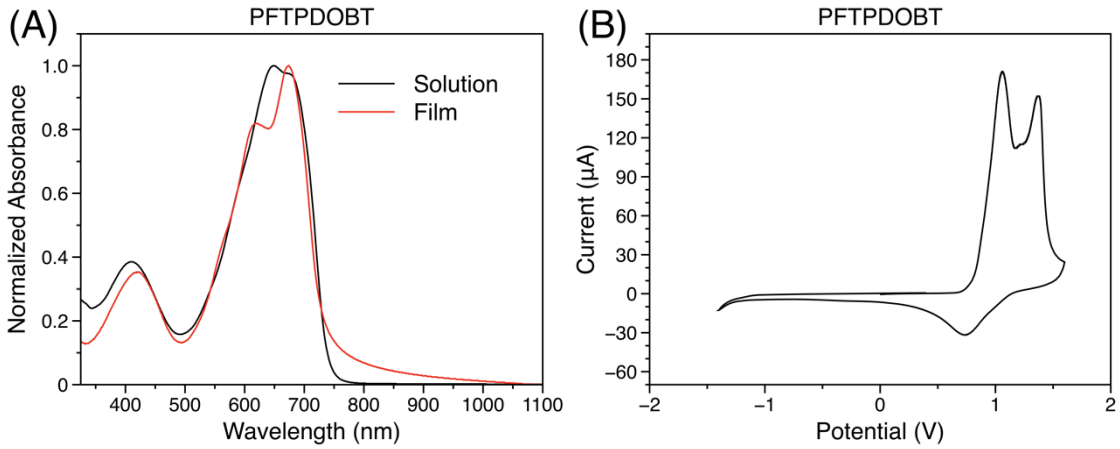

Figure 3-4. UV-Vis-NIR absorption spectra (A) and CV curve (B) of **PFTPDOBT**.

3.4.3 Molecular Ordering and Morphological Analysis

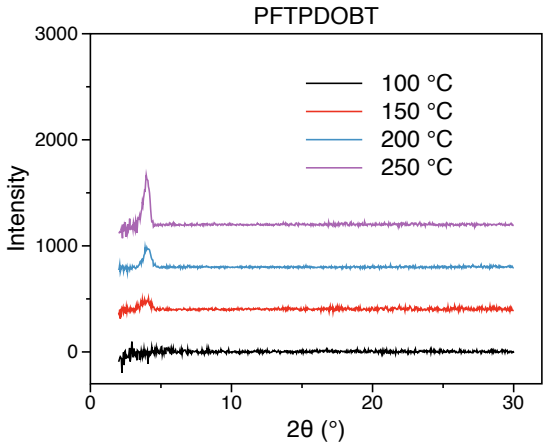

Figure 3-5. Reflection XRD diagram of polymer thin films spin-coated on DDTS-modified SiO_2/Si substrates and annealed at various temperatures with Cu Kα radiation (λ = 0.15406 nm).

To determine the molecular ordering or crystallinity, **PFTPDOBT** films were prepared by spin-coating a polymer solution in chloroform on DDTS-modified SiO_2/Si substrates and annealed at various temperatures, which were subject to XRD measurements. No distinct reflection peak was observed, suggesting the polymer film annealed at this temperature is amorphous (Figure 3-5). Once the annealing temperature is increased to 150 °C, a weak diffraction peak appeared at 2θ = ~4 °, which corresponds to a *d*-spacing of 2.21 nm. Further increasing the annealing temperature intensifies this diffraction peak. However, the intensity of this peak is still very weak even at a high annealing temperature of 250 °C. The poor molecular organization of this polymer is most likely due to the existence of three isomeric

FTPDO units (Scheme 1), which results in kinked polymer main chains, hampering the formation of ordered chain packing [183]. The morphology of the polymer films changes with annealing temperature were characterized by AFM (Figure 3-6). The 100 °C- and 150 °C-annealed films are quite smooth with a small square root roughness (R_q) of 0.6 nm. Once the annealing temperature is increased to 200 °C, large grains begin to appear and the film becomes rougher (R_q =1.2 nm). The grain size further grows as the temperature increases to 250 °C, which is accompanied with the increased crystallinity of the film verified by the XRD data.

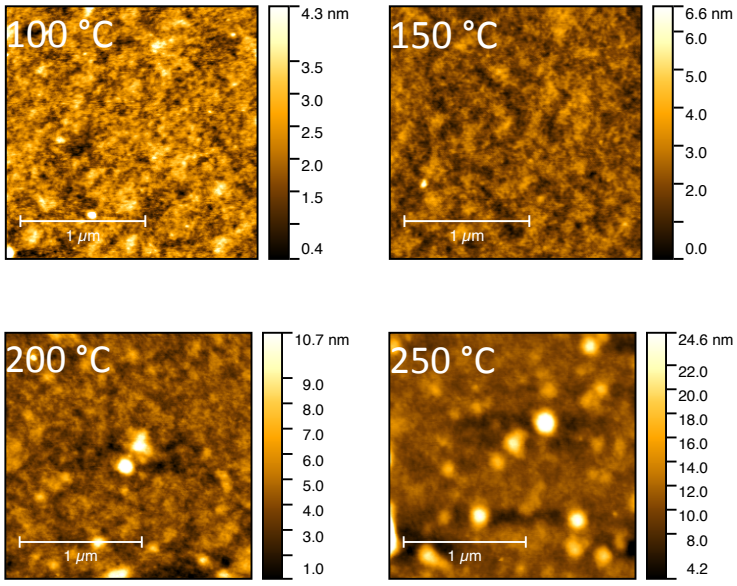

Figure 3-6. AFM images of **PFTPDOBT** (2 μm × 2 μm, 1 μm scale bars) thin films after annealing at various temperatures.

3.4.4 I-V Characterization

For detailed device fabrication refer to Appendix D.

3.4.4.1 Nitrogen and Air Stability Study

PFTPDOBT was evaluated as a channel semiconductor in BGBC devices. A solution of **PFTPDOBT** in chloroform was spin-coated on a dodecyltrichlorosilane modified SiO_2/n^{++}-Si wafer substrate with prepatterned Au source and drain pairs and annealed at different temperatures for 15 min in a glove box filled with nitrogen. All devices showed typical p-channel field effect transistor performance (Figure 3-7, Figure 3-8 and Figure 3-9; Appendix, Table D-1). The best hole mobility of 5.27×10^{-3} $cm^2 V^{-1} s^-$

[1] was obtained for a device annealed at 200 °C (Figure 3-7; Appendix, Table D-1). To evaluate the air stability of this polymer under operation, the devices were characterized in air (with a relative humidity of 45%) with the polymer semiconductor layer exposed to air. Surprisingly, the devices at all annealing temperatures showed significant improvements in the hole mobilities (Figure 3-7, Figure 3-8 and Figure 3-9; Appendix, Table D-2). The highest mobility of 1.44×10^{-2} cm^2 V^{-1} s^{-1} was obtained for a device with the polymer film annealed at 200 °C (Figure 3-8).

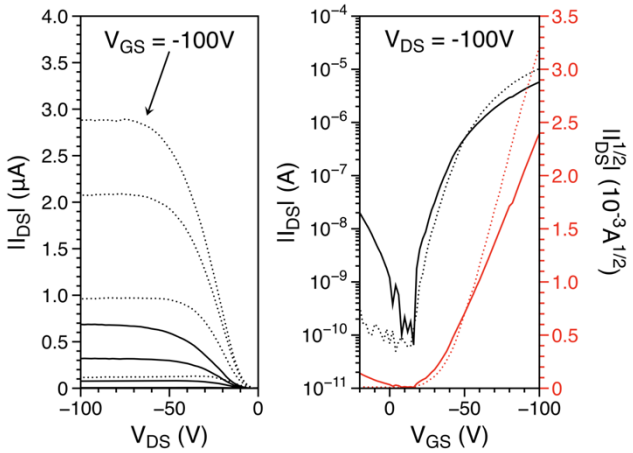

Figure 3-7. Output (left) and transfer (right) characteristics of an OTFT device with a **PFTPDOBT** film annealed at 200 °C in nitrogen and tested in nitrogen (solid lines) and air (dotted lines). Device dimensions: L = 30 μm; W = 1000 μm. Output curves are measured from 0 to - 100 V at - 20 V increments.

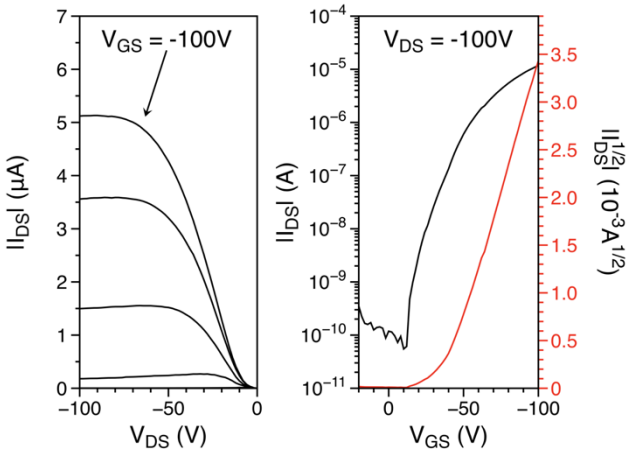

Figure 3-8. Output (left) and transfer (right) characteristics of an OTFT device with a **PFTPDOBT** film annealed at 200 °C in air and tested in air. Device dimensions: L = 30 μm; W = 1000 μm. Output curves are measured from 0 to - 100 V at - 20 V increments.

To further study the influence of air on the charge transport performance of this polymer, the polymer thin films were annealed in air at different temperatures ranging from 50 °C to 250 °C and tested in air. Unexpectedly, the average mobilities increased further at all annealing temperatures (Figure 3-7, Figure 3-8 and Figure 3-9; Appendix, Table D-3). The highest mobility of 1.57×10^{-2} cm^2 V^{-1} s^{-1} was achieved at an annealing temperature of 200 °C (Figure 3-7 and Figure 3-8). It appears that oxygen, moisture, or some other component in air promoted the device performance. To investigate if the polymer is intact after annealing in air, the polymer films annealed in nitrogen or air were characterized by UV-Vis spectrometry. The absorption profiles and the λ_{max} of the polymer films annealed in nitrogen or air are very similar at all respective annealing temperatures (Appendix; Figure C-1 and Figure C-2). In both environments, the λ_{max} increases with annealing temperature, which was associated with the increased molecular ordering as evidenced by the XRD measurement. Based on the above UV-Vis study, it seems that air had minimal influences on this polymer at an annealing temperature up to 250 °C. It should be noted that when the devices measured in air were transferred into the nitrogen-filled glove box for re-testing, the mobilities decreased compared to the values measured in air. Once the devices were taken out of the glove box and measured again in air, the mobilities recovered. Reproducible results were obtained when this process was repeated. The stability of polymer semiconductors at high temperatures in air is very important for device manufacturing because it allows the annealing step to be conducted in air, which facilitates the roll-to-roll high throughput production of printed electronics. The reason for the marked enhancement of the device performance of the polymer films annealed and/or measured

in air is still unclear. One possible reason might be the interaction of oxygen with the Au source and drain contacts. A previous study showed that the work function of gold increased from 4.7–4.9 eV to 5.0–5.5 eV, which could reduce the hole injection barrier from the Au source to the polymer semiconductor layer [184]. The effect might be particularly prominent for this polymer because its HOMO energy level is rather low (-5.61 eV).

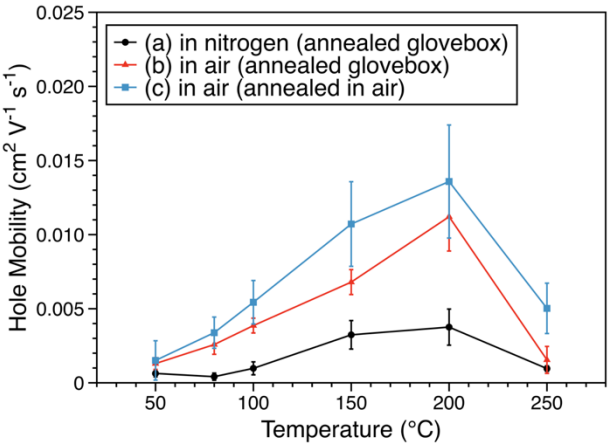

Figure 3-9. The hole mobilities of BGBC OTFT devices with **PFTPDOBT** films at different annealing temperatures: (a) polymer films annealed in nitrogen and devices tested in nitrogen, (b) polymer films annealed in nitrogen and devices tested in air, and (c) polymer films annealed in air and devices tested in air. Device dimensions: L = 30 µm; W = 1000 µm.

3.4.4.2 Preliminary Water-Gated Transistor Study

As previously mentioned in Chapter 2, OTFTs in aqueous conditions may operate under two different device principles (OECT and OFET). In either case, with the potential of fabricating flexible devices, simple design, and implementation, OTFTs have been and still are heavily investigated as chemo- and bio-sensors. Further details are given in 2.3.3.2; but OECTs essentially operate *via* a gate potential drift mediated by the diffusion of ions into the OSC. The ions modulate the doping which, in effect, modulates the conductivity. As such, OECTs can translate ionic currents into electronic equivalents thereby creating an applicable device for numerous applications [161,185,186]. OFETs operate in a much different fashion (see 2.3.3.1) and effectively rely on a charge sheet that amasses in the semiconducting channel. Detection of substances is achievable *via* capacitive coupling of charges at the gate, semiconductor, or the dielectric interface or by alteration of the capacitance at these interfaces which either reflects in a change of μ and/or V_{TH} [187].

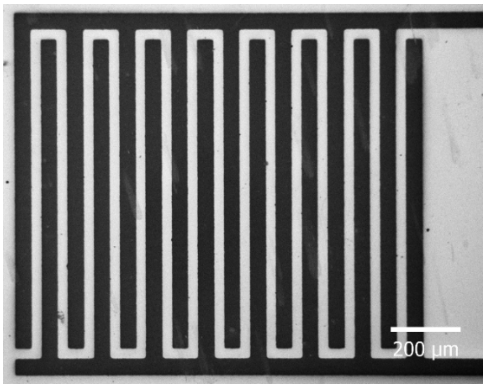

Figure 3-10. Scanning electron microscopy (SEM) image of the interdigitated BGBC OPT, wherein the dark pattern represents the interdigitated source and drain contacts, with a W = 15,800 µm and a L = 30 µm.

Herein, we present the preliminary study of **PFTPDOBT** water-gated transistor (Figure 3-11A) as this OSC demonstrated excellent stability in ambient conditions (see 3.4.4.1). In all cases these devices operate under OFET principles (supported by the low effective capacitance per unit area discussed later) [188,189]. The devices were prepared on SiO_2/n^{++}-doped Si substrates with gold contacts for source and drain. Polymer solutions (5 mg mL^{-1}) were spin-coated at 3000 rpm for 80 s and subsequently annealed from 50 to 200 at 50 °C steps and 20 min intervals in air. The device dimensions were 15,800 µm × 30 µm (W × L) as seen in Figure 3-10. Similar to an ISOFET or EGOFET (discussed in 2.3.3.1), water-gated transistors have a gate, in this case a tungsten probe, placed into an electrolyte, 16.8 MΩ water droplet, on top of the OSC. Forward and reverse sweeps were performed to demonstrate stability (hysteresis) of devices when in operation. **PFTPDOBT** devices exhibit hysteresis typical of water-gated devices. The apparent hysteresis may be due to the combination of low ionic strength ($[H3O^+] = [OH^-] = 10^{-7}$ M) for pure water and the poor capacitive coupling between the ions in solution and the charge carriers in the active channel of the OSC. Alternatively, the hysteresis may be indicative of an ion doping process [190]. **PFTPDOBT** gave an average mobility of ~1×10^{-3} cm^2 V^{-1} s^{-1} with an I_{ON}/I_{OFF} of ~10^2. The V_{GS} in the transfer curves were swept from 0.2 V to -1 V whereas the V_{DS} in the output curves were swept from 0 V to -1 V. However, only at high V_{GS} (V_{ON} > -0.8 V) will the devices operate with a p-channel. In the off-state regime the V_{GS} < -0.8 V depletes the interfacial holes under the influence a V_{GS} approaching positive V_{GS}; however, the off-state current is quite high suggesting potential ambipolar charge transport characteristics.

The device gate leakage current was also monitored during the transfer sweep (Figure 3-11B). Gate leakage currents remained below 70 nA. Moreover, no redox peak was observed further supporting the stability of these OSCs.

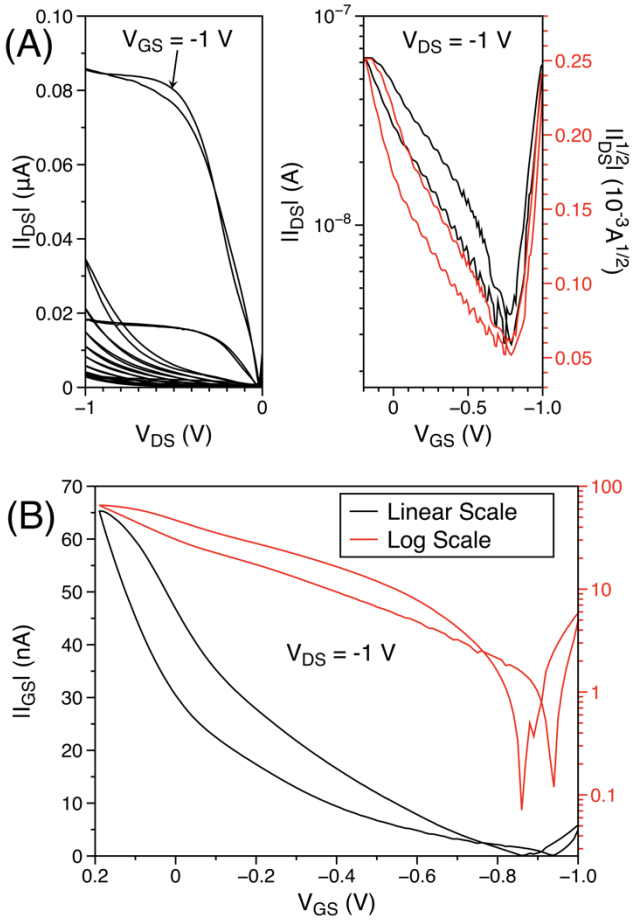

Figure 3-11. The output (left) and transfer (right) curves of **PFTPDOBT** (A) water-gated transistor and gate leakage current (linear and log scales) (B) for the aforesaid water-gated transistor in 16.8 MΩ water. A tungsten probe was used as the gate electrode.

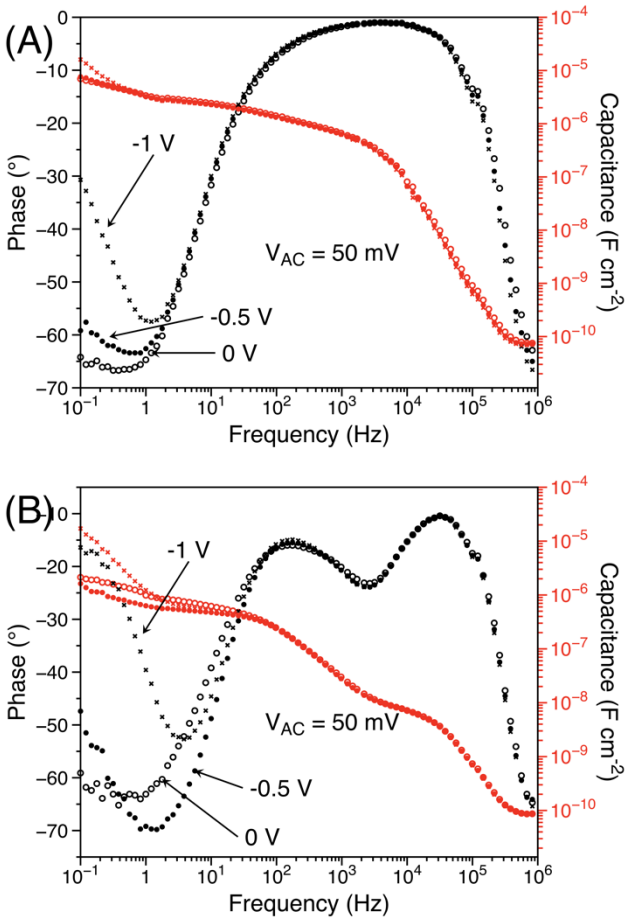

Figure 3-12. Phase and capacitance versus frequency for Au/water/Au (A) and Au/water/**PFTPDOBT**/Au structures (B) when used in an equivalent electrical circuit with deionized water at different V_{DC} bias'.

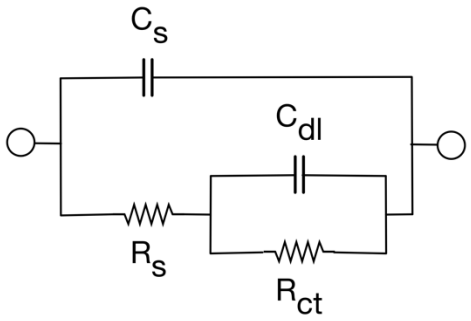

Figure 3-13. Scheme of the equivalent electrical circuit for the Au/water/OSC/Au structure where C_{dl} and Cs are the double layer and solution capacitance, respectively, R_s and R_{ct} are the electrolyte solution and charge transfer processes resistance, respectively.

Elucidating the charge polarization dynamics within the water droplet between gate and OSC would help in predicting the transient behaviour of the I_{DS} but also provide the C_i. Electrochemical impedance spectroscopy (EIS) was performed on both Au/water/Au and Au/water/OSC/Au (Figure 3-12). The effective capacitance C versus frequency is extracted from the complex impedance by using a simple equivalent circuit (Figure 3-13). The gold only capacitor exhibits characteristic behaviour as reported in literature [188]. The double layer capacitance of the Au/water/OSC/Au structure is ~2 μF cm^{-2} which is lower than the Au/water/Au structure (~7 μF cm^{-2}) suggests no bulk doping is occurring in the **PFTPDOBT** film. Capacitance values were obtained from the lowest frequency at 0 V DC bias (discussed below). The low double layer capacitance supports the hypothesis that these devices operate under OFET principles and not as OECTs [189].

In order to simulate the presence of a gate bias, as utilized in a transistor, a DC bias was applied between the two electrodes of the capacitor structure. The applied voltage at -0.5 V appears to slightly slow down the formation double layers indicated by the small shift towards lower frequencies whereby decreasing the resistive behaviour. At -1 V a small shift to higher frequencies is observed, thus increasing the formation of the double layers while dramatically increasing the resistive behaviour at lower frequencies which is attributed to the hydrolysis of water. The resistive behaviour begins at lower biases and higher frequencies for the Au/water/OSC/Au structure than that observed for the Au/water/Au structure.

3.5 Conclusion

In conclusion, a novel electron acceptor building block, fluorene-fused triphenodioxazine (**FTPDO**), and a donor-acceptor polymer based on **FTPDO** and bithiophene, **PFTPDOBT**, are presented. This new polymer showed good hole transport performance with hole mobilities of up to 1.57×10^{-2} $cm^2 V^{-1} s^{-1}$ in OTFTs despite of its poor molecular ordering due to the existence of several isomeric **FTPDO** units. Particularly important is that the highest device performance was achieved by annealing the polymer films and testing the devices in air. The excellent air stability, good charge transport performance, and narrow band gap (1.66 eV) make the **FTPDO**-based polymers promising for stable printed electronics where air exposure during the manufacturing and operation of these electronics is inevitable. The charge transport performance is expected to improve if an isomerically pure **FTPDO** monomer can be isolated or synthesized, which is the is the subject of future study on this new class of polymers.

As a water-gated transistor the charge transport performance significantly decreased. Furthermore, high operation voltages are required to operate the devices in such conditions. Nonetheless, as a preliminary study, **PFTPDOBT** based water-gated transistors show promising results and such deserve further study.

Chapter 4

Pyrazino[2,3-*g*]quinoxaline-2,7-dione Based Polymers

This chapter is based on the following publication:

J. Quinn, C. Guo, L. Ko, B. Sun, Y. He, Y. Li, *RSC Adv.* **2016**, *6*, 22043–22051.

4.1 Introduction

Quinoxalinones (Figure 4-1) have been reported in literature as natural-inspired compounds demonstrating appealing properties useful for biological, and pharmaceutical studies. They have been found useful as anticancer and antimicrobial agents [191]. As active GABA/benzodiazepine receptors agonists/antagonists, cAMP, and cGMP phosphodiesterase inhibitors, and A1- and A2a-adenosine receptor agonists [192], aldose reductase inhibitors [193], and as HIV-1 reverse transcriptase inhibitors [194,195].

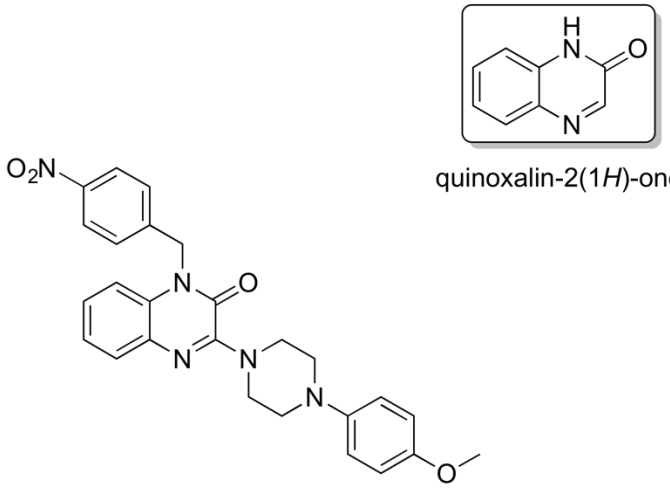

Figure 4-1. Example quinoxalinone derivatives that have been actively used as aldose reductase inhibitors [193], and as HIV-1 reverse transcriptase inhibitors [194,195].

To the best of our knowledge, synthesis of the pyrazino[2,3-*g*]quinoxaline-2,7-dione moiety, Figure 4-2, was only reported in one paper in 1970, where benzene-1,2,4,5-tetraamine and arylenediglyoxylates were condensed to form polymeric materials [196]. Due to the extremely low solubility of these polymers, no definitive structural assignments were made.

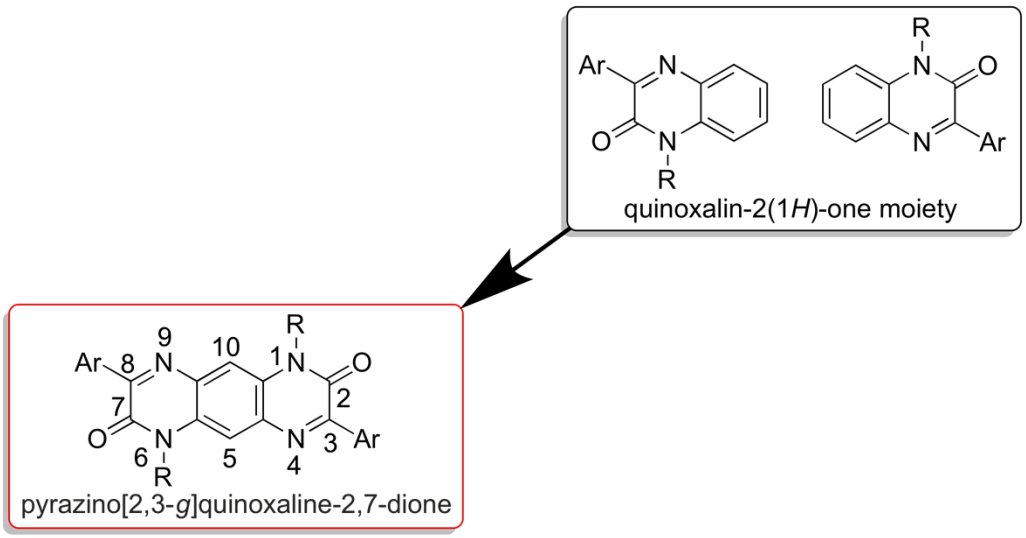

Figure 4-2. A general structure of 3,7-di(hetero)arylpyrazino[2,3-*g*]quinoxaline-2,7-dione, where Ar is a (hetero)aryl such as phenyl and 2-thienyl, and R is a suitable substituent such as an alkyl group.

4.2 Theoretical Study of Proposed Polymers

We conducted a computational study by density functional theory (DFT) using the B3LYP/6-31G(d) level of theory under tight convergence to investigate the geometry, molecular energy levels, and electron distributions of a simple 2,7-dithienyl-substituted PQx molecule, **PQx2T-Me** (Figure 4-3). The optimized geometry results revealed that the PQx unit is coplanar and there is no twisting between the flanking thiophenes and the PQx unit. The LUMO and HOMO wavefunctions are evenly distributed throughout the molecule. The LUMO and HOMO energy levels of **PQx2T-Me** were calculated to be -2.75 eV and -5.53 eV, respectively. The LUMO energy level of **PQx2T-Me** is much lower than that of **PQ2T-Me** (-1.97 eV) [197], indicating PQx is a stronger electron acceptor than PQ (see 5.2). To investigate the polymer geometry and molecular energy levels, the dimer of **PQx2T-BT-Me** and **PQx2T-TT-Me** were simulated (Appendix; Figure A-5 and Figure A-6). The LUMO and HOMO energy levels were calculated to be -2.95 eV and -4.90 eV for **PQx2T-BT-Me** and -2.99 eV and -4.96 eV for **PQx2T-TT-Me**, respectively. For both **PQx2T-BT-Me** and **PQx2T-TT-Me**, the LUMO wavefunctions are evenly distributed across the dimer. However, the HOMO wavefunctions appear largely distributed on the thiophene and thienothiophene moieties and only slightly scattered on the PQx moiety. The results suggest that the HOMO energy levels for both dimers are mostly influenced by the thiophene and/or thienothiophene units. The dihedral angles between the PQx unit and thiophene units in **PQx2T-BT-Me** were < 1 °. However, greater twisting was observed between thiophene units

with dihedral angles ranging from 6 to 8 °. **PQx2T-TT-Me** was nearly coplanar with dihedral angles < 1 ° throughout the thiophene and thienothiophene units.

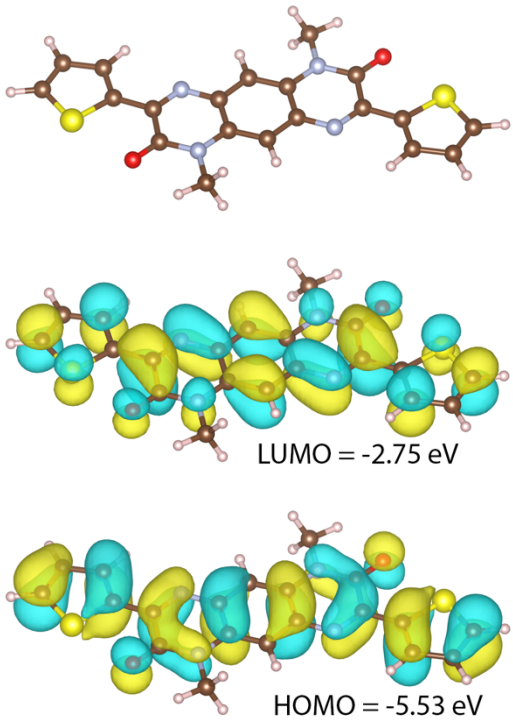

Figure 4-3. Optimized geometry and HOMO and LUMO wavefunctions for **PQx2T-Me** obtained by DFT calculations with B3LYP/6-31G(d).

4.3 Synthesis of Pyrazino[2,3-*g*]quinoxaline-2,7-dione Based Polymers

A similar synthetic procedure for the synthesis of quinoxalin-2(1*H*)-one compounds [198] is followed to synthesize the target 3,8-di(thiophen-2-yl)-1,6-dihydropyrazino[2,3-*g*]quinoxaline-2,7-dione (**PQx2T-H**) from 1,2,4,5-benzenetetramine tetrahydrochloride and 2-thiopheneglyoxylic acid (Scheme 4-1). A similar amount of the isomeric by-product, ***iso*-PQx2T-H**, is expected to form during the reaction.

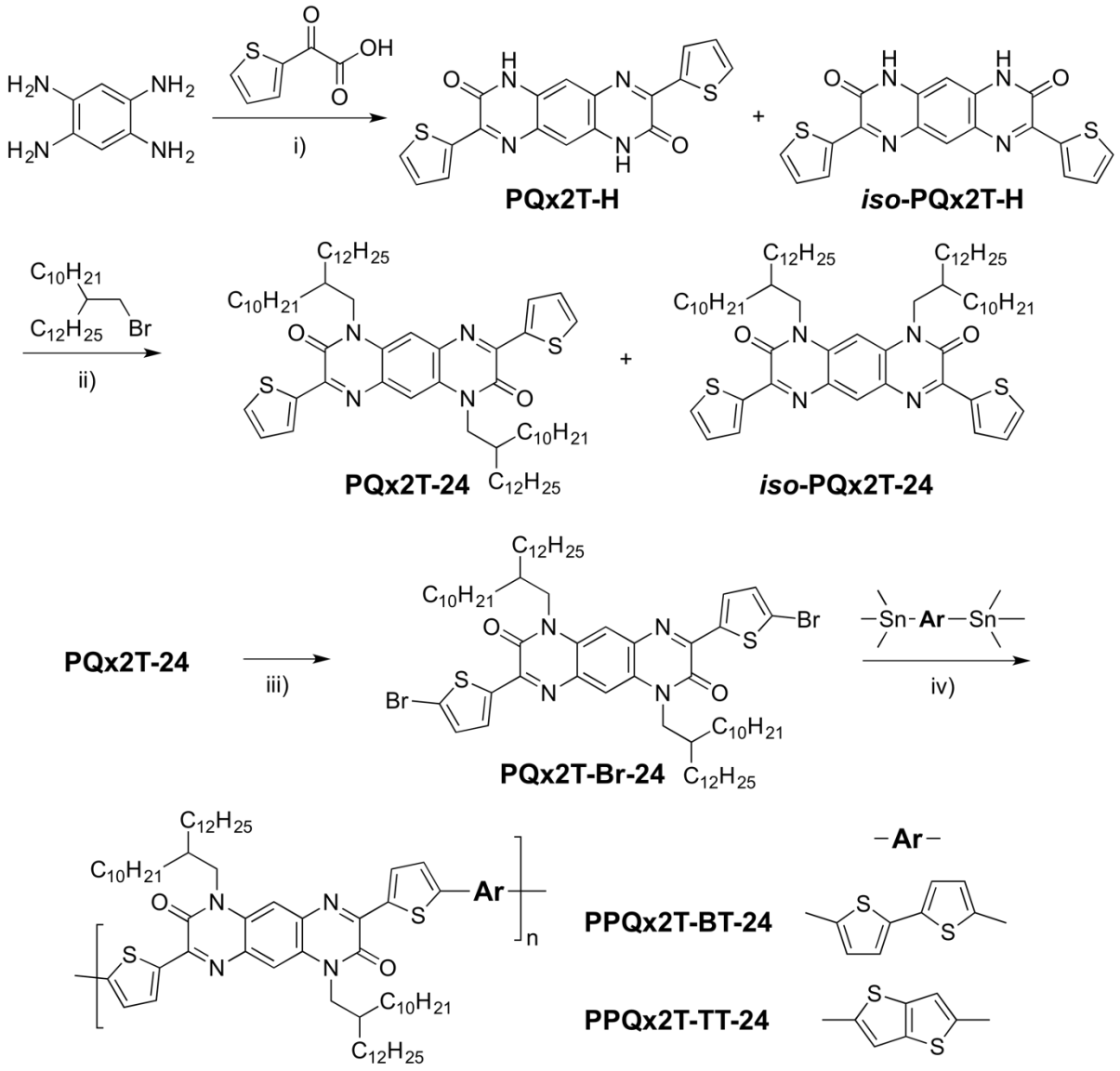

Scheme 4-1. The synthetic route to **PPQx2T-BT-24** and **PPQx2T-TT-24** polymers. Reagents and conditions: i) acetic acid/reflux/overnight; ii) K_2CO_3/DMF/130 °C; iii) NBS/Chloroform; iv) $Pd_2(dba)_3$/P(*o*-tolyl)$_3$/chlorobenzene/130 °C.

The crude product mixture is insoluble in any solvents and thus was used for the next step without further purification. *N*-Alkylation of the crude **PQx2T-H** was conducted using 11-(bromomethyl)tricosane in the presence of K_2CO_3 in DMF at 130 °C to afford **PQx2T-24** in 9% yield. The alkylated by-product, ***iso*-PQx2T-24**, was probably produced based on the TLC analysis. However, this by-product could not be isolated from other impurities. Next, **PQx2T-24** was brominated with *N*-bromosuccinimide (NBS) to obtain **PQx2T-Br-24** in 64% yield. Polymers **PPQx2T-BT-24** and

PPQx2T-TT-24 were synthesized *via* Stille coupling polymerization of **PQx2T-Br-24** with 5,5'-bis(trimethylstannyl)-2,2'-bithiophene and 2,5-bis(trimethylstannyl)thieno[3,2-*b*]thiophene, respectively, and purified using Soxhlet extraction. Most of **PPQx2T-BT-24** (68%) was dissolved in refluxing chloroform, while 22% of this polymer was obtained by using 1,1,2,2-tetrachloroethane. **PPQx2T-TT-24** showed much better solubility with 97% of it being extracted with chloroform.

4.4 Characterization of Aforementioned Polymers

4.4.1 Molecular Weight and Thermal Analysis

As discussed in Section 3.4.1, the narrowest PDI that can be achieved in theory for Stille coupling is 2. The M_n and PDI were measured to be 24.6 kg mol^{-1} and 7.86 for **PPQx2T-BT-24** and 14.4 kg mol^{-1} and 2.05 for **PPQx2T-TT-24**, respectively (Appendix; Figure C-3). The broad PDI exhibited by **PPQx2T-BT-24** and trimodal distribution in the GPC trace might suggest aggregation of the polymer chains that have been often observed for conjugated polymers [199–201]. As mentioned previously, **PPQx2T-BT-24** showed much poorer solubility than **PPQx2T-TT-24**, indicating a stronger aggregation tendency of the former. **PPQx2T-BT-24** showed good thermal stability with a $T_{-5\%}$ at 325 °C, while **PPQx2T-TT-24** showed slightly higher thermal stability with a $T_{-5\%}$ at 332 °C (Appendix; Figure C-4). No noticeable endo- or exothermic transitions were observed on their DSC thermograms (Appendix; Figure C-5).

4.4.2 Optical and Electrochemical Analysis

The UV-Vis absorption properties of **PPQx2T-BT-24** and **PPQx2T-TT-24** in chloroform and in thin-films are shown in Figure 4-4. In solution, **PPQx2T-BT-24** showed a broad featureless absorption profile with the λ_{max} to be 600 nm while a similar absorption profile and λ_{max} of 598 nm were observed with the film. **PPQx2T-TT-24** showed clearly two major peaks in both solution and film absorption profiles. The λ_{max} in solution appeared at 627 nm along with a slightly weaker peak at 582 nm. From solution to film, positions of these two peaks (at 632 nm and 576 nm) changed very little. The E_g^{opt} of **PPQx2T-BT-24** and **PPQx2T-TT-24** calculated from the onset absorption wavelengths of their thin-films are ~1.66 eV and ~1.82 eV, respectively. Compared to its analogous PQ polymer **PPQ2T-BT-24** (see 5.4.2), which has an optical band gap of 2.03 eV, **PPQx2T-BT-24** has a much narrower band gap because PQx is a stronger electron acceptor than PQ, which resulted in more efficient intramolecular donor-to-acceptor charge transfer, and a more coplanar backbone.

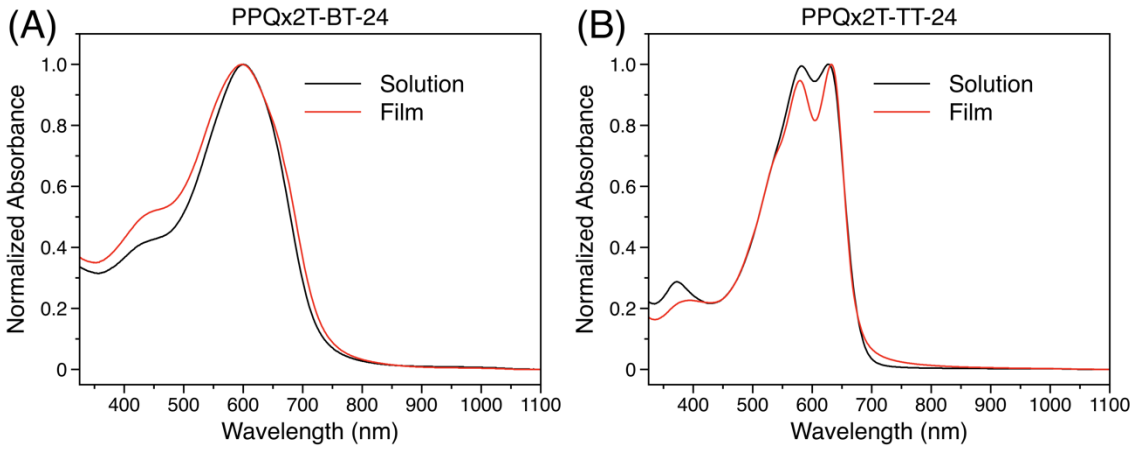

Figure 4-4. UV-Vis-NIR absorption spectra of polymers in chloroform and thin film.

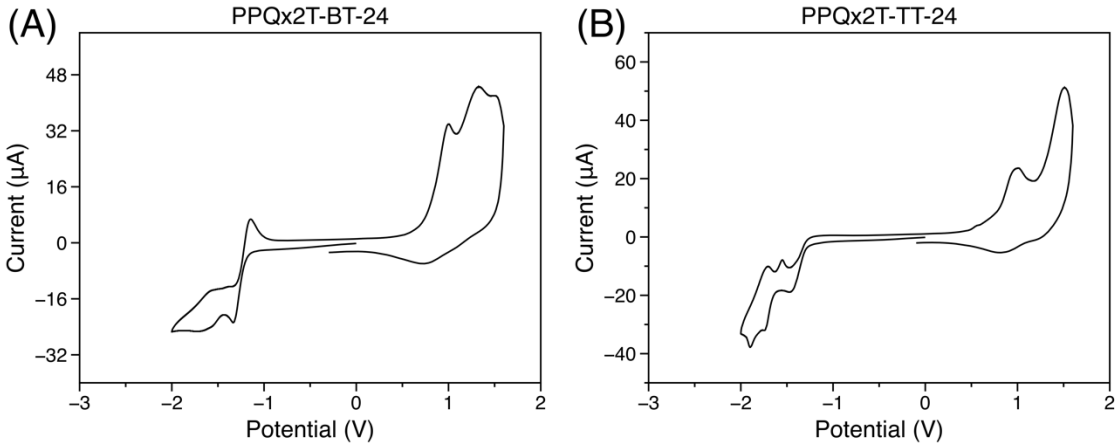

Figure 4-5. CV curves of polymers in a 0.1 M tetrabutylammonium hexafluorophosphate (Bu_4NPF_6) solution in anhydrous acetonitrile at a scan rate of 50 mV s^{-1}.

The frontier energy levels of these polymers were determined from the oxidation and reduction onset potentials on their thin film CV (Figure 4-5). The HOMO and LUMO energy levels of **PPQx2T-BT-24** are -5.54 eV and -3.59 eV, respectively. **PPQx2T-TT-24** has a same HOMO energy level of -5.54 eV, but a slightly higher LUMO energy level of -3.52 eV. The electrochemical band gaps are thus 1.95 eV for **PPQx2T-BT-24** and 2.01 eV for **PPQx2T-TT-24**. The greater electrochemical band gaps than the optical bandgaps are possibly caused by the large exciton binding energy that is typical of π-conjugated polymers [202].

4.4.3 Acid Study

The basic 1,6-pyridyl nitrogen atoms of PQx are expected to allow the PQx-based polymers to interact strongly with acids. Similar behaviour has been reported for conjugated polymers and small molecules incorporating pyridine moieties [203,204] and benzothiadiazoles [205–211]. In contrast, azulene-based conjugated polymers and small molecules, which do not contain a basic site, have also shown noteworthy responses to various acids [207,208,211]. In all cases reversible bathochromic shifts in the absorption maxima occur with some cases reaching near infrared (NIR) [208,209,211]. To elucidate the acid effects of these PQx polymers, trifluoroacetic acid (TFA), which has a pK_a of -0.25 [208], was first tested. As shown in Figure 4-6, **PPQx2T-BT-24** exhibited a slight decrease in absorbance at a TFA concentration as low as 1 mM. With increasing TFA concentration, the λ_{max} bathochromically shifted and the long wavelength tail intensified. At 500 mM TFA, the λ_{max} appeared at ~840 nm. Further increasing the TFA concentration caused a bathochromic shift in the new λ_{max} peak. At 2 M TFA, near the solubility limit for TFA in chlorobenzene, very little spectral change occurred and a largest λ_{max} of 846 nm was reached, which corresponds to a bathochromic shift of 246 nm from that of the solution without TFA. In the case of **PPQx2T-TT-24**, a slight decrease in absorption also started at 1 mM TFA. A new λ_{max} peak appeared at ~780 nm, similar to **PPQx2T-BT-24**, but at a lower TFA concentration (50 mM) and a shorter wavelength. This new λ_{max} peak bathochromically shifted up to 804 nm at 100 mM TFA. Surprisingly, the peak at 804 nm disappeared and a very intense peak appeared at ~900 nm as the TFA concertation increased to 500 mM. At 2 M TFA, the λ_{max} shifted to 914 nm, which corresponds to a bathochromic shift of 287 nm from that of the solution without TFA.

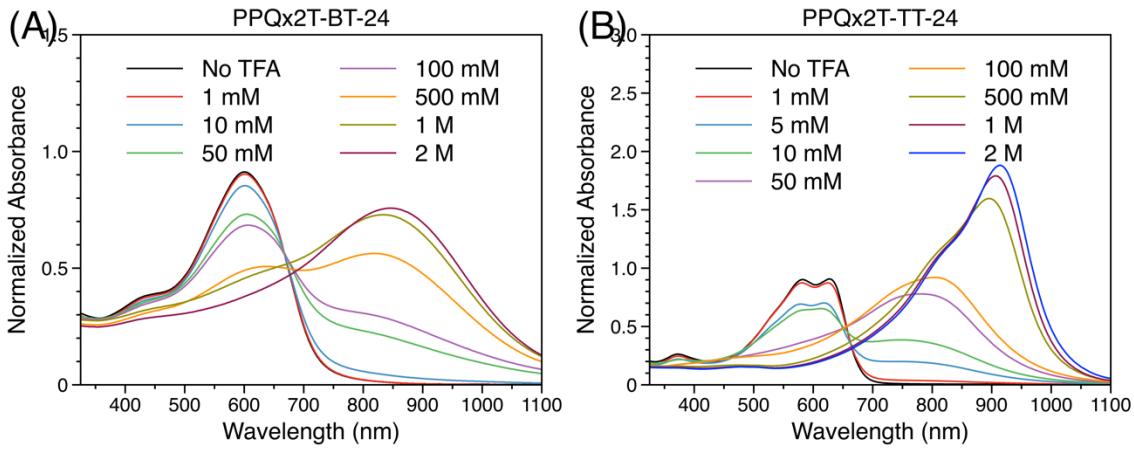

Figure 4-6. The UV-Vis-NIR absorption spectra of **PPQx2T-BT-24** and **PPQx2T-TT-24** in chlorobenzene with various concentrations of TFA. The measurements were conducted under nitrogen with a molar concentration of the polymer repeat unit at ~1 × 10^{-5} M.

The effect of boron tribromide (BBr_3), a strong Lewis acid, on the absorption spectra of **PPQx2T-BT-24** and **PPQx2T-TT-24** was also studied (Figure 4-7). Both polymers at a BBr_3 concentration of 1 μM show absorption spectra similar to those observed for TFA at a concentration of 50 mM, indicating a much stronger interaction of BBr_3 with both polymers than that of TFA. At a BBr_3 concentration of 4 μM, **PPQx2T-BT-24** bathochromically shifted with a λ_{max} of 621 nm accompanied by the appearance of a strong absorption peak at 796 nm, which appears to be similar to that observed in the TFA solution at 500 mM. At a BBr_3 concertation beyond 4 μM, precipitates formed, which are assumed to be the polymer-BBr_3 complexes. For **PPQx2T-TT-24**, at a BBr_3 concentration of 6 μM, which is the maximum BBr_3 concentration without formation of precipitates, the λ_{max} bathochromically shifted to 846 nm, which is comparable to that observed for the TFA solution at 500 mM. In either case, with the addition of pyridine the original spectra of the pristine polymers could be completely recovered.

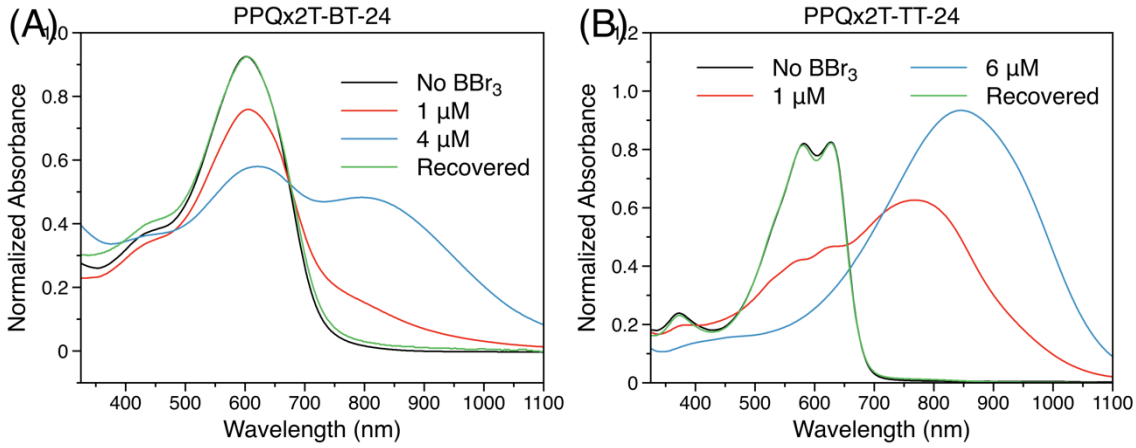

Figure 4-7. The UV-Vis-NIR absorption spectra of **PPQx2T-BT-24** and **PPQx2T-TT-24** in chlorobenzene with various concentrations of BBr_3. The measurements were conducted under nitrogen with a molar concentration of the polymer repeat unit at ~1 × 10^{-5} M.

To reveal if the polymers have amplified sensitivity towards acids, the UV-Vis-NIR spectra of the monomer compound **PQx2T-24** solutions with various concentrations of TFA were measured. **PQx2T-24** showed a significant change at 25 mM TFA (Figure 4-8). At 50 mM TFA, a broad featureless absorption peak with a λ_{max} of 516 nm was observed. There was little change as the TFA concentration

was increased up to 100 mM. With a higher TFA concentration of 1 M, three well-defined peaks at 473 nm, 505 nm, and 542 nm (λ_{max}) appeared. Further increasing the TFA concentration to 2 M, the absorption profile remained the same, but the overall intensity increased. The overall bathochromic shift from the absence of TFA to 2 M of TFA is ~88 nm. **PPQx2T-TT-24** clearly demonstrates an amplification effect since this polymer exhibited a dramatic spectrum change at a much lower TFA concentration of ~1–5 mM than **PQx2T-24**. On other hand, it appears that **PPQx2T-BT-24** has a similar sensitivity to TFA (at ~10–50 mM) compared to **PQx2T-24**. The reason for the dramatically differed responses to acids observed for these two polymers is unclear. The basicity of the 1,6-nitrogen atoms in PQx in these two polymers should be similar because they have similar HOMO energy levels (see above). As aforementioned, **PPQx2T-BT-24** might form chain aggregates in solution, which would hinder the access of TFA molecules to the polymer chains inside the aggregates, resulting in the low sensitivity of this polymer.

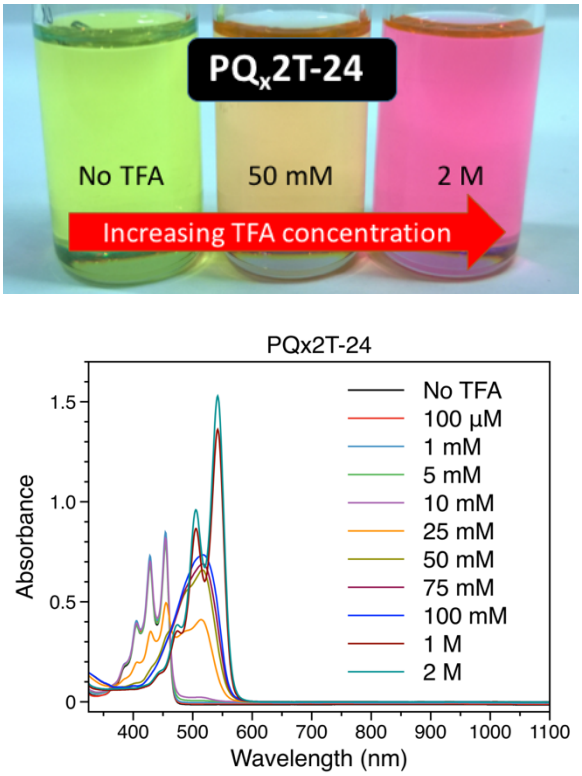

Figure 4-8. The UV-Vis-NIR absorption spectra and photos of **PQx2T-24** in chlorobenzene with various concentrations of TFA until little variations were observed. The measurements were conducted under nitrogen with a molar concentration at ~1 × 10^{-5} M. Photos of neutral and pronated **PQx2T-24** (left: neutral in chlorobenzene; middle: protonated with 50 mM TFA; right: protonated with 2 M TFA).

4.4.4 Morphological Analysis

The surface morphology of the polymer thin films was characterized with atomic force microscopy (Figure 4-9 and Figure 4-10). The polymer thin films were prepared under the same conditions as those used for the OTFT devices. In the AFM images of the **PPQx2T-BT-24** films annealed at 100, 150 and 200 °C, smooth surfaces with a low root mean squared roughness (R_q) of 0.5 nm were observed with very little difference. At 250 °C, the polymer thin film appears rougher with an increase of R_q to 1.1 nm. Under scrutiny, all **PPQx2T-BT-24** films are comprised of tiny grains, which is in agreement with its poor crystallinity verified by XRD (see below). On the other hand, the 100 °C-annealed **PPQx2T-TT-24** film shows distinct worm-like grains, indicative of its higher crystallinity. With increasing annealing temperature, the worm-like grains disappeared and pinholes formed concurrently. Layered structures comprising large pinholes are observed for the 250 °C-annealed film, which might cause the degraded OTFT performance at this annealing temperature (discussed latter).

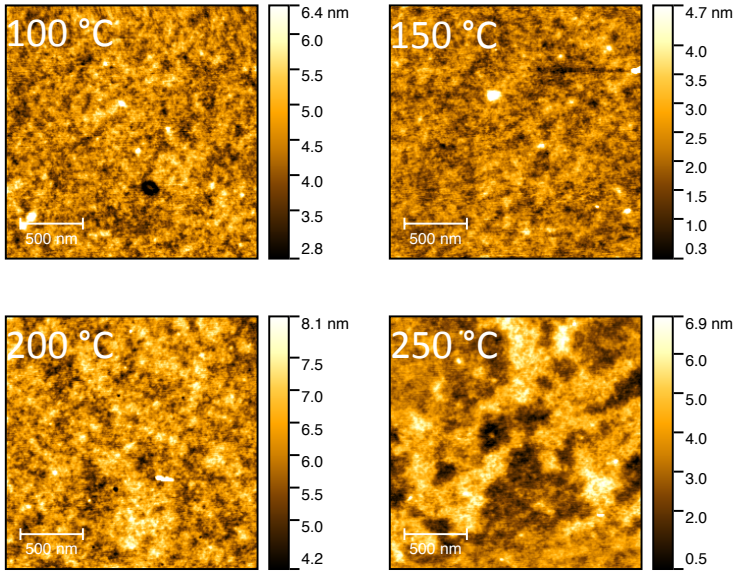

Figure 4-9. AFM images of **PPQx2T-BT-24** (2 μm × 2 μm, 500 nm scale bars) thin films after annealing at various temperatures.

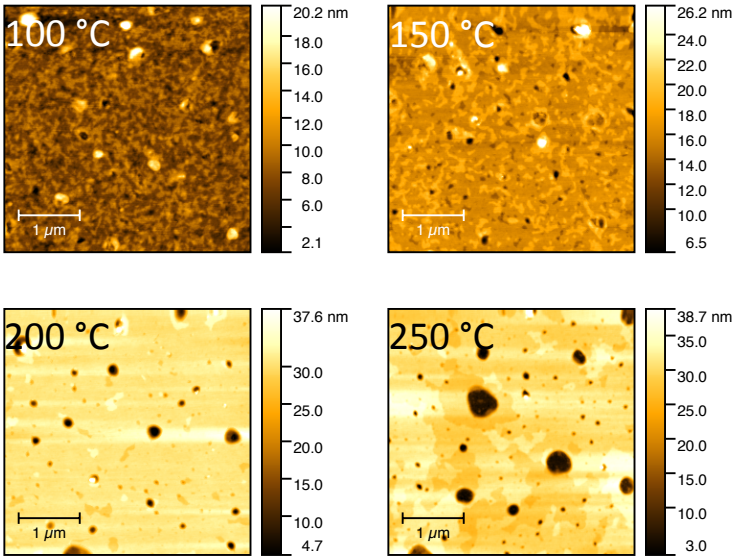

Figure 4-10. AFM images of **PPQx2T-TT-24** (4 μm × 4 μm, 1 μm scale bars) thin films after annealing at various temperatures.

The polymer thin films, which were prepared similarly as those for the OTFTs and AFM measurement, were subject to the XRD measurement to study their crystallinity and molecular organization. At all annealing temperatures (100, 150, 200 and 250 °C), **PPQx2T-BT-24** thin films showed no obvious diffraction peaks (Figure 4-11). In contrast, **PPQx2T-TT-24** thin film annealed at 100 °C exhibited a clear primary (100) diffraction peak at $2\theta = 3.68$ °, which corresponds to a *d*-spacing distance of 2.40 nm (Figure 4-11). When the annealing temperature was increased to 150 °C, the (100) peak shifted slightly to $2\theta = 4.00$ ° (*d*-spacing = 2.21 nm) accompanied by the appearance of a secondary (200) diffraction peak at $2\theta = 7.84$ °, indicating that long range ordering formed [212]. At an annealing temperature of 200 °C, the intensity of both (100) and (200) peaks further increased and shifted to $2\theta = 3.92$ ° (*d*-spacing = 2.25 nm) and $2\theta = 7.72$ °, respectively. Further increasing the annealing temperature to 250 °C resulted in a decrease of intensity for the (100) peak and a decrease in the *d*-spacing to 2.21 nm ($2\theta = 4.00$ °). However, the (200) peak became stronger and a tertiary (300) diffraction peak at $2\theta = 11.52$ ° can be seen. Transmission XRD measurements were also performed using polymer flakes (Figure 4-12). **PPQx2T-BT-24** and **PPQx2T-TT-24** showed strong (100) peaks at $2\theta = 3.31$ ° and 3.63 °, which correspond to the inter-lamellar distances of 2.67 nm and 2.43 nm, respectively. The hump centered at $2\theta = 23.58$ ° observed for **PPQx2T-BT-24** could be assigned to the (010) peak originating from the co-facial π-π distance of adjacent polymer backbones [213], which was calculated to be 0.38 nm. In comparison, a much stronger (010) peak was observed for **PPQx2T-TT-**

24 at 2θ = 25.39 ° corresponding to a π-π distance of 0.35 nm. Thus, the higher crystallinity and a shorter π-π distance could be accounted for the higher charge mobility observed for **PPQx2T-TT-24**.

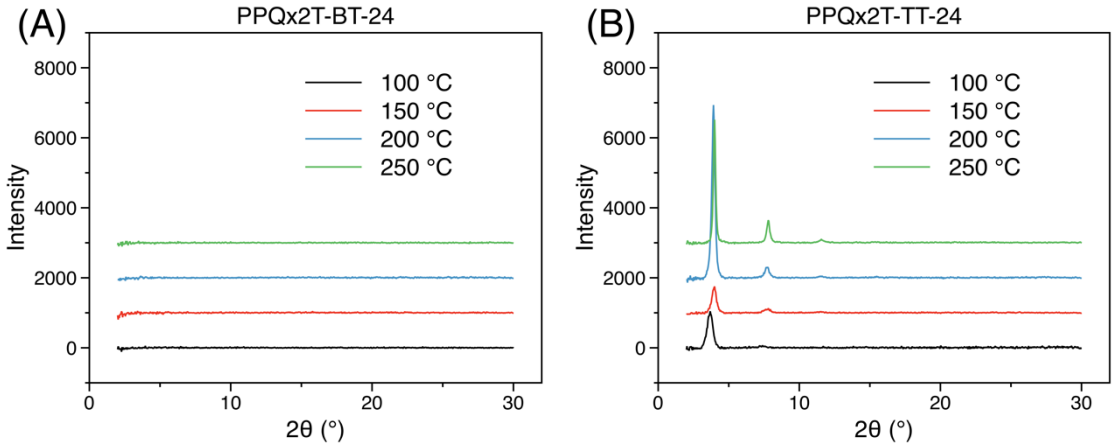

Figure 4-11. Reflection XRD diagram of polymer thin films spin-coated on dodecyltrichlorosilane-modified SiO_2/Si substrates and annealed at different temperatures with Cu Kα radiation (λ = 0.15406 nm).

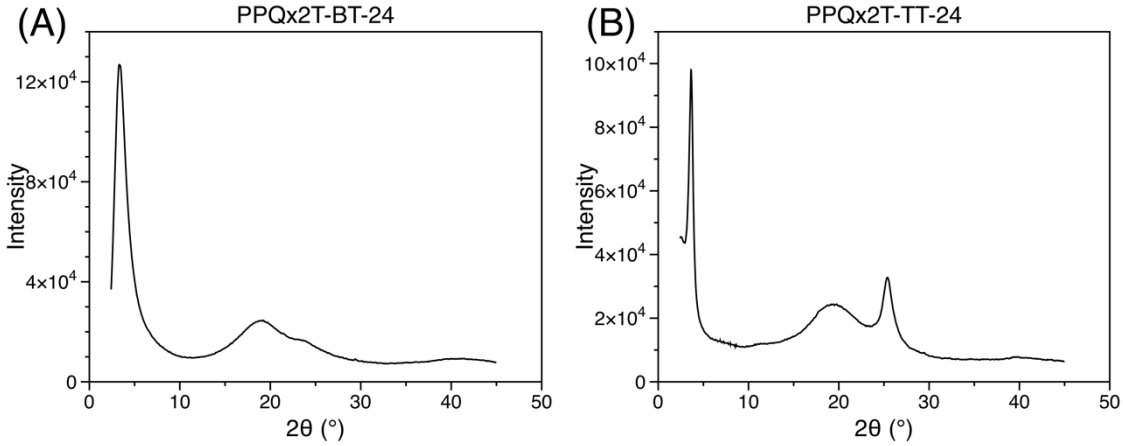

Figure 4-12. The transmission XRD pattern **PPQx2T-BT-24** (left) and **PPQx2T-TT-40** (right) flakes stacked between two polyester film substrates with a Cu Kα (Rigaku) X-ray source (λ = 0.15406 nm).

4.4.5 I-V Characterization

For detailed device fabrication refer to Appendix D.

Both PQx based polymers were evaluated as channel semiconductors in BGBC devices. Both polymers showed ambipolar charge transport characteristics with **PPQx2T-BT-24** being electron-dominant and **PPQx2T-TT-24** being hole-dominant (Figure 4-13; Appendix, Table D-4). The electron-

dominant transport behaviour of **PPQx2T-BT-24** is most likely due to its slightly lower LUMO energy level than that of **PPQx2T-TT-24**, which facilitated electron injection and stabilized electron transport [214–216]. For devices based on **PPQx2T-BT-24**, the best performance was observed at 200 °C with the highest hole mobility of 5.22×10^{-4} cm^2 V^{-1} s^{-1} with an average mobility of 5.04×10^{-4} cm^2 V^{-1} s^{-1} and the highest electron mobility of 4.28×10^{-3} cm^2 V^{-1} s^{-1} with an average mobility of 3.97×10^{-3} cm^2 V^{-1} s^{-1}. At a higher annealing temperature of 250 °C, both hole and electron mobilities decreased. For **PPQx2T-TT-24**, the highest hole mobility of 4.82×10^{-2} cm^2 V^{-1} s^{-1} with an average mobility of 3.79×10^{-2} cm^2 V^{-1} s^{-1} and the highest electron mobility of 3.95×10^{-3} cm^2 V^{-1} s^{-1} with an average mobility of 3.12×10^{-3} cm^2 V^{-1} s^{-1} were achieved also at the annealing temperature of 200 °C. The electron transport characteristics of devices with **PPQx2T-TT-24** started to appear only at a very high V_{GS} of > 60 V in the n-channel operation mode. Both polymers showed decreased mobilities at a higher annealing temperature of 250 °C due to the deteriorated film morphology (discussed in 4.4.4).

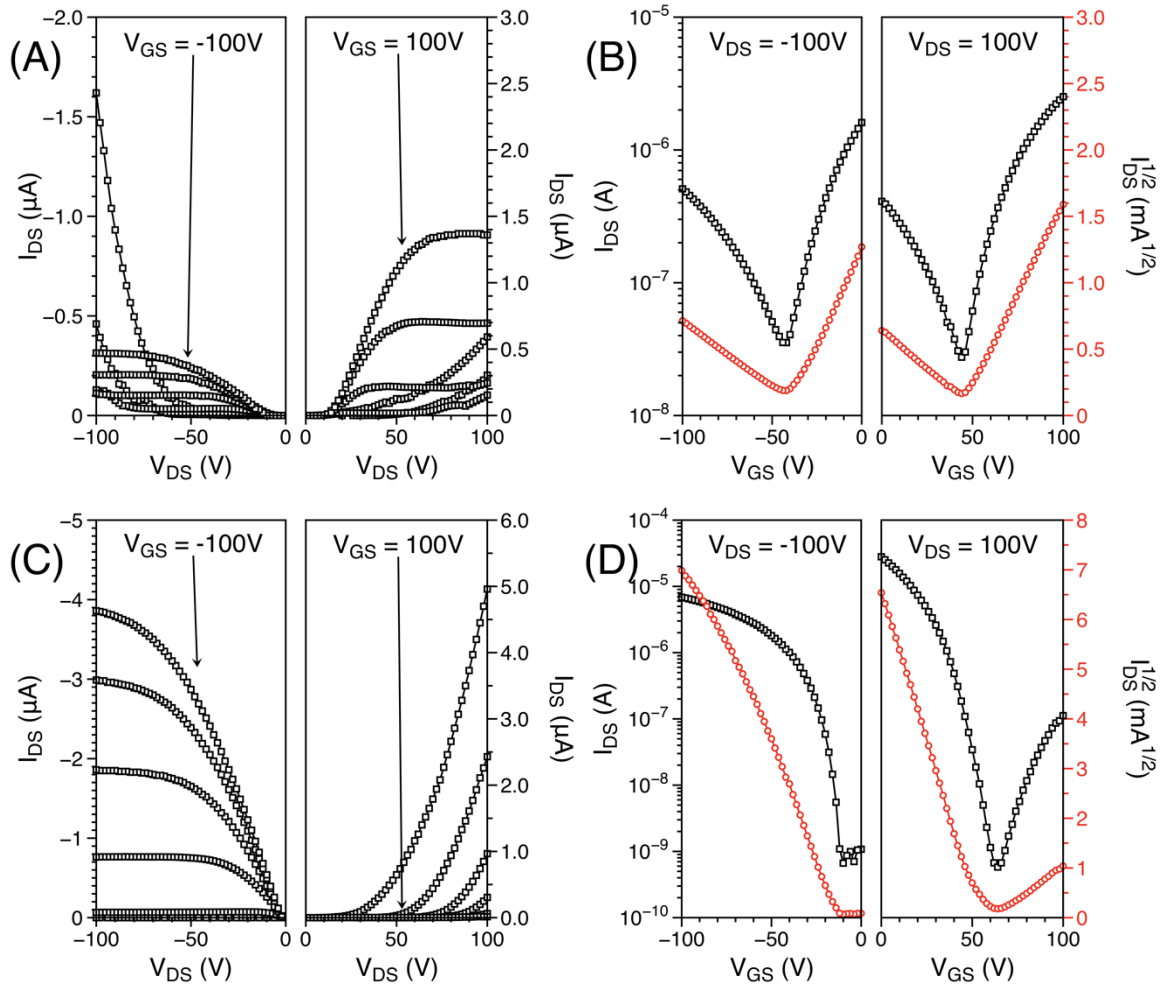

Figure 4-13. Output (left) and transfer (right) curves of an OTFT device with a thin-film of **PPQx2T-BT-24** (A and B) and **PPQx2T-TT-24** (C and D) annealed at 200 °C. Device dimensions: L = 30 μm; W = 1000 μm. Output curves are measured from 0 to ±100 V at ±20 V increments.

4.5 Conclusion

Two polymers, **PPQx2T-BT-24** and **PPQx2T-TT-24**, based on the new building block, pyrazino[2,3-*g*]quinoxaline-2,7-dione (PQx) are presented. These polymers showed dramatic bathochromic shifts in their UV-Vis-NIR absorption spectra in the presence of trifluoroacetic acid and the Lewis acid boron tribromide. In OTFTs, **PPQx2T-BT-24** exhibited electron-dominant ambipolar transport characteristics with hole mobilities of up to 5.22×10^{-4} cm^2 V^{-1} s^{-1} and electron mobilities reaching 4.28×10^{-3} cm^2 V^{-1} s^{-1}. **PPQx2T-TT-24** exhibited hole-dominant ambipolar transport characteristics with hole mobilities of up to 4.82×10^{-2} cm^2 V^{-1} s^{-1} and electron mobilities of up to 3.95×10^{-3} cm^2 V^{-1} s^{-1}. Our preliminary results demonstrate that PQx is a promising new building block for polymer semiconductors for OTFTs that can be used for chemo- and bio-sensors.

Chapter 5
Pyrimido[4,5-*g*]quinazoline-4,9-dione Based Polymers

This chapter is based on the following publications:

[1] J. Quinn, Y. He, D. A. Khan, J. Rasmussen, H. Patel, F. Haider, W. Kapadia, Y. Li, *RSC Adv.* **2016**, *6*, 78477–78485.

[2] J. Quinn, C. Guo, B. Sun, A. Chan, Y. He, E. Jin, Y. Li, *J. Mater. Chem. C* **2015**, *3*, 11937–11944.

[3] J. Quinn, E. Jin, Y. Li, *Tetrahedron Lett.* **2015**, *56*, 2280–2282.

5.4.5.3 is not yet published and in near-verbatim state to what is intended for submission. The following is the authorship order:

J. Quinn, F. Haider, H. Patel, D. A. Khan, Z. Y. Wang, Y. Li.

5.1 Introduction

Quinazolinones (Figure 5-1), an isomer of quinoxalinones (introduced in 4.1), are naturally occurring and can be found in over 150 alkaloids [217]. Quinazolinones have been actively studied as they represent an important class of compounds due to their wide range of intrinsic biological activities [218]. For example, they have demonstrated anti-microbial, anti-tumor, anti-inflammatory, anti-convulsant, anti-hypertensive, and anti-malarial activities [219,220]. Due to the importance of quinazolinones for biological activity and pharmaceutical relevance, research in synthesis of various quinazolinones has been conducted [217–234].

Interesting enough, quinazolinone and quinoxalinone derivatives (discussed earlier in Chapter 4) may offer further benefits as they contain amide and imine bonds, which are found in many n-type, some p-type, and ambipolar PSCs [98]. For instance, poly(benzobismidazobenzophenanthroline) (BBL) [235–239], poly(*N*-(2-octyldodecyl)-2,2'-bithiophene-3,3'-dicarboximide) (PDTI) [240], diketopyrrolopyrrole (DPP) [241,242], indigo [243–247], and isoindigo [248] all contain similar nitrogen carbonyl containing rings. Because n-type PSCs have been underdeveloped compared to p-type PSCs due to lack of materials available, the incorporation of quinazolinone and quinoxalinone moieties into a PSC provides a new synthetic approach to possibly making new n-type material. On another note, recently an isoindigo based PSC has been demonstrated as an useful heavy-metal ion

sensor stable in aqueous environments, which has been stated above, is not that different from our novel quinazolinone and quinoxalinone derived PSCs [249]. Thus, our motivation to study the quinazolinone and quinoxalinone moieties as PSCs for their charge carrier properties, stability to ambient/aqueous environments, and as potential low-cost chemo- and bio-sensors, has greatly increased. Our thought is that by taking advantage of the biological activity of quinazolinones and quinoxalinones, OTFT-based sensors containing such moieties may utilize their intrinsic properties as biologically active entities to obtain an electrical response towards chemical or biological analytes [23–25,250,251].

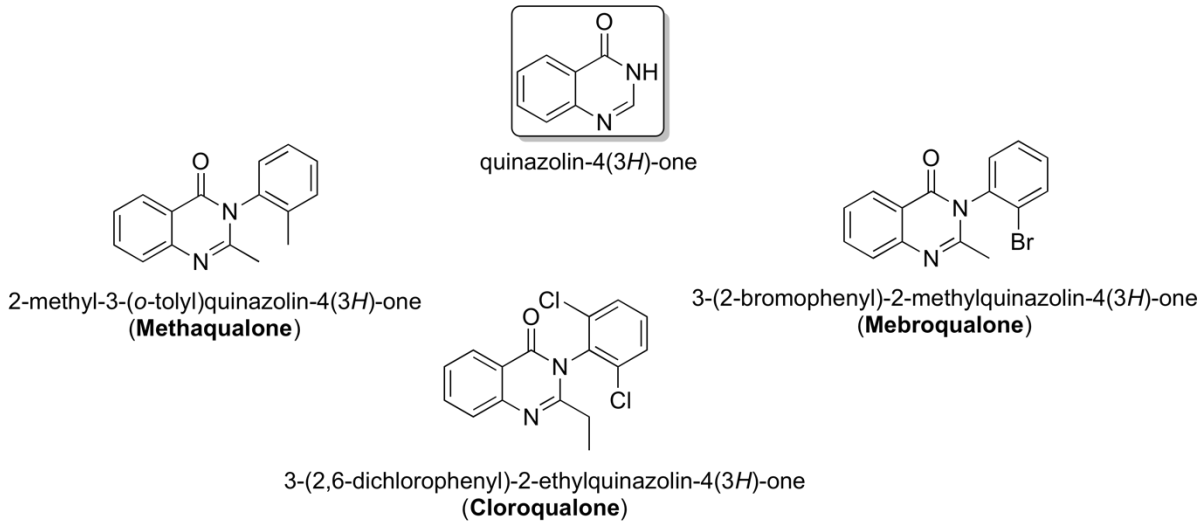

Figure 5-1. Example quinazolinone derivatives that have been actively used as sedatives or antitussives while others are being studied for general cancer treatment [252].

Pyrimido[4,5-*g*]quinazoline-4,9-diones were prepared in the early 1900s (Figure 5-2) [253,254]. However, in comparison to quinazolinones, there have been much fewer reports on the synthesis of pyrimido[4,5-*g*]quinazoline-4,9-diones, because most of the usual methods to prepare quinazolinones were unsuccessful [253]. The majority of pyrimido[4,5-*g*]quinazoline-4,9-diones reported to date have no substituents or have alkyl substituents at the 2,7-positions [229,253–256]. Thus, we were presented with a synthetic challenge.

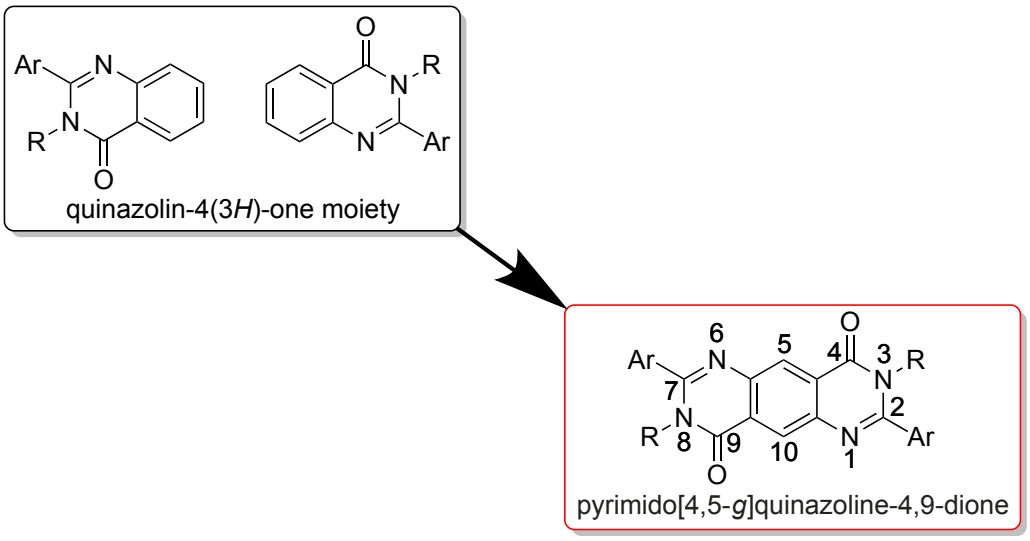

Figure 5-2. A general structure of 2,7-di(hetero)arylpyrimido[4,5-*g*]quinazoline-4,9-dione where Ar is a (hetero)aryl such as phenyl and 2-thienyl, and R is a suitable substituent such as an alkyl group.

5.2 Theoretical Study of Proposed Polymers

Our study began with conducting theoretical calculations by quickly optimizing a given structure at a low level of theory such as Hartree-Fock (HF) with a Slate-type orbital (STO) with 3 Gaussian orbitals (3G) followed by density functional theory (DFT) using the functional B3LYP and the basis set 6-31G(d) under tight convergence to investigate the geometry, molecular energy levels, and electron distributions of simple molecules and their corresponding oligomers. All theoretical calculations were accomplished through Gaussian 09 Revision D.01 [257]. A simple 2,7-dithienyl-substituted pyrimido[4,5-*g*]quinazoline-4,9-dione (PQ) molecule, **PQ2T-Me** (Figure 5-3), was used as an initial structure. The modelling results showed that the PQ unit is nearly coplanar with the pyrimidinone rings to be slightly raised off by 2-3 ° due to steric effects from the neighbouring thiophene rings. A large dihedral angle of ~30 ° between the PQ unit and thiophene was observed. The LUMO and HOMO wavefunctions are evenly distributed throughout the molecule. The LUMO and HOMO energy levels of **PQ2T-Me** were calculated to be -1.97 and -5.59 eV, respectively. To gain further insight into the polymer properties, the dimer of **PQ2T-BT-Me** was simulated (Appendix; Figure A-7). The LUMO and HOMO energy levels were calculated to be -2.57 and -5.17 eV, respectively. The HOMO wavefunction is evenly distributed across the dimer, while the LUMO wavefunction is localized to the thiophene units. The dihedral angles between the PQ unit and thiophene units were slightly lower (~27 °) than that calculated for **PQ2T-Me**. The result suggests that the LUMO is mostly influenced by the

thiophene units in the dimer. The calculated frontier energy levels for **PQ2T-TT-Me** and **PQ2T-TVT-Me** dimers are -2.57 eV/-5.26 eV and -2.62 eV/-5.04 eV, respectively (Appendix; Figure A-8 and Figure A-9). The LUMO wavefunction localizes at TT (or TVT) and the flanking thiophene units and thus give relatively high LUMO energy levels, whereas the HOMO wavefunction is delocalized along the dimer backbones across the PQ and TT (or TVT) units. In comparison with the LUMO/HOMO of **PQ2T-BT-Me** (-2.57 eV/-5.17 eV), it appears that the HOMO levels changed notably with differing donor comonomer units (HOMO: TT < BT < TVT), while their LUMO levels remain similar. The dihedral angle between the PQ moiety and the flanking thiophene unit is again ~27 °, which is considered a limiting factor for achieving a high coplanarity.

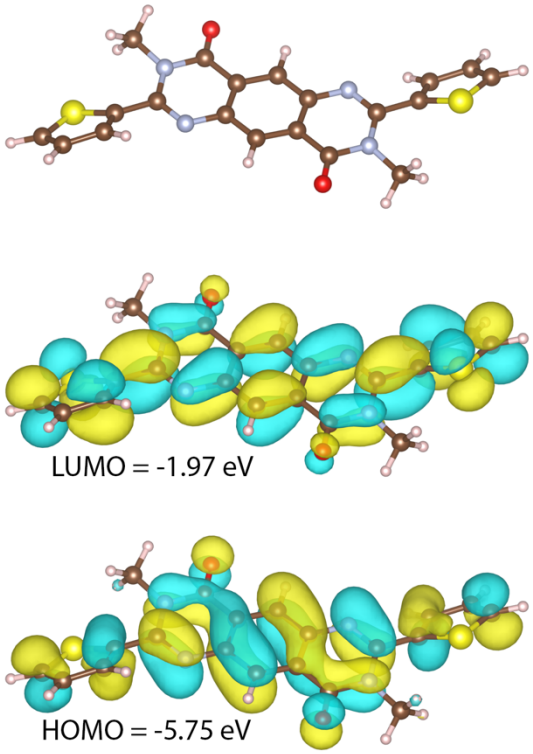

Figure 5-3. Optimized geometry and HOMO and LUMO wavefunctions for **PQ2T-Me** obtained by DFT calculations with B3LYP/6-31G(d).

5.3 Synthesis of Pyrimido[4,5-*g*]quinazoline-4,9-dione Based Polymers

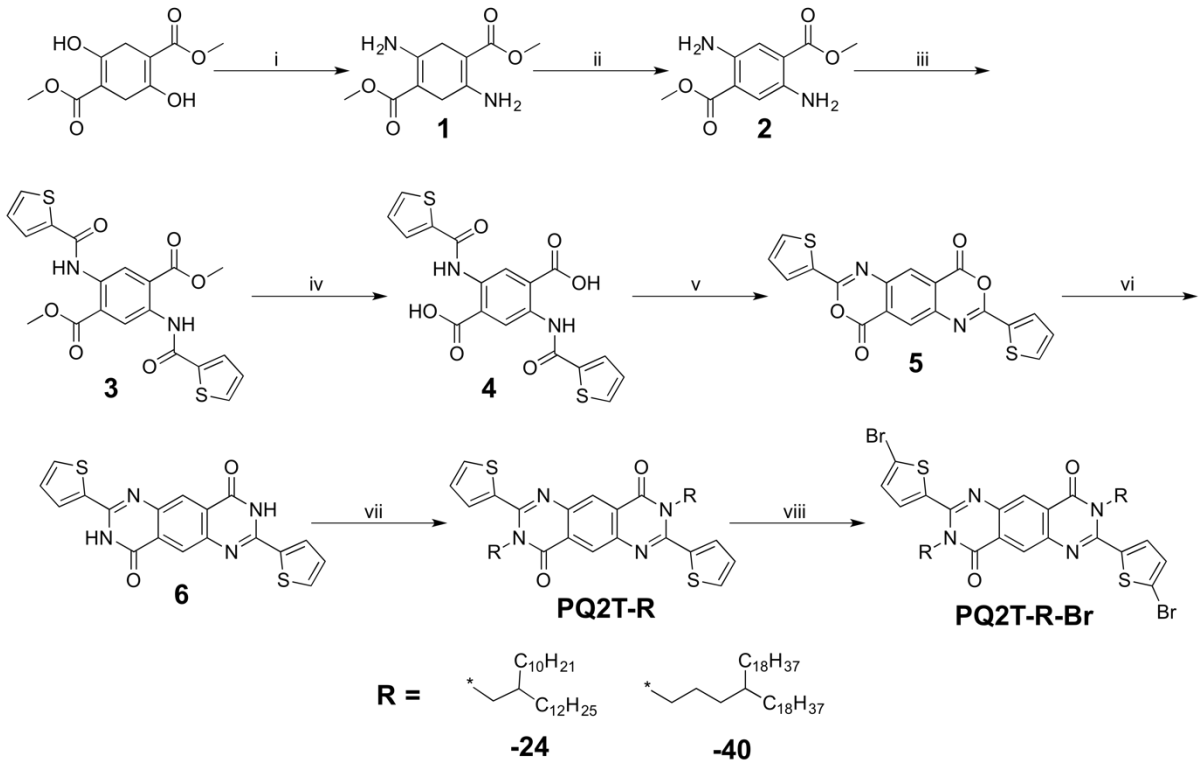

Scheme 5-1. Reagents and conditions: (i) toluene, ammonium acetate, catalytic amount of acetic acid, 16 h (95%); (ii) *n*-butanol, sulfur, gentle reflux, 18 h (90%); (iii) DCM, 2-thiophenecarbonyl chloride, pyridine, 0 °C, 30 min, rt, 18 h (79%); (iv) ethanol, lithium hydroxide, 60 °C, 3 h (86%); (v) acetic anhydride, reflux, 3 h (78%); (vi) ammonium acetate, 170 ° C, 1 h, 30% sodium hydroxide, ethanol, reflux, 1 h (95%); (vii) DMF, K_2CO_3, 130 ° C, 16 h (73%); (viii) NBS, chloroform, 0 °C, rt, overnight (75%).

The synthesis of di(thiophen-2-yl)pyrimido[4,5-*g*]quinazoline-4,9-dione (**6**), and its derivatives based on a newly established route (Scheme 5-1) are described within. Synthesis of the key compound 2,5-diamino-1,4-benzene-dicarboxylic acid 1,4-dimethyl ester (**2**) was initially attempted by refluxing dimethyl 2,5-dihydroxycyclohexa-1,4-diene-1,4-dicarboxylate and excess ammonium acetate in the presence of a catalytic amount of glacial acetic acid in toluene and air following a literature procedure.[258] However, only **1** was produced in high yield (95%). To oxidize **1**, sulfur was added portion wise to a solution of **1** in *n*-butanol and the mixture was heated to gentle reflux for 18 h, forming **2** in high yield (90%). Attempts to convert **2** directly to **6** by reacting with 2-thiophenecarbonitrile using 4M hydrochloric acid in 1,4-dioxane in a sealed reaction vessel at 100 °C for several days [259] were

unsuccessful. Therefore, *N*-acetylation of **2** followed routine acetylation procedures [260] was conducted to afford **3** in moderate yield (79%). A direct synthesis of **6** from **3** was also attempted using a pressure reactor in aqueous ammonium hydroxide at 120 °C for several days [261]. However, ring closure did not occur due probably to the limited solubility of **3** in the reaction medium. Subsequently the diacid **4**, which was prepared in 86% yield by hydrolyzation of **3** with lithium hydroxide, was reacted with formamide at 150 °C [262] in order to produce **6**, but the target compound was not formed. Finally compound **6** was successfully synthesized (95% yield) through the oxidative ring closure [263] of **4** in refluxing acetic anhydride to form compound **5** (78% yield) and the subsequent amination [264] of **5** by heating in ammonium acetate at 170 °C and successively with 30% sodium hydroxide.

Due to the extremely low solubility of **6** in all solvents tested, *N*-alkylation was performed to solubilize **6**. Compound **6**, K_2CO_3, with 2-decyltetradecyl or 4-octadecyldocosanyl in DMF were heated to 130 °C and left for 16 h to afford **PQ2T-24** (73% yield) or **PQ2T-40** (67% yield). To demonstrate potential functionalization of this pyrimido[4,5-*g*]quinazoline-4,9-diones derivative, the thiophene moieties were then brominated at the 5 positions with NBS. A catalytic amount of bromine was added to accelerate the bromination to afford **PQ2T-24-Br** (75% yield) and **PQ2T-40-Br** (80% yield), respectively. Polymers **PPQ2T-BT-24** and **PPQ2T-BT-40** were synthesized *via* Stille coupling polymerization of **PQ2T-24-Br** and **PQ2T-40-Br**, respectively, with 5,5'-bis(trimethylstannyl)-2,2'-bithiophene (Scheme 5-2). Likewise, polymers **PPQ2T-TT-24** and **PPQ2T-TVT-24** were synthesized *via* Stille coupling polymerization of **PQ2T-24-Br** with 2,5-bis(trimethylstannyl)thieno[3,2-*b*]thiophene and 1,2-bis(5-(trimethylstannyl)thiophen-2-yl)ethene, respectively. All polymers were purified using Soxhlet extraction sequentially with acetone, hexanes, and chloroform. **PPQ2T-BT-24** was insoluble in chloroform and required further treatment with a high boiling point solvent, 1,1,2,2-tetrachloroethane (TCE) and as obtained with 95% yield whereas **PPQ2T-BT-40** was quite soluble in chloroform, which was more than likely due to its much larger side chains, and was obtained at 74% yield. **PPQ2T-TT-24** and **PPQ2T-TVT-24** were also soluble in chloroform and were obtained in 82% and 87% yields, respectively.

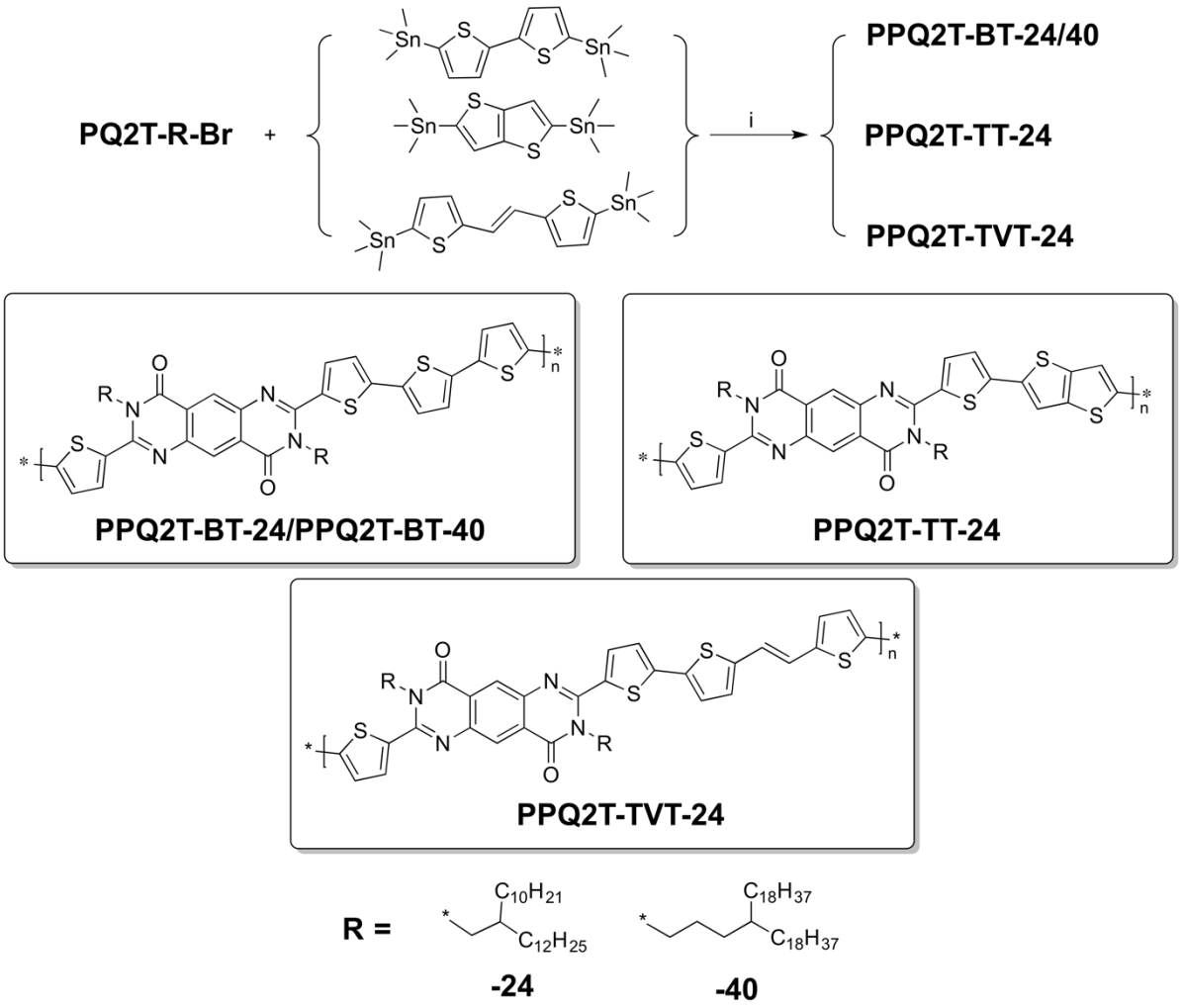

Scheme 5-2. Reagents and conditions: (i) $Pd_2(dba)_3$/P(*o*-tolyl)$_3$/chlorobenzene/130 °C.

5.4 Characterization of Aforementioned Polymers

5.4.1 Molecular Weight and Thermal Analysis

The M_n and *PDI* were measured to be 38.9 kg mol^{-1} and 3.68 for **PPQ2T-BT-24** and 43.5 kg mol^{-1} and 2.95 for **PPQ2T-BT-40**, respectively (Appendix; Figure C-6). The M_n and *PDI* were measured to be 18.3 kg mol^{-1} and 2.23 for **PPQ2T-TT-24** and 19.4 kg mol^{-1} and 2.52 for **PPQ2T-TVT-24**, respectively. In all cases, monomodal distributions were observed suggesting consistent linear growth in the polymer chains. **PPQ2T-BT-24** showed good thermal stability with a 5% weight loss temperature ($T_{-5\%}$) at 340 °C, while **PPQ2T-BT-40** showed slightly lower thermal stability with a $T_{-5\%}$ at 317 °C (Appendix; Figure C-7). No visible glass transition (T_g) or endo/exotherm was observed before ~200

°C from differential scanning calorimetry (DSC) thermograms (Appendix; Figure C-8). **PPQ2T-TT-24** and **PPQ2T-TVT-24** showed much higher $T_{-5\%}$ of 366 °C and 376 °C, respectively. Both polymers showed visible T_g temperatures at °60–70 °C on their DSC thermograms.

5.4.2 Optical and Electrochemical Analysis

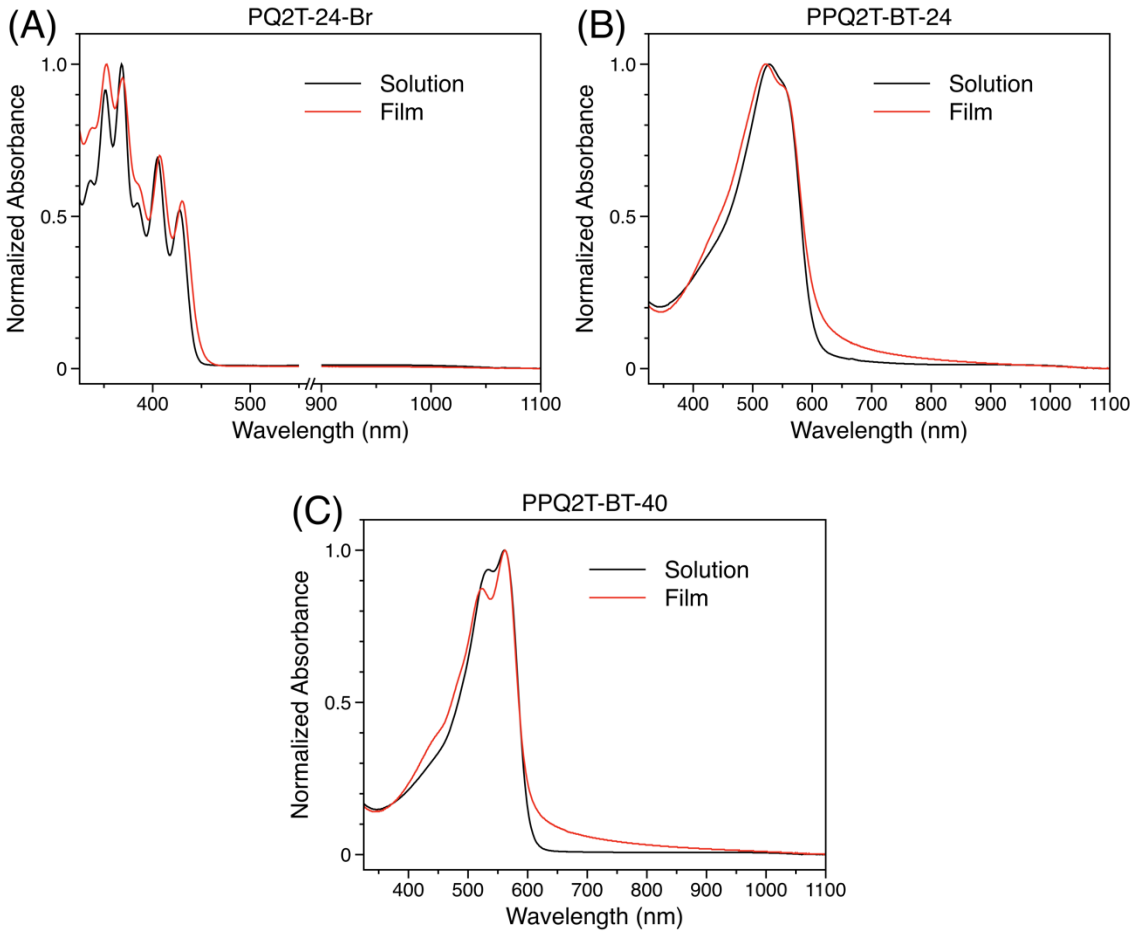

Figure 5-4. UV-Vis-NIR absorption spectra of **PQ2T-24-Br** (A) in toluene and thin film, **PPQ2T-BT-24** (B) in TCE and thin film, and **PPQ2T-BT-40** (C) in chloroform and thin film.

As shown in Figure 5-4, **PQ2T-24-Br** exhibited a wavelength of maximum absorbance (λ_{max}) for solution and film at 353 and 367 nm, respectively. The optical band gap (E_g^{opt}) calculated from the absorption onset of the film is 2.71 eV. As polymer, **PPQ2T-BT-24** in TCE showed a poorly resolved vibronic splitting absorption profile with the λ_{max} at 526 nm and a weak absorption shoulder at ~550 nm. The thin film exhibited a slight hypsochromic shift (λ_{max} = 522 nm) relative to that of solution. **PPQ2T-BT-40** in chloroform showed a slightly better resolved vibronic splitting absorption pattern

with λ_{max} at 562 nm accompanied by the appearance of an absorption shoulder at 531 nm. The thin film exhibited the same λ_{max} at 562 nm with a more resolved absorption shoulder at 524 nm. The larger λ_{max} observed for **PPQ2T-BT-40** both in solution and film compared to **PPQ2T-BT-24** is considered due to the farther distance of the bifurcation point of C40 side chain in the former, which allows for achieving higher coplanarity of the polymer backbone [265]. The hypsochromic shift from solution to film observed for **PPQ2T-BT-24** can be attributed to the H-aggregation over the J-aggregation as a result of the delicate competition between interchain coupling and intrachain coupling [266,267]. The E_g^{opt} of **PPQ2T-BT-24** and **PPQ2T-BT-40** calculated from the onset absorption wavelengths of their thin films is ~2.03 eV.

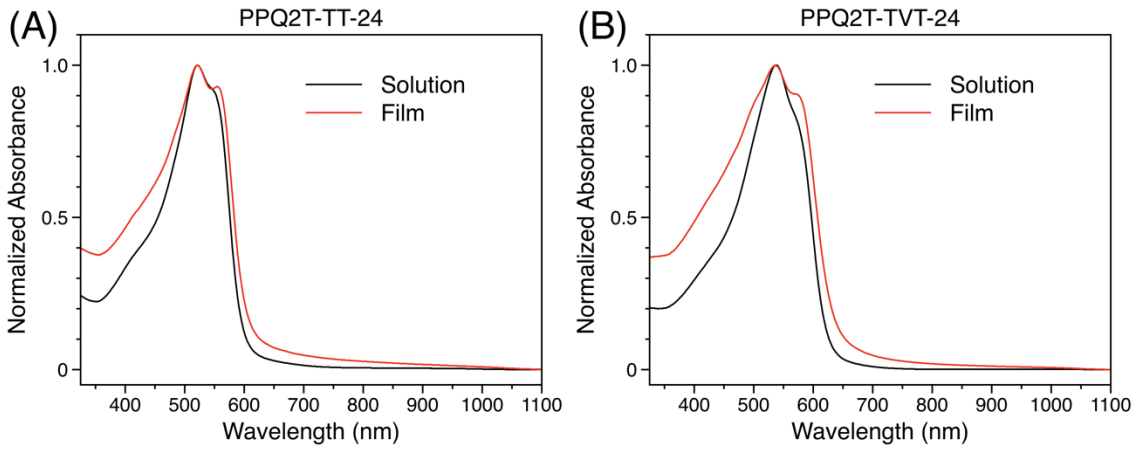

Figure 5-5. UV-Vis-NIR absorption spectra of **PPQ2T-TT-24** (left) and **PPQ2T-TVT-24** (right) in chloroform and thin film.

The UV-vis absorption spectra of **PPQ2T-TT-24** and **PPQ2T-TVT-24** in chloroform and in thin films are shown in Figure 5-5. **PPQ2T-TT-24** showed a λ_{max} at 522 nm (along with a shoulder at ~548 nm) for solution and 521 nm (along with a shoulder at ~556 nm) for the thin film. **PPQ2T-TVT-24** showed a similar absorption pattern with the λ_{max} at 537 nm (along with a shoulder at ~571 nm) in solution and 536 nm (along with a shoulder at ~575 nm) for the thin film. The more resolvable vibronic splitting or the more pronounced absorption shoulders at the long wavelength side of the spectra of the thin film compared to the solution spectra are characteristic of more ordered polymer chains in the solid state [266–268] and were also observed for **PPQ2T-BT-24** and **PPQ2T-BT-40**. The E_g^{opt} were found to equal 2.0 eV and 1.9 eV for **PPQ2T-TT-24** and **PPQ2T-TVT-24**, respectively.

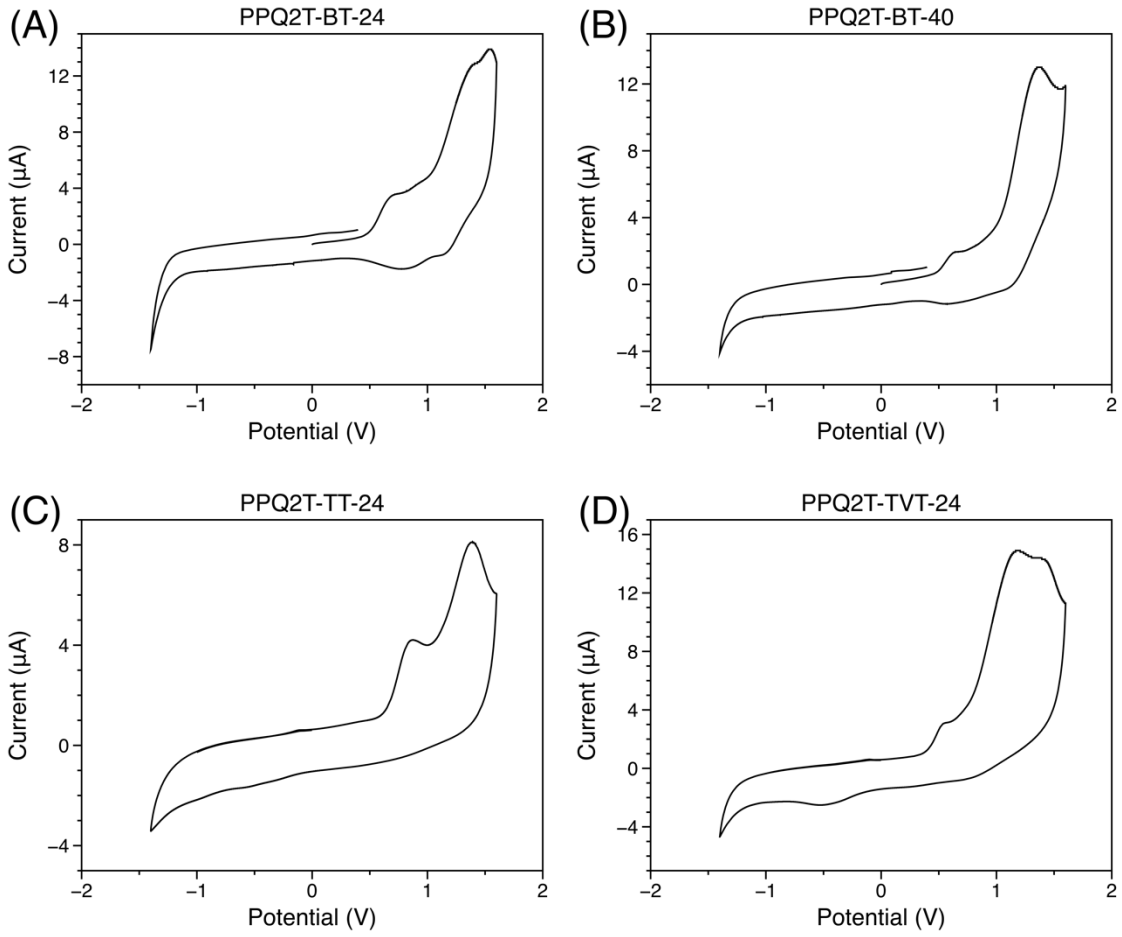

Figure 5-6. CV curves of polymers in a 0.1 M tetrabutylammonium hexafluorophosphate (Bu_4NPF_6) solution in anhydrous acetonitrile at a scan rate of 50 mV s^{-1}.

CV measurements of polymer thin-films showed that **PPQ2T-BT-24** and **PPQ2T-BT-40** have HOMO energy levels of -5.30 eV and -5.29 eV, respectively, calculated from their oxidative onset potentials (Figure 5-6). Neither of the two polymers showed reversible reductive processes. Hence, the LUMO energy levels were calculated from the HOMO energy levels obtained from the CV and the E_g^{opt} from the UV-Vis-NIR data to be equal to -3.27 eV for **PPQ2T-BT-24** and -3.26 eV for **PPQ2T-BT-40**. Likewise, the HOMO energy levels for **PPQ2T-TT-24** and **PPQ2T-TVT-24** were calculated to be -5.42 eV and -5.18 eV, falling below and above that of **PPQ2T-BT-24** (-5.30 eV), respectively, which are also in good agreement with the trend observed in the computational study. It should be noted that most of the p-type polymer semiconductors with high hole mobility have a relatively high HOMO level between -5.1 eV to -5.3 eV [265,269,270]. Therefore, the HOMO level of **PPQ2T-TVT-24** should

be more favoured for hole injection and transport. Again, no peaks were observed during the reduction cycles, so the LUMO energy levels were calculated from the corresponding HOMO energy levels and E_g^{opt} to be -3.41 eV and -3.27 eV for **PPQ2T-TT-24** and **PPQ2T-TVT-24**, respectively. All CV measurements were conducted on the polymer thin-films using ferrocene as a reference with a reported HOMO energy level of -4.8 eV against vacuum [271].

5.4.3 Acid Study

Conjugated polymers containing pyridine,[272] imidazole,[273] benzimidazole,[274–276] quinoxaline,[276] phenanthroline,[272] benzothiadiazole,[206] and pyridalthiadiazole[206] have been reported to strongly interact with acids due to the available lone pairs on the nitrogen atoms in these moieties. Similarly, the in-plane electron lone pairs of the nitrogen atoms at the 1 and 6 positions in the PQ moiety are not involved in π-conjugation, which would act as basic sites to interact with acids. To investigate the acid effects on these PQ polymers, a strong organic acid, trifluoroacetic acid (TFA: pK_a = -0.25)[208] and a weak organic acid, acetic acid (AcOH: pK_a = 4.8)[208] were chosen, because they are readily soluble in the organic solvent used (chlorobenzene) and their concentration can be easily controlled. As shown in Figure 5-7, at a TFA concentration as low as 10 μM, a level similar to that of the PQ units in **PPQ2T-BT-24** (~1×10^{-5} M), a long wavelength shoulder at ~650 nm appeared. As the TFA concentration further increases, the λ_{max} bathochromically shifts. At a TFA concentration of 10 mM, no further spectral change occurs and a largest λ_{max} of 673 nm is reached, which corresponds to a bathochromic shift of 145 nm from that of the solution without acid. For the much weaker acid, AcOH, a very high concentration of 2 M was needed to make a noticeable spectral change. The largest λ_{max} of 634 nm, or a bathochromic shift of 106 nm from the solution without acid, was observed at an AcOH concentration of 5 M. Further increasing the AcOH concentration resulted in precipitation of the polymer since AcOH is a non-solvent for **PPQ2T-BT-24**. The smaller achievable bathochromic shift observed in AcOH than in TFA is most likely due to the lower H^+ concentration in the former, being unable to fully protonate the 1,6-nitrogen atoms in the polymer. To demonstrate binding of Lewis acids to the 1,6-nitrogen atoms, a strong Lewis acid, boron tribromide (BBr_3), was used. At a very low BBr_3 concentration of 1 μM, a shoulder appeared at ~650 nm in the UV-Vis-NIR spectrum of **PPQ2T-BT-24**, similar to the solution containing TFA, but the latter required a much higher acid (TFA) concentration of ~10 μM, which is due to the stronger acidity of BBr_3. At a BBr_3 concentration of 6 μM the absorption spectrum bathochromically shifted with a λ_{max} of 673 nm, which appears to be identical to that of the longest λ_{max} obtained in the TFA solution at ~10 mM. Greater concentrations of

BBr_3 lead to precipitation of the polymer-BBr_3 complexes. It should be noted that the spectral changes are reversible; the original spectra of the pristine polymers could be recovered by adding a base such as pyridine to neutralize the acid in the polymer solution. Similar responses to TFA, AcOH, and BBr_3 were observed for **PPQ2T-BT-40** (Appendix, Figure C-12) although the largest λ_{max} obtained in TFA, AcOH, and BBr_3 are at longer wavelengths of 659 nm, 686 nm, and 707 nm, respectively, which result from the more coplanar backbone of **PPQ2T-BT-40** as discussed above.

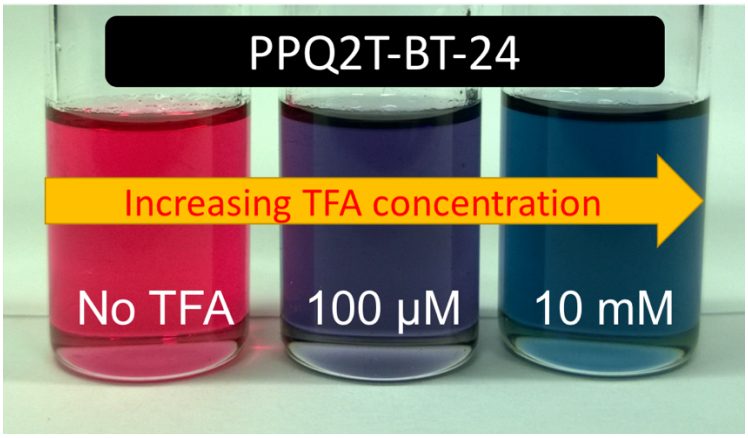

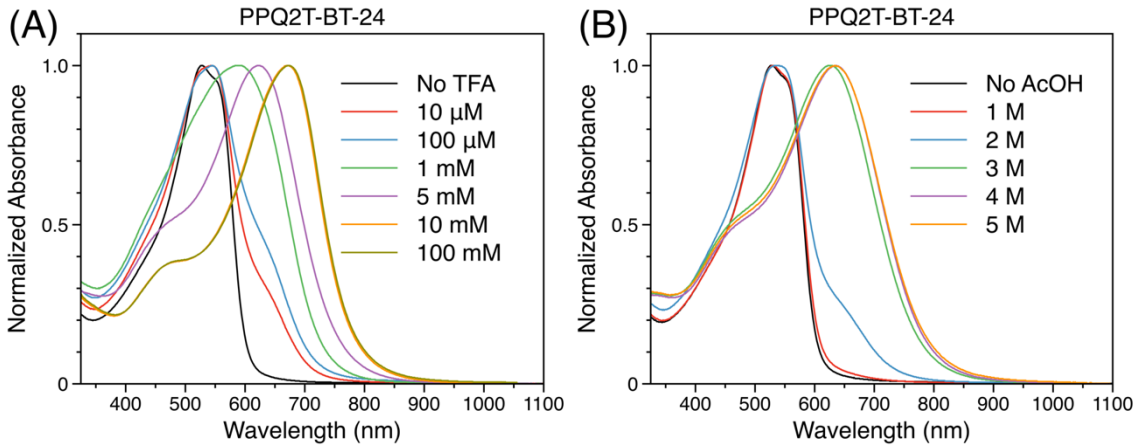

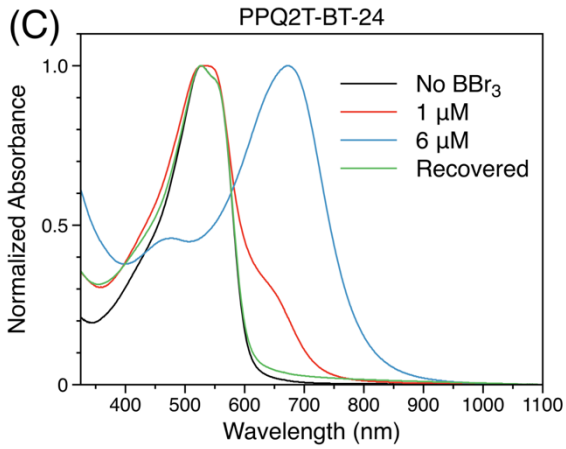

Figure 5-7. Top: Colour change of **PPQ2T-BT-24** solutions with increasing concentration of trifluoroacetic acid (TFA) from 0 M (left), to 10^{-4} M (middle) and 10^{-2} M (right) with a molar concentration of the polymer repeat unit at ~1×10^{-5} M. The UV-Vis-NIR absorption spectra of **PPQ2T-BT-24** in chlorobenzene with various concentrations of TFA (A), AcOH (B), and BBr_3 (C). The measurements were conducted under nitrogen with a molar concentration of the polymer repeat unit at ~1×10^{-5} M.

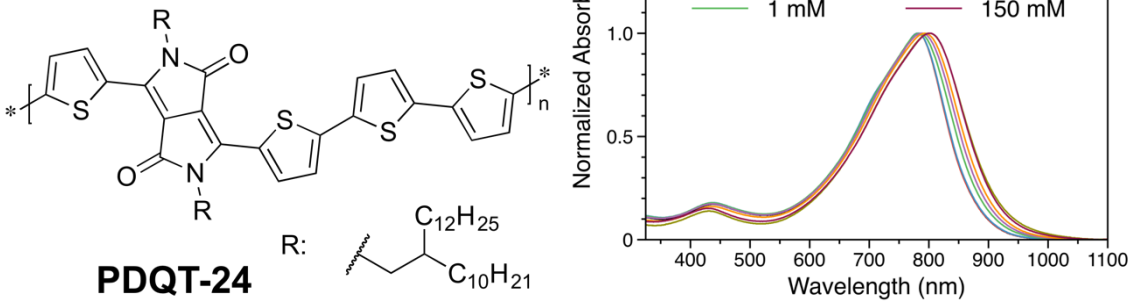

Figure 5-8. The structure of diketopyrrolopyrrole (DPP)-quaterthiophene copolymer with 2-decyltetradecyl side chain (**PDQT-24**). The UV-Vis-NIR absorption spectra of **PDQT-24** in chlorobenzene with various concentrations of TFA. The measurements were conducted under nitrogen with a molar concentration of the polymer repeat unit at ~1×10^{-5} M.

Two other nitrogen atoms at the 3,8-position in PQ, which reside in the amide moieties, are not expected to strongly interact with acids because typical amides are very weak bases with their conjugate

acids having a pK_a value of ~1.[277] To demonstrate that the basic 1,6-nitrogen atoms are mainly responsible to the marked bathochromic shifts in the presence of acids, a diketopyrrolopyrrole (DPP)-quaterthiophene copolymer with the same 2-decyltetradecyl side chain (**PDQT-24**, Figure 5-8),[265] was tested at various concentrations of TFA for comparison (Figure 5-8). **PDQT-24** contains amide nitrogen atoms in the DPP unit, which are similar to the 3,8-nitrogen atoms in the PQ unit. As expected, only a subtle bathochromic shift of ~3 nm was observed in 1 mM TFA solution and the maximum bathochromic shift of ~20 nm was achieved at a TFA concentration of 150 mM, which is 15 times larger than that required for **PPQ2T-BT-24** (~10 mM TFA). To further corroborate the interaction of 1,6-nitrogen atoms in PQ with acids, a similar UV-Vis-NIR study was performed on the monomers **PQ2T-24-Br** and **D2T-24-Br** (the monomer for **PDQT-24**) at various concentrations of TFA (Figure 5-9). **PQ2T-24-Br** showed a small shoulder at ~460 nm at 1 mM of TFA and then a significant change at 5 mM. When the TFA concertation is ≥ 100 mM, the spectra remain unchanged, indicating that all 1,6-nitrogen atoms were protonated. The maximum bathochromic shift (determined from the first peaks from the right side) is ~39 nm. The changes in the shape and relative intensities of absorption peaks with increasing TFA concentration from 1 mM to 100 mM are considered due to the formation of varied amounts of mono- and di-protonated species. On the contrary, **D2T-24-Br** showed no changes in peak positions when the TFA concertation was increased up to as high as 2 M. Variations in the relative intensities of some peaks are observed, which might be due to the solvent effect of TFA on **D2T-24-Br** molecules, since the polarity of TFA is much higher than the bulk solvent chlorobenzene and TFA is a poor solvent for **D2T-24-Br**. These results support that the 1,6-nitrogen atoms in the PQ units of **PPQ2T-BT-24** and **PPQ2T-BT-24** predominantly contribute to the large bathochromic shifts in the presence of acids. It is also noticed that the monomeric compound **PQ2T-24-Br** requires a two order of magnitude higher concentration (~1 mM) to make a notable change in its absorption spectrum compared with its polymer **PPQ2T-BT-24** (~10 μM), indicating that the polymer has greatly enhanced sensitivity towards an acid. It is assumed that protonation of one or a few PQ units would cause a notable change of the electronic state of the whole polymer main chain. This magnification effect might result from the extended delocalization of π-electrons along the polymer backbone as reported for other conjugated polymers that have been successfully used as highly sensitive chemosensors [278].

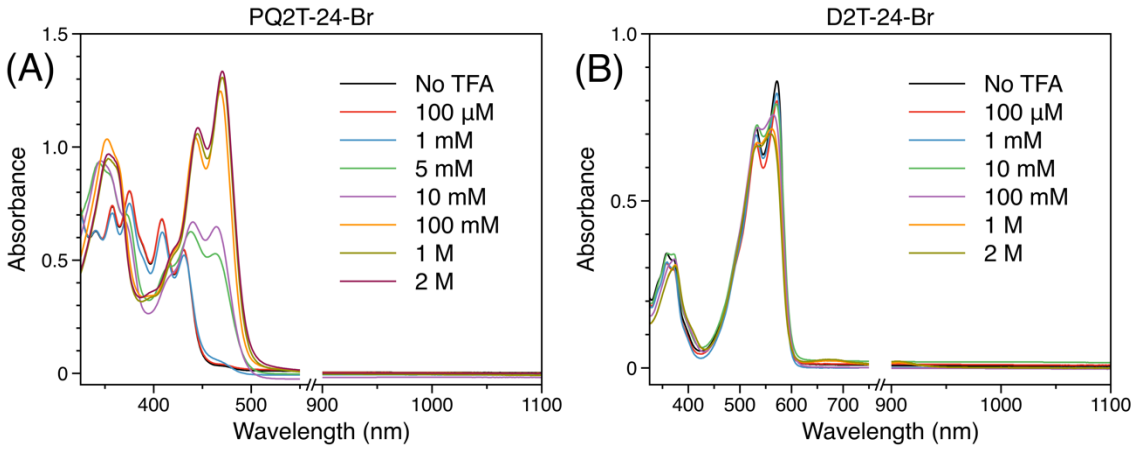

Figure 5-9. The UV-Vis-NIR absorption spectra of (A) **PQ2T-24-Br** and (B) **D2T-24-Br** in chlorobenzene with various concentrations of TFA until little variation was observed. The measurements were conducted under nitrogen with a molar concentration of **PQ2T-24-Br** or **D2T-24-Br** at ~1×10^{-5} M.

5.4.4 Morphological Analysis

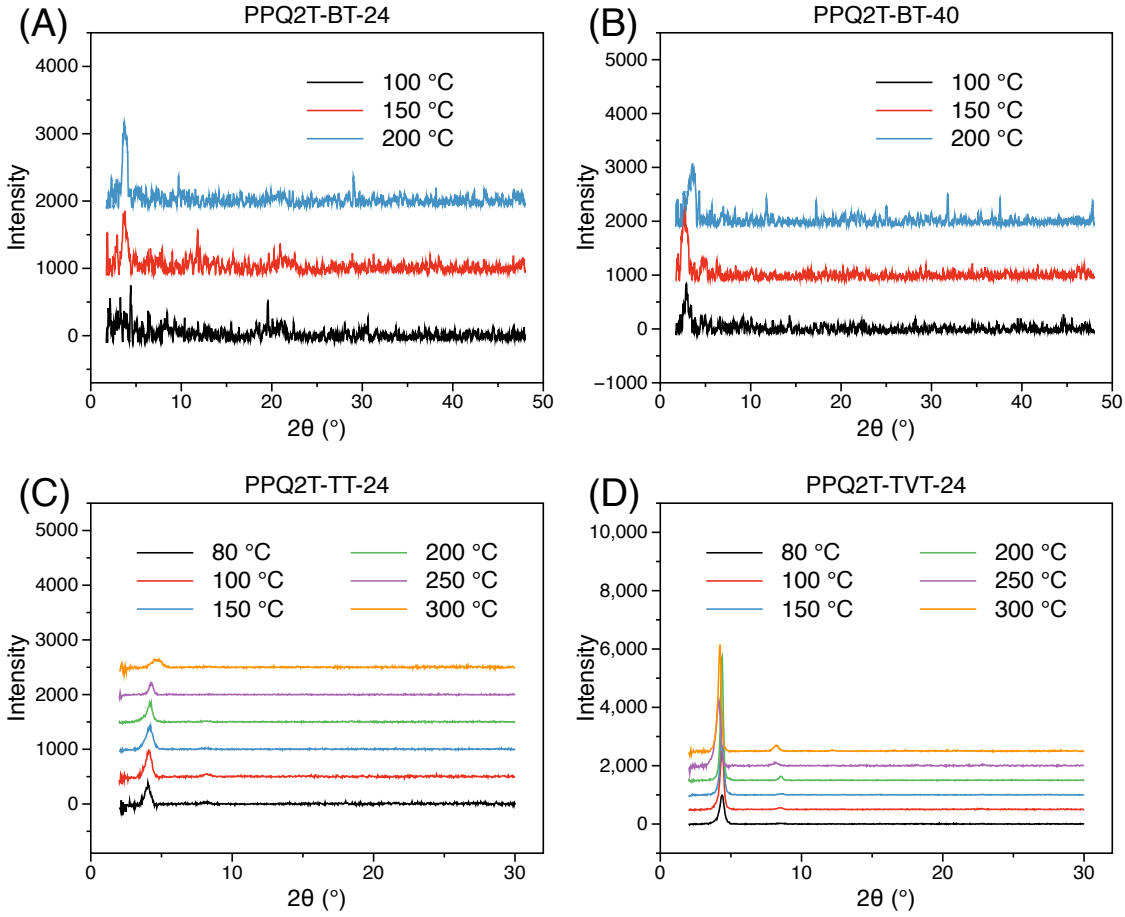

Figure 5-10. Reflection XRD diagram of polymer thin films spin-coated on dodecyltrichlorosilane-modified SiO_2/Si substrates and annealed at different temperatures with Cu Kα radiation (λ = 0.15406 nm).

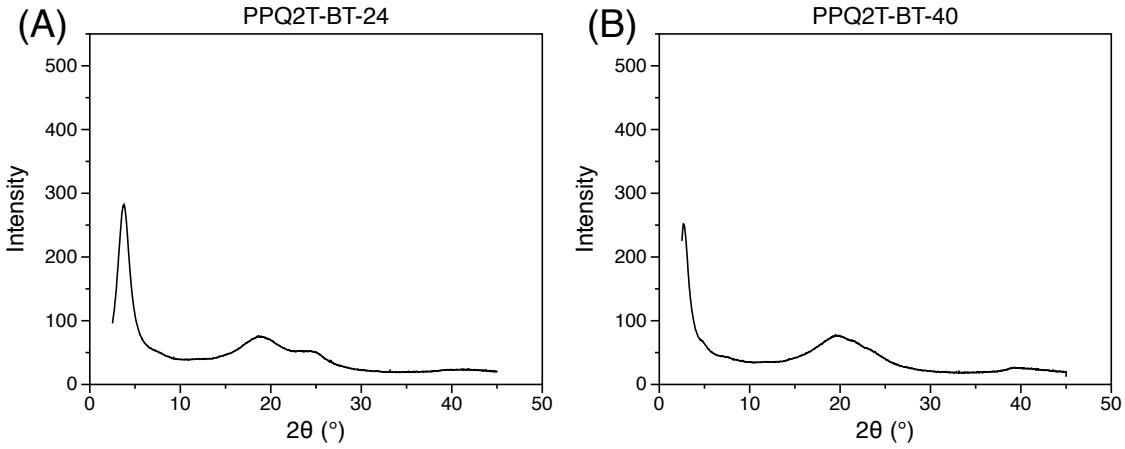

Figure 5-11. The transmission XRD pattern **PPQ2T-BT-24** (left) and **PPQ2T-BT-40** (right) flakes stacked between two polyester film substrates with a Cu Kα (Rigaku) X-ray source (λ = 0.15406 nm).

To elucidate the molecular ordering of these polymers, reflection X-ray diffraction (XRD) measurements were performed with polymer thin films spin coated on a SiO_2/Si wafer and annealed at desired temperatures. Both **PPQ2T-BT-24** and **PPQ2T-BT-40** showed low intensity primary (001) diffraction peaks at 2θ = 3.74 ° and at 2θ = 2.80 ° at 100 °C, respectively, corresponding to a *d*-spacing distance of 1.18 nm and 1.58 nm, respectively (Figure 5-10). When annealing, temperatures were increased up to 200 °C little change was observed for **PPQ2T-BT-24**. However, at 200 °C **PPQ2T-BT-40** showed a new primary diffraction peak at 3.58 ° corresponding to a *d*-spacing distance of 1.23 nm indicative of better interlayer ordering, but with little change in overall crystallinity. Transmission XRD measurements were also performed using polymer flakes (Figure 5-11). **PPQ2T-BT-24** and **PPQ2T-BT-40** showed low intensity primary (100) diffraction peaks at 2θ = 3.80 ° and 2.68 °, which correspond to the inter-lamellar distances of 2.33 nm and 3.30 nm, respectively. The small hump centred at 2θ = 24.73 ° observed for **PPQ2T-BT-24** could be assigned to the (010) peak, originating from the co-facial π-π stacking distance of adjacent polymer backbones [213], which was calculated to be 0.36 nm. However, **PPQ2T-BT-40** does not show a noticeable diffraction peak representing the π-π stacking distance due to the concurrent broad amorphous peak (~19–20 °) in the same region. At an annealing temperature of 80 °C, a primary (100) diffraction peak at 2θ = 4.03 °, which corresponds to a *d*-spacing distance of 2.19 nm, and a low intensity secondary (200) diffraction peak (2θ = 8.22 °) were observed for **PPQ2T-TT-24**. A slight increase in the intensity for the (100) and (200) peaks occurred at an annealing temperature of 100 °C, whereas further increasing the annealing temperature (50 °C increments) results in a gradual increase in the intensity of the (100) and (200) peaks. At an

annealing temperature of 250 °C and above, a decrease in the peak intensity was observed. Since the TGA thermograms show that these polymers are stable at 250 and 300 °C and the UV-vis spectra of the films showed no significant changes in the 250 °C- and 300 °C-annealed films compared with films annealed at lower temperatures (Appendix; Figure C-9), this reduction of the peak intensity might be caused by the creation of pin-holes at these high temperatures (see the AFM images in Figure 5-13), which reduced the coverage of the substrate by the polymer film. For the **PPQ2T-TVT-24** thin film annealed at 80 °C, a weak (100) peak at 2θ = 4.39 ° (*d*-spacing = 2.01 nm) appeared. With increasing annealing temperature, the intensity of the (100) peak grew, along with the appearance of a secondary (200) diffraction peak (2θ = 8.58 °). For the 250 °C- and 300 °C-annealed films, a reduction in the peak intensity was also observed that is probably due to the formation of pin-holes discussed as above for **PPQ2T-TT-24** (Appendix; Figure C-11).

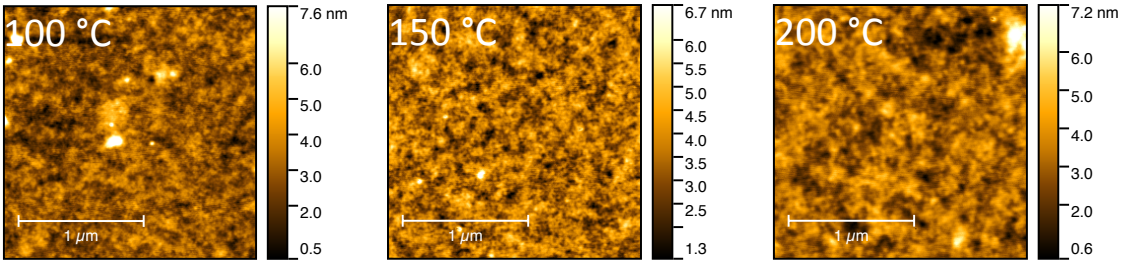

Figure 5-12. AFM images (2 μm × 2 μm, 1 μm scale bars) of **PPQ2T-BT-24** thin films after annealing at various temperatures.

The film morphology of the polymer thin-films spin-coated on dodecyltrichlorosilane modified SiO_2/Si wafer substrates was examined by atomic force microscopy (AFM). **PPQ2T-BT-24** thin films on DDTS-modified SiO_2/Si 1substrates showed poorly defined domains at all annealing temperatures tested, 100 °C, 150 °C, and 200 °C (Figure 5-12). **PPQ2T-BT-40** films, especially for the 200 °C-annealed film, have more defined domains than the **PPQ2T-BT-24** films (Appendix; Figure C-10). The root mean square (RMS) roughness of the **PPQ2T-BT-40** films (~2 to 3 nm) is larger than that of the **PPQ2T-BT-24** films (< 1 nm). The **PPQ2T-TT-24** film annealed at temperatures lower than 200 °C showed large particles (irregular shaped bright spots) of a few hundred nanometers in size (Figure 5-13). The formation of large particles might be due to the poor solubility of this polymer that caused precipitation of polymer aggregates as solvent evaporated during spin coating. As the annealing temperature was increased to 250 °C, these particles disappeared accompanied with the formation of pin-holes (dark spots). The number of pin-holes increased as the annealing temperature was increased

to 300 °C. The formation of pin-holes is likely due to the weakened interfacial interaction between the polymer film and the substrate at high temperatures. The 80 °C-annealed **PPQ2T-TVT-24** film showed some round-shaped particles (bright spots) and well-defined grains (Appendix; Figure C-11). Similar to **PPQ2T-TT-24**, the number of (bright) particles decreases with increasing annealing temperature. The particles almost disappeared at the annealing temperature of 200 °C, 50 °C lower compared with **PPQ2T-TT-24**. However, pin-holes also start to appear at 200 °C, indicating that the interfacial interaction between the **PPQ2T-TVT-24** film and the substrate is weaker than that between **PPQ2T-TT-24** and the substrate.

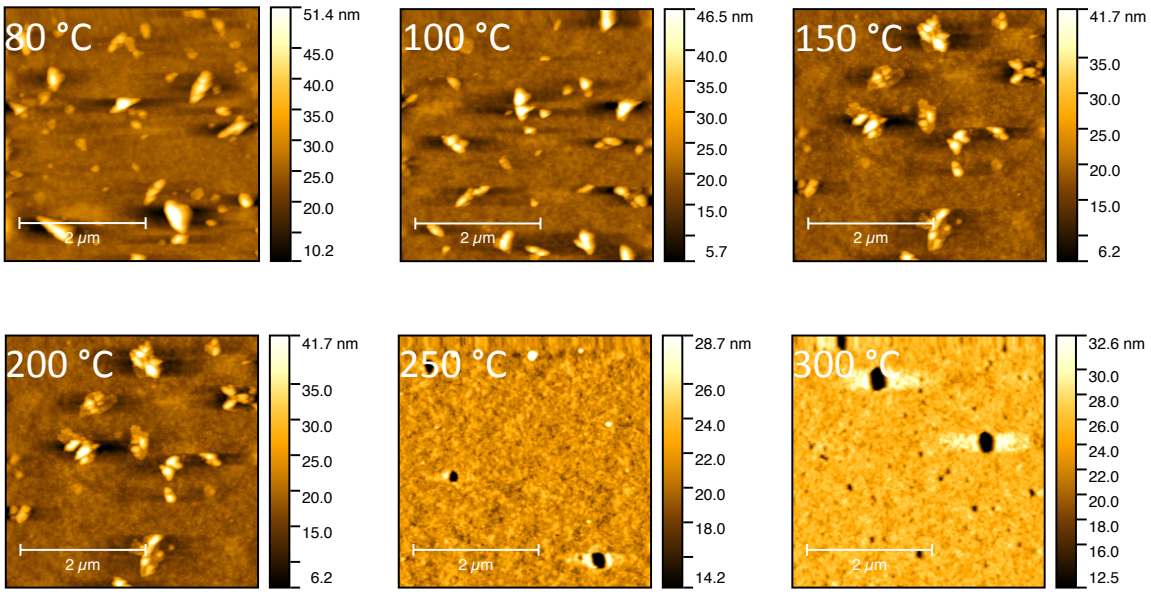

Figure 5-13. AFM images (4 µm × 4 µm, 2 µm scale bars) of **PPQ2T-TT-24** thin films after annealing at various temperatures.

5.4.5 I-V Characterization

For detailed device fabrication refer to Appendix D.

5.4.5.1 Nitrogen Study

All PQ based polymers showed typical hole transport behaviour in BGBC devices (Figure 5-14 and Table 5-1). A deep LUMO level of ~-3.7 eV to ~-4.0 eV is required for stable n-type performance [279–281]. Devices based on the 250 °C-annealed **PPQ2T-BT-24** films showed the best performance with the highest hole mobility of 6.4×10^{-3} cm^2 V^{-1} s^{-1} (Figure 5-14A) and an average value of $5.9 \times 10^{-}$

^{3} cm^2 V^{-1} s^{-1}. Devices based on **PPQ2T-BT-40** showed the best average mobility of 3.2×10^{-3} cm^2 V^{-1} s^{-1} with the highest value of 3.5×10^{-3} cm^2 V^{-1} s^{-1} for the films annealed at 300 °C (Figure 5-14B). The slightly higher hole mobility of **PPQ2T-BT-24** may be attributed to its slightly better film morphology (discussed in 5.4.4). **PPQ2T-TT-24** devices showed the best performance with the 300 °C-annealed films reaching a maximum hole mobility of 3.08×10^{-3} cm^2 V^{-1} s^{-1} (Figure 5-15A) and an average mobility of 2.33×10^{-3} cm^2 V^{-1} s^{-1}. **PPQ2T-TVT-24** devices performed the best for the 150 °C-annealed films, reaching a maximum hole mobility of 5.34×10^{-3} cm^2 V^{-1} s^{-1} (Figure 5-15B) and an average mobility of 4.81×10^{-3} cm^2 V^{-1} s^{-1}. At an annealing temperature, greater than 200 °C, the mobility values dropped. This mobility reduction trend coincidently agrees with the formation of pin-holes as observed in the AFM images (discussed in 5.4.4). These pin-holes would interrupt the charge transport pathways. As aforementioned, the formation of pin-holes is due to the weakened polymer-substrate interface, which would also negatively influence the charge carrier mobility due to the poorer polymer-dielectric contact [282–284].

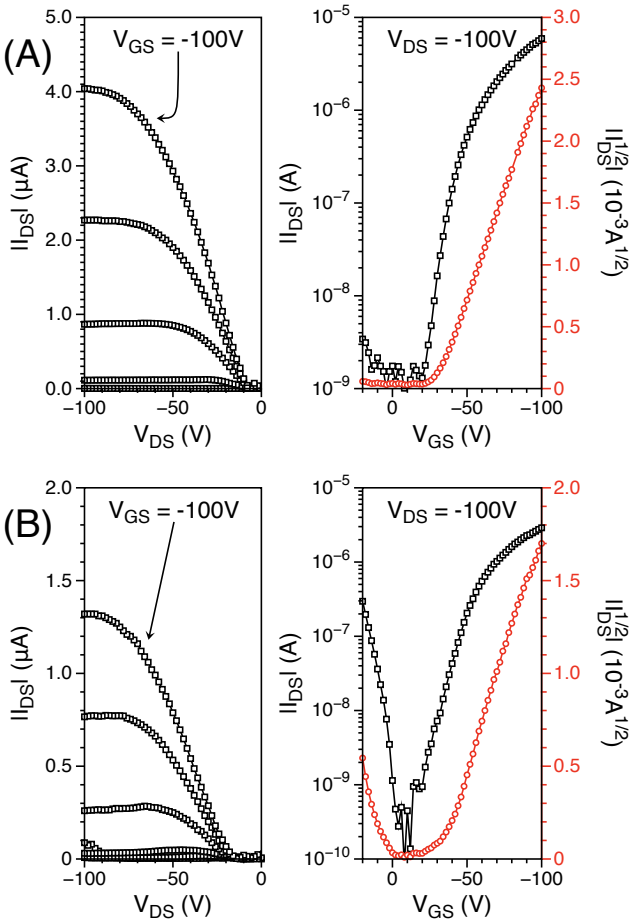

Figure 5-14. Output (left) and transfer (right) curves of a BGBC device with a thin-film of **PPQ2T-BT-24** (A) annealed at 250 °C and **PPQ2T-BT-40** (B) annealed at 300 °C. Device dimensions: L = 30 μm; W = 1000 μm. Output curves are measured from 0 to -100 V at -20 V increments.

Table 5-1. The summary of BGBC device performance of **PPQ2T-BT-24** and **PPQ2T-BT-40**.

Polymer	Annealing temperature (°C)	Hole mobility[a] (10^{-3} cm^2 V^{-1} s^{-1})	Average V_{th} (V)	I_{on} / I_{off}
PPQ2T-BT-24	100	3.42 (3.21 ± 0. 15)	-26.52	~10^3
	150	4.68 (4.49 ± 0. 18)	-27.20	~10^3
	200	5.88 (5.50 ± 0. 28)	-29.15	~10^3
	250	6.43 (5.86 ± 0. 36)	-28.76	~10^3
	300	3.80 (3.43 ± 0. 30)	-23.45	~10^3
PPQ2T-BT-40	100	1.37 (0.86 ± 0. 31)	-15.52	~10^3
	150	2.42 (1.90 ± 0. 75)	-25.43	~10^3
	200	2.97 (2.61 ± 0. 45)	-30.35	~10^5
	250	3.59 (3.12 ± 0. 49)	-30.43	~10^5
	300	3.49 (3.20 ± 0. 21)	-24.30	~10^4

[a] The maximum (average ± standard deviation) mobility was calculated from the saturated regime of at least five devices for each condition.

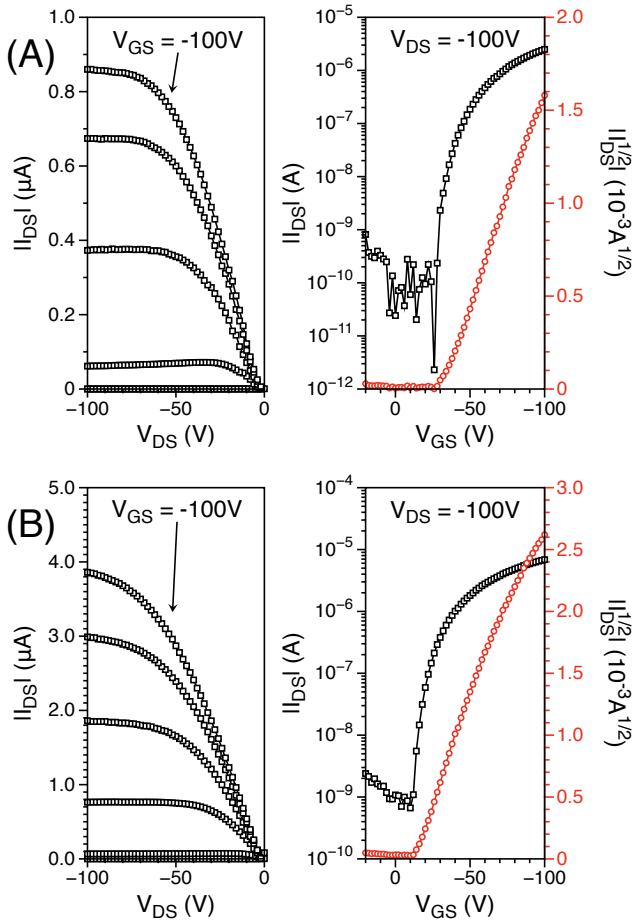

Figure 5-15. Output (left) and transfer (right) curves of a BGBC device with a thin film of **PPQ2T-TT-24** (A) annealed at 300 °C and **PPQ2T-TVT-40** (B) annealed at 150 °C. Device dimensions: L = 30 μm; W = 1000 μm. Output curves are measured from 0 to -100 V at -20 V increments.

Table 5-2. The summary of OTFT performance of **PPQ2T-TT-24** and **PPQ2T-TVT-24** thin films annealed at different temperatures and characterized under dry nitrogen atmosphere.

Polymer	Annealing temperature (°C)	Hole mobility[a] (10^{-3} $cm^2V^{-1}s^{-1}$)	Average V_{th} (V)	I_{on}/I_{off}
PPQ2T-TT-24	80	1.92 (1.59 ± 0.26)	-22.08	~10^4
	100	1.90 (1.77 ± 0.18)	-6.31	~10^4
	150	2.27 (2.11 ± 0.16)	-9.28	~10^4
	200	2.27 (2.19 ± 0.05)	-25.05	~10^4
	250	2.63 (2.13 ± 0.48)	-29.59	~10^4
	300	3.08 (2.33 ± 0.58)	-13.43	~10^4
PPQ2T-TVT-24	80	3.80 (3.58 ± 0.18)	-6.50	~10^4
	100	4.96 (4.39 ± 0.46)	-7.70	~10^4

	150	5.34 (4.81 ± 0.39)	-3.32	~10^4
	200	5.26 (4.85 ± 0.40)	-7.88	~10^4
	250	3.99 (3.62 ± 0.35)	-4.60	~10^4
	300	3.81 (3.53 ± 0.32)	-3.93	~10^4

[a] The maximum (average ± standard deviation) mobility was calculated from the saturated regime of at least five devices for each condition.

As with the BGBC devices, the TGBC devices of the polymers **PPQ2T-BT-24**, **PPQ2T-TT-24**, and **PPQ2T-TVT-24** showed hole-only transport behaviour. The TGBC devices were annealed at 200 °C as this was the best average mobility temeprature for their corresponding BGBC devices. Both **PPQ2T-BT-24** and **PPQ2T-TT-24** (Figure 5-16) based devices showed the best performance with and identical high hole mobility of 1.7×10^{-2} cm^2 V^{-1} s^{-1} and an average value of 1.4×10^{-2} cm^2 V^{-1} s^{-1} and 1.3×10^{-2} cm^2 V^{-1} s^{-1}, respectively. **PPQ2T-TVT-24** (Figure 5-16) based devices had the highest hole mobility of 1.3×10^{-2} cm^2 V^{-1} s^{-1} and an average value of 1.2×10^{-2} cm^2 V^{-1} s^{-1}.

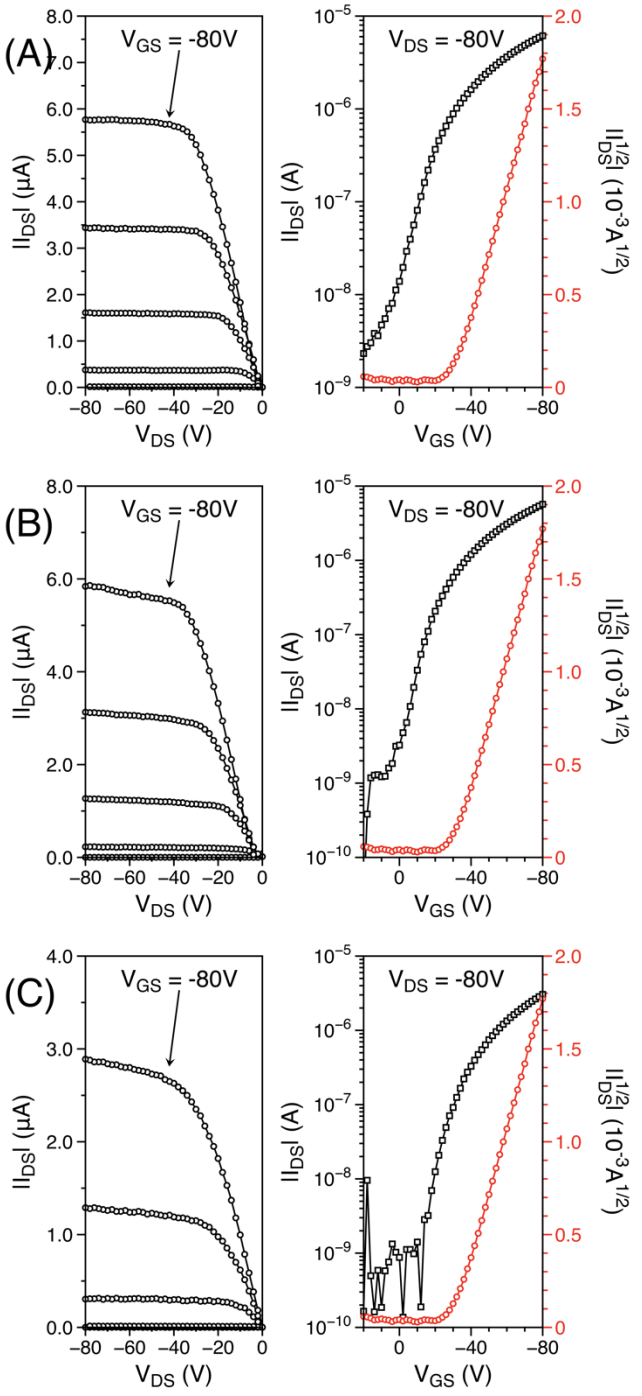

Figure 5-16. Output (left) and transfer (right) curves of a TGBC device with a thin film of **PPQ2T-BT-24** (A), **PPQ2T-TT-24** (B) and **PPQ2T-TVT-24** (C) annealed at 200 °C. Device dimensions: L = 30 μm; W = 1000 μm. Output curves are measured from 0 to -80 V at -20 V increments.

5.4.5.2 Air Stability Study

The devices based on **PPQ2T-BT-24**, **PPQ2T-TT-24**, and **PPQ2T-TVT-24** annealed at 200 °C were subject to testing in the ambient air (with 52% RH) after testing in dry nitrogen in a glove box (Figure 5-17). **PPQ2T-BT-24** based devices measured in the ambient air showed a decrease of ~49% in mobility compared with the value measured in dry nitrogen whereas **PPQ2T-TT-24** based devices showed a decrease of 18% in the average mobility with respect to that measured in dry nitrogen. On the other hand, the mobility of the **PPQ2T-TVT-24** based devices dropped almost completely (~94%) upon exposed to the ambient air. These devices were then moved back to the nitrogen-filled glove box, baked at 100 °C for 1 h to remove adsorbed moisture and oxygen, and tested again. The average mobility of the **PPQ2T-BT-24** based devices recovered by 70% of the value initially measured in the glove box in dry nitrogen. The **PPQ2T-TVT-24** based devices showed negligible field effect performance, indicating that once these devices measured in the ambient air, they underwent permanent damages. Interestingly, the **PPQ2T-TT-24** based devices exhibited a 17% increase in the average mobility compared to that obtained initially in dry nitrogen. It has been reported that numerous factors might influence the ambient stability of OTFT materials/devices [285–287], which is still a subject of intense research [288,147,289,290]. As reported by Lu *et al.*,[291] the ambient stability of polymer semiconductors in regard to oxidative doping is governed by the ionization potential or the HOMO energy level of the polymers. This is evident by the trend observed in this study (Figure 5-17A) where **PPQ2T-TT-24** with the deepest HOMO level of -5.42 eV shows the greatest stability, while **PPQ2T-TVT-24** with the highest HOMO level of -5.18 eV shows the poorest stability in the ambient air. Since air is composed of nitrogen, oxygen, water vapour, and small amounts of other gases, it is reasonable to assume that oxygen and moisture (H_2O) are the two major components that may degrade the device performance of these polymers. It has been reported that dry oxygen had little effect on the field effect characteristics [292] or some enhancement effects on the saturation current and mobility [293] of pentacene based OTFTs. It was also found that the absorbed moisture at the grain boundaries of the pentacene film could either decrease the mobility by trapping charge carriers and altering the film morphology [292,294] or increase the mobility by forming water clusters [292,293]. To gain a better understanding of the influences of air (free of moisture) and moisture (free of oxygen) separately on the performance of our polymers, devices were characterized sequentially under dry nitrogen (in a glove box), dry air (in a container filled with dry air), dry nitrogen (in the same glove box), moist nitrogen (in a container filled with nitrogen saturated with water vapor), and finally in dry nitrogen (in a glove box) (Figure 5-18). For all three polymers, their devices showed increased hole mobilities in dry air with the

largest increase by ~33% observed for **PPQ2T-TT-24**, indicating dry oxygen is not harmful but beneficial for the hole transport, which agrees with the observation in a report on pentacene OTFTs [293]. This enhancement in hole mobility, which was also observed for another p-type polymer reported by our group [290], can be interpreted by the increased work function by oxygen [184]. For the pentacene devices, the increases in the saturation current and mobility were attributed to the formation of a charge transfer complex (or p-doping) between pentacene and O_2 [293]. However, it is unlikely the case for our polymers, because **PPQ2T-TT-24**, which has the deepest HOMO level, or is the most difficult to be p-doped by oxygen, showed the largest enhancement in mobility among three polymers (Figure 5-18).

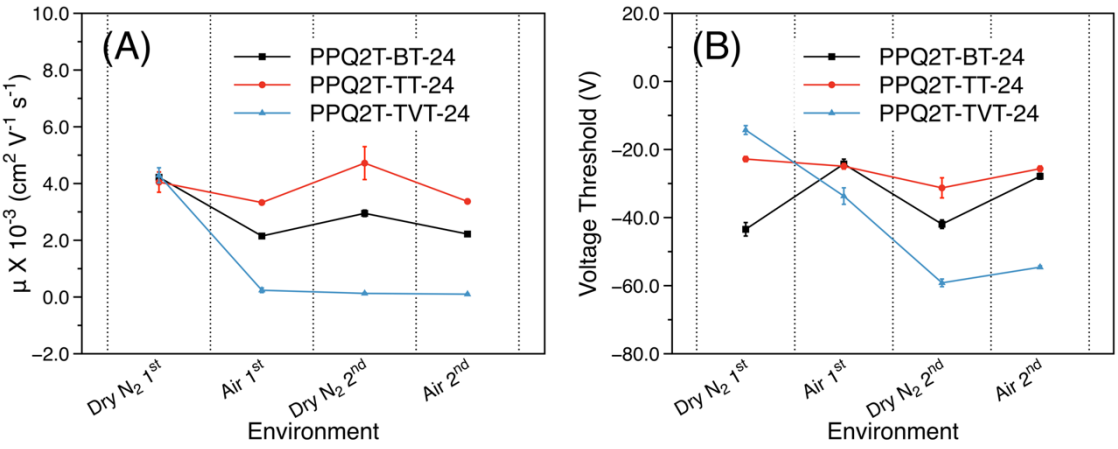

Figure 5-17. Hole mobility comparison (A) and voltage threshold comparison (B) for OTFT devices using different polymers in nitrogen and subsequently in air (~52% relative humidity) consecutively.

Once the devices were returned to the glove box for re-testing under dry nitrogen, the mobilities dropped to similar levels obtained in the first measurement in dry nitrogen. This further demonstrated that dry oxygen did not damage the polymers. Once the devices were taken to the moist nitrogen atmosphere and tested, the mobilities of **PPQ2T-TT-24** and **PPQ2T-BT-24** dropped by 15% and 19%, respectively. The **PPQ2T-TVT-24** devices showed the largest drop in mobility by 43%. To examine if the effect of moisture on the device performance is reversible, the devices were measured in the N_2-filled glove box again (for the 3rd time). It was shown that the average mobility of the **PPQ2T-TT-24** based devices fully recovered to the value obtained in the first and second measurements in dry N_2 (Figure 5-18A). On the other hand, the **PPQ2T-BT-24** and **PPQ2T-TVT-24** based devices partially recovered by ~90% and ~50% of the mobilities obtained before exposing to the moist nitrogen,

respectively, indicating that part of the performance degradation in moist nitrogen is permanent for these two polymers. These results manifest that water, not oxygen, in the ambient air has a detrimental effect on the hole transport performance of these polymers. Our study also showed that different donor comonomers have dramatic influences on the ambient air stability or more precisely the stability towards moisture. The TT-containing polymer, **PPQ2T-TT-24**, showed the best stability in the ambient air and the device performance can be recovered once the devices were returned to a dry nitrogen atmosphere, which indicates that the drop in mobility for this polymer is mainly caused by physisorption of water molecules that might function as hole traps. On the other hand, **PPQ2T-BT-24** and **PPQ2T-TVT-24**, in particular, undergo chemical reactions with water, causing permanent damages to the polymers and the device performance cannot be fully recovered. Since these polymers are stable when stored in the ambient air, the chemical reactions of these polymers with water presumably occur under a positively charged state during the device operation in the hole accumulation mode.

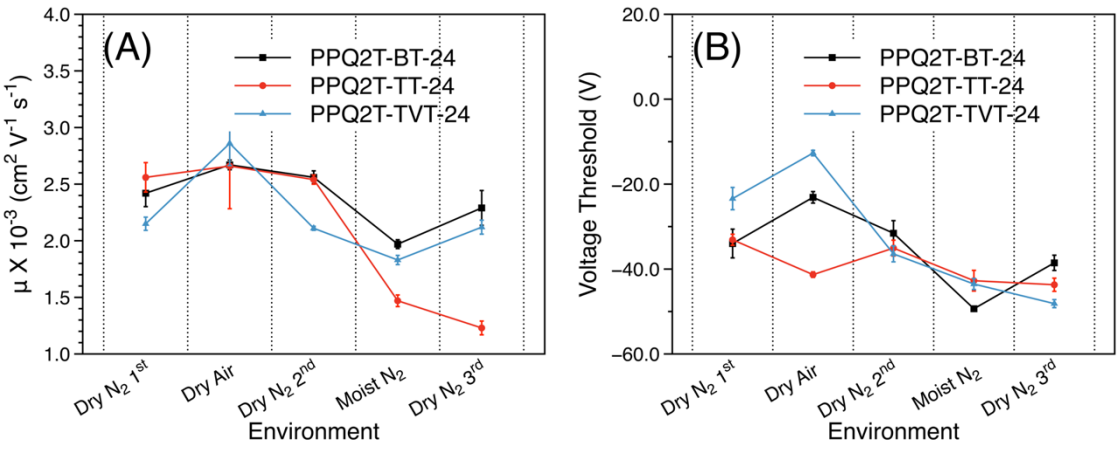

Figure 5-18. Hole mobility comparison (A) and voltage threshold comparison (B) for OTFT devices using different polymers under specific environments.

5.4.5.3 Preliminary Water-Gated OTFT Study

Herein, we present the preliminary study of **PPQ2T-BT-24** and **PPQ2T-TT-24** water-gated transistors (Figure 5-19) as these two OSCs demonstrated modest stability in ambient conditions (see 5.4.5.2). An identical fabrication process to **PFTPDOBT** was followed (see 3.4.4.2). Forward and reverse sweeps were performed to demonstrate stability (hysteresis) of devices when in operation. **PPQ2T-BT-24** gave an average mobility of ~2 × 10^{-3} cm^2 V^{-1} s^{-1} with an I_{ON}/I_{OFF} of ~10^2. **PPQ2T-TT-24** gave an average mobility of ~3 × 10^{-3} cm^2 V^{-1} s^{-1} with an I_{ON}/I_{OFF} of ~10^2. The V_{GS} in the output curves were swept from

0.2 V to -0.9 V whereas the V_{DS} in the transfer curves were swept from 0 V to -0.9 V. The forward and reverse sweeps overlap for **PPQ2T-BT-24** demonstrating excellent stability and limited hysteresis. However, **PPQ2T-TT-24** devices exhibit hysteresis typical of water-gated devices. As for discussed in 3.4.4.2 the apparent hysteresis may be due to the combination of low ionic strength ($[H3O^+] = [OH^-] = 10^{-7}$ M) for pure water and the poor capacitive coupling between the ions in solution and the charge carriers in the active channel of the OSC. Alternatively, the hysteresis may be indicative of an ion doping process [190].

The device gate leakage current was also monitored during the transfer sweep (Figure 5-20). Gate leakage currents remained below 140 nA and 20 nA for **PPQ2T-BT-24** and **PPQ2T-TT-24**, respectively. Moreover, no redox peak was observed further supporting the stability of these OSCs.

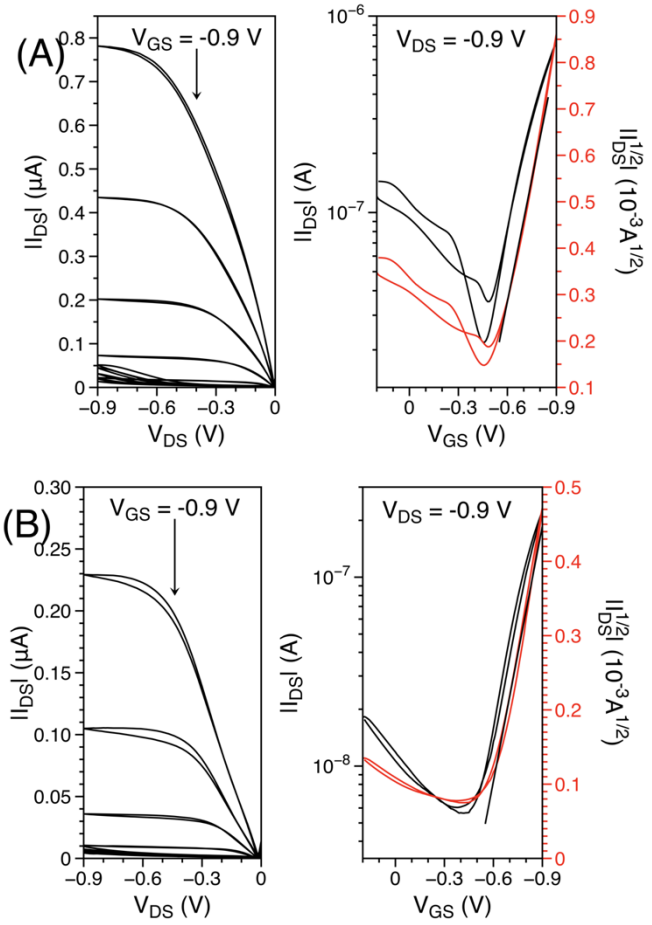

Figure 5-19. The output (left) and transfer (right) curves of **PPQ2T-BT-24** (A) and **PPQ2T-TT-24** (B) water-gated transistors.

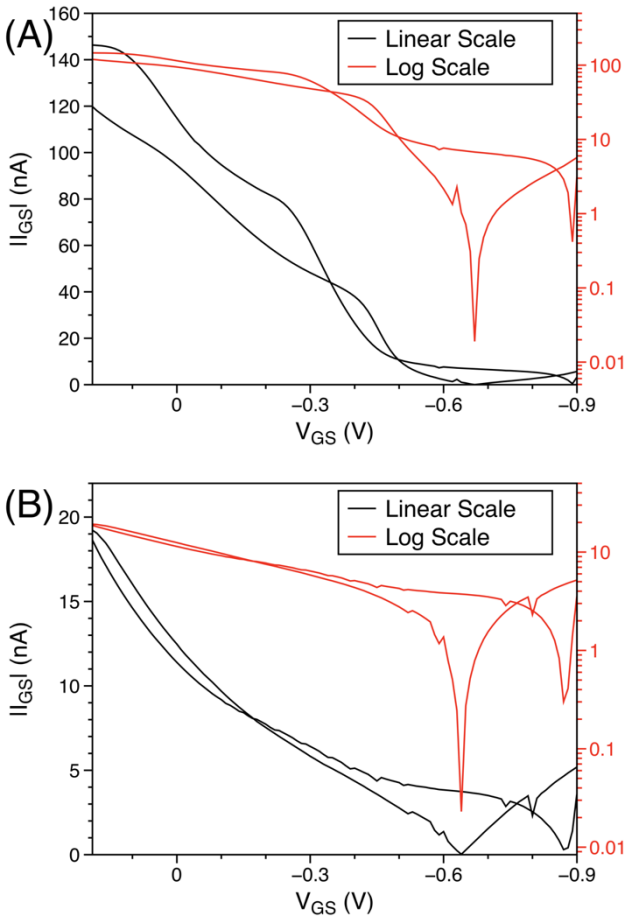

Figure 5-20. Gate leakage current (linear and log scales) for **PPQ2T-BT-24** (A) and **PPQ2T-TT-24** (B) water-gated transistors in 16.8 MΩ water. A tungsten probe was used as the gate electrode.

The charge polarization dynamics within the water droplet between gate and OSC were also studied by EIS using a simple equivalent circuit and an Au/water/OSC/Au structure (Appendix, Figure C-13 and Figure C-14). The effective capacitance C versus frequency is extracted from the complex impedance by using a simple equivalent circuit (Figure 3-13). For **PPQ2T-BT-24** and **PPQ2T-TT-24**, the Au/water/OSC/Au structures behave comparably to the **PFTPDOBT**-based structure. The double layer capacitance of **PPQ2T-BT-24**-based structure is ~6 μF cm^{-2} which is higher than the **PPQ2T-TT-24**-based structure (~2 μF cm^{-2}). Capacitance values were obtained from the lowest frequency at 0 V DC bias. The low double layer capacitance supports the hypothesis that these devices operate under OFET principles and not as OECTs [189]. Under DC bias, a similar behaviour is observed as discussed in 3.4.4.2 for **PFTPDOBT**-based structures.

As a reference, **P3HT** [188] was examined in water-gated transistors (Figure 5-21). **P3HT** displayed comparable mobility to that observed in literature [188], an average of ~2 × 10^{-3} cm^2 V^{-1} s^{-1} with an I_{ON}/I_{OFF} of ~10^2. **P3HT** exhibit typical hysteresis for water-gated devices. However, **P3HT** V_{TH} (~-0.04 V) is much lower than the said PQ OSCs (~-0.44 V – ~-0.51 V). This may be due to the shorter sidechain attached to **P3HT** than the bulkier counterparts used in the PQ materials. The reduction of mobility can be clarified by the point that with increasing gate insulator capacitance compression of the charge carriers distribution occurs placing it nearer to the insulator–semiconductor interface thereby rendering charge transport more sensitive to interface defects and surface roughness [188]. The larger sidechains present on the PQ and FTPDO (discussed in 3.4.4.2) materials, and differences in film morphology, may inadvertently act as defects further hindering charge transport. Gate leakage currents remained below 20 nA and 80 nA for **P3HT** along with no redox peak.

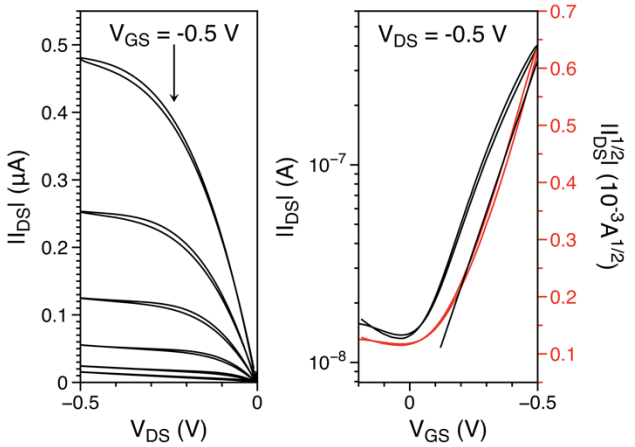

Figure 5-21. The output (left) and transfer (right) curves of **P3HT** water-gated transistors.

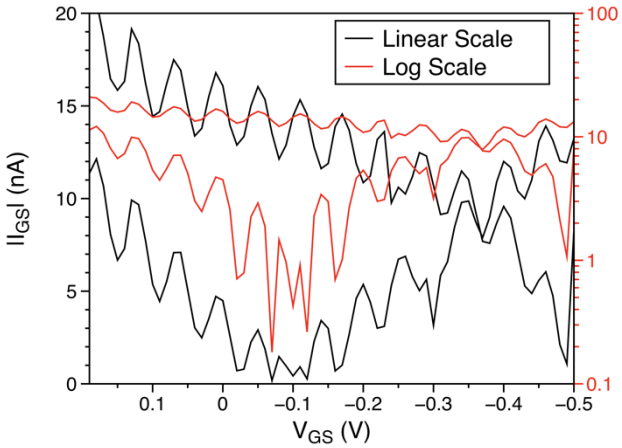

Figure 5-22. Gate leakage current (linear and log scales) for **P3HT** water-gated transistors in 16.8 MΩ water. A tungsten probe was used as the gate electrode.

5.4.5.4 Phototransistor Study

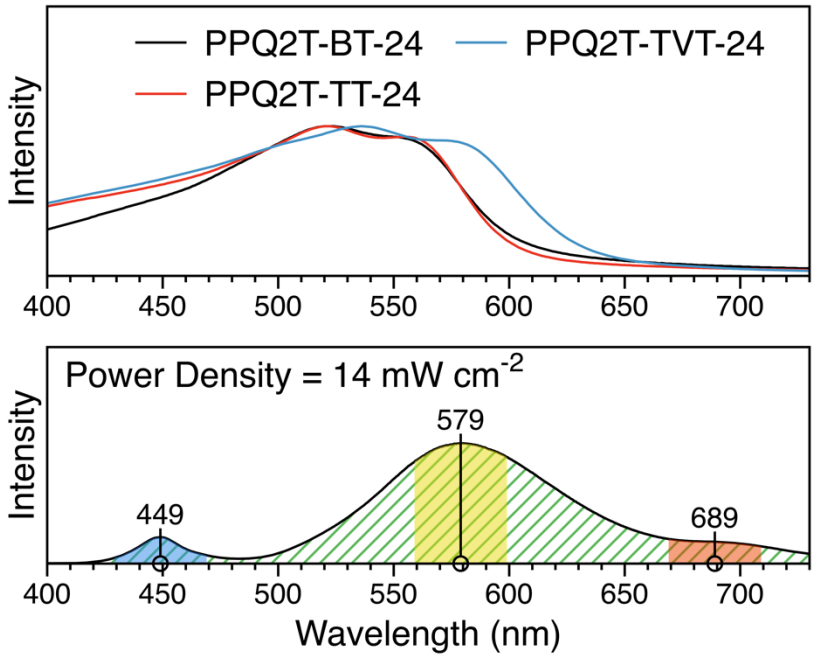

Figure 5-23. Spectral analysis of the 10W LED 3000 to 3500K light source with stacked overlaid UV-Vis-NIR absorption profile of polymer thin films.

An interdigitated BGBC OPT used in this study as seen in Figure 3-10. The devices were prepared on SiO_2/n^{++}-doped Si substrates with gold contacts for source and drain. Polymer solutions (5 mg mL^{-1}) were spin-coated at 3000 rpm for 80 s and subsequently annealed from 100 to 200 °C at 50 °C steps and 20 min intervals. To measure the transient photocurrent responses, a 10W LED with a color temperature of 3000 to 3500 K with an emission peak at 579 nm (Figure 5-23) was utilized, which overlaps with the long wavelength portion of the thin film absorption spectra of **PPQ2T-TT-24** and **PPQ2T-BT-24** and coincides with the long wavelength absorption peak of **PPQ2T-TVT-24** (Figure 5-23) [295,296]. The typical output and transfer characteristics of the devices based on these polymers in the absence of light (black) and under illumination (red) are shown in Figure 5-24. The output curves were swept between 0 V and -100 V for drain voltage (V_{DS}), while gate voltage (V_{GS}) was held constant at values chosen from 0 V to -100 V with 10 V increments. For all devices, there was an increase in drain current (I_{DS}) under illumination compared with their corresponding devices measured in dark.

The I_{DS} for the transfer curves, where V_{DS} was held constant at -100 V and V_{GS} was swept from 20 to -100 V, also increased under illumination compared to those in dark. The OTFT characteristics (measured in dark) are shown in Table 5-3. The devices showed typical p-type semiconductor characteristics with hole mobilities in the order of 10^{-3}, which are comparable with our previously reported values for these polymers [295,296].

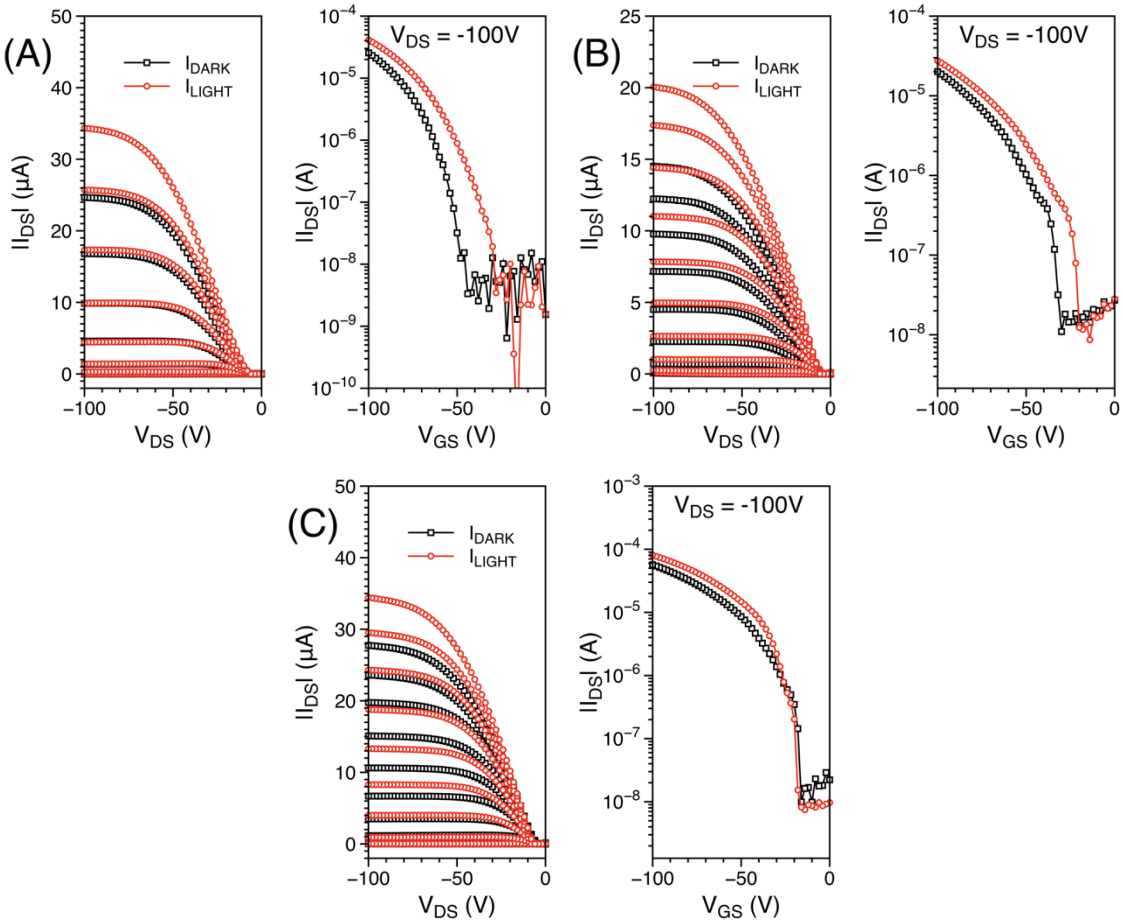

Figure 5-24. Output (left) and transfer (right) of **PPQ2T-BT-24** (A), **PPQ2T-TT-24** (B), and **PPQ2T-TVT-24** (C) in the dark and illuminated at 14 mW cm^{-2}.

Table 5-3. Summary of OTFT characteristics in dark at 200 °C annealed.

Polymer	Average μ ($\times 10^{-3}$ cm^2 V^{-1} s^{-1})	V_{TH}	I_{ON}/I_{OFF}
PPQ2T-BT-24	3.90 ± 0.06	-53.1	~10^5
PPQ2T-TT-24	2.25 ± 0.03	-14.2	~10^4
PPQ2T-TVT-24	2.63 ± 0.09	-22.8	~10^4

The transient photocurrent responses of OPTs over time are shown in Figure 5-25 and Figure 5-26, where the devices were under illumination (on-state) for a 5 s interval, followed by a 12 s interval without illumination (off-state). The response times, T_R and T_F, were measured at constant V_{DS} and V_{GS} values of -100 V. The T_R is defined as the time required for the current to increase from 10% to 90% of its peak on-state value, while the inverse is defined for the T_F [297]. **PPQ2T-TVT-24** demonstrated a T_R of 2 ms and a T_F of 1060 ms. This T_R is shorter than those of many previously reported polymer OPTs [75,298–300] and is nearly 4-fold shorter than the reported rise times for some inorganic photodetectors [301,302]. **PPQ2T-BT-24** and **PPQ2T-TT-24** also displayed relatively short T_R of 3 and 15 ms, respectively (Table 5-4). **PPQ2T-BT-24** showed the shortest T_F of 59 ms.

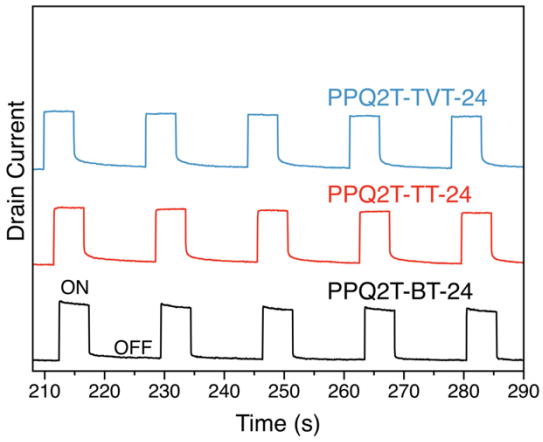

Figure 5-25. Transient photocurrent responses of polymers as a function of time in response to illumination at 14 mW cm^{-2} with 5 s illumination on-state followed by 12 s illumination off-state (dark). Data collected at 1 ms intervals.

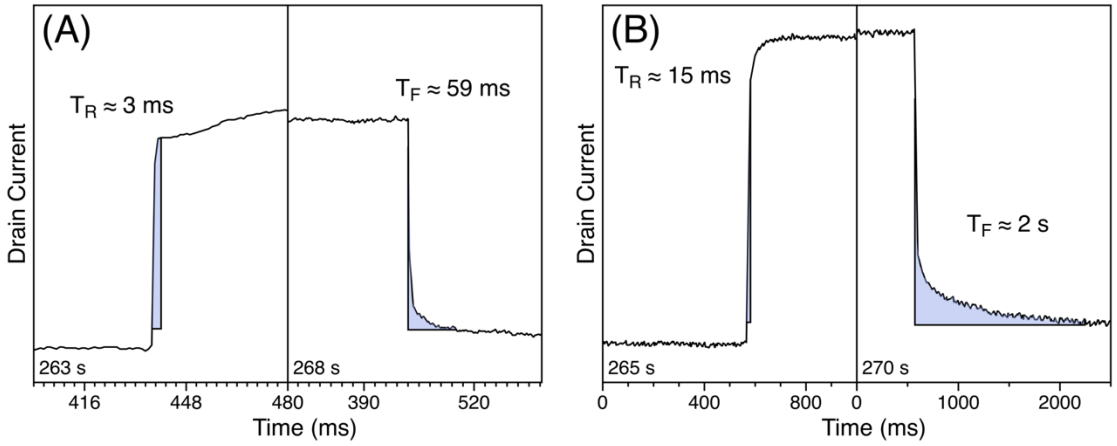

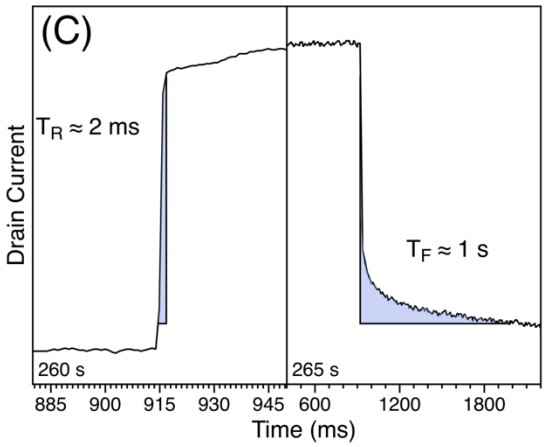

Figure 5-26. The estimated T_R and T_F time of **PPQ2T-BT-24** (A), **PPQ2T-TT-24** (B), and **PPQ2T-TVT-24** (C), respectively. Data collected at 1 ms intervals.

Table 5-4. Transient photocurrent response times at 200 °C; the utmost *R* and *EQE* achieved.

Channel layer	**Response Time (ms)**		***R* (A W^{-1})**	***EQE* (%)**
	Rise time (T_R)	**Fall time (T_F)**		
PPQ2T-BT-24	3	59	0.24	50
PPQ2T-TT-24	15	1670	0.25	53
PPQ2T-TVT-24	2	1060	0.39	83

The other important parameter for OPTs, *R*, was calculated using the following equation (discussed in 2.3.2) [303]:

$$R = \frac{I_{ill} - I_{dark}}{AP_{inc}} \quad (8)$$

Figure 5-27 shows the plot of *R* as a function of V_{GS}, which ranges from 20 to -100 V, while the V_{DS} was kept constant at -100 V. The devices showed no or minimal *R* at V_{GS} values between 20 and -20 V; however, the *R* values improved greatly as the V_{GS} increased further. Among these pristine polymers, the highest *R* value of 0.39 A W^{-1} was achieved with the **PPQ2T-TVT-24** polymer. Smaller *R* values were obtained for the other two polymers, which can be attributed to their absorption profiles that do not match with the LED light source as well as that of **PPQ2T-TVT-24**. The *R* values of OPTs based on these polymers are greater than those of some previously reported OPTs [300,304]. The *R* values of **PPQ2T-BT-24** and **PPQ2T-TT-24** may be further enhanced by using separate monochromatic light sources with emission peaks centered on the absorption maxima of these polymers.

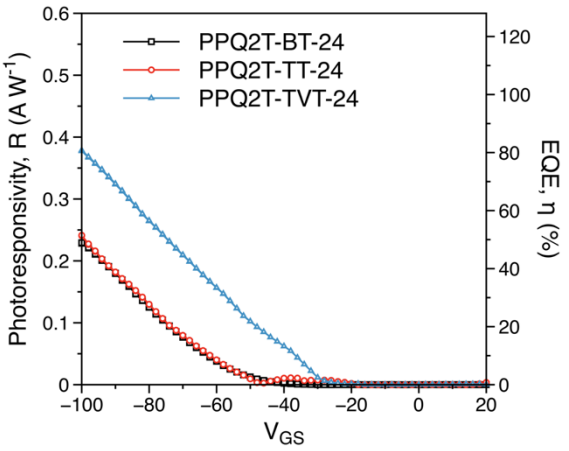

Figure 5-27. *R* and *EQE* of all pristine polymer based devices at a constant V_{DS} of -100 V.

An analogous parameter to *R* is known as the *EQE* or η, which is defined as the ratio of generated carriers to incident photons in the transistor channel area [303]. The *EQE* values can be calculated by using the equation (discussed in 2.3.2) [303]:

$$EQE = \frac{(I_{ill} - I_{dark})hc}{AP_{inc}\lambda_{peak}e} \qquad (9)$$

For the convenience of *EQE* calculation, the LED light source was assumed to be monochromatic with a λ_{peak} of 579 nm, similar to the method adopted by *Labram et al.* [303]. The OPTs with the pristine **PPQ2T-TVT-24** showed an *EQE* of up to 83%, whereas those with **PPQ2T-BT-24** and **PPQ2T-TT-24** showed modest values of up to 50% and 53%, respectively.

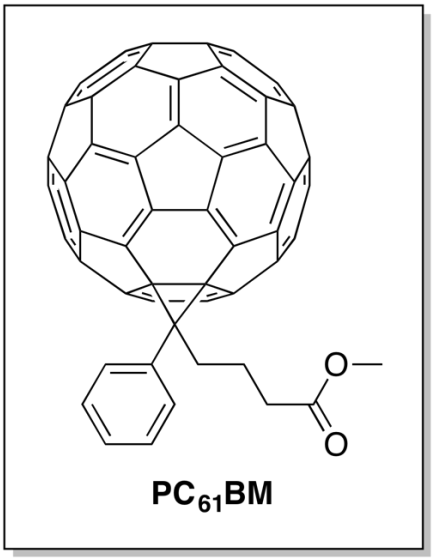

Figure 5-28. Structure of the $PC_{61}BM$.

Table 5-5. Summary of OTFT characteristics in dark at 200 °C annealed.

Polymer	Average μ ($\times 10^{-3}$ cm² V^{-1} s^{-1})	V_{TH}	I_{ON}/I_{OFF}
PPQ2T-BT-24:PC$_{61}$BM	16.25 ± 1.32	-25.3	~10^4
PPQ2T-TT-24:PC$_{61}$BM	4.87 ± 0.08	-26.4	~10^4
PPQ2T-TVT-24:PC$_{61}$BM	5.65 ± 0.03	-18.5	~10^4

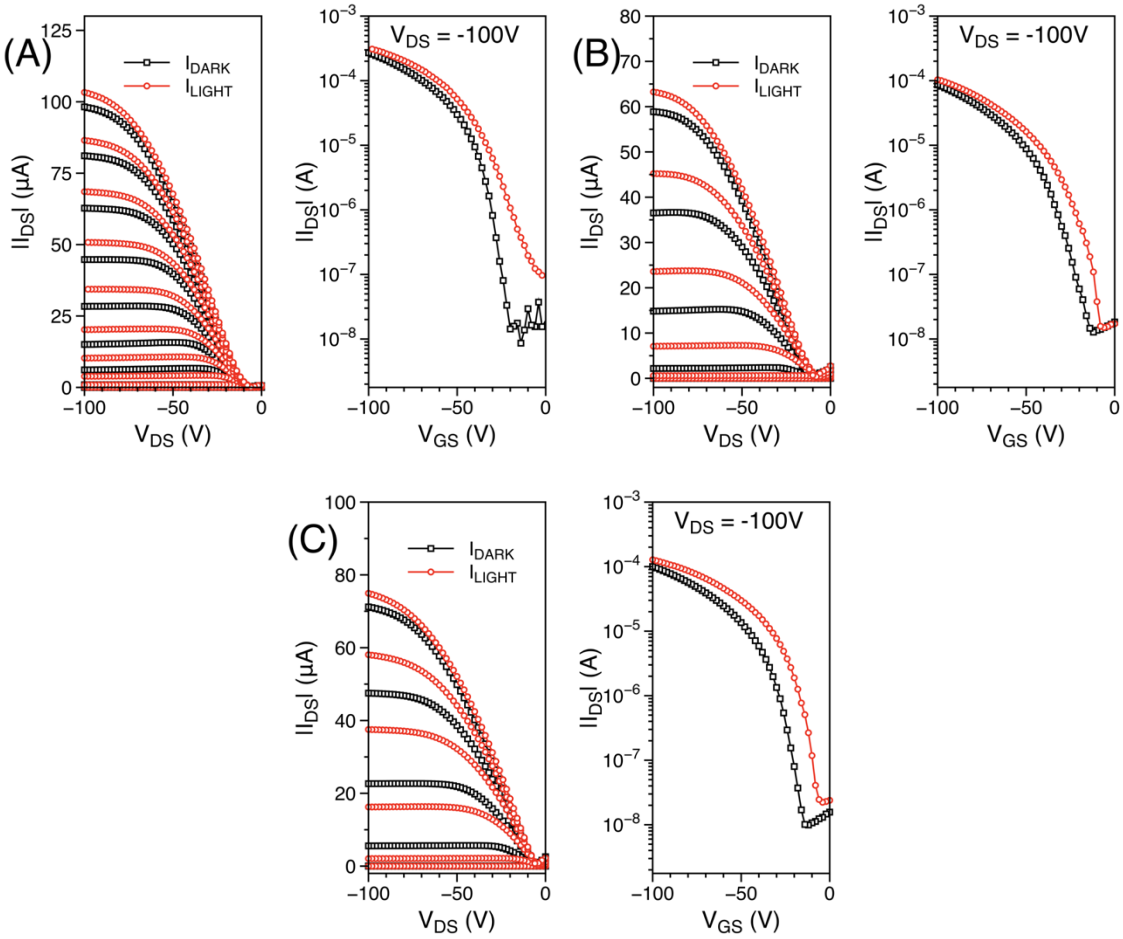

Figure 5-29. Output (left) and transfer (right) of **PPQ2T-BT-24:PC$_{61}$BM** (A), **PPQ2T-TT-24:PC$_{61}$BM** (B), and **PPQ2T-TVT-24:PC$_{61}$BM** (C) in the dark and illuminated at 14 mW cm^{-2}.

Table 5-6. Transient photocurrent response times at 200 °C; the utmost *R* and *EQE* achieved.

Channel layer	Response Time (ms)		*R* (A W^{-1})	*EQE* (%)
	Rise time (T_R)	Fall time (T_F)		
PPQ2T-BT-24:PC$_{61}$BM	1	8	0.88	189
PPQ2T-TT-24:PC$_{61}$BM	10	18	0.48	103

PPQ2T-TVT-24:PC$_{61}$BM	1	15	0.69	147

Incorporating a fullerene derivative (an n-type semiconductor), such as $PC_{61}BM$ (Figure 5-28), into a p-type organic semiconductor to construct a bulk-heterojunction structure has been reported to be able to improve OPT performance [297,75,305] by improving the efficiency of photoinduced charge generation [306]. Therefore, $PC_{61}BM$ was blended with the polymers at a polymer:$PC_{61}BM$ ratio of 1:1 (w/w) to improve their OPT performance (Table 5-5 and Figure 5-29). The OTFT characteristics (measured in dark) all show an increase in mobility compared to their pristine counterparts. However, **PPQ2T-BT-24:PC$_{61}$BM** devices achieved hole mobilities of 10^{-2}. All blends displayed slight improvement in T_R while T_F showed significant shortening (Table 5-6, and Figure 5-31). For the **PPQ2T-BT-24:PC$_{61}$BM**, which had the best intrinsic response times (3 ms and 50 ms) decreased to 1 ms and 8 ms for T_R and T_F, respectively. The **PQ2T-TT-24:PC$_{61}$BM** blend decreased from 15 ms and 1607 ms to 10 ms and 18 ms for T_R and T_F, respectively, when compared to pristine **PPQ2T-TT-24** devices. The **PPQ2T-TVT-24:PC$_{61}$BM** blend showed a similar T_R to the **PPQ2T-BT-24:PC$_{61}$BM** (1 ms) and T_F of 15 ms, respectively, which are distinctly shorter than those of the devices with the pristine **PPQ2T-TVT-24** (2 ms and 1060 ms). These values are superior to those of some inorganic and hybrid materials based phototransistors **[75,301,302,307–311]** and are among the best for small molecule, polymer, and polymer blend based phototransistors **[74,298–300,303,312–314]**.

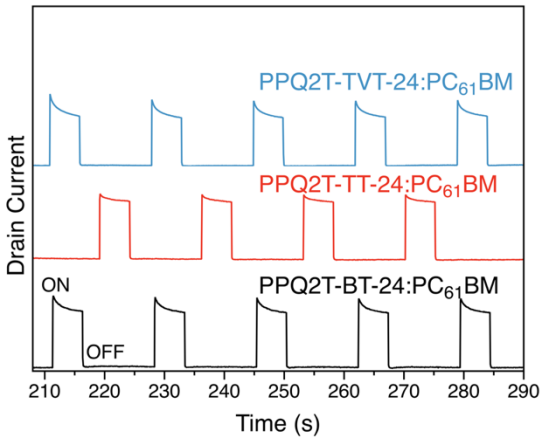

Figure 5-30. Transient photocurrent responses of blended polymers as a function of time in response to illumination at 14 mW cm^{-2} with 5 s illumination on-state followed by 12 s illumination off-state (dark). Data collected at 1 ms intervals.

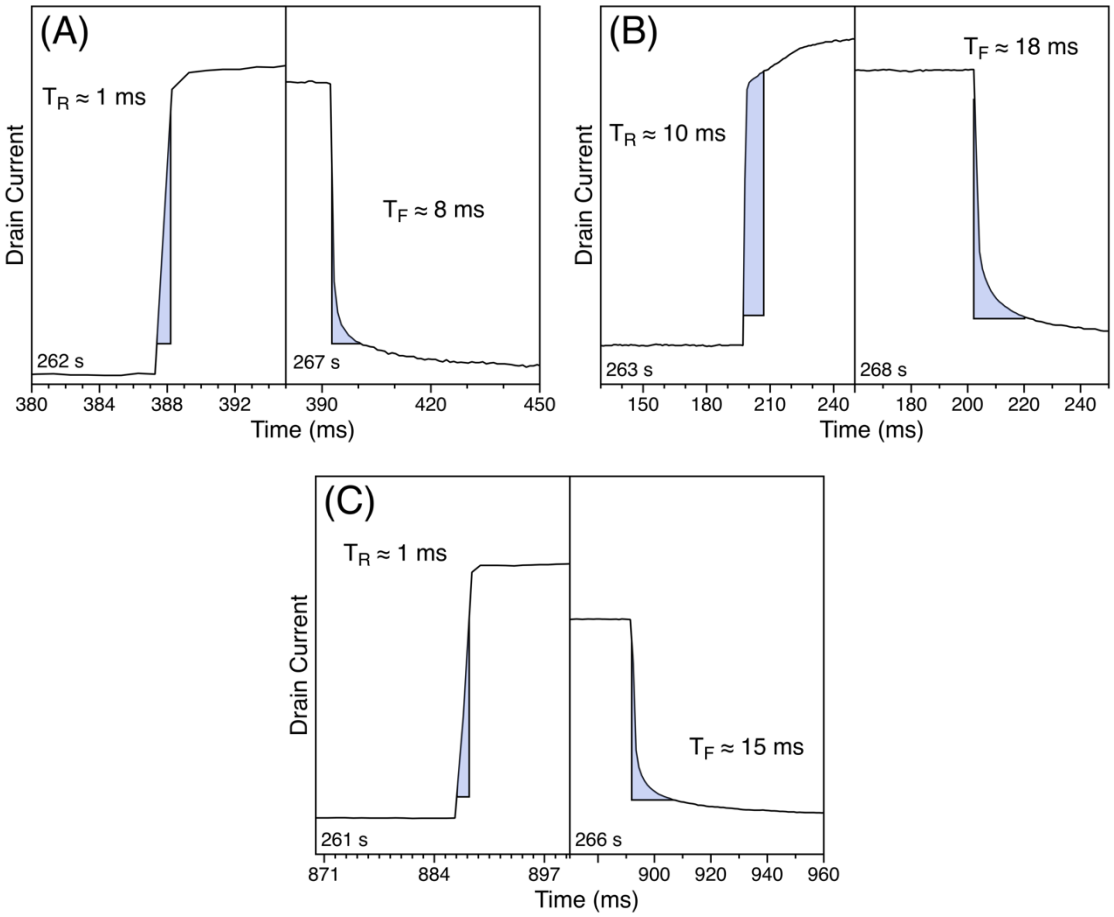

Figure 5-31. The estimated T_R and T_F time of **PPQ2T-BT-24**:**PC$_{61}$BM** (A), **PPQ2T-TT-24**:**PC$_{61}$BM** (B), and **PPQ2T-TVT-24**: **PC$_{61}$BM** (C), respectively. Data collected at 1 ms intervals.

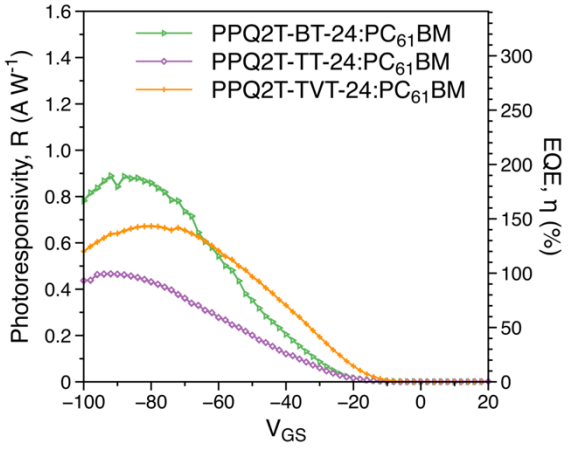

Figure 5-32. The *R* and *EQE* of all polymer blend based devices at a constant V_{DS} of -100 V.

The *EQE* values were improved to 189% for the **PPQ2T-BT-24**:**PC$_{61}$BM** blend, 103% for the **PPQ2T-TT-24**:**PC$_{61}$BM** blend and 147% for the **PPQ2T-TVT-24**:**PC$_{61}$BM** blend (Table 5-6 and Figure 5-32). Compared to a photodiode, which has a maximum *EQE* of 100%, a phototransistor can realize an *EQE* greater than 100% likely due to the photomultiplication phenomenon enabled by the field-induced tunneling as well as the nature of the semiconductor layer [315,316]. The maximum *EQE* values were attained at lower V_{GS} (~-80 V for **PPQ2T-TVT-24**:**PC$_{61}$BM** and ~-90 V for **PPQ2T-BT-24**:**PC$_{61}$BM** and **PPQ2T-TT-24**:**PC$_{61}$BM**) in comparison to those for pristine polymers (at V_{GS} of -100 V). This observation may be attributed to the photo-induced shift of V_{TH} due to the photovoltaic effect [120] and an oversaturation behavior in the I_{DS} [317]. The photovoltaic effect, where the generated electron-hole pairs (or excitons) dissociate into electrons and holes which drift as polarons in opposing directions under source-drain bias, contributes to the increased I_{DS} and *EQE* [317]. In the case of p-type semiconductors, holes flow to the drain contact whereas the electrons accumulate at the source contact where they effectively lower the injection barrier for holes. The induced lowered hole injection barrier results in a decrease in contact resistance with a positive shift of V_{TH} (or a reduction in $|V_{TH}|$) thereby increasing I_{DS} [318]. The $PC_{61}BM$ domains in the blends would facilitate the electron transport (*i.e.* movement of electrons towards the source contact) and increase photocurrent [75] and thus their accumulation at the source. The lowered hole injection barrier due to the accumulation of electrons at the source might also have contributed to the afore mentioned photomultiplication phenomenon. On the contrary, large polaron densities resulting from a change in the power density (*i.e.* increasing power densities of the light source) can increase the chance of recombining polarons, which reduces the I_{DS} and hence, *R* and *EQE* values [317].

5.4.5.5 Preliminary Gas Sensor Study

With tremendous efforts from both academia and industry in designing and synthesizing novel OSCs as active channel layers in OTFTs to reach higher and higher performances, one of the most unfavorable matters always faced is that their performances are susceptible to chemical interactions, photo-excitation, dimensional deformation, etc. Although these are undesirable aspects for OTFTs, in general, they may be utilized in a positive way to detect external chemical and physical stimuli. The intrinsic capability of OTFTs to directly transduce chemical or physical events to electrical signals renders them applicable for numerous applications [160,319,320].

In this work, we have fabricated BGBC OTFTs with **PPQ2T-BT-24** and **PPQ2T-TT-24** as active channel layers. As explained in 5.4.5.3, we believe **PPQ2T-BT-24** and **PPQ2T-TT-24** are robust

materials with modest stability in ambient conditions. While, many potential analytes exist, we chose to work with butane-1,4-diamine or what is better known as putrescine. Putrescine is a foul-smelling organic chemical compound with the following chemical formula: $NH_2(CH_2)_4NH_2$. It is produced by the breakdown of amino acids (*i.e.* arginine and ornithine) found in most organic matter and when at high concentrations it is considered toxic (acute oral toxicity of 2000 mg/kg body weight) [321]. Putrescine in small quantities is generated in healthy living cells and has been reported to play a role in skin physiology and neuroprotection [322,323]. Nonetheless, it contributes to the odor of bad breath [324,325], bacterial vaginosis [326] and rotten meat [327,328]. However, our interests lie in that latter point as monitoring meat spoilage is important to meat providers and general consumers. Recently, a chemiresistor based on single-walled carbon nanotubes and metalloporphyrin composites was utilized as an economical and practical sensor for the detection of various biogenic amines (*i.e.* putrescine). Liu *et al.* achieved sub-ppm levels in a range of conditions and meats [329]. Therefore, our goal was simply. Observe the detection limits of putrescine using **PPQ2T-BT-24** and **PPQ2-TT-24** as active channel layer in OTFTs and use the aforementioned report as a baseline.

We began the study with **PPQ2T-TT-24** (Figure 5-33) as it demonstrated the best stability in ambient conditions. A home-made chamber with four conduits was made where three conduits were dedicated to the source, drain, and gate connections for the floating transistor. The fourth conduit was dedicated to dry air (influent and effluent) and analyte injection. The devices were operated at V_{GS} and V_{DS} = -100 V and the I_{DS} was measured over time. At around 200 seconds an injection with an allotted concentration of putrescine was injected into the sealed chamber. After a few seconds, dry air was passed into the chamber. Putrescine at 20 ppm lead to complete device failure. Attempts to recover the device by annealing or vacuum failed. At an approximate concentration of 1.30 ppm, partial decay was observed and devices recovered quickly (few minutes). At 0.12 ppm, the current increased, which was unexpected as amines should act as hole traps thereby decreasing current. This phenomenon is still unclear, but it may be due to doping from an ionic species formed intermittently during putrescine decomposition in vapour phase that intermingles with the PQ moiety.

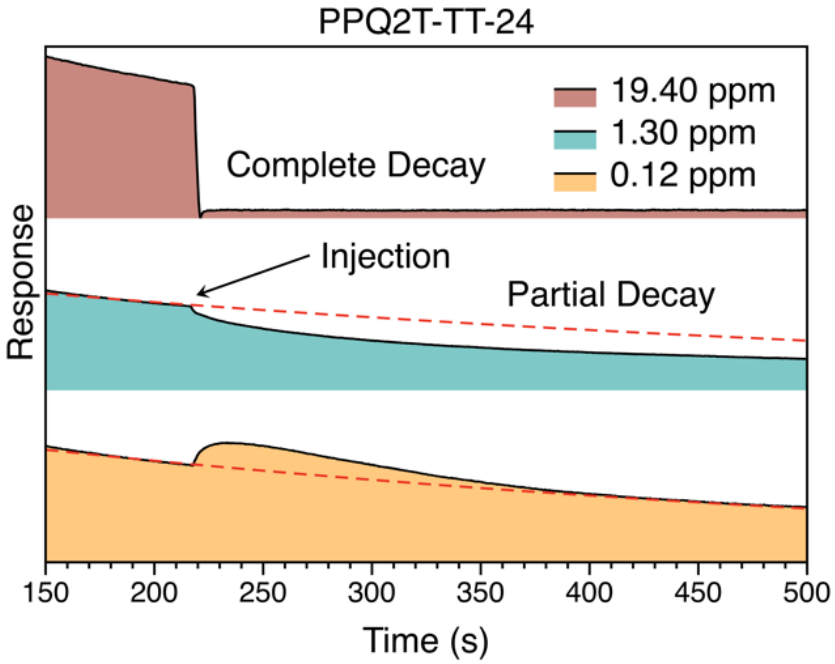

Figure 5-33. Current changes in response to various putrescine concentrations using **PPQ2T-TT-24** based gas sensor devices. Dotted red line represents typical decay without analyte.

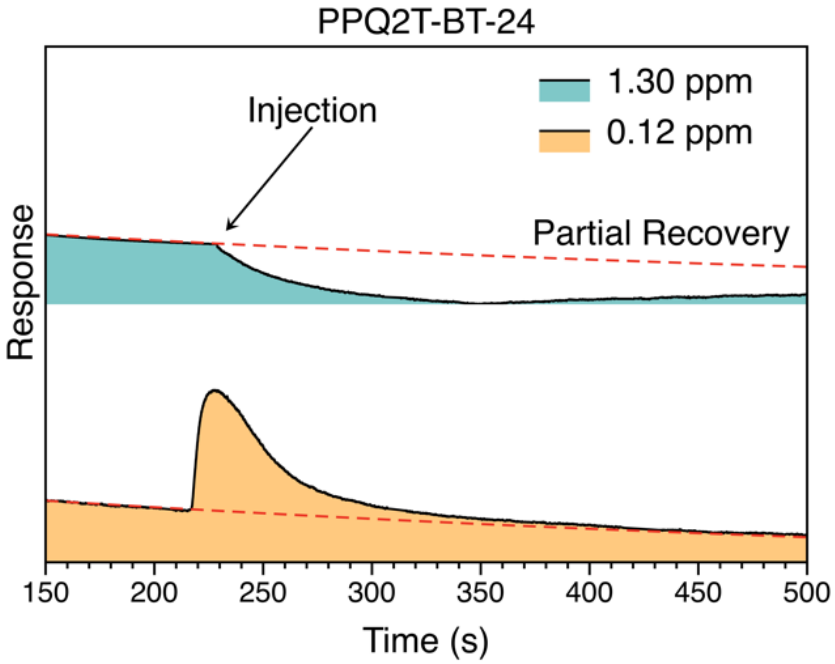

Figure 5-34. Current changes in response to various putrescine concentrations using **PPQ2T-BT-24** based gas sensor devices. Dotted red line represents typical decay without analyte.

PPQ2T-BT-24 (Figure 5-34) exhibited similar behaviour to that observed for **PPQ2T-TT-24** at low concentrations of putrescine. Recovery of devices was short and required no intervention.

P3HT was used as a comparative material and was found to elicit a different response at low concentrations of putrescine. At 0.12 ppm, **P3HT** devices exhibited partial decay with long recovery times. Although, all materials demonstrated a response to putrescine, fast recovery time and strong responses are ideal.

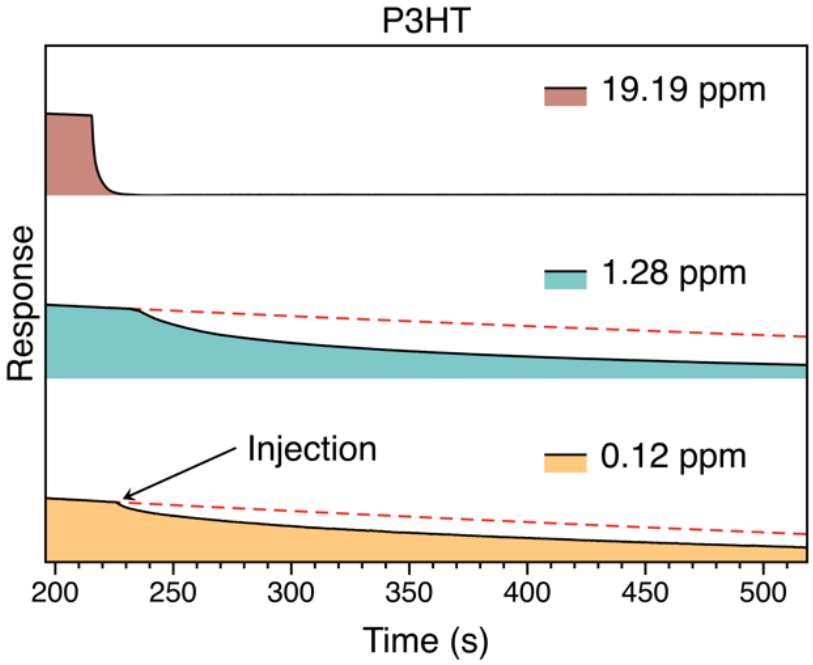

Figure 5-35. Current changes in response to various putrescine concentrations using **P3HT** based gas sensor devices. Dotted red line represents typical decay without analyte.

5.5 Conclusion

In summary, a facile method for the synthesis of 2,7-di(thiophen-2-yl)pyrimido[4,5-*g*]quinazoline-4,9-diones (PQ) has been presented. Several novel polymers based on this PQ moiety were synthesized (**PPQ2T-BT-24**, **PPQ2T-BT-40**, **PPQ2T-TT-24**, and **PPQ2T-TVT-24)**. Similar to the PQx based polymers discussed in Chapter 4, these polymers showed marked bathochromic shifts in their UV-Vis-NIR absorption spectra in the presence of various organic acids and the Lew acid boron tribromide. In OTFTs, they exhibited modest hole mobility (~10^2 cm^2 V^{-1} s^{-1} in TGBC) and air stability. As OPTs, they flaunted excellent response times using a blend of polymer and $PC_{61}BM$ at 1:1 (w:w). **PPQ2T-**

BT-24:**$PC_{61}BM$** achieved a T_R as low as 1 ms with a corresponding T_F of 8 ms along with a R of 0.88 A W^{-1} and *EQE* of 189%. Both **PPQ2T-BT-24** and **PPQ2T-TT-24** showed excellent operation in water-gated transistors with unhindered device performance (hole mobility of ~10^{-3} cm^2 V^{-1} s^{-1}) demonstrating their potential use as aqueous based sensors. Finally, **PPQ2T-BT-24** and **PPQ2T-TT-24** were utilized as gas sensors for the analyte putrescine. Both materials showed low detection limits (~0.12 ppm) and fast recovery times that required no intervention. All in all, these results demonstrate that PQ-based polymers are very promising materials for OTFT based sensors.

Chapter 6
Conclusions and Future Outlook

6.1 Conclusions

Science and engineering are often inspired by natural materials. Viable examples of semiconductors that are naturally derived or inspired are indigoid and perylene diimide dyes. Thus, it is believed that natural or nature-inspired semiconductors may be a promising route to develop novel, but useful new materials. This thesis describes several promising organic semiconductors that were inspired by nature and may be utilized as active channel layers in OTFT-based sensors.

In Chapter 3 a novel fluorene-fused triphenodioxazine based polymer was presented with a thorough account of properties and OTFT performances. The combination of facile synthesis, excellent air stability, and good charge transport makes **PFTPDOBT** a promising semiconductor for OTFT-based sensors. Despite poor molecular ordering, **PFTPDOBT** showed hole transport performance with hole mobilities of up to 1.57×10^{-2} $cm^2 V^{-1} s^{-1}$ in air. Furthermore, **PFTPDOBT** showed robustness to high temperature when annealed in air up to 250 °C. Notwithstanding, if an isomerically pure **FTPDO** monomer can be isolated or synthesized the charge transport performance is expected to improve further.

Chapter 4 follows suit and describes the development of an alternative polymeric semiconductor based on the pyrazino[2,3-*g*]quinoxaline-2,7-dione (PQx) moiety that exhibits strong affinity for organic and Lewis acids along with modest OTFT performances. Unlike the aforementioned material, and the latter discussed material, PQx-based polymers showed ambipolar electrical characteristics. **PPQx2T-BT-24** exhibited electron-dominant ambipolar transport characteristics with hole mobilities of up to 5.22×10^{-4} $cm^2 V^{-1} s^{-1}$ and electron mobilities reaching 4.28×10^{-3} $cm^2 V^{-1} s^{-1}$. **PPQx2T-TT-24** exhibited hole-dominant ambipolar transport characteristics with hole mobilities of up to 4.82×10^{-2} $cm^2 V^{-1} s^{-1}$ and electron mobilities of up to 3.95×10^{-3} $cm^2 V^{-1} s^{-1}$. Moreover, both PQx polymers showed obvious bathochromic shifts in their UV-Vis-NIR absorption spectra in the presence of acids which occurs due to a strong interaction between an acid and the basic 5,10-nitrogen atoms in the PQx moiety.

Chapter 5 details an array of research that is focused on the pyrimdo[4,5-*g*]quinazoline-4,9-dione (PQ) moiety. As expected, PQ-based polymers behaved in a similar fashion to the aforesaid PQx-based

polymers when in the presence of acids. Significant bathochromic shifts in their absorption profiles resulted from the strong interaction of the basic 1,6-nitrogen atoms in the PQ moiety with the acids. As an active channel layer in OTFTs, these polymers exhibited characteristic p-type semiconductor performance with hole mobility as high as 1.3×10^{-2} cm^2 V^{-1} s^{-1}. Moreover, we systematically investigated a series of PQ-based polymers in different atmospheres and presented our thoughts for useful guidance on the design of ambient air stable polymer semiconductors. An expansion of this investigation involved the use of two PQ-based polymers in water-gated transistors. Both materials demonstrated excellent stability with minimal hysteresis and gate leakage. Device performance was unhindered by operation in aqueous environment. As mentioned previously in Chapter 5, organic semiconductors are prone to photo-excitation; therefore, we conducted a phototransistor study of a series of PQ-based polymers and we were pleasantly surprised to observe excellent response times reaching as low as 1 ms in rise and 8 ms in fall when blended with $PC_{61}BM$. Lastly, we performed a preliminary study of several PQ-based polymers as active channel layers in OTFT gas sensors. We achieved low detection limits and fast recover times in response to our chosen analyte.

The major contributions of this study include:

- Highly air stable polymeric semiconductor (**PFTPDOBT**) that demonstrates modest p-type characteristics in OTFTs under ambient conditions
- First fully characterized PQx-based polymer reported with hole mobility as high as ~10^{-2} cm^2 V^{-1} s^{-1} and electron mobilities of ~10^{-3} cm^2 V^{-1} s^{-1}
- First to report a series of PQ-based polymers with hole mobilities as high as ~10^{-2} cm^2 V^{-1} s^{-1}
- Systematic investigation of PQ-based polymer operation in different atmospheres and environments
- Low response times in phototransistors using PQ-based polymers as active channel layers

6.2 Recommend Future Research

6.2.1 Synthesize or isolate isomerically pure FTPDO monomer

As previously mentioned in Chapter 3, if an isomerically pure **FTPDO** monomer could be isolated or synthesized, a systematic investigation of the various isomers would provide greater insight into the excellent stability of **PFTPDOBT**.

6.2.2 Alternative synthetic route to PQx or optimization of current route

Although the PQx synthetic route presented achieved our goals the yield for the crude intermediate was 9%. In actual fact, this yield is much lower due to the presence of an isomer. Thus, further exploration in the synthesis of the PQx moiety is necessary.

6.2.3 Alternative blends and weight ratios for phototransistor

In this study $PC_{61}BM$ was used at a 1:1 (w:w) with a series of PQ-based polymers. Although, response times were excellent, could lower response times be obtained while simultaneously gaining increased photoresponsivity and *EQE*. Some of the highest performing bulk heterojunction organic solar cells incorporate $PC_{71}BM$ [330]. Furthermore, the addition of additives typically used in solar cell research may enhance merits of performance.

6.2.4 Aqueous based OTFT sensors

We presented preliminary results using PQ-based polymers as active channel layers in water-gated OTFTs. The next step would be to detect various concentrations of heavy metals, antibiotics, and other well-known water pollutants. Modification of the gate electrode may also enhance sensitivity and selectivity.

6.2.5 OTFT-based gas sensors

We presented preliminary results using PQ-based polymers as active channel layers in OTFT-based gas sensors. Further investigation at various temperatures typical of practical application should be conducted. Furthermore, devices should be fabricated on flexible substrates allowing them to conform to typical packaging for commercial meat products and various types of containers.

Bibliography

[1] A. Dodabalapur, Z. Bao, A. Makhija, J.G. Laquindanum, V.R. Raju, Y. Feng, H.E. Katz, J. Rogers, Appl. Phys. Lett. 73 (1998) 142.

[2] H. Sirringhaus, N. Tessler, R.H. Friend, Science 280 (1998) 1741–1744.

[3] T.N. Jackson, Y.-Y. Lin, D.J. Gundlach, H. Klauk, Sel. Top. Quantum Electron. IEEE J. Of 4 (1998) 100–104.

[4] C.D. Sheraw, L. Zhou, J.R. Huang, D.J. Gundlach, T.N. Jackson, M.G. Kane, I.G. Hill, M.S. Hammond, J. Campi, B.K. Greening, J. Francl, J. West, Appl. Phys. Lett. 80 (2002) 1088–1090.

[5] C.H. Mueller, N. Theofylaktos, F.A. Miranda, A.T. Johnson Jr., N.J. Pinto, Thin Solid Films 496 (2006) 494–499.

[6] E. Delamarche, M. Geissler, J. Vichiconti, W.S. Graham, P.A. Andry, J.C. Flake, P.M. Fryer, R.W. Nunes, B. Michel, E.J. O'Sullivan, H. Schmid, H. Wolf, R.L. Wisnieff, Langmuir 19 (2003) 5923–5935.

[7] Y. Fujisaki, Y. Nakajima, T. Takei, H. Fukagawa, T. Yamamoto, H. Fujikake, IEEE Trans. Electron Devices 59 (2012) 3442–3449.

[8] J.A. Rogers, Z. Bao, K. Baldwin, A. Dodabalapur, B. Crone, V.R. Raju, V. Kuck, H. Katz, K. Amundson, J. Ewing, P. Drzaic, Proc. Natl. Acad. Sci. 98 (2001) 4835–4840.

[9] G.H. Gelinck, H.E.A. Huitema, E. van Veenendaal, E. Cantatore, L. Schrijnemakers, J.B.P.H. van der Putten, T.C.T. Geuns, M. Beenhakkers, J.B. Giesbers, B.-H. Huisman, E.J. Meijer, E.M. Benito, F.J. Touwslager, A.W. Marsman, B.J.E. van Rens, D.M. de Leeuw, Nat. Mater. 3 (2004) 106–110.

[10] D. Voss, Nature 407 (2000) 442–444.

[11] P.F. Baude, D.A. Ender, M.A. Haase, T.W. Kelley, D. V Muyres, S.D. Theiss, Appl. Phys. Lett. 82 (2003) 3964.

[12] C.J. Drury, C.M.J. Mutsaers, C.M. Hart, M. Matters, D.M. de Leeuw, Appl. Phys. Lett. 73 (1998) 108.

[13] E. Cantatore, C.M. Hart, M. Digioia, G.H. Gelinck, T.C.T. Geuns, H.E.A. Huitema, L.R.R. Schrijnemakers, E. van Veenendaal, D.M. de Leeuw, in:, IEEE Int. Solid-State Circuits Conf., IEEE, 2003, pp. 382–501.

[14] Y. Watanabe, K. Kudo, Appl. Phys. Lett. 87 (2005) 223505.

[15] C.D. Dimitrakopoulos, P.R.L. Malenfant, Adv. Mater. 14 (2002) 99–117.

[16] M. Fadlallah, G. Billiot, W. Eccleston, D. Barclay, Solid-State Electron. 51 (2007) 1047–1051.

[17] barrett comiskey, J.D. Albert, H. Yoshizawa, joseph jacobson, Nature 394 (1998) 253–255.

[18] Z.-T. Zhu, J.T. Mason, R. Dieckmann, G.G. Malliaras, Appl. Phys. Lett. 81 (2002) 4643.

[19] B.K. Crone, A. Dodabalapur, R. Sarpeshkar, A. Gelperin, H.E. Katz, Z. Bao, J. Appl. Phys. 91 (2002) 10140.

[20] B. Crone, A. Dodabalapur, A. Gelperin, L. Torsi, H.E. Katz, A.J. Lovinger, Z. Bao, Appl. Phys. Lett. 78 (2001) 2229.

[21] L. Torsi, A. Dodabalapur, L. Sabbatini, P.G. Zambonin, Sens. Actuators B Chem. 67 (2000) 312–316.

[22] J.T. Mabeck, G.G. Malliaras, Anal. Bioanal. Chem. 384 (2005) 343–353.

[23] O. Knopfmacher, M.L. Hammock, A.L. Appleton, G. Schwartz, J. Mei, T. Lei, J. Pei, Z. Bao, Nat. Commun. 5 (2014) 2954.

[24] L. Torsi, M. Magliulo, K. Manoli, G. Palazzo, Chem. Soc. Rev. 42 (2013) 8612–28.

[25] M.C. Tanese, D. Fine, A. Dodabalapur, N. Cioffi, L. Torsi, in:, Org. Field-Eff. Transistors III, 2004, pp. 22–26.

[26] C. Liao, F. Yan, Polym. Rev. 53 (2013) 352–406.
[27] H.E. Katz, Electroanalysis 16 (2004) 1837–1842.
[28] R. Das, P. Harrop, (n.d.).
[29] C. Reese, M. Roberts, M. Ling, Z. Bao, Mater. Today 7 (2004) 20–27.
[30] Y. Fujisaki, H. Koga, Y. Nakajima, M. Nakata, H. Tsuji, T. Yamamoto, T. Kurita, M. Nogi, N. Shimidzu, Adv. Funct. Mater. 24 (2014) 1657–1663.
[31] A. Dodabalapur, Mater. Today 9 (2006) 24–30.
[32] A. Facchetti, Mater. Today 10 (2007) 28–37.
[33] H. Sirringhaus, T. Kawase, R.H. Friend, T. Shimoda, M. Inbasekaran, W. Wu, E.P. Woo, Science 290 (2000) 2123–2126.
[34] D.A. Pardo, G.E. Jabbour, N. Peyghambarian, Adv. Mater. 12 (2000) 1249–1252.
[35] T. Mäkelä, S. Jussila, H. Kosonen, T.G. Bäcklund, H.G.O. Sandberg, H. Stubb, Synth. Met. 153 (2005) 285–288.
[36] G.M. Sessler, D.A. Seanor, Electrical Properties of Polymers, Academic, 1982.
[37] A. Tsumura, H. Koezuka, T. Ando, Appl. Phys. Lett. 49 (1986) 1210.
[38] P. Lin, F. Yan, Adv. Mater. 24 (2011) 34–51.
[39] F.G. Brunetti, R. Kumar, F. Wudl, J. Mater. Chem. 20 (2010) 2934–2948.
[40] W.A. Little, Sci. Am. 212 (1965) 21–27.
[41] W. Little, Phys. Rev. 134 (1964) A1416--A1424.
[42] C.K. Chiang, C.R.J. Fincher, Y.W. Park, A.J. Heeger, H. Shirakawa, E.J. Louis, S.C. Gau, A.G. MacDiarmid, Phys. Rev. Lett. 39 (1977) 1098–1101.
[43] C.K. Chiang, M.A. Druy, S.C. Gau, A.J. Heeger, E.J. Louis, A.G. MacDiarmid, Y.W. Park, H. Shirakawa, J. Am. Chem. Soc. 100 (1978) 1013–1015.
[44] R.M. Owens, G.G. Malliaras, MRS Bull. 35 (2010) 449–456.
[45] G. Horowitz, Adv. Mater. Deerfield Beach Fla 10 (1998) 365–377.
[46] X. Peng, G. Horowitz, D. Fichou, F. Garnier, Appl. Phys. Lett. 57 (1990) 2013–2015.
[47] G. a Prinz, Science 282 (1998) 1660–1663.
[48] H.M. Fahad, M.M. Hussain, Sci. Rep. 2 (2012) 2–8.
[49] T. Mendívil, L.P.R. Rodríguez, M.A.Q.- López, R. Ramírez, 10 (2015) 3291–3300.
[50] M. a. Lampert, J. Phys. Chem. Solids 22 (1961) 189–197.
[51] H.E. Katz, J. Mater. Chem. 7 (1997) 369–376.
[52] S. Allard, M. Forster, B. Souharce, H. Thiem, U. Scherf, Angew. Chem. Int. Ed. 47 (2008) 4070–4098.
[53] C. Wang, H. Dong, W. Hu, Y. Liu, D. Zhu, Chem. Rev. 112 (2012) 2208–2267.
[54] Q. Miao, Adv. Mater. 26 (2014) 5541–5549.
[55] H. Sirringhaus, Adv. Mater. 26 (2014) 1319–1335.
[56] E.D. Głowacki, G. Voss, L. Leonat, M. Irimia-Vladu, S. Bauer, N.S. Sariciftci, Isr. J. Chem. 52 (2012) 540–551.
[57] E.D. Głowacki, L. Leonat, G. Voss, M.-A. Bodea, Z. Bozkurt, A.M. Ramil, M. Irimia-Vladu, S. Bauer, N.S. Sariciftci, AIP Adv. 1 (2011) 42132.
[58] M. Irimia-Vladu, E.D. Głowacki, P.A. Troshin, G. Schwabegger, L. Leonat, D.K. Susarova, O. Krystal, M. Ullah, Y. Kanbur, M.A. Bodea, V.F. Razumov, H. Sitter, S. Bauer, N.S. Sariciftci, Adv. Mater. 24 (2012) 375–380.
[59] E.D. Głowacki, G. Voss, N.S. Sariciftci, Adv. Mater. 25 (2013) 6783–6800.
[60] H.Z. Chen, M.M. Ling, X. Mo, M.M. Shi, M. Wang, Z. Bao, Chem. Mater. 19 (2007) 816–824.
[61] M.-M. Ling, P. Erk, M. Gomez, M. Koenemann, J. Locklin, Z. Bao, Adv. Mater. 19 (2007) 1123–1127.

[62] H.-W. Ting, S.-Y. Chen, T.-C. Huang, J.-H. Wei, T.-R. Yew, ChemPhysChem 12 (2011) 871–877.
[63] M. Irimia-Vladu, P.A. Troshin, M. Reisinger, L. Shmygleva, Y. Kanbur, G. Schwabegger, M. Bodea, R. Schwödiauer, A. Mumyatov, J.W. Fergus, V.F. Razumov, H. Sitter, N.S. Sariciftci, S. Bauer, Adv. Funct. Mater. 20 (2010) 4069–4076.
[64] K.-J. Baeg, M. Binda, D. Natali, M. Caironi, Y.-Y. Noh, Adv. Mater. 25 (2013) 4267–4295.
[65] T.P.I. Saragi, R. Pudzich, T. Fuhrmann, J. Salbeck, Appl. Phys. Lett. 84 (2004) 2334–2336.
[66] K.S. Narayan, N. Kumar, Appl. Phys. Lett. 79 (2001) 1891–1893.
[67] M.C. Hamilton, S. Martin, J. Kanicki, IEEE Trans. Electron Devices 51 (2004) 877–885.
[68] S. Dutta, K.S. Narayan, Adv. Mater. 16 (2004) 2151–2155.
[69] K.-J. Baeg, M. Binda, D. Natali, M. Caironi, Y.-Y. Noh, Adv. Mater. 25 (2013) 4267–4295.
[70] S. Dutta, K.S. Narayan, Phys. Rev. B 68 (2003) 125208.
[71] Y.-Y. Noh, D.-Y. Kim, K. Yase, J. Appl. Phys. 98 (2005) 74505.
[72] Y.-Y. Noh, D.-Y. Kim, Y. Yoshida, K. Yase, B.-J. Jung, E. Lim, H.-K. Shim, Appl. Phys. Lett. 86 (2005) 43501.
[73] J.-M. Choi, J. Lee, D.K. Hwang, J.H. Kim, S. Im, E. Kim, Appl. Phys. Lett. 88 (2006) 43508.
[74] H. Dong, H. Li, E. Wang, H. Nakashima, K. Torimitsu, W. Hu, J. Phys. Chem. C 112 (2008) 19690–19693.
[75] H. Xu, J. Li, B.H.K. Leung, C.C.Y. Poon, B.S. Ong, Y. Zhang, N. Zhao, Nanoscale 5 (2013) 11850–11855.
[76] Q. Wang, M. Zhu, D. Wu, G. Zhang, X. Wang, H. Lu, X. Wang, L. Qiu, J. Mater. Chem. C 3 (2015) 10734–10741.
[77] L. Torsi, M. Magliulo, K. Manoli, G. Palazzo, Chem. Soc. Rev. 42 (2013) 8612–8628.
[78] J.W. Gardner, P.N. Bartlett, Meas. Sci. Technol. 11 (2000) 1087.
[79] A. Loutfi, S. Coradeschi, G.K. Mani, P. Shankar, J.B.B. Rayappan, J. FOOD Eng. 144 (2015) 103–111.
[80] P. Boeker, Sens. Actuators B Chem. 204 (2014) 2–17.
[81] L. Capelli, S. Sironi, R. Del Rosso, Sensors 14 (2014) 19979–20007.
[82] L. Lvova, R. Pudi, P. Galloni, V. Lippolis, C. Di Natale, I. Lundström, R. Paolesse, Sens. Actuators B Chem. 207 (2015) 1076–1086.
[83] C.M. Daikuzono, C.A.R. Dantas, D. Volpati, C.J.L. Constantino, M.H.O. Piazzetta, A.L. Gobbi, D.M. Taylor, O.N. Oliveira Jr, A. Riul Jr, Sens. Actuators B Chem. 207 (2015) 1129–1135.
[84] P. Ciosek, M. Weso\ly, M. Zabadaj, J. Lisiecka, K. So\l\lohub, K. Cal, W. Wróblewski, Sens. Actuators B Chem. 207 (2015) 1087–1094.
[85] S. Sasaki, 194 (1987).
[86] A. Köhler, H. Bässler, Electronic Processes in Organic Semiconductors: An Introduction, Wiley-VCH, Weinheim, 2015.
[87] D. Gargi, R.J. Kline, D.M. DeLongchamp, D.A. Fischer, M.F. Toney, B.T. O'Connor, J. Phys. Chem. C 117 (2013) 17421–17428.
[88] B.T. O'Connor, O.G. Reid, X. Zhang, R.J. Kline, L.J. Richter, D.J. Gundlach, D.M. DeLongchamp, M.F. Toney, N. Kopidakis, G. Rumbles, Adv. Funct. Mater. 24 (2014) 3422–3431.
[89] B. Meredig, A. Salleo, R. Gee, ACS Nano 3 (2009) 2881–2886.
[90] H. Kim, B. Yoon, J. Sung, D.-G. Choi, C. Park, J. Mater. Chem. 18 (2008) 3489.
[91] Y. Fu, C. Lin, F.-Y. Tsai, Org. Electron. 10 (2009) 883–888.
[92] Y.-Y. Lin, D.J. Gundlach, S.F. Nelson, T.N. Jackson, IEEE Electron Device Lett. 18 (1997) 606–608.
[93] C.D. Sheraw, T.N. Jackson, D.L. Eaton, J.E. Anthony, Adv. Mater. 15 (2003) 2009–2011.

[94] S.K. Park, T.N. Jackson, J.E. Anthony, D.A. Mourey, Appl. Phys. Lett. 91 (2007) 63514.
[95] T.L. Brown, Chemistry: The Central Science., 2015.
[96] R.M. Metzger, D.L. Allara, eds., Unimolecular and Supramolecular Electronics: Chemistry and Physics Meet at Metal-Molecule Interfaces, Springer, Heidelberg ; New York, 2012.
[97] H. Klauk, U. Zschieschang, M. Halik, J. Appl. Phys. 102 (2007) 74514.
[98] A. Facchetti, Chem. Mater. 23 (2011) 733–758.
[99] A. Rogalski, J. Antoszewski, L. Faraone, J. Appl. Phys. 105 (2009) 91101.
[100] E. H. Sargent, Adv. Mater. 17 (2005) 515–522.
[101] L. Du, X. Luo, F. Zhao, W. Lv, J. Zhang, Y. Peng, Y. Tang, Y. Wang, Carbon 96 (2016) 685–694.
[102] X. Luo, L. Du, W. Lv, L. Sun, Y. li, Y. Peng, F. Zhao, J. Zhang, Y. Tang, Y. Wang, Synth. Met. 210 (2015) 230–235.
[103] H. Hwang, H. Kim, S. Nam, D.D.C. Bradley, C.-S. Ha, Y. Kim, Nanoscale 3 (2011) 2275.
[104] Y. Liu, H. Wang, H. Dong, J. Tan, W. Hu, X. Zhan, Macromolecules 45 (2012) 1296–1302.
[105] J. Kim, S. Cho, Y.-H. Kim, S.K. Park, Org. Electron. 15 (2014) 2099–2106.
[106] Y. Guo, C. Du, C.-A. Di, J. Zheng, X. Sun, Y. Wen, L. Zhang, W. Wu, G. Yu, Y. Liu, Appl. Phys. Lett. 94 (2009).
[107] N.M. Johnson, A. Chiang, Appl. Phys. Lett. 45 (1984) 1102–1104.
[108] H. Xu, J. Li, B.H.K. Leung, C.C.Y. Poon, B.S. Ong, Y. Zhang, N. Zhao, Nanoscale 5 (2013) 11850.
[109] T.D. Anthopoulos, Appl. Phys. Lett. 91 (2007) 113513.
[110] H. Liu, Q. Sun, J. Xing, Z. Zheng, Z. Zhang, Z. Lü, K. Zhao, ACS Appl. Mater. Interfaces 7 (2015) 6645–6651.
[111] Z. Wang, M. Safdar, C. Jiang, J. He, Nano Lett. 12 (2012) 4715–4721.
[112] P. Hu, J. Zhang, M. Yoon, X.-F. Qiao, X. Zhang, W. Feng, P. Tan, W. Zheng, J. Liu, X. Wang, J.C. Idrobo, D.B. Geohegan, K. Xiao, Nano Res. 7 (2014) 694–703.
[113] H. Dong, H. Zhu, Q. Meng, X. Gong, W. Hu, Chem. Soc. Rev. 41 (2012) 1754–1808.
[114] J. Li, L. Niu, Z. Zheng, F. Yan, Adv. Mater. 26 (2014) 5239–5273.
[115] R.M. Pinto, W. Gouveia, A.I.S. Neves, H. Alves, Appl. Phys. Lett. 107 (2015) 223301.
[116] A. Armin, M. Hambsch, I.K. Kim, P.L. Burn, P. Meredith, E.B. Namdas, Laser Photonics Rev. 8 (2014) 924–932.
[117] J.G. Labram, P.H. Wöbkenberg, D.D.C. Bradley, T.D. Anthopoulos, Org. Electron. 11 (2010) 1250–1254.
[118] A.J. Seeds, A.A.A.D. Salles, IEEE Trans. Microw. Theory Tech. 38 (1990) 577–585.
[119] M.A. Romero, M.A.G. Martinez, P.R. Herczfeld, IEEE Trans. Microw. Theory Tech. 44 (1996) 2279–2287.
[120] H.-S. Kang, C.-S. Choi, W.-Y. Choi, D.-H. Kim, K.-S. Seo, Appl. Phys. Lett. 84 (2004) 3780–3782.
[121] R.H. Bube, Photoconductivity of Solids, Wiley, 1960.
[122] F. Yan, J. Li, S.M. Mok, J. Appl. Phys. 106 (2009).
[123] M.D. Angione, S. Cotrone, M. Magliulo, a. Mallardi, D. Altamura, C. Giannini, N. Cioffi, L. Sabbatini, E. Fratini, P. Baglioni, G. Scamarcio, G. Palazzo, L. Torsi, Proc. Natl. Acad. Sci. 109 (2012) 6429–6434.
[124] S. Lai, M. Demelas, G. Casula, P. Cosseddu, M. Barbaro, a. Bonfiglio, Adv. Mater. 25 (2013) 103–107.
[125] M. Magliulo, A. Mallardi, M.Y. Mulla, S. Cotrone, B.R. Pistillo, P. Favia, I. Vikholm-Lundin, G. Palazzo, L. Torsi, Adv. Mater. 25 (2013) 2090–2094.

[126] K. Manoli, M. Magliulo, M.Y. Mulla, M. Singh, L. Sabbatini, G. Palazzo, L. Torsi, Angew. Chem. Int. Ed. 54 (2015) 12562–12576.
[127] M. Magliulo, K. Manoli, E. Macchia, G. Palazzo, L. Torsi, Adv. Mater. 27 (2015) 7528–7551.
[128] M. Magliulo, M.Y. Mulla, M. Singh, E. Macchia, A. Tiwari, L. Torsi, K. Manoli, J. Mater. Chem. C 3 (2015) 12347–12363.
[129] M.E. Roberts, S.C.B. Mannsfeld, N. Queraltó, C. Reese, J. Locklin, W. Knoll, Z. Bao, Proc. Natl. Acad. Sci. U. S. A. 105 (2008) 12134–12139.
[130] P. Stoliar, E. Bystrenova, S.D. Quiroga, P. Annibale, M. Facchini, M. Spijkman, S. Setayesh, D. de Leeuw, F. Biscarini, Biosens. Bioelectron. 24 (2009) 2935–2938.
[131] Q. Zhang, L. Jagannathan, V. Subramanian, Biosens. Bioelectron. 25 (2010) 972–977.
[132] Q. Zhang, V. Subramanian, Biosens. Bioelectron. 22 (2007) 3182–3187.
[133] H.U. Khan, M.E. Roberts, O. Johnson, R. Förch, W. Knoll, Z. Bao, Adv. Mater. 22 (2010) 4452–4456.
[134] M.L. Hammock, O. Knopfmacher, B.D. Naab, J.B.H. Tok, Z. Bao, ACS Nano 7 (2013) 3970–3980.
[135] M. Magliulo, D. Altamura, C. Di Franco, M.V. Santacroce, K. Manoli, A. Mallardi, G. Palazzo, G. Scamarcio, C. Giannini, L. Torsi, J. Phys. Chem. C 118 (2014) 15853–15862.
[136] J.T. Mabeck, G.G. Malliaras, Anal. Bioanal. Chem. 384 (2006) 343–353.
[137] C. Bartic, a. Campitelli, S. Borghs, Appl. Phys. Lett. 82 (2003) 475–477.
[138] K. Melzer, A.M. Münzer, E. Jaworska, K. Maksymiuk, A. Michalska, G. Scarpa, Org. Electron. Phys. Mater. Appl. 15 (2014) 595–601.
[139] S.P. White, K.D. Dorfman, C.D. Frisbie, Anal. Chem. 87 (2015) 1861–1866.
[140] D. Khodagholy, J. Rivnay, M. Sessolo, M. Gurfinkel, P. Leleux, L.H. Jimison, E. Stavrinidou, T. Herve, S. Sanaur, R.M. Owens, G.G. Malliaras, Nat. Commun. 4 (2013).
[141] X. Strakosas, M. Bongo, 41735 (2015) 1–14.
[142] H. Minemawari, T. Yamada, H. Matsui, J. Tsutsumi, S. Haas, R. Chiba, R. Kumai, T. Hasegawa, Nature 475 (2011) 364–367.
[143] W. Xie, K. Willa, Y. Wu, R. Häusermann, K. Takimiya, B. Batlogg, C.D. Frisbie, Adv. Mater. 25 (2013) 3478–3484.
[144] G. Schweicher, V. Lemaur, C. Niebel, C. Ruzié, Y. Diao, O. Goto, W.-Y. Lee, Y. Kim, J.-B. Arlin, J. Karpinska, A.R. Kennedy, S.R. Parkin, Y. Olivier, S.C.B. Mannsfeld, J. Cornil, Y.H. Geerts, Z. Bao, Adv. Mater. 27 (2015) 3066–3072.
[145] Y. He, M. Sezen, D. Zhang, A. Li, L. Yan, H. Yu, C. He, O. Goto, Y.-L. Loo, H. Meng, Adv. Electron. Mater. 2 (2016) n/a-n/a.
[146] K. Takimiya, H. Ebata, K. Sakamoto, T. Izawa, T. Otsubo, Y. Kunugi, J. Am. Chem. Soc. 128 (2006) 12604–12605.
[147] T. Lei, Y. Cao, Y. Fan, C.-J. Liu, S.-C. Yuan, J. Pei, J. Am. Chem. Soc. 133 (2011) 6099–6101.
[148] H. Ebata, T. Izawa, E. Miyazaki, K. Takimiya, M. Ikeda, H. Kuwabara, T. Yui, J. Am. Chem. Soc. 129 (2007) 15732–15733.
[149] U. Zschieschang, F. Ante, T. Yamamoto, K. Takimiya, H. Kuwabara, M. Ikeda, T. Sekitani, T. Someya, K. Kern, H. Klauk, Adv. Mater. 22 (2010) 982–985.
[150] K. Takimiya, T. Yamamoto, H. Ebata, T. Izawa, Sci. Technol. Adv. Mater. 8 (2007) 273–276.
[151] C.-H. Wang, S.-D. Jian, S.-W. Chan, C.-S. Ku, P.-Y. Huang, M.-C. Chen, Y.-W. Yang, J. Phys. Chem. C 116 (2012) 1225–1231.
[152] H. Yu, W. Li, H. Tian, H. Wang, D. Yan, J. Zhang, Y. Geng, F. Wang, ACS Appl. Mater. Interfaces 6 (2014) 5255–5262.
[153] D. Zhang, L. Zhao, Y. Zhu, A. Li, C. He, H. Yu, Y. He, C. Yan, O. Goto, H. Meng, ACS Appl. Mater. Interfaces 8 (2016) 18277–18283.

[154] B. Kang, R. Kim, S.B. Lee, S.-K. Kwon, Y.-H. Kim, K. Cho, J. Am. Chem. Soc. 138 (2016) 3679–3686.
[155] L. Zhao, D. Zhang, Y. Zhu, S. Peng, H. Meng, W. Huang, J. Mater. Chem. C 5 (2017) 848–853.
[156] Z. Zhao, Z. Yin, H. Chen, L. Zheng, C. Zhu, L. Zhang, S. Tan, H. Wang, Y. Guo, Q. Tang, Y. Liu, Adv. Mater. 29 (2017) n/a-n/a.
[157] Y. Zang, D. Huang, C. Di, D. Zhu, Adv. Mater. 28 (2016) 4549–4555.
[158] B. Wang, J. Ding, T. Zhu, W. Huang, Z. Cui, J. Chen, L. Huang, L. Chi, Nanoscale 8 (2016) 3954–3961.
[159] J. Lu, D. Liu, J. Zhou, Y. Chu, Y. Chen, X. Wu, J. Huang, Adv. Funct. Mater. (2017) n/a-n/a.
[160] C. Zhang, P. Chen, W. Hu, Chem. Soc. Rev. 44 (2015) 2087–2107.
[161] P. Lin, F. Yan, Adv. Mater. 24 (2012) 34–51.
[162] Y. Guo, G. Yu, Y. Liu, Adv. Mater. 22 (2010) 4427–4447.
[163] W. Liang, L. Xu, S. Sun, L. Lan, X. Qiu, R. Chen, Y. Li, ACS Sustain. Chem. Eng. 5 (2017) 460–468.
[164] H.-W. Zan, W.-W. Tsai, Y. Lo, Y.-M. Wu, Y.-S. Yang, IEEE Sens. J. 12 (2012) 594–601.
[165] B. Kang, M. Jang, Y. Chung, H. Kim, S.K. Kwak, J.H. Oh, K. Cho, Nat. Commun. 5 (2014) 4752.
[166] S. Wu, G. Wang, Z. Xue, F. Ge, G. Zhang, H. Lu, L. Qiu, ACS Appl. Mater. Interfaces (2017).
[167] S.G. Surya, S.S. Nagarkar, S.K. Ghosh, P. Sonar, V. Ramgopal Rao, Sens. Actuators B Chem. 223 (2016) 114–122.
[168] A.H.M. Renfrew, Rev. Prog. Color. Relat. Top. 15 (1985) 15–20.
[169] G. Fischer, J. Für Prakt. Chem. 19 (1879) 317–321.
[170] H.M. Smith, ed., High Performance Pigments, Wiley-VCH, Weinheim, 2002.
[171] K. Hunger, ed., Industrial Dyes: Chemistry, Properties, Applications, Wiley-VCH, Weinheim, 2003.
[172] S. Yoshida, K. Kozawa, T. Uchida, Bull. Chem. Soc. Jpn. 68 (1995) 738–743.
[173] F. Qiao, A. Liu, Y. Xiao, Y.P. Ou, J. quan Zhang, Y. chang Sang, Microelectron. J. 39 (2008) 1568–1571.
[174] Y. Nicolas, F. Allama, M. Lepeltier, J. Massin, F. Castet, L. Ducasse, L. Hirsch, Z. Boubegtiten, G. Jonusauskas, C. Olivier, T. Toupance, Chem. – Eur. J. 20 (2014) 3678–3688.
[175] C. Di, J. Li, G. Yu, Y. Xiao, Y. Guo, Y. Liu, X. Qian, D. Zhu, Org. Lett. 10 (2008) 3025–3028.
[176] Y. Nicolas, F. Castet, M. Devynck, P. Tardy, L. Hirsch, C. Labrugère, H. Allouchi, T. Toupance, Org. Electron. 13 (2012) 1392–1400.
[177] G. Gruntz, H. Lee, L. Hirsch, F. Castet, T. Toupance, A.L. Briseno, Y. Nicolas, Adv. Electron. Mater. 1 (2015) n/a-n/a.
[178] T. Yokozawa, Y. Ohta, (2016) 1–37.
[179] R.C. Coffin, J. Peet, J. Rogers, G.C. Bazan, Nat. Chem. 1 (2009) 657–661.
[180] W. Li, L. Yang, J.R. Tumbleston, L. Yan, H. Ade, W. You, Adv. Mater. 26 (2014) 4456–4462.
[181] G. L. Gibson, D. Gao, A. A. Jahnke, J. Sun, A. J. Tilley, D. S. Seferos, J. Mater. Chem. A 2 (2014) 14468–14480.
[182] G. Odian, Principles of Polymerization, John Wiley & Sons, Inc., Hoboken, NJ, USA, 2004.
[183] I. Osaka, T. Abe, S. Shinamura, K. Takimiya, J. Am. Chem. Soc. 133 (2011) 6852–6860.
[184] Z. Chen, M.J. Lee, R. Shahid Ashraf, Y. Gu, S. Albert-Seifried, M. Meedom Nielsen, B. Schroeder, T.D. Anthopoulos, M. Heeney, I. McCulloch, H. Sirringhaus, Adv. Mater. 24 (2012) 647–652.
[185] S. Cotrone, D. Cafagna, S. Cometa, E.D. Giglio, M. Magliulo, L. Torsi, L. Sabbatini, Anal. Bioanal. Chem. 402 (2012) 1799–1811.
[186] X. Strakosas, M. Bongo, R.M. Owens, J. Appl. Polym. Sci. 132 (2015) n/a-n/a.

[187] F.X. Werkmeister, B.A. Nickel, Org. Electron. 39 (2016) 113–117.
[188] L. Kergoat, L. Herlogsson, D. Braga, B. Piro, M.-C. Pham, X. Crispin, M. Berggren, G. Horowitz, Adv. Mater. 22 (2010) 2565–2569.
[189] A. Giovannitti, C.B. Nielsen, D.-T. Sbircea, S. Inal, M. Donahue, M.R. Niazi, D.A. Hanifi, A. Amassian, G.G. Malliaras, J. Rivnay, I. McCulloch, Nat. Commun. 7 (2016) 13066.
[190] R.F. de Oliveira, L. Merces, T.P. Vello, C.C. Bof Bufon, Org. Electron. 31 (2016) 217–226.
[191] D. a. E. Issa, N.S. Habib, A.E. Abdel Wahab, Med Chem Commun 6 (2015) 202–211.
[192] V. a. Mamedov, A. a. Kalinin, N. a. Zhukova, V. V. Syakaev, I.K. Rizvanov, S.K. Latypov, O.G. Sinyashin, Tetrahedron 71 (2015) 147–157.
[193] S. Hussain, S. Parveen, X. Hao, S. Zhang, W. Wang, X. Qin, Y. Yang, X. Chen, S. Zhu, C. Zhu, B. Ma, Eur. J. Med. Chem. 80 (2014) 383–392.
[194] B. Xu, Y. Sun, Y. Guo, Y. Cao, T. Yu, Bioorg. Med. Chem. 17 (2009) 2767–2774.
[195] J. Zhou, M. Ba, B. Wang, H. Zhou, J. Bie, D. Fu, Y. Cao, B. Xu, Y. Guo, MedChemComm 5 (2014) 441.
[196] G. Rabilloud, B. Sillion, Bull. Soc. Chim. Fr. (1970) 4052–4057.
[197] S.A. Galal, S.H.M. Khairat, F.A.F. Ragab, A.S. Abdelsamie, M.M. Ali, S.M. Soliman, J. Mortier, G. Wolber, H.I. El Diwani, Eur. J. Med. Chem. 86 (2014) 122–132.
[198] J. Guillon, J. Louchahi-Raoul, M. Boulouard, P. Dallemagne, M. Daoust, S. Rault, Pharm. Pharmacol. Commun. 4 (1998) 319–324.
[199] Y. Li, G. Vamvounis, S. Holdcroft, Chem. Mater. 14 (2002) 1424–1429.
[200] H. Zhou, L. Yang, S. Liu, W. You, Macromolecules 43 (2010) 10390–10396.
[201] Y. Li, P. Sonar, S.P. Singh, M.S. Soh, M. van Meurs, J. Tan, J. Am. Chem. Soc. 133 (2011) 2198–2204.
[202] Y. Li, S.P. Singh, P. Sonar, Adv. Mater. 22 (2010) 4862–6.
[203] P. Zalar, Z.B. Henson, G.C. Welch, G.C. Bazan, T.-Q. Nguyen, Angew. Chem. Int. Ed. 51 (2012) 7495–7498.
[204] P. Zalar, M. Kuik, Z.B. Henson, C. Woellner, Y. Zhang, A. Sharenko, G.C. Bazan, T.-Q. Nguyen, Adv. Mater. 26 (2014) 724–727.
[205] G.C. Welch, R. Coffin, J. Peet, G.C. Bazan, J. Am. Chem. Soc. 131 (2009) 10802–10803.
[206] G.C. Welch, G.C. Bazan, J. Am. Chem. Soc. 133 (2011) 4632–4644.
[207] T. Tang, G. Ding, T. Lin, H. Chi, C. Liu, X. Lu, F. Wang, C. He, Macromol. Rapid Commun. 34 (2013) 431–436.
[208] T. Tang, T. Lin, F. Wang, C. He, Polym. Chem. 5 (2014) 2980.
[209] T. Tang, H. Chi, T. Lin, F. Wang, C. He, Phys. Chem. Chem. Phys. 16 (2014) 20221.
[210] E. Poverenov, N. Zamoshchik, A. Patra, Y. Ridelman, M. Bendikov, J. Am. Chem. Soc. 136 (2014) 5138–5149.
[211] T. Tang, T. Lin, F. Wang, C. He, J. Phys. Chem. B 119 (2015) 8176–8183.
[212] Y. He, C. Guo, B. Sun, J. Quinn, Y. Li, Polym. Chem. 6 (2015) 6689–6697.
[213] M.J. Winokur, D. Spiegel, Y. Kim, S. Hotta, A.J. Heeger, Synth. Met. 28 (1989) 419–426.
[214] D.M. de Leeuw, M.M.J. Simenon, A.R. Brown, R.E.F. Einerhand, Synth. Met. 87 (1997) 53–59.
[215] T.D. Anthopoulos, G.C. Anyfantis, G.C. Papavassiliou, D.M. de Leeuw, Appl. Phys. Lett. 90 (2007) 122105.
[216] H. Yan, Z. Chen, Y. Zheng, C. Newman, J.R. Quinn, F. Dötz, M. Kastler, A. Facchetti, Nature 457 (2009) 679–686.
[217] H. Chai, J. Li, L. Yang, H. Lu, Z. Qi, D. Shi, RSC Adv 4 (2014) 44811–44814.
[218] U. a. Kshirsagar, S.B. Mhaske, N.P. Argade, Tetrahedron Lett. 48 (2007) 3243–3246.
[219] C. Wéber, A. Bielik, G.I. Szendrei, I. Greiner, Tetrahedron Lett. 43 (2002) 2971–2974.

[220] M. Narasimhulu, K.C. Mahesh, T.S. Reddy, K. Rajesh, Y. Venkateswarlu, Tetrahedron Lett. 47 (2006) 4381–4383.
[221] M.J. Fray, J.P. Mathias, C.L. Nichols, Y.M. Po-Ba, H. Snow, Tetrahedron Lett. 47 (2006) 6365–6368.
[222] A. Kamal, a. V. Ramana, K.S. Reddy, K.V. Ramana, a. Hari Babu, B.R. Prasad, Tetrahedron Lett. 45 (2004) 8187–8190.
[223] R. Yang, A. Kaplan, Tetrahedron Lett. 41 (2000) 7005–7008.
[224] H. Takeuchi, S. Eguchi, Tetrahedron Lett. 30 (1989) 3313–3314.
[225] S.G. Yerande, S.D. More, M. Bhandari, K.M. Newase, K. Khoury, K. Wang, A. Dömling, J. Heterocycl. Chem. 51 (2014) E358--E363.
[226] Y. Liu, L. Lu, Y.-J. Zhou, X.-S. Wang, Res. Chem. Intermed. 40 (2014) 2823–2835.
[227] Z. Zhang, X. Liang, X. Li, T. Song, Q. Chen, H. Sheng, Eur. J. Med. Chem. 69 (2013) 711–718.
[228] M.-M. Zhang, L. Lu, X.-S. Wang, J. Heterocycl. Chem. 51 (2014) 1363–1368.
[229] R.H. Lemus, E.B. Skibo, J. Org. Chem. 57 (1992) 5649–5660.
[230] M.T. Bogert, H.C. Breneman, W.F. Hand, J. Am. Chem. Soc. 25 (1903) 372–380.
[231] M.T. Bogert, V.J. Chambers, J. Am. Chem. Soc. 27 (1905) 649–658.
[232] M.T. Bogert, A.H. Gotthelf, J. Am. Chem. Soc. 22 (1900) 522–535.
[233] M.T. Bogert, W.F. Hand, J. Am. Chem. Soc. 25 (1903) 935–947.
[234] M.T. Bogert, W.F. Hand, J. Am. Chem. Soc. 24 (1902) 1031–1050.
[235] A. Babel, S. a. Jenekhe, J. Am. Chem. Soc. 125 (2003) 13656–13657.
[236] A.L. Briseno, S.C.B. Mannsfeld, P.J. Shamberger, F.S. Ohuchi, Z. Bao, S. a. Jenekhe, Y. Xia, Chem. Mater. 20 (2008) 4712–4719.
[237] a Babel, a Jenekhe, Adv. Mater. 14 (2002) 371–374.
[238] F. Sunjoo Kim, D.K. Hwang, B. Kippelen, S. a. Jenekhe, Appl. Phys. Lett. 99 (2011) 2012–2015.
[239] A.L. Briseno, F.S. Kim, A. Babel, Y. Xia, S. a. Jenekhe, J. Mater. Chem. 21 (2011) 16461.
[240] J.A. Letizia, M.R. Salata, C.M. Tribout, A. Facchetti, M.A. Ratner, T.J. Marks, J. Am. Chem. Soc. 130 (2008) 9679–94.
[241] M.J. Cho, J. Shin, T.R. Hong, H.A. Um, T.W. Lee, G.W. Kim, J.H. Kwon, D.H. Choi, Polym Chem 6 (2015) 150–159.
[242] J.-R. Pouliot, B. Sun, M. Leduc, A. Najari, Y. Li, M. Leclerc, Polym Chem 6 (2015) 278–282.
[243] E.D. Głowacki, D.H. Apaydin, Z. Bozkurt, U. Monkowius, K. Demirak, E. Tordin, M. Himmelsbach, C. Schwarzinger, M. Burian, R.T. Lechner, N. Demitri, G. Voss, N.S. Sariciftci, J Mater Chem C 2 (2014) 8089–8097.
[244] O. Pitayatanakul, T. Higashino, T. Kadoya, M. Tanaka, H. Kojima, M. Ashizawa, T. Kawamoto, H. Matsumoto, K. Ishikawa, T. Mori, J Mater Chem C 2 (2014) 9311–9317.
[245] D. V Anokhin, L.I. Leshanskaya, A. a Piryazev, D.K. Susarova, N.N. Dremova, E. V Shcheglov, D. a Ivanov, V.F. Razumov, P. a Troshin, Chem. Commun. Camb. Engl. 50 (2014) 7639–41.
[246] I. V Klimovich, L.I. Leshanskaya, S.I. Troyanov, D. V Anokhin, D. V Novikov, a a Piryazev, D. a Ivanov, N.N. Dremova, P. a Troshin, J. Mater. Chem. C (2014).
[247] H. Fukumoto, H. Nakajima, T. Kojima, T. Yamamoto, Materials 7 (2014) 2030–2043.
[248] T. Lei, J. Wang, J. Pei, (2013).
[249] O. Knopfmacher, M.L. Hammock, A.L. Appleton, G. Schwartz, J. Mei, T. Lei, J. Pei, Z. Bao, Nat. Commun. 5 (2014) 2954.
[250] D. Duarte, A. Dodabalapur, J. Appl. Phys. 111 (2012) 44509–1.
[251] D.-E. Wu, Q.-C. Yao, M. Xia, Phys Chem Chem Phys 17 (2015) 3287–3294.
[252] K. Chen, K. Wang, A.M. Kirichian, A.F. Al Aowad, L.K. Iyer, S.J. Adelstein, A.I. Kassis, Mol. Cancer Ther. 5 (2006) 3001–3013.

[253] M.T. Bogert, A.W. Dox, J. Am. Chem. Soc. 27 (1905) 1127–1140.
[254] M.T. Bogert, J.M. Nelson, J. Am. Chem. Soc. 29 (1907) 729–739.
[255] E.B. Skibo, J.H. Gilchrist, J. Org. Chem. 53 (1988) 4209–4218.
[256] E.B. Skibo, X. Huang, R. Martinez, R.H. Lemus, W. a Craigo, R.T. Dorr, J. Med. Chem. 45 (2002) 5543–55.
[257] M.J. Frisch, G.W. Trucks, H.B. Schlegel, G.E. Scuseria, M.A. Robb, J.R. Cheeseman, G. Scalmani, V. Barone, B. Mennucci, G.A. Petersson, H. Nakatsuji, M. Caricato, X. Li, H.P. Hratchian, A.F. Izmaylov, J. Bloino, G. Zheng, J.L. Sonnenberg, M. Hada, M. Ehara, K. Toyota, R. Fukuda, J. Hasegawa, M. Ishida, T. Nakajima, Y. Honda, O. Kitao, H. Nakai, T. Vreven, J.A. Montgomery Jr., J.E. Peralta, F. Ogliaro, M.J. Bearpark, J. Heyd, E.N. Brothers, K.N. Kudin, V.N. Staroverov, R. Kobayashi, J. Normand, K. Raghavachari, A.P. Rendell, J.C. Burant, S.S. Iyengar, J. Tomasi, M. Cossi, N. Rega, N.J. Millam, M. Klene, J.E. Knox, J.B. Cross, V. Bakken, C. Adamo, J. Jaramillo, R. Gomperts, R.E. Stratmann, O. Yazyev, A.J. Austin, R. Cammi, C. Pomelli, J.W. Ochterski, R.L. Martin, K. Morokuma, V.G. Zakrzewski, G.A. Voth, P. Salvador, J.J. Dannenberg, S. Dapprich, A.D. Daniels, Ö. Farkas, J.B. Foresman, J.V. Ortiz, J. Cioslowski, D.J. Fox, Gaussian 09 Revision D.01, Gaussian, Inc., Wallingford, CT, USA, 2009.
[258] N. Wache, C. Schröder, K.-W. Koch, J. Christoffers, Chembiochem Eur. J. Chem. Biol. 13 (2012) 993–8.
[259] A. V Bogolubsky, S. V Ryabukhin, A.S. Plaskon, S. V Stetsenko, D.M. Volochnyuk, A. a Tolmachev, J. Comb. Chem. 10 (2008) 858–62.
[260] A.I. Sánchez, V. Martínez-Barrasa, C. Burgos, J.J. Vaquero, J. Alvarez-Builla, E. Terricabras, V. Segarra, Bioorg. Med. Chem. 21 (2013) 2370–8.
[261] A.I. Sánchez, V. Martínez-Barrasa, C. Burgos, J.J. Vaquero, J. Alvarez-Builla, E. Terricabras, V. Segarra, Bioorg. Med. Chem. 21 (2013) 2370–8.
[262] M. Nilsson, A.K. Belfrage, S. Lindström, H. Wähling, C. Lindquist, S. Ayesa, P. Kahnberg, M. Pelcman, K. Benkestock, T. Agback, L. Vrang, Y. Terelius, K. Wikström, E. Hamelink, C. Rydergård, M. Edlund, A. Eneroth, P. Raboisson, T.-I. Lin, H. de Kock, P. Wigerinck, K. Simmen, B. Samuelsson, S. Rosenquist, Bioorg. Med. Chem. Lett. 20 (2010) 4004–11.
[263] L.A. Errede, H.T. Oien, D.R. Yarian, J. Org. Chem. 42 (1977) 12–18.
[264] a. a. Laeva, E. V. Nosova, G.N. Lipunova, a. V. Golovchenko, N.Y. Adonin, V.N. Parmon, V.N. Charushin, Russ. J. Org. Chem. 45 (2009) 913–920.
[265] S. Chen, B. Sun, W. Hong, H. Aziz, Y. Meng, Y. Li, J. Mater. Chem. C 2 (2014) 2183–2190.
[266] F.C. Spano, C. Silva, Annu. Rev. Phys. Chem. 65 (2014) 477–500.
[267] H. Yamagata, F.C. Spano, J. Chem. Phys. 136 (2012) 184901–14.
[268] R. Noriega, J. Rivnay, K. Vandewal, F.P.V. Koch, N. Stingelin, P. Smith, M.F. Toney, A. Salleo, Nat. Mater. 12 (2013) 1038–1044.
[269] G. Kim, S.-J. Kang, G.K. Dutta, Y.-K. Han, T.J. Shin, Y.-Y. Noh, C. Yang, J. Am. Chem. Soc. 136 (2014) 9477–9483.
[270] I. Kang, H.-J. Yun, D.S. Chung, S.-K. Kwon, Y.-H. Kim, J. Am. Chem. Soc. 135 (2013) 14896–14899.
[271] J. Pommerehne, H. Vestweber, W. Guss, R.F. Mahrt, H. Bässler, M. Porsch, J. Daub, H. Bassler, M. Porsch, J. Daub, Adv. Mater. 7 (1995) 551–554.
[272] T. Yasuda, T. Yamamoto, Macromolecules 36 (2003) 7513–7519.
[273] T. Yamamoto, T. Uemura, A. Tanimoto, S. Sasaki, Macromolecules 36 (2003) 1047–1053.
[274] T. Yamamoto, K. Sugiyama, T. Kanbara, H. Hayashi, H. Etori, Macromol. Chem. Phys. 199 (1998) 1807–1813.
[275] I. Nurulla, A. Tanimoto, K. Shiraishi, S. Sasaki, T. Yamamoto, Polymer 43 (2002) 1287–1293.
[276] I. Nurulla, K. Sugiyama, B.-L. Lee, T. Yamamoto, React. Funct. Polym. 46 (2000) 49–53.

[277] C.A. Matuszak, A.J. Matuszak, J. Chem. Educ. 53 (1976) 280.
[278] J.-S. Yang, T.M. Swager, J. Am. Chem. Soc. 120 (1998) 11864–11873.
[279] D.M. de Leeuw, M.M.J. Simenon, A.R. Brown, R.E.F. Einerhand, Synth. Met. 87 (1997) 53–59.
[280] T.D. Anthopoulos, G.C. Anyfantis, G.C. Papavassiliou, D.M. de Leeuw, Appl. Phys. Lett. 90 (2007) 122105.
[281] H.T. Nicolai, M. Kuik, G. a. H. Wetzelaer, B. de Boer, C. Campbell, C. Risko, J.L. Brédas, P.W.M. Blom, Nat. Mater. 11 (2012) 882–887.
[282] A. Virkar, S. Mannsfeld, J.H. Oh, M.F. Toney, Y.H. Tan, G. Liu, J.C. Scott, R. Miller, Z. Bao, Adv. Funct. Mater. 19 (2009) 1962–1970.
[283] Y. Lei, B. Wu, W.-K.E. Chan, F. Zhu, B.S. Ong, J. Mater. Chem. C 3 (2015) 12267–12272.
[284] B. Park, Thin Solid Films 598 (2015) 141–148.
[285] X. Yan, H. Wang, D. Yan, Thin Solid Films 515 (2006) 2655–2658.
[286] R. Schmidt, J.H. Oh, Y.-S. Sun, M. Deppisch, A.-M. Krause, K. Radacki, H. Braunschweig, M. Könemann, P. Erk, Z. Bao, F. Würthner, J. Am. Chem. Soc. 131 (2009) 6215–6228.
[287] J.H. Oh, S. Suraru, W.-Y. Lee, M. Könemann, H.W. Höffken, C. Röger, R. Schmidt, Y. Chung, W.-C. Chen, F. Würthner, Z. Bao, Adv. Funct. Mater. 20 (2010) 2148–2156.
[288] X. Guo, R.P. Ortiz, Y. Zheng, M.-G. Kim, S. Zhang, Y. Hu, G. Lu, A. Facchetti, T.J. Marks, J. Am. Chem. Soc. 133 (2011) 13685–13697.
[289] S. Lee, D.C. Borrelli, K.K. Gleason, Org. Electron. 33 (2016) 253–262.
[290] L. Guo, J. Quinn, J. Wang, C. Guo, X. Li, J. Wang, Y. Li, Dyes Pigments 132 (2016) 329–335.
[291] G. Lu, H. Usta, C. Risko, L. Wang, A. Facchetti, M.A. Ratner, T.J. Marks, J. Am. Chem. Soc. 130 (2008) 7670–7685.
[292] Z.-T. Zhu, J.T. Mason, R. Dieckmann, G.G. Malliaras, Appl. Phys. Lett. 81 (2002) 4643–4645.
[293] R. Ye, M. Baba, K. Suzuki, Y. Ohishi, K. Mori, Thin Solid Films 464–465 (2004) 437–440.
[294] Y. Qiu, Y. Hu, G. Dong, L. Wang, J. Xie, Y. Ma, Appl. Phys. Lett. 83 (2003) 1644–1646.
[295] J. Quinn, C. Guo, B. Sun, A. Chan, Y. He, E. Jin, Y. Li, J Mater Chem C 3 (2015) 11937–11944.
[296] J. Quinn, Y. He, D.A. Khan, J. Rasmussen, H. Patel, F. Haider, W. Kapadia, Y. Li, RSC Adv. 6 (2016) 78477–78485.
[297] Z. Qi, J. Cao, H. Li, L. Ding, J. Wang, Adv. Funct. Mater. 25 (2015) 3138–3146.
[298] B. Lucas, A. El Amrani, M. Chakaroun, B. Ratier, R. Antony, A. Moliton, Thin Solid Films 517 (2009) 6280–6282.
[299] S. Dutta, K.S. Narayan, Phys. Rev. B 68 (2003) 125208.
[300] Q. Wang, M. Zhu, D. Wu, G. Zhang, X. Wang, H. Lu, X. Wang, L. Qiu, J Mater Chem C 3 (2015) 10734–10741.
[301] P. Hu, J. Zhang, M. Yoon, X.-F. Qiao, X. Zhang, W. Feng, P. Tan, W. Zheng, J. Liu, X. Wang, J.C. Idrobo, D.B. Geohegan, K. Xiao, Nano Res. 7 (2014) 694–703.
[302] Z. Wang, M. Safdar, C. Jiang, J. He, Nano Lett. 12 (2012) 4715–4721.
[303] J.G. Labram, P.H. Wöbkenberg, D.D.C. Bradley, T.D. Anthopoulos, Org. Electron. 11 (2010) 1250–1254.
[304] G. Zhang, J. Guo, J. Zhang, W. Li, X. Wang, H. Lu, L. Qiu, Dyes Pigments 126 (2016) 20–28.
[305] T.D. Anthopoulos, Appl. Phys. Lett. 91 (2007) 113513.
[306] C.H. Lee, G. Yu, D. Moses, K. Pakbaz, C. Zhang, N.S. Sariciftci, A.J. Heeger, F. Wudl, Phys. Rev. B 48 (1993) 15425–15433.
[307] H. Liu, Q. Sun, J. Xing, Z. Zheng, Z. Zhang, Z. Lü, K. Zhao, ACS Appl. Mater. Interfaces 7 (2015) 6645–6651.
[308] F. Yan, J. Li, S.M. Mok, J. Appl. Phys. 106 (2009) 74501.

[309] X. Fan, X.M. Meng, X.H. Zhang, M.L. Zhang, J.S. Jie, W.J. Zhang, C.S. Lee, S.T. Lee, J. Phys. Chem. C 113 (2009) 834–838.
[310] J. Zhou, Y. Gu, Y. Hu, W. Mai, P.-H. Yeh, G. Bao, A.K. Sood, D.L. Polla, Z.L. Wang, Appl. Phys. Lett. 94 (2009) 191103.
[311] Y. Hu, J. Zhou, P.-H. Yeh, Z. Li, T.-Y. Wei, Z.L. Wang, Adv. Mater. 22 (2010) 3327–3332.
[312] T.P.I. Saragi, R. Pudzich, T. Fuhrmann, J. Salbeck, Appl. Phys. Lett. 84 (2004) 2334–2336.
[313] K.H. Kim, S.Y. Bae, Y.S. Kim, J.A. Hur, M.H. Hoang, T.W. Lee, M.J. Cho, Y. Kim, M. Kim, J.-I. Jin, S.-J. Kim, K. Lee, S.J. Lee, D.H. Choi, Adv. Mater. 23 (2011) 3095–3099.
[314] M.Y. Cho, S.J. Kim, Y.D. Han, D.H. Park, K.H. Kim, D.H. Choi, J. Joo, Adv. Funct. Mater. 18 (2008) 2905–2912.
[315] H. Yu, Z. Bao, J.H. Oh, Adv. Funct. Mater. 23 (2013) 629–639.
[316] R.M. Pinto, W. Gouveia, A.I.S. Neves, H. Alves, Appl. Phys. Lett. 107 (2015) 223301.
[317] K. Wasapinyokul, W.I. Milne, D.P. Chu, J. Appl. Phys. 105 (2009) 24509.
[318] K.-J. Baeg, M. Binda, D. Natali, M. Caironi, Y.-Y. Noh, Adv. Mater. 25 (2013) 4267–4295.
[319] L. Torsi, N. Cioffi, C. Di Franco, L. Sabbatini, P.G. Zambonin, T. Bleve-Zacheo, Solid-State Electron. 45 (2001) 1479–1485.
[320] F. Liao, C. Chen, V. Subramanian, Sens. Actuators B Chem. 107 (2005) 849–855.
[321] H.P. Til, H.E. Falke, M.K. Prinsen, M.I. Willems, Food Chem. Toxicol. Int. J. Publ. Br. Ind. Biol. Res. Assoc. 35 (1997) 337–348.
[322] J. Jänne, L. Alhonen, M. Pietilä, T.A. Keinänen, Eur. J. Biochem. 271 (2004) 877–894.
[323] J. Jänne, L. Alhonen, T.A. Keinänen, M. Pietilä, A. Uimari, E. Pirinen, M.T. Hyvönen, A. Järvinen, J. Cell. Mol. Med. 9 (2005) 865–882.
[324] M. Rosenberg, Sci. Am. 286 (2002) 72–79.
[325] C.M. Bollen, T. Beikler, Int. J. Oral Sci. 4 (2012) 55–63.
[326] C.J. Yeoman, S.M. Thomas, M.E.B. Miller, A.V. Ulanov, M. Torralba, S. Lucas, M. Gillis, M. Cregger, A. Gomez, M. Ho, S.R. Leigh, R. Stumpf, D.J. Creedon, M.A. Smith, J.S. Weisbaum, K.E. Nelson, B.A. Wilson, B.A. White, PloS One 8 (2013) e56111.
[327] R.A. Edwards, R.H. Dainty, C.M. Hibbard, J. Appl. Bacteriol. 58 (1985) 13–19.
[328] G. Drabik-Markiewicz, B. Dejaegher, E. De Mey, T. Kowalska, H. Paelinck, Y. Vander Heyden, Food Chem. 126 (2011) 1539–1545.
[329] S.F. Liu, A.R. Petty, G.T. Sazama, T.M. Swager, Angew. Chem. Int. Ed. 54 (2015) 6554–6557.
[330] Y. Li, Z. Xu, S. Zhao, D. Huang, L. Zhao, C. Zhang, J. Zhao, P. Wang, Y. Zhu, Org. Electron. 28 (2016) 275–280.
[331] X. Guo, M.D. Watson, Org. Lett. 10 (2008) 5333–6.
[332] Y. Li, Monomeric, Oligomeric and Polymeric Semiconductors Containing Fused Rings and Their Devices, WO2014071524 A1, 2014.
[333] H.E. Gottlieb, V. Kotlyar, A. Nudelman, J. Org. Chem. 62 (1997) 7512–7515.
[334] N. Wache, C. Schröder, K.W. Koch, J. Christoffers, ChemBioChem 13 (2012) 993–998.
[335] D.J. Sikemma, D.B. van Guldener, Polymer 34 (1993) 4373–4376.
[336] L.A. Errede, H.T. Oien, D.R. Yarian, J. Org. Chem. 42 (1977) 12–18.
[337] A.A. Laeva, E. V Nosova, G.N. Lipunova, A. V Golovchenko, N.Y. Adonin, V.N. Parmon, V.N. Charushin, Russ. J. Org. Chem. 45 (2009) 913–920.
[338] G. Horowitz, Adv. Mater. 10 (1998) 365–377.

Appendix A

Theoretical Calculations

Our theoretical calculations began by quickly optimizing a given structure at a low level of theory such as Hartree-Fock (HF) with a Slate-type orbital (STO) with 3 Gaussian orbitals (3G) followed by density functional theory (DFT) using the functional B3LYP and the basis set 6-31G(d) under tight convergence to investigate the geometry, molecular energy levels, and electron distributions of simple molecules and their corresponding oligomers. Theoretical calculations were all performed through Gaussian 09 Revision D.01 [257].

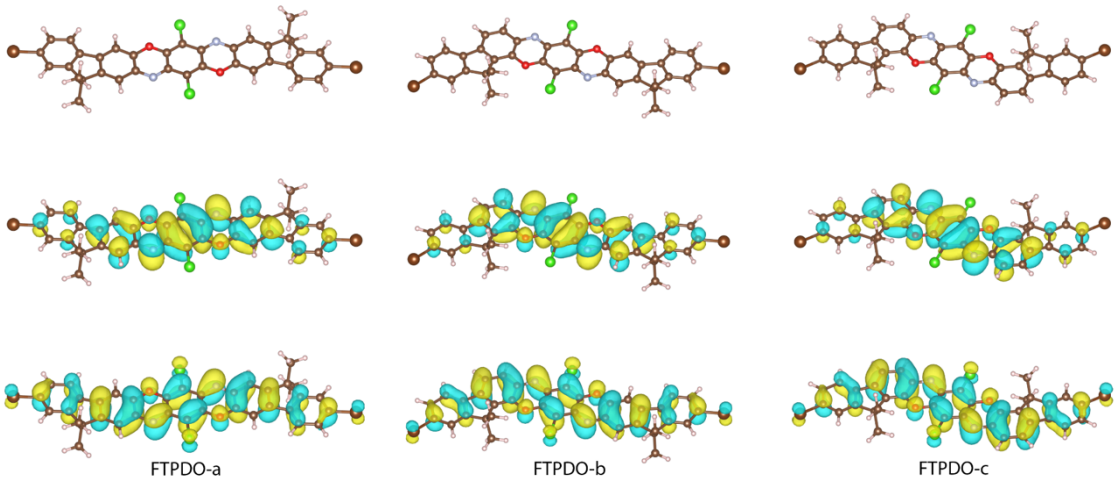

Figure A-1. Optimized geometry and HOMO and LUMO wavefunctions of **FTPDO-a**, **b** and **c** obtained by DFT calculations with B3LYP/6-31G(d).

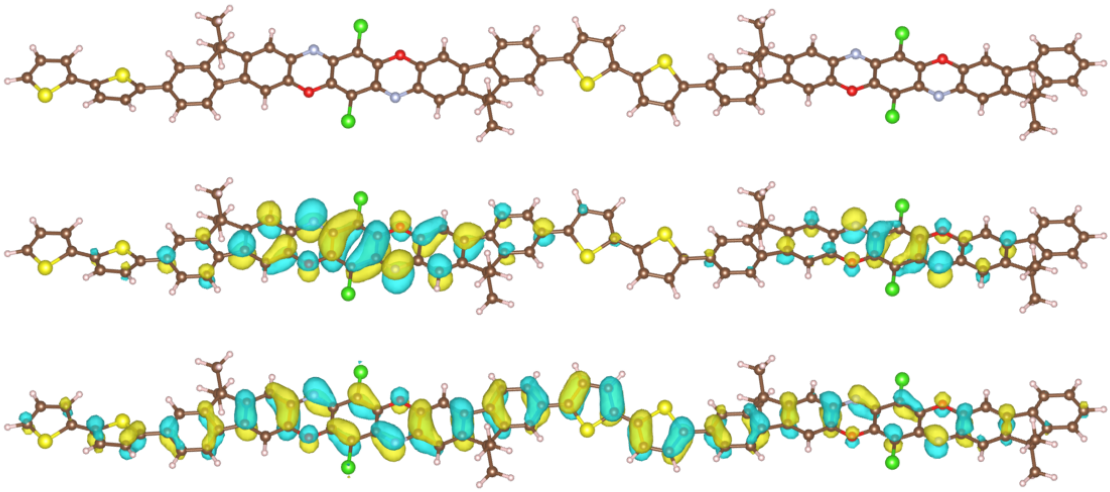

Figure A-2. Optimized geometry and HOMO (below) and LUMO (above) wavefunctions of **FTPDOBT-a** dimer obtained by DFT calculations with B3LYP/6-31G(d).

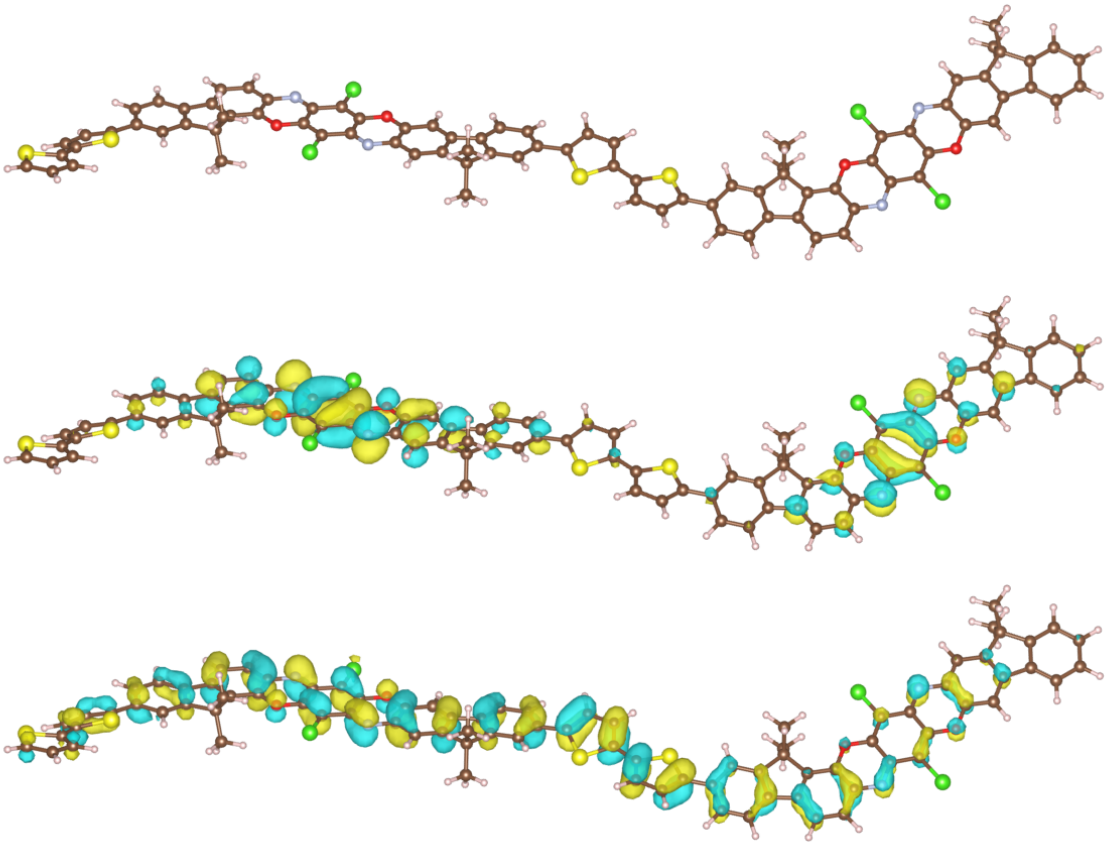

Figure A-3. Optimized geometry and HOMO (below) and LUMO (above) wavefunctions of **FTPDOBT-b** dimer obtained by DFT calculations with B3LYP/6-31G(d).

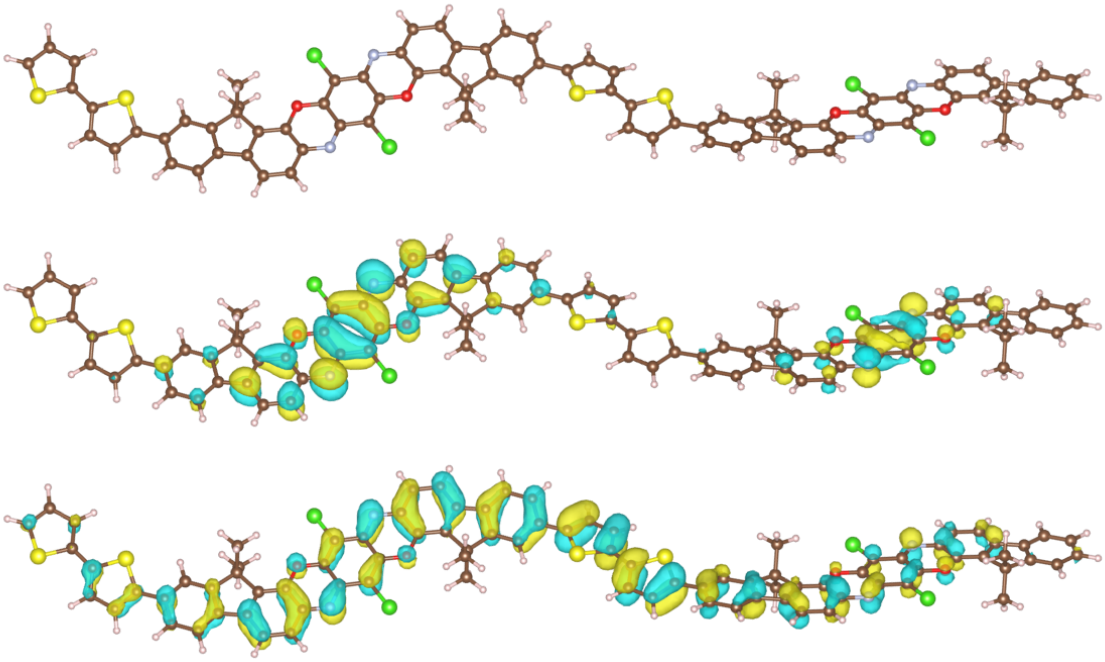

Figure A-4. Optimized geometry and HOMO (below) and LUMO (above) wavefunctions of **FTPDOBT-c** dimer obtained by DFT calculations with B3LYP/6-31G(d).

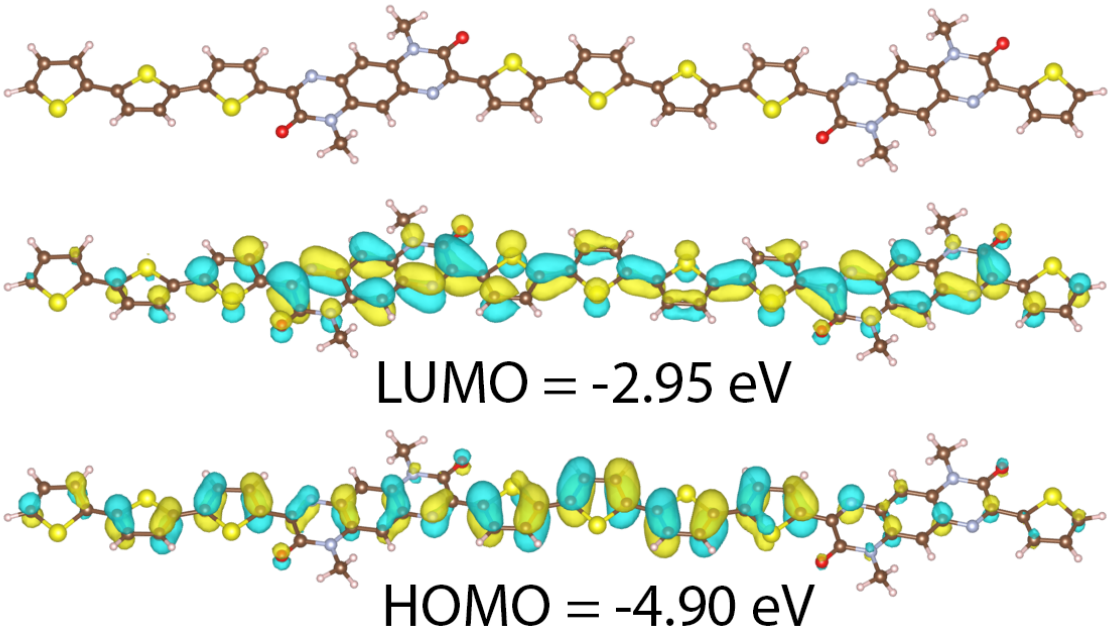

Figure A-5. Optimized geometry and HOMO (below) and LUMO (above) wavefunctions for **PQx2T-BT-Me** dimer obtained by DFT calculations with B3LYP/6-31G(d).

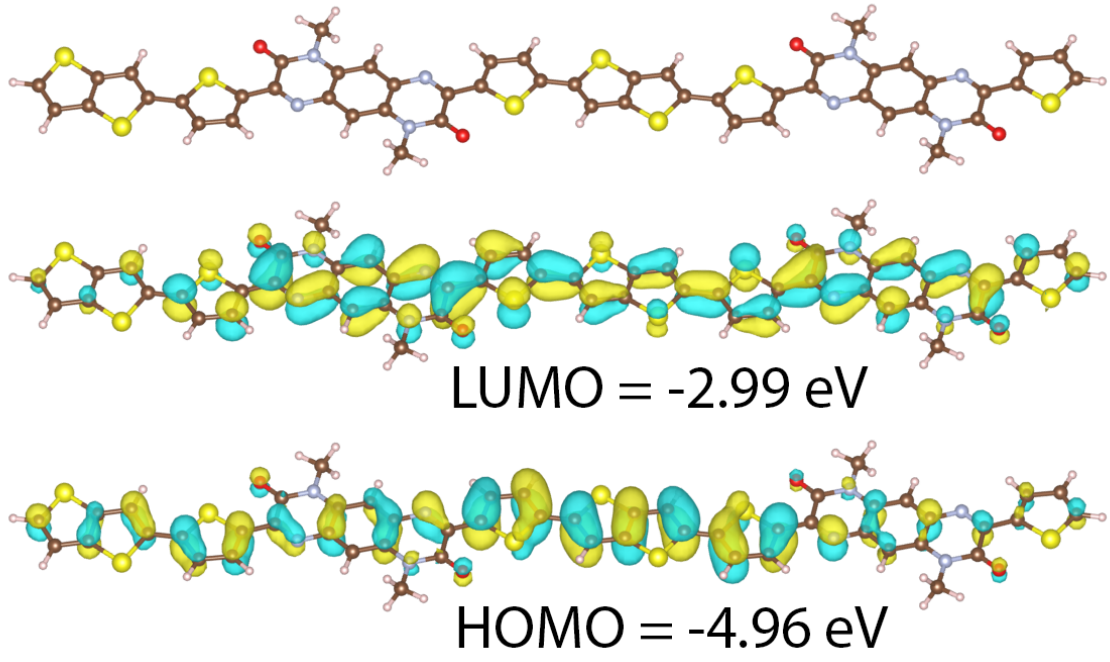

Figure A-6. Optimized geometry and HOMO (below) and LUMO (above) wavefunctions for **PQx2T-TT-Me** dimer obtained by DFT calculations with B3LYP/6-31G(d).

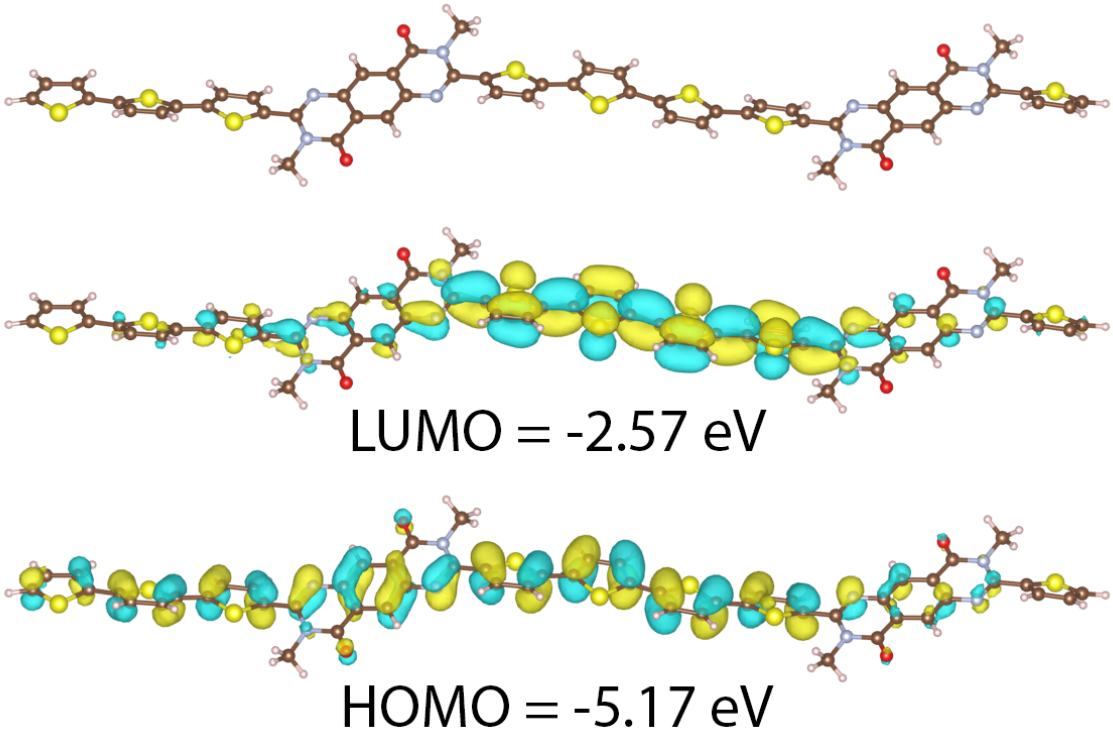

Figure A-7. Optimized geometry and HOMO (below) and LUMO (above) wavefunctions for **PQ2T-BT-Me** dimer obtained by DFT calculations with B3LYP/6-31G(d).

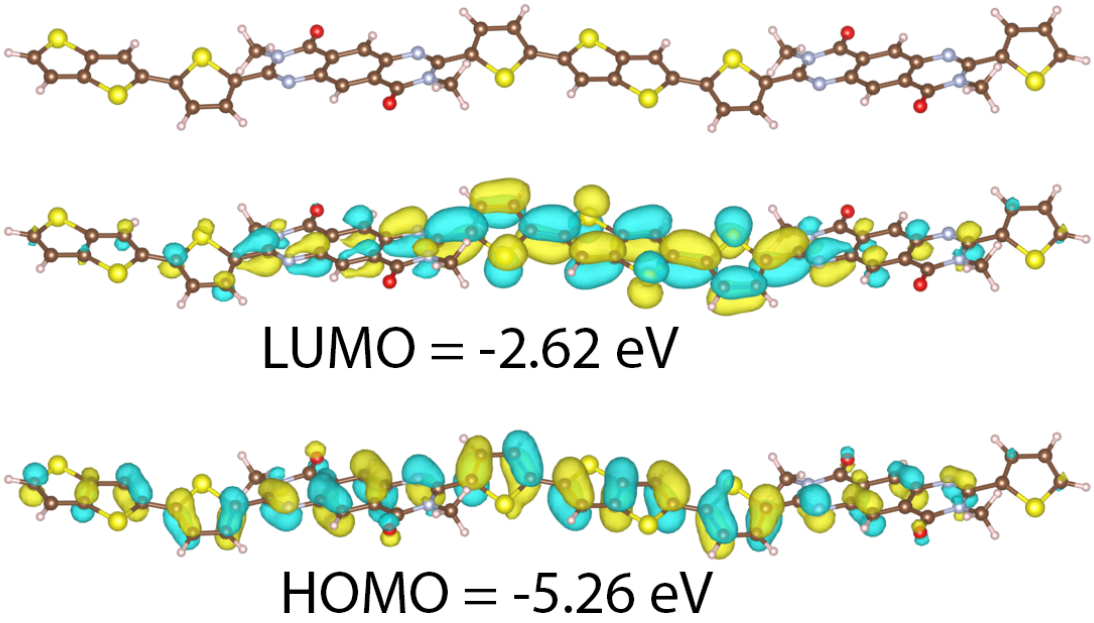

Figure A-8. Optimized geometry and HOMO (below) and LUMO (above) wavefunctions for **PQ2T-TT-Me** dimer obtained by DFT calculations with B3LYP/6-31G(d).

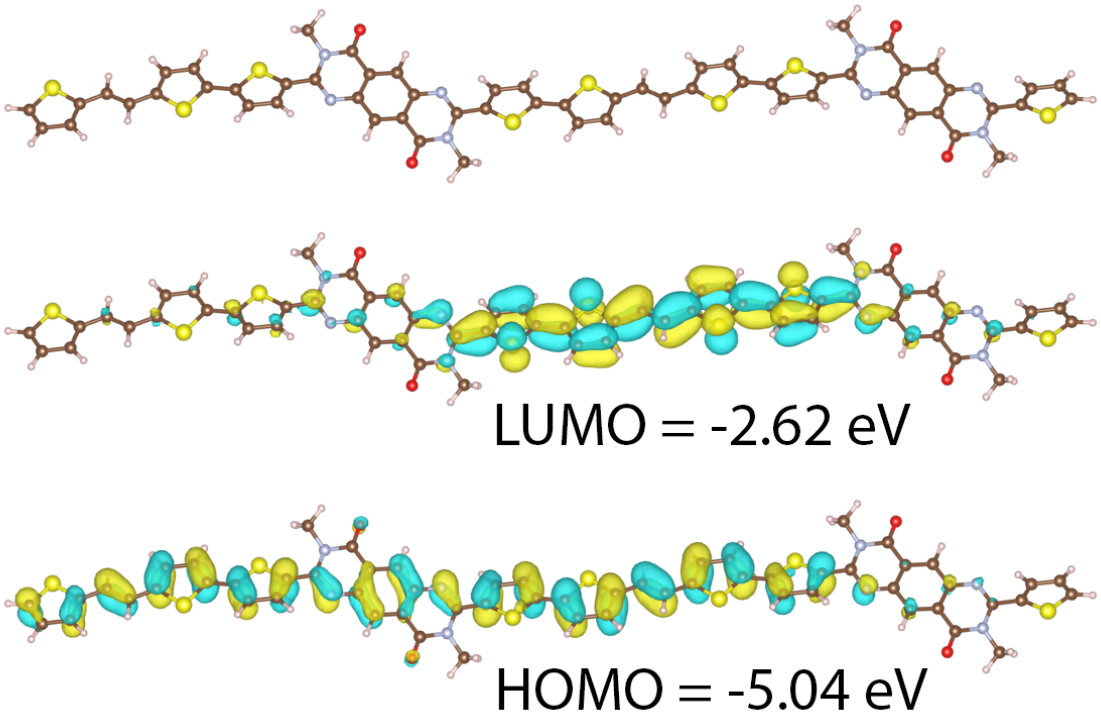

Figure A-9. Optimized geometry and HOMO (below) and LUMO (above) wavefunctions for **PQ2T-TVT-Me** dimer obtained by DFT calculations with B3LYP/6-31G(d).

Appendix B

Syntheses

All chemicals were purchased from commercial sources and used without further purification. 11-(Bromomethyl)tricosane (C_{24}-Br) [331] and 19-(3-iodopropyl)heptatriacontane [332] was synthesized using a method previously reported. NMR data were recorded on a Bruker DPX 300 MHz spectrometer with chemical shift relative to the deuterated solvent (2.50 ppm DMSO-d_6 or 7.26 ppm $CDCl_3$) [333]. All reactions were carried out under nitrogen atmosphere or otherwise stated. Column chromatography was performed on silica gel (230-400 mesh).

Synthesis of PFTPDOBT

To a 25 mL Schlenk flask, FTPDO (110 mg, 0.07 mmol), 5,5'-bis(trimethylstannyl)-2,2'-bithiophene (34 mg, 0.07 mmol) and tri(*o*-tolyl)phosphine (P(*o*-tolyl)$_3$) (1.7 mg, 0.006 mmol) were added. After degassing and refilling argon three times, chlorobenzene (3 mL) and tris(dibenzylideneacetone)-dipalladium ($Pd_2(dba)_3$) (1.3 mg, 0.001 mmol) were added. The reaction mixture was stirred at 130 °C for 72 h. Upon cooling to room temperature, the reaction mixture was poured into methanol (100 mL). The precipitate was collected by filtration and subjected to Soxhlet extraction with acetone, hexanes, and chloroform successively. The residue was dissolved in chloroform to give PFTPDOBT upon removal of solvent in *vacuo*. Yield: 90 mg (82%). GPC data: M_n = 15,432; PDI = 2.64. The ^{1}H NMR spectrum can be found in Appendix, Figure B-2. The ^{1}H NMR spectrum of the starting material FPTDO can be found in Appendix, Figure B-1.

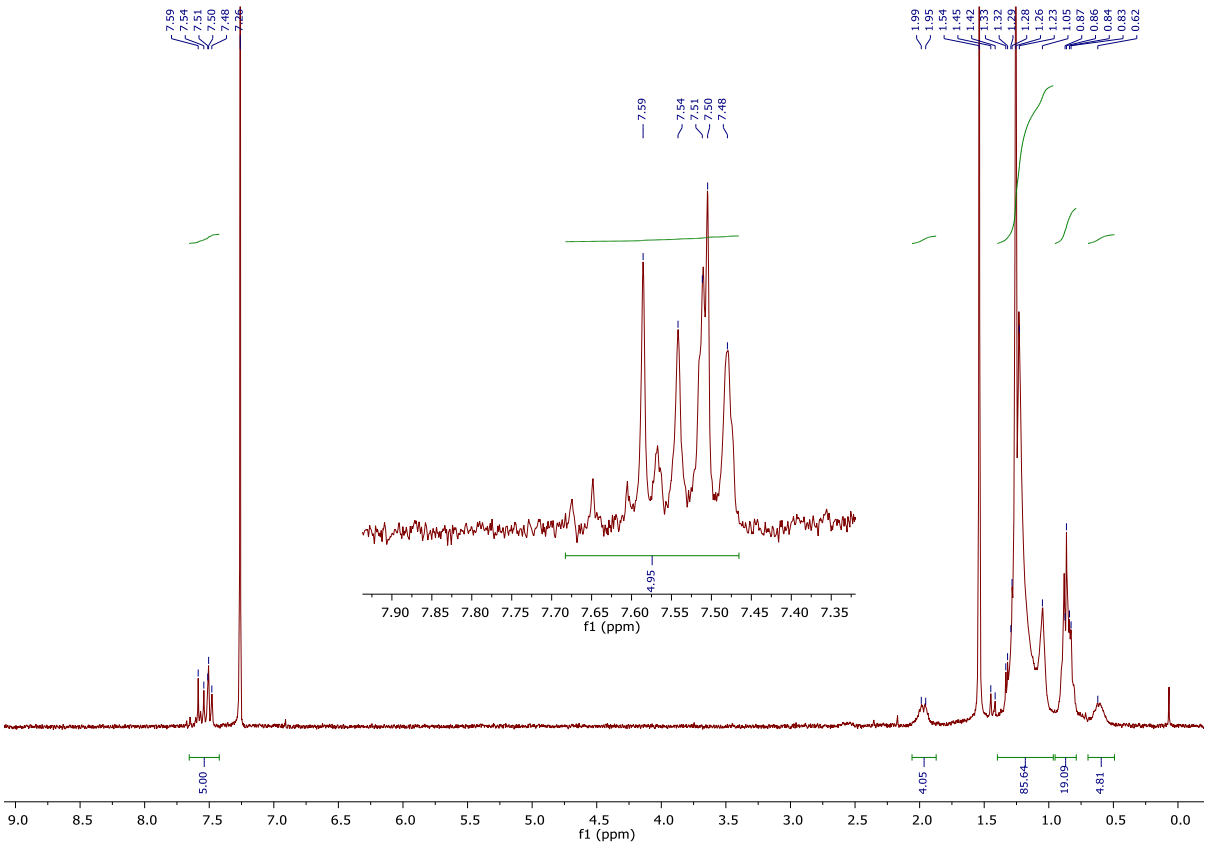

Figure B-1. 300 MHz ^{1}H NMR spectrum of **FTPDO** measured in $CDCl_3$.

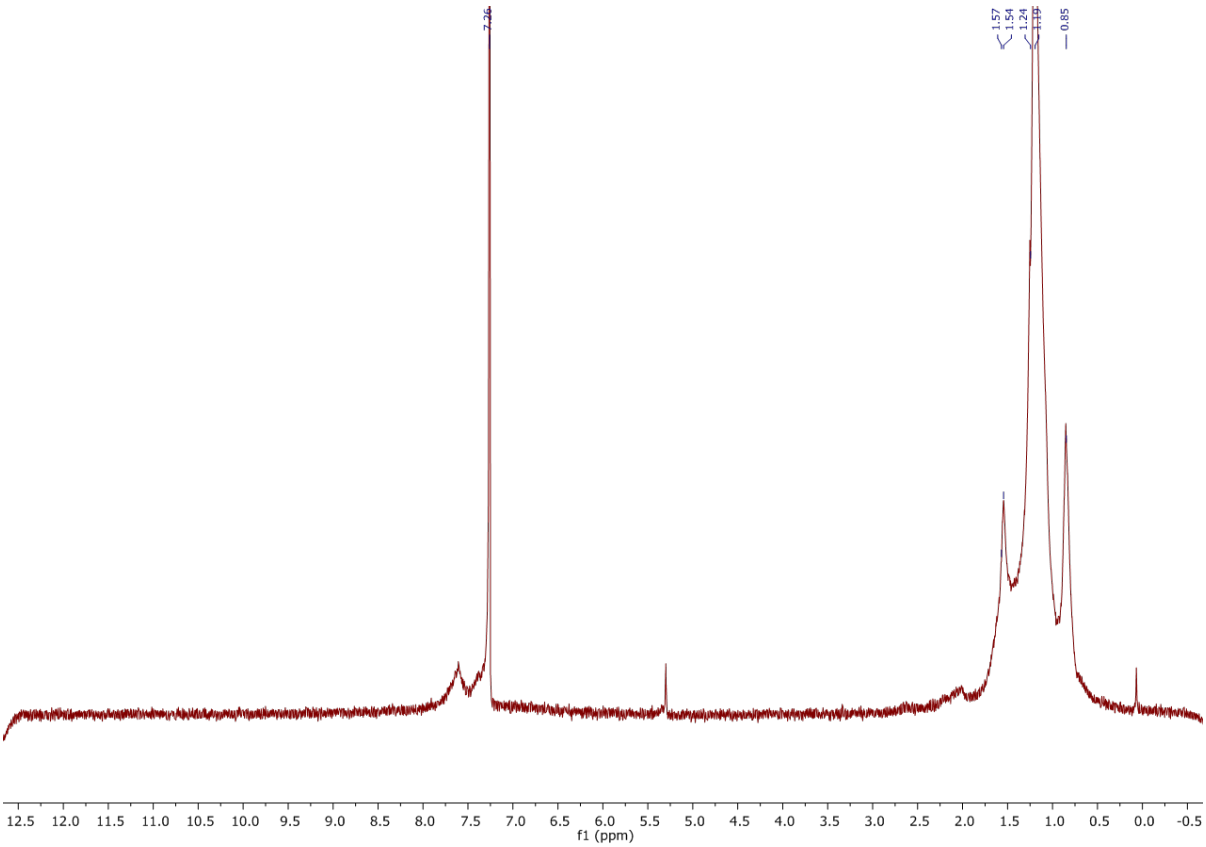

Figure B-2. 300 MHz ^{1}H NMR spectrum of **PFTPDOBT** measured in $CDCl_3$.

Synthesis of 3,8-di(thiophen-2-yl)-1,6-dihydropyrazino[2,3-*g*]quinoxaline-2,7-dione (PQx2T-H)

A 100 mL two-neck round-bottom flask was charged with 1,2,4,5-benzenetetramine tetrahydrochloride (1.1 g, 3.92 mmol), 2-thiopheneglyoxylic acid (1.2 g, 7.84 mmol) and acetic acid (80 mL). The mixture was then refluxed for 16 h. Subsequently, the reaction mixture was cooled to room temperature, added to water, filtered and washed with methanol to afford a yellow/brown solid (0.84 g, 56%). Due to its poor solubility, this product was used for the next step without further purification. An isomeric by-product, *iso*-PQx2T-H, is expected to form with a similar yield to that of PQx2T-H and present in this crude product.

Synthesis of 1,6-bis(2-decyltetradecyl)-3,8-di(thiophen-2-yl)-1,6-dihydropyrazino[2,3-*g*]quinoxaline-2,7-dione (PQx2T-24)

A 100 mL two-neck round-bottom flask was charged with the crude PQx2T-H (0.81 g, 2.2 mmol) and potassium carbonate (1.49 g, 10.8 mmol) and purged with argon. *N*,*N*-Dimethylformamide (DMF) (24 mL) was added and the reaction mixture was heated to 80 °C and stirred for 1 h before 11-(bromomethyl)tricosane (4.49 g, 10.8 mmol) was added. The reaction mixture was stirred at the same temperature for an additional 48 h. After cooling, the reaction mixture was extracted with dichloromethane and the separated organic phase was washed with water. The combined organic phases were dried and the solvent was removed. The residue was purified by column chromatography using 33% dichloromethane in hexanes to give a yellow liquid, which was treated with isopropanol three times to afford a yellow solid as the target product PQx2T-24 (0.21 g, 9%). Based on the TLC analysis, a spot similar to that of PQx2T-24 in size was observed, which could be the isomeric by-product, *iso*-PQx2T-24 (Scheme 3-1), produced by alkylation of *iso*-PQx2T-H present in the crude starting material. However, *iso*-PQx2T-24 could not be isolated by column chromatography due to its similar polarity to that of other impurities.

Data for PQx2T-24 follows. ^{1}H-NMR (300 MHz, $CDCl_3$) δ 8.40 (s, 2H), 8.31 (d, J = 3.8 Hz, 2H), 7.59 (d, J = 5.1 Hz, 2H), 7.21 (t, J = 4.5 Hz, 2H), 4.62 (d, J = 5.3 Hz, 4H), 2.00 (br, 2H), 1.71-1.15 (m, 80H), 0.87 (t, J = 6.5 Hz, 12H). ^{13}C-NMR (75 MHz, $CDCl_3$) δ 154.23, 142.47, 140.75, 138.80, 137.78, 131.52, 130.96, 128.28, 124.19, 70.22, 37.74, 32.08, 31.86, 30.16, 29.85, 29.81, 29.52, 27.06, 22.85, 14.29. MS (ESI+) [M+H]+: 1051.

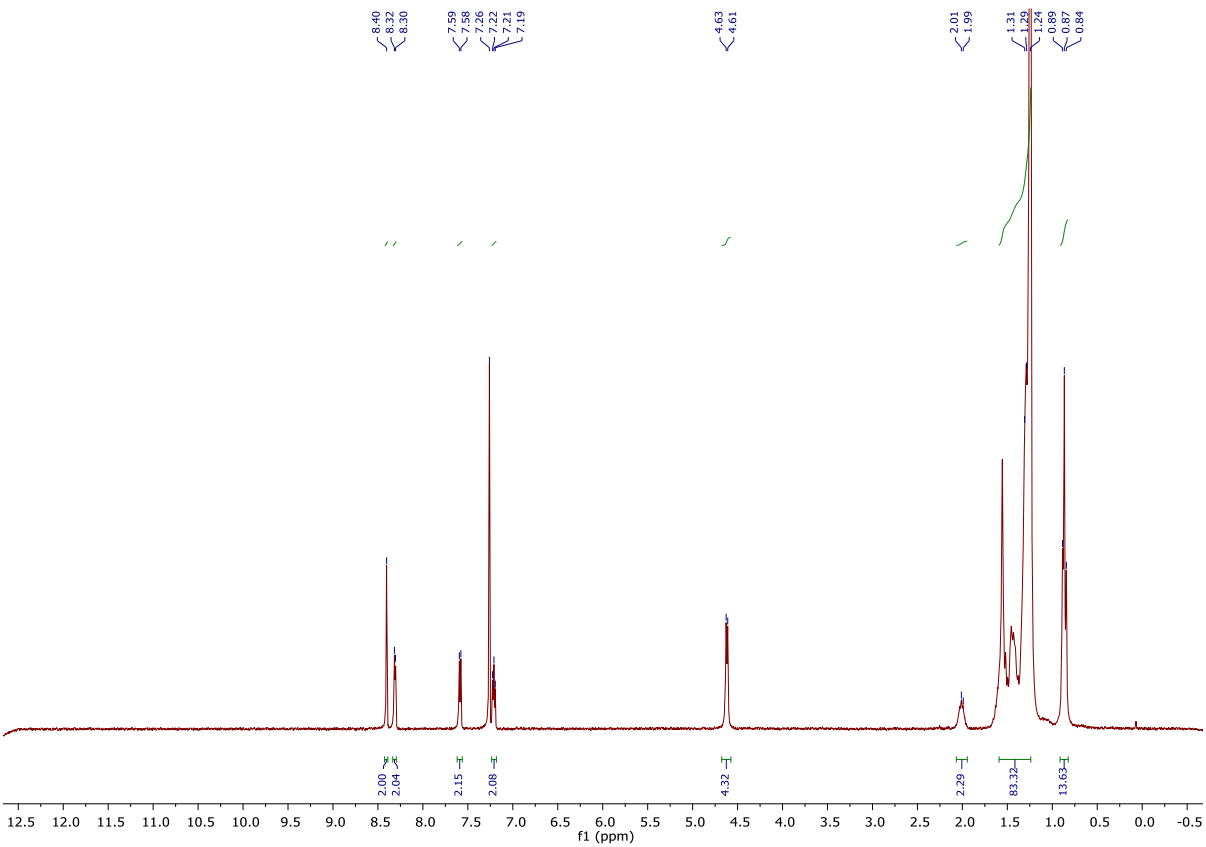

Figure B-3. 300 MHz ^{1}H NMR spectrum for 1,6-bis(2-decyltetradecyl)-3,8-di(thiophen-2-yl)-1,6-dihydropyrazino[2,3-*g*]quinoxaline-2,7-dione (**PQx2T-24**) in $CDCl_3$.

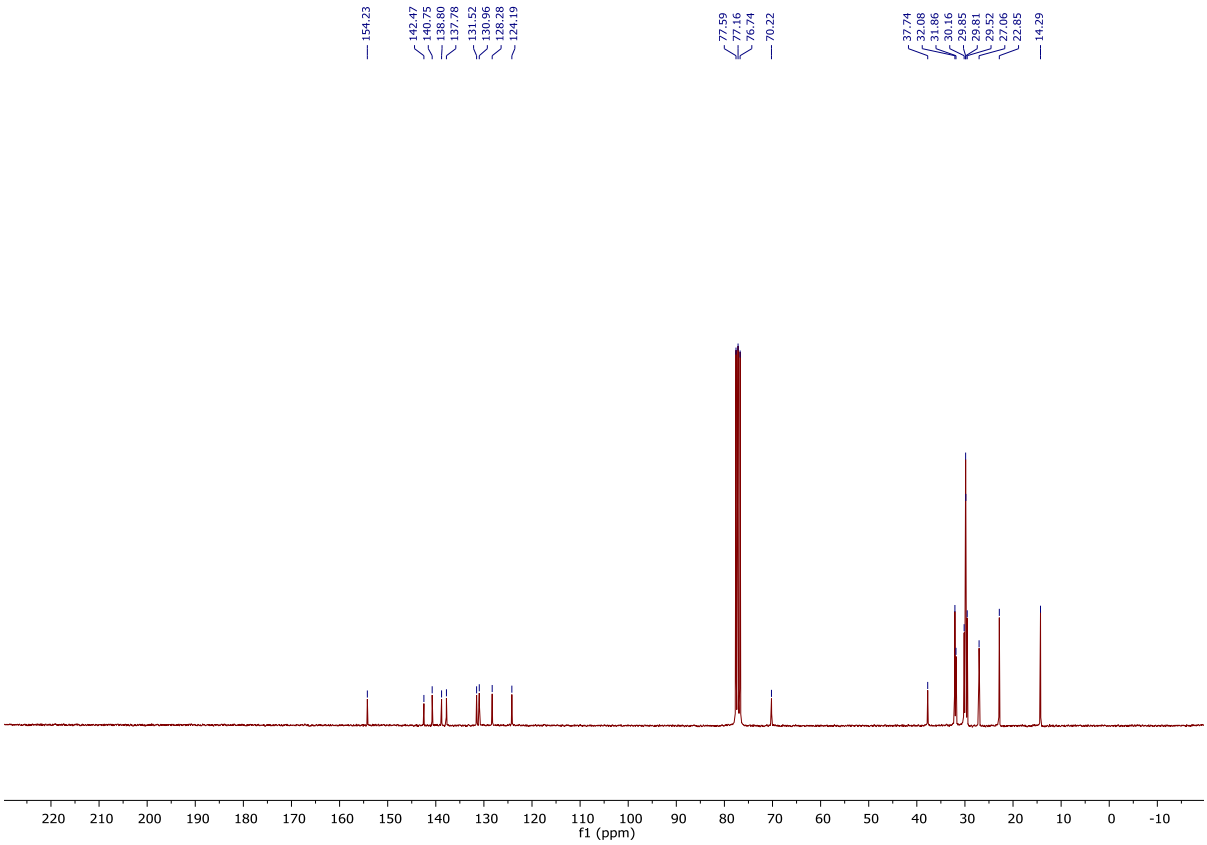

Figure B-4. 75 MHz ^{13}C NMR spectrum for 1,6-bis(2-decyltetradecyl)-3,8-di(thiophen-2-yl)-1,6-dihydropyrazino[2,3-*g*]quinoxaline-2,7-dione (**PQx2T-24**) in $CDCl_3$.

Synthesis of 3,8-bis(5-bromothiophen-2-yl)-1,6-bis(2-decyltetradecyl)-1,6-dihydropyrazino[2,3-*g*]quinoxaline-2,7-dione (PQx2T-Br-24)

A 100 mL two-neck round-bottom flask was charged with PQx2T-24 (0.18 g, 0.17 mmol) and chloroform (7 mL). The reaction mixture was cooled to 0 °C and *N*-bromosuccinimide (NBS) (0.064 g, 0.36 mmol) was added. The reaction mixture was gradually warmed to room temperature. After stirring overnight in the absence of light, the reaction mixture was washed with a sodium sulfite solution and water, and dried over sodium sulfate. Purification using column chromatography with a mixture of 20% dichloromethane in hexanes afforded an orange solid (0.13 g, 64%). ^{1}H-NMR (300 MHz, $CDCl_3$) δ 8.35 (s, 2H), 8.03 (d, J = 4.1 Hz, 2H), 7.16 (d, J = 4.1 Hz, 2H), 4.61 (d, J = 5.6 Hz, 4H), 2.00 (s, 32H), 1.65 – 1.17 (m, 80H), 0.87 (t, J = 6.2 Hz, 12H). ^{13}C-NMR (75 MHz, $CDCl_3$) δ 153.74, 142.26, 141.14, 138.43, 137.54, 131.84, 131.60, 124.12, 119.17, 70.34, 68.90, 37.68, 32.09, 31.85, 30.20, 29.88, 29.84,

29.53, 27.09, 22.85, 14.27. HRMS (ESI+) calculated for $C_{66}H_{104}Br_2N_4O_2S_2$ (M+H)+: 1207.5996 found 1207.6046.

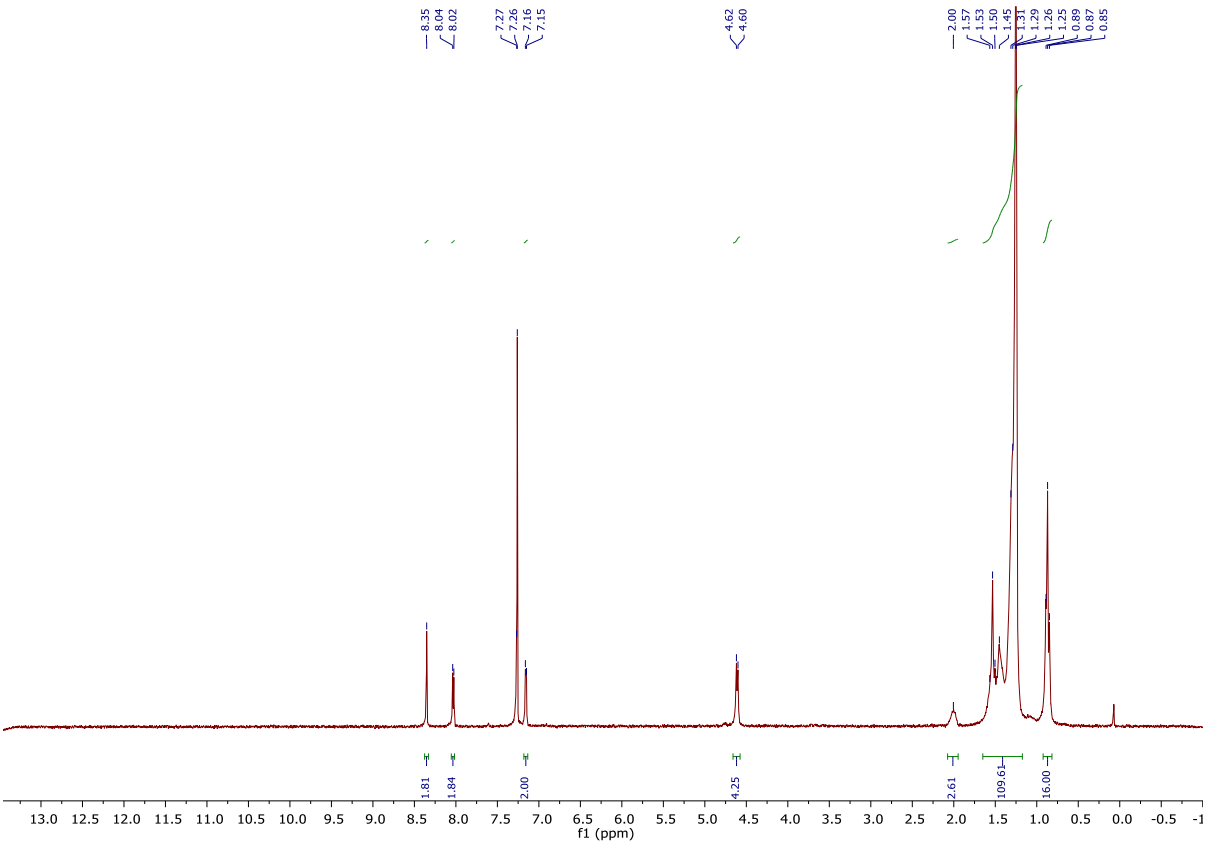

Figure B-5. 300 MHz ^{1}H NMR spectrum for 3,8-bis(5-bromothiophen-2-yl)-1,6-bis(2-decyltetradecyl)-1,6-dihydropyrazino[2,3-*g*]quinoxaline-2,7-dione (**PQx2T-Br-24**) in $CDCl_3$.

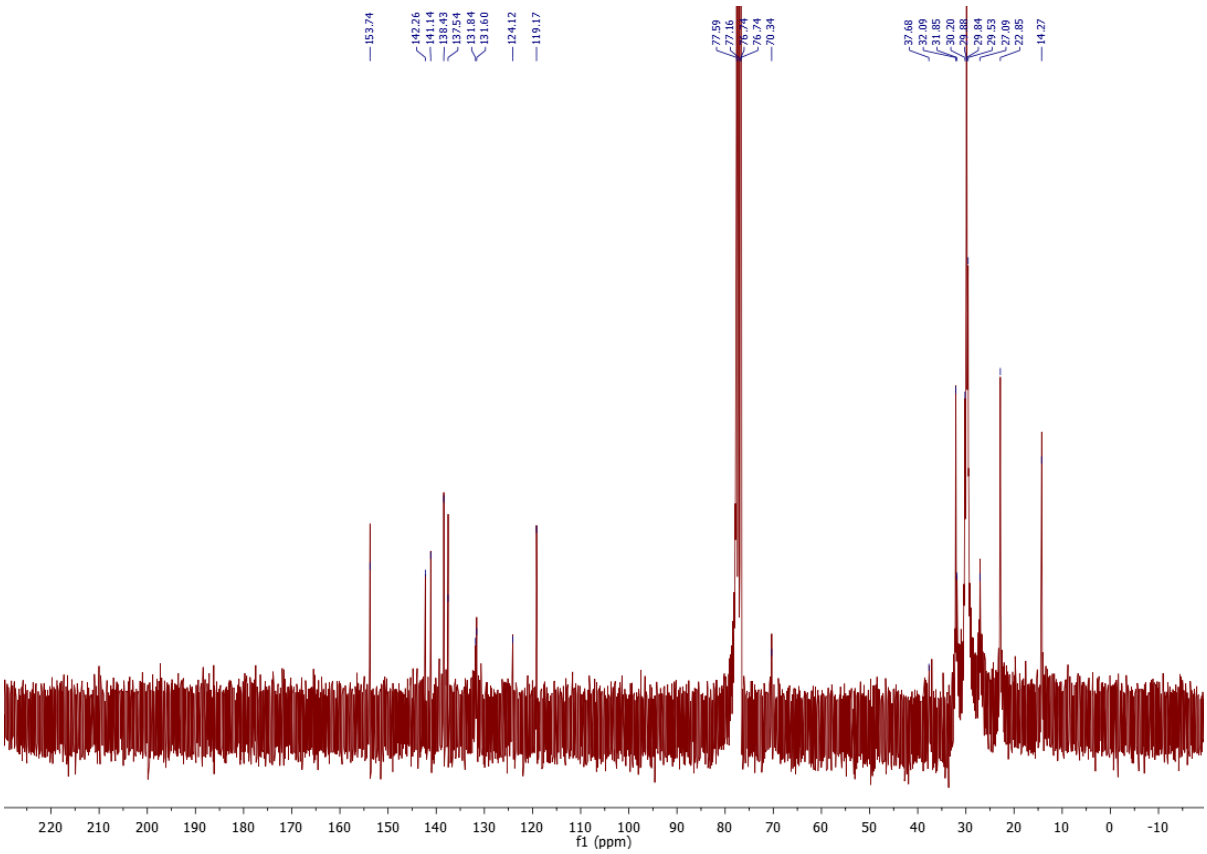

Figure B-6. 75 MHz ^{13}C NMR spectrum for 3,8-bis(5-bromothiophen-2-yl)-1,6-bis(2-decyltetradecyl)-1,6-dihydropyrazino[2,3-*g*]quinoxaline-2,7-dione (**PQx2T-Br-24**) in $CDCl_3$.

Synthesis of PPQx2T-BT-24

To a 25 mL Schlenk flask, PQx2T-Br-24 (101.3 mg, 0.084 mmol), 5,5'-bis(trimethylstannyl)-2,2'-bithiophene (41.3 mg, 0.084 mmol) and tri(*o*-tolyl)phosphine (P(*o*-tolyl)$_3$) (2.1 mg, 0.007 mmol) were charged. After degassing and refilling argon three times, chlorobenzene (3 mL) and tris(dibenzylideneacetone)-dipalladium ($Pd_2(dba)_3$) (1.5 mg, 0.002 mmol) were added. The reaction mixture was stirred at 130 °C for 72 h. Upon cooling to room temperature, the reaction mixture was poured into methanol (100 mL). The precipitate was collected by filtration and subject to Soxhlet extraction with acetone, hexanes, and chloroform successively. Upon removal of solvent *in vacuo*, the chloroform extract gave 70 mg (68%) of PPQx2T-BT-24. Further extraction with 1,1,2,2-tetrachloroethane dissolved the remaining polymer, which gave 22 mg (21%) of the less soluble fraction upon removal of solvent *in vacuo*. Only the chloroform-extracted fraction was used for characterization.

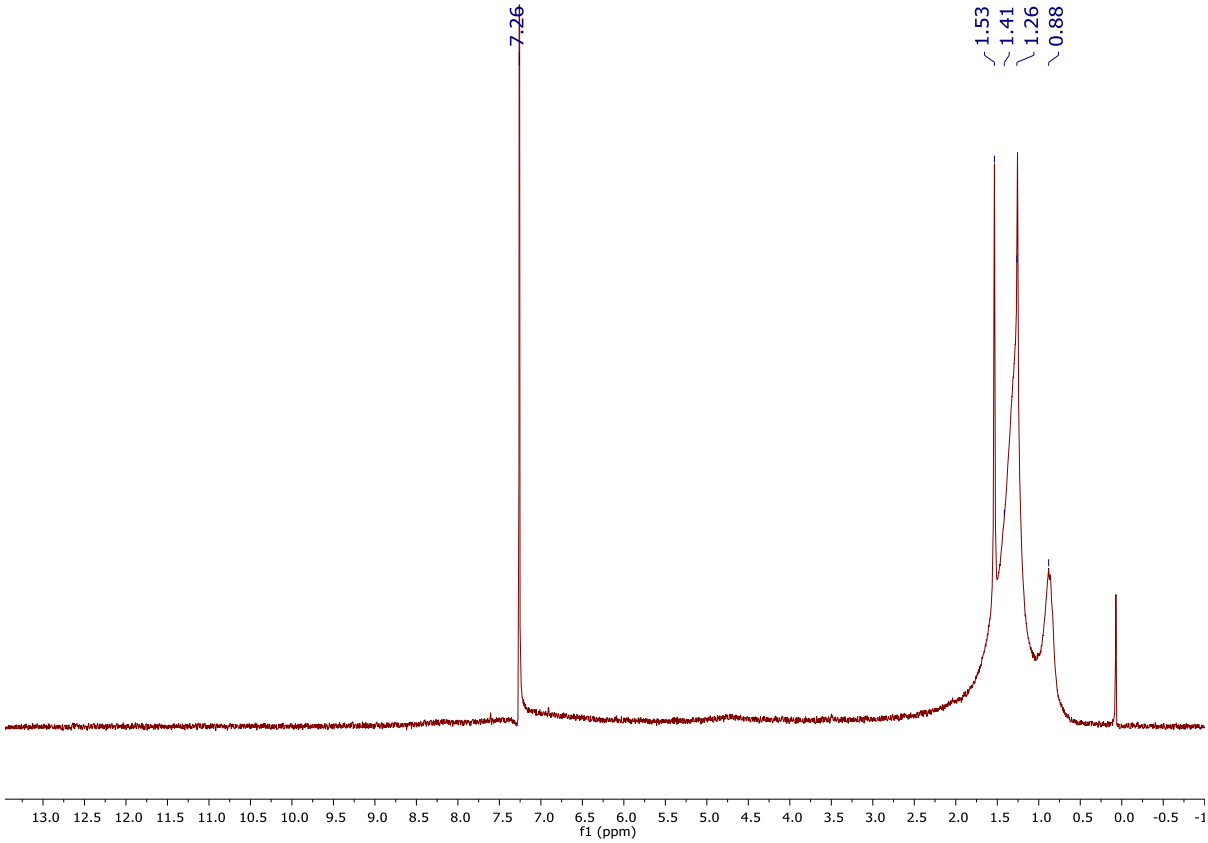

Figure B-7. 300 MHz ^{1}H NMR spectrum for **PPQx2T-BT-24** in $CDCl_3$.

Synthesis of PPQx2T-TT-24

To a 25 mL Schlenk flask, PQx2T-Br-24 (67.0 mg, 0.055 mmol), 2,5-bis(trimethylstannyl)-thieno[3,2-*b*]thiophene (25.6 mg, 0.084 mmol) and P(*o*-tolyl)$_3$ (1.3 mg, 0.004 mmol) were charged. After degassing and refilling argon three times, chlorobenzene (2 mL) and $Pd_2(dba)_3$ (1.0 mg, 0.001 mmol) were added. The reaction mixture was stirred at 130 °C for 72 h. Upon cooling to room temperature, the reaction mixture was poured into methanol (100 mL). The precipitate was collected by filtration and subjected to Soxhlet extraction with acetone, hexanes, and chloroform successively. Upon removal of solvent *in vacuo*, the chloroform extract gave PPQx2T-TT-24. Yield: 63 mg (97%).

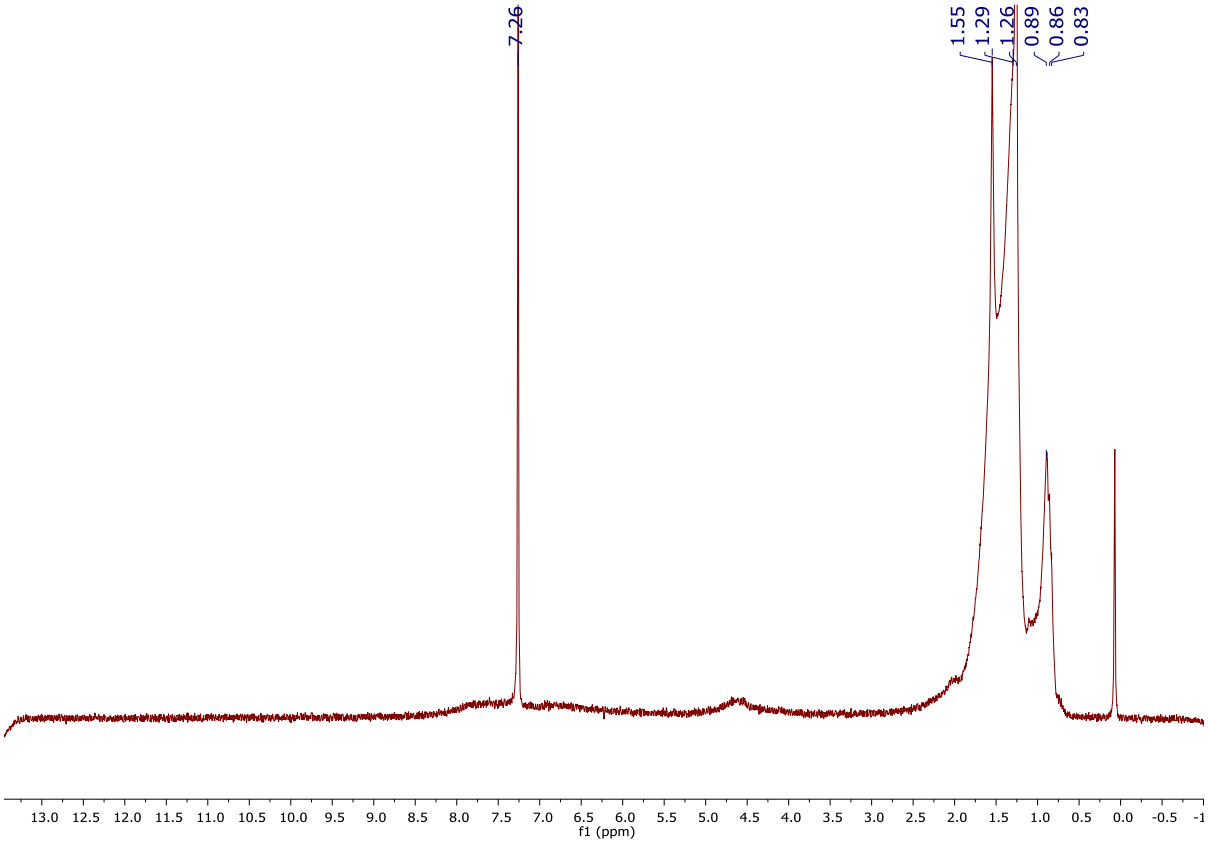

Figure B-8. 300 MHz ^{1}H NMR spectrum for **PPQx2T-TT-24** in $CDCl_3$.

Synthesis of Dimethyl 2,5-diaminocyclohexa-1,4-diene-1,4-dicarboxylate (1) [334]

A 250 mL three-neck flask equipped with condenser, Dean-Stark apparatus, and magnetic stir bar was charged with ammonium acetate (35.13 g, 455.7 mmol), dimethyl 2,5-dioxocyclohexane-1,4-dicarboxylate (5.20 g, 22.79 mmol), toluene (160 mL), and acetic acid (3 mL). The reaction mixture was heated to reflux under atmospheric oxygen (*i.e.* air) and left for 16 h. Once cooled to room temperature, ethyl acetate was added and the organic phase was washed with water three times. The organic phases were collected and dried with sodium sulfate and filtered. The organic phase was then condensed under vacuum and a white solid with an orange hue was collected (4.90 g, 95.0%). ^{1}H NMR (300 MHz; DMSO-d_6): δ 7.74 (br, 2H, NH_2), 6.88 (br, 2H, NH_2), 3.58 (s, 6H, CH_3), 3.03 (s, 4H, CH_2). MS (ESI+) [M+H, Na]+: 227, and 249.

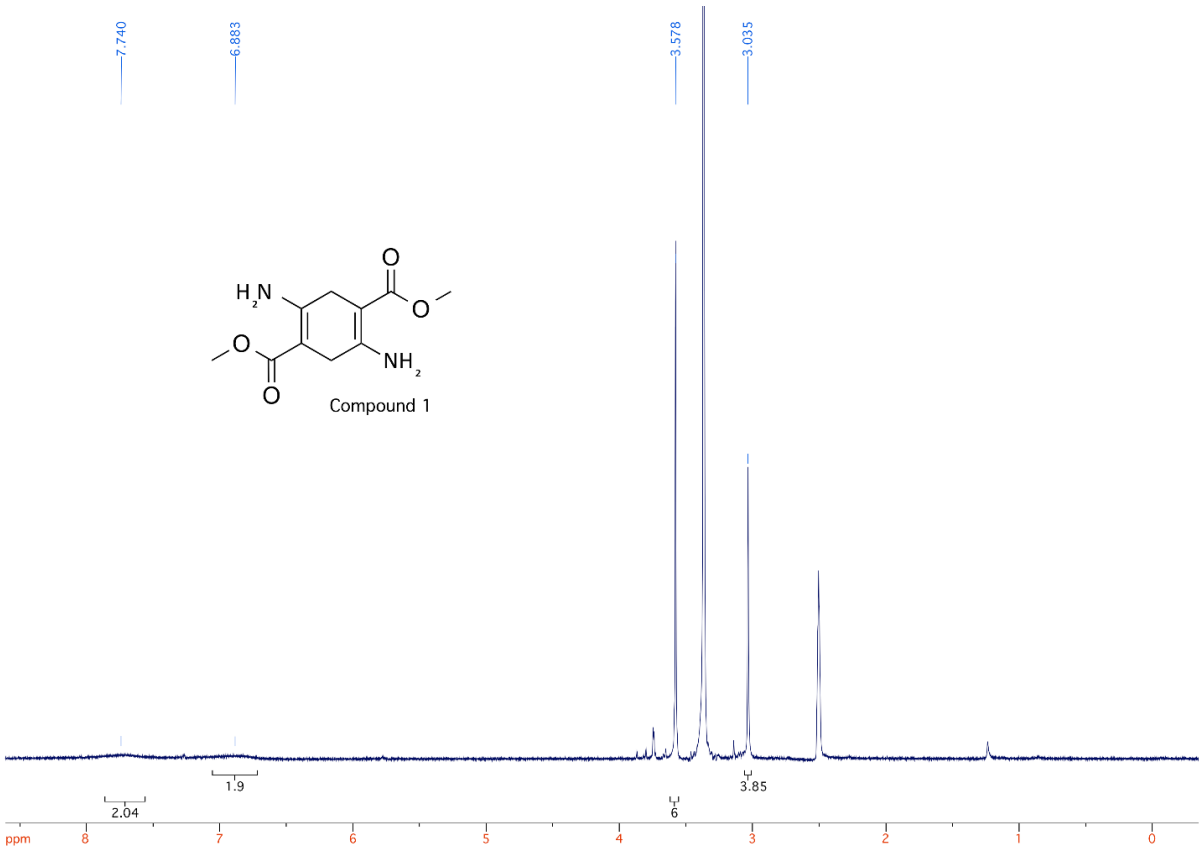

Figure B-9. 300 MHz ^{1}H NMR spectrum of dimethyl 2,5-diaminocyclohexa-1,4-diene-1,4-dicarboxylate (compound **1**) measured in DMSO-d_6.

Synthesis of Dimethyl 2,5-diaminoterephthalate (2)

This compound was prepared following a reported procedure with modification [335]. A 250 mL three-neck flask was charged with 1 (4.90 g, 21.66 mmol), sulfur (1.04 g, 32.49 mmol), and *n*-butanol (52 mL). The reaction mixture was then heated to gentle reflux and left for 2 h before additional sulfur (1.04 g, 32.49 mmol) was added. After 18 h the reaction mixture was cooled to room temperature and transferred to a beaker containing hexanes (400 mL). The mixture was stirred for 2 h and then filtered. The precipitate was then dispersed in hexanes, filtered and dried under vacuum at 50 °C. An orange solid was obtained (4.38 g, 90.1%). ^{1}H NMR (300 MHz; DMSO-d_6): δ 7.26 (s, 2H, ArH), 5.77 (s, 4H, NH_2), 3.79 (s, 6H, CH_3). MS (ESI+) [M+H]+: 225.

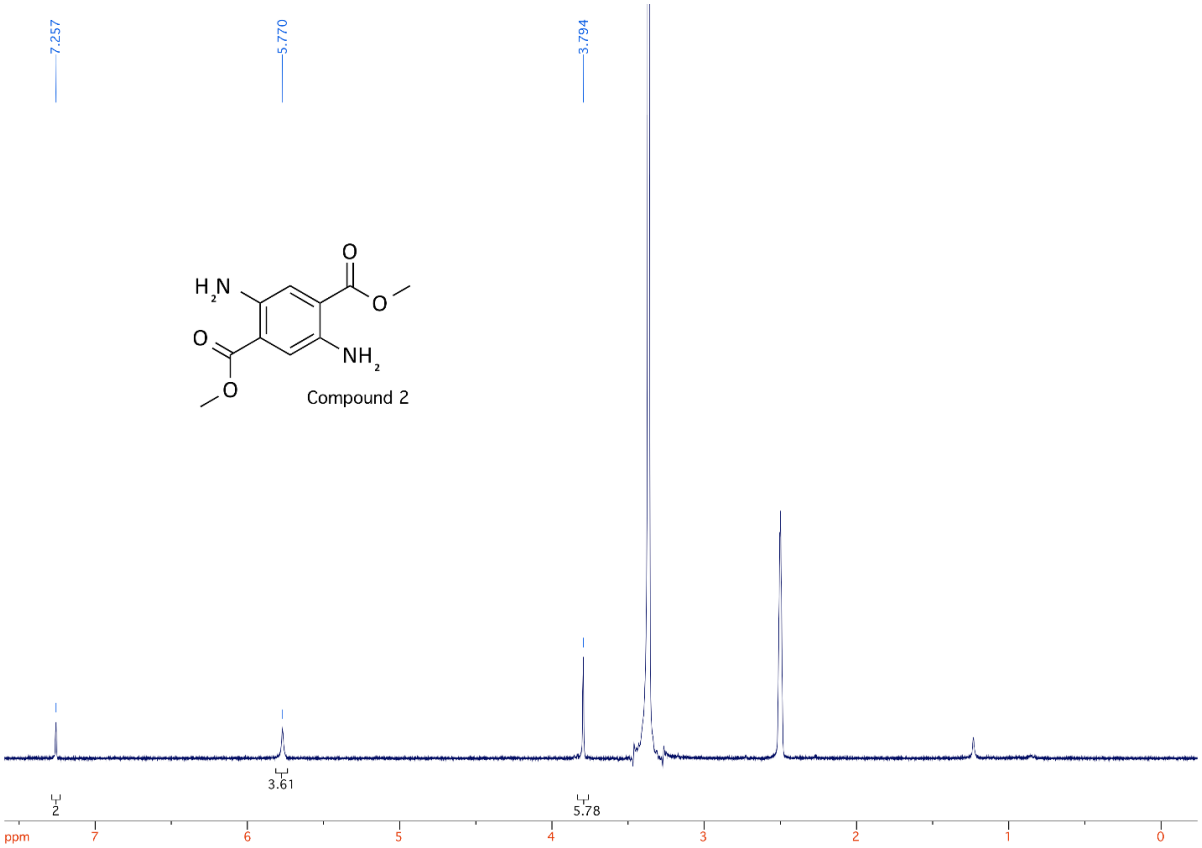

Figure B-10. 300 MHz ^{1}H NMR of dimethyl 2,5-diaminoterephthalate (compound **2**) measured in DMSO-d_6.

Synthesis of Dimethyl 2,5-bis(thiophene-2-carboxamido)terephthalate (3)

This compound was prepared following a reported procedure with modification [261]. A 250 mL two-neck flask was charged with 2 (1.77 g, 7.89 mmol), anhydrous dichloromethane (100 mL), and pyridine (80 mL). The reaction mixture was then cooled to 0 °C with an ice-water bath for 30 min. 2-Thiophenecarbonyl chloride (4.22 mL, 39.47 mmol) was drop-wise added to the reaction mixture. The reaction mixture was stirred at 0 °C for 1 h and at room temperature for 18 h, during which the reaction mixture turned from orange to yellow with a yellow precipitate. The resultant reaction mixture was washed with 2N HCl (*ca.* 600 mL) to remove the excess pyridine. The precipitate was filtered off and dried to give a bright yellow solid (2.78 g, 79.2%). ^{1}H NMR (300 MHz; DMSO-d_6): δ 11.21 (s, 2H, NH), 8.83 (s, 2H, ArH), 7.94 (d, J = 4.9 Hz, 2H, CH), 7.85 (d, J = 3.9 Hz, 2H, CH), 7.28 (t, J = 4.4 Hz, 2H, CH), 3.90 (s, 6H, CH_3). MS (ESI+) [M+H, NH4, Na, K]+: 445, 462, 467, and 483.

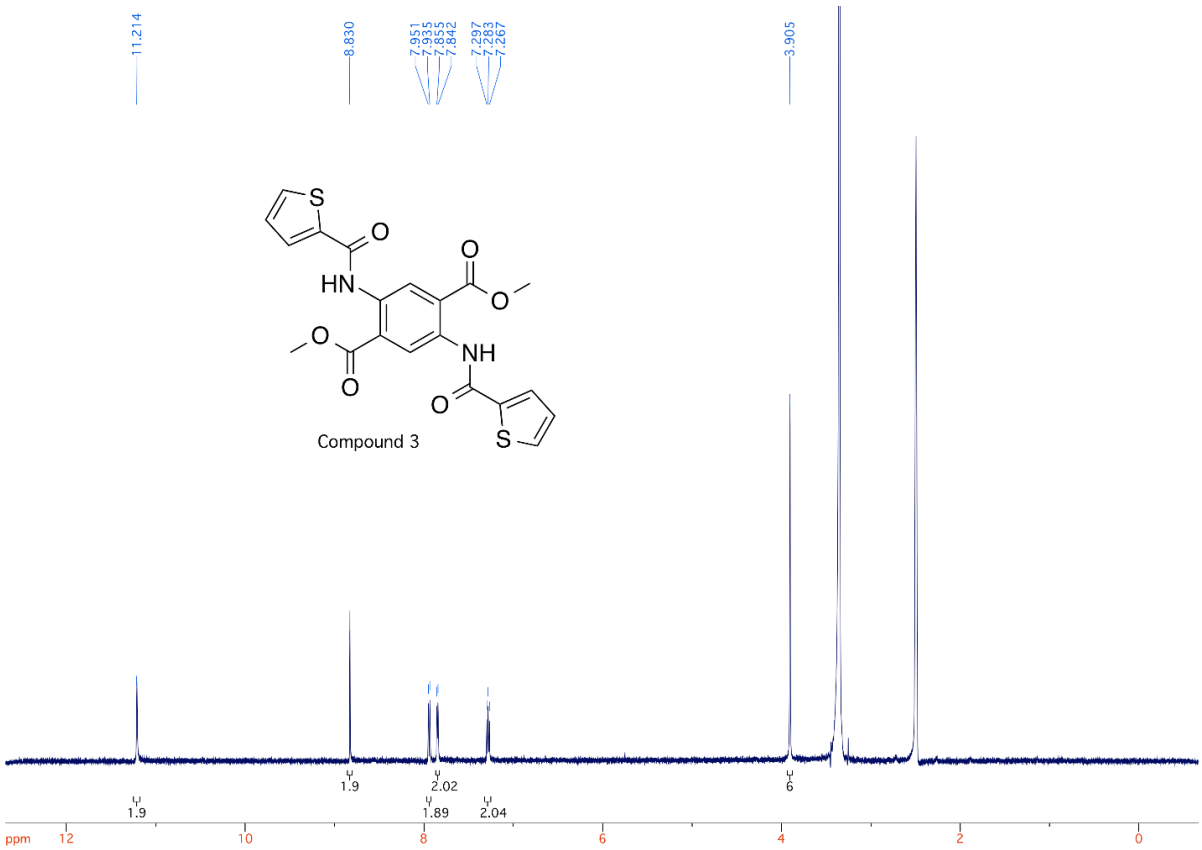

Figure B-11. 300 MHz ^{1}H NMR of dimethyl 2,5-bis(thiophene-2-carboxamido)terephthalate (compound **3**) measured in DMSO-d_6.

Synthesis of 2,5-Bis(thiophene-2-carboxamido)terephthalic acid (4) [262]

A 100 mL one-neck flask was charged with **3** (1.20 g, 2.69 mmol), ethanol (20 mL), and 1M lithium hydroxide (20 mL). The reaction mixture was heated to 60 °C and allowed to stir for 3 h. After cooling to room temperature, 5% HCl was added slowly to neutralize the excess lithium hydroxide. The precipitate was filtered off and dried to give a bright yellow solid (0.959 g, 85.5%). ^{1}H NMR (300 MHz; DMSO-d_6): δ 11.85 (s, 2H, NH), 9.15 (s, 2H, ArH), 7.94 (d, J = 4.9 Hz, 2H, CH), 7.77 (d, J = 3.7 Hz, 2H, CH), 7.28 (t, J = 4.4 Hz, 2H, CH). MS (ESI+) [M+H]+: 417.

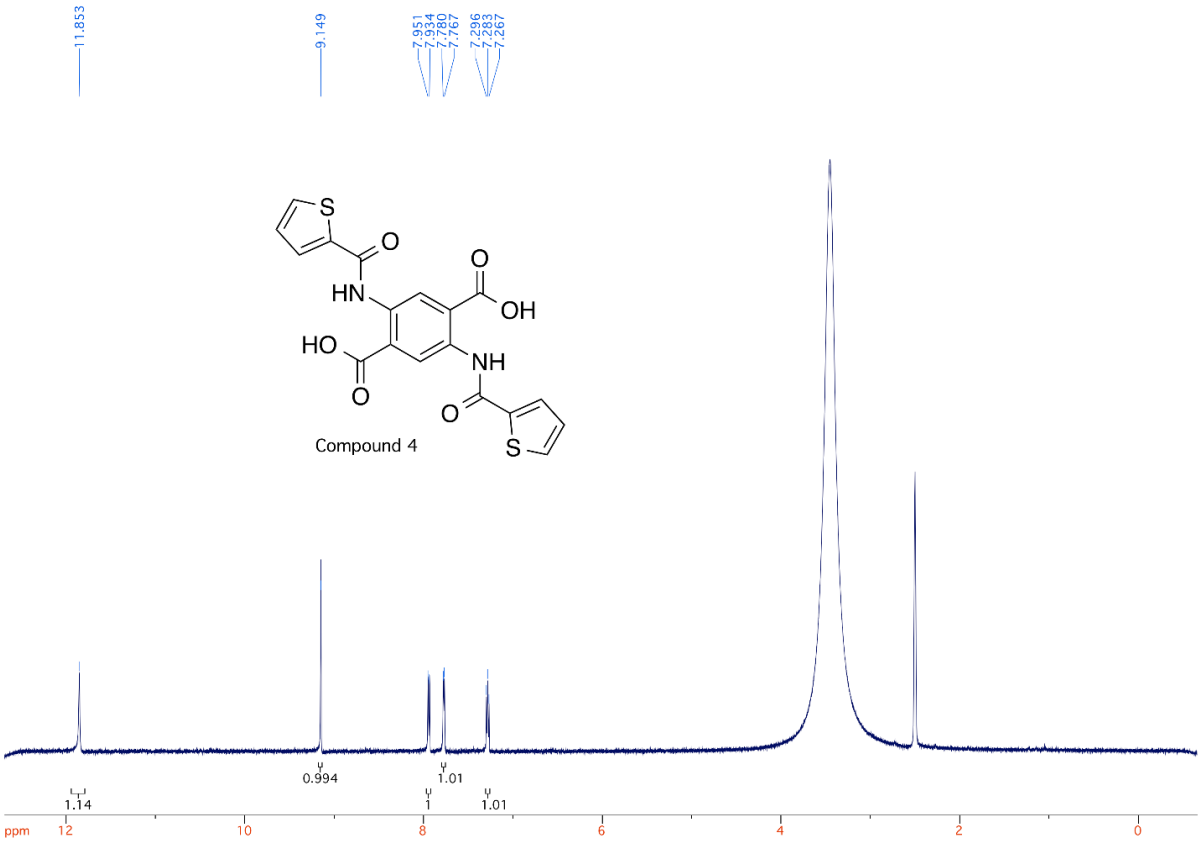

Figure B-12. 300 MHz ^{1}H NMR of 2,5-bis(thiophene-2-carboxamido)terephthalic acid (compound **4**) measured in DMSO-d_6.

Synthesis of 2,7-Di(thiophen-2-yl)benzo[1,2-d:4,5-d']bis([1,3]oxazine)-4,9-dione (5) [336]

Compound **4** (0.92 g, 2.22 mmol) was placed into a 100 mL round bottom flask. Acetic anhydride (12 mL) was added under stirring under argon protection. The mixture was gradually heated to 140 °C and maintained for 3 h. The reaction mixture gradually turned from pale yellow to bright yellow. Upon cooling, the reaction mixture was filtered and washed with water and acetone. The precipitate was dispersed in water, filtered, and then dried at 50 °C under vacuum to give a yellow solid (0.654 g, 77.5%). ^{1}H NMR (300 MHz; DMSO-d_6): δ 8.18 (s, 2H, ArH), 8.05 (d, J = 4.5 Hz, 2H, CH), 8.00 (d, J = 3.1 Hz, 2H, CH), 7.32 (t, J = 4.2 Hz, 2H, CH). MS (EI+) M+: 380.

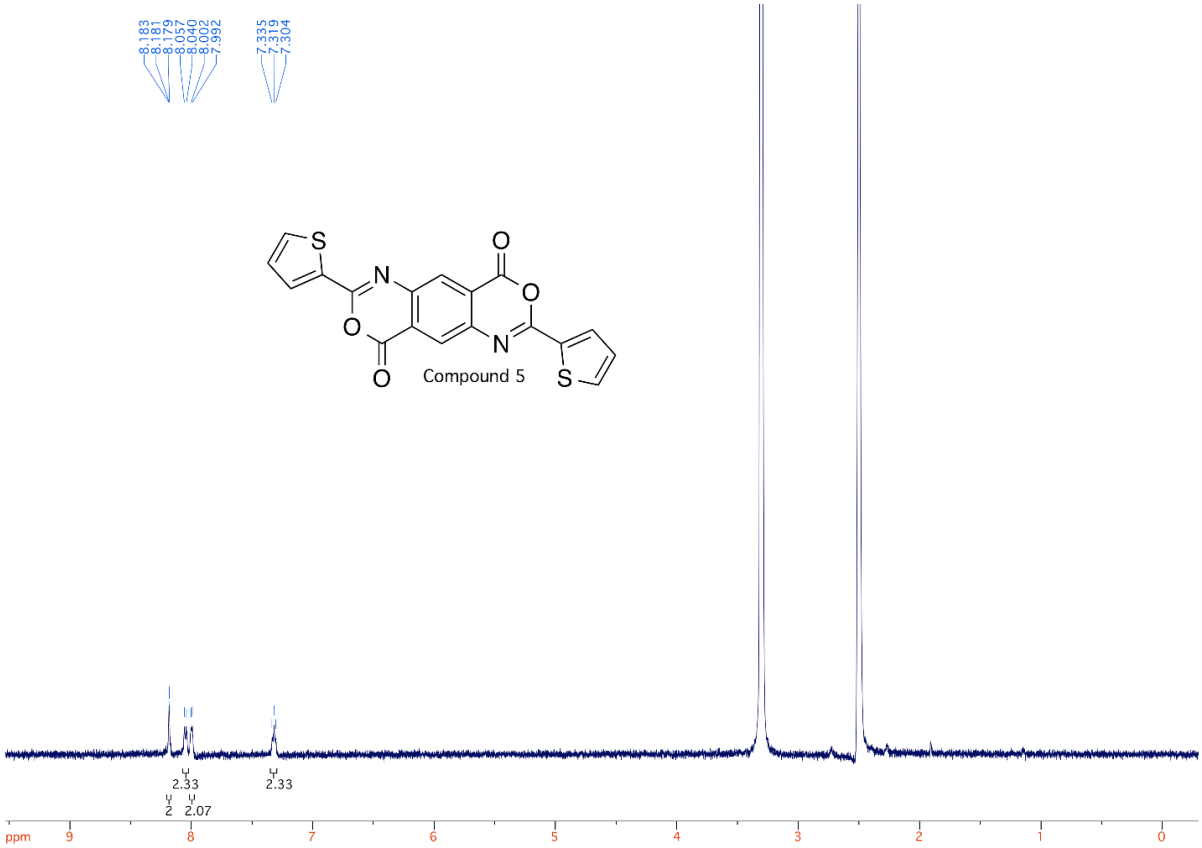

Figure B-13. 300 MHz ^{1}H NMR of 2,7-di(thiophen-2-yl)benzo[1,2-*d*:4,5-*d*']bis([1,3]oxazine)-4,9-dione (compound **5**) measured in DMSO-d_6.

Synthesis of 2,7-Di(thiophen-2-yl)pyrimido[4,5-*g*]quinazoline-4,9(3*H*,8*H*)-dione (6)

This compound was prepared following a reported procedure with modification [337]. A mixture of **5** (0.619 g, 1.630 mmol) and ammonium acetate (25.09 g, 0.325 mol) was heated at 170 °C under stirring for 1 h under argon. The resultant solution was cooled to room temperature and filtered. A pale-yellow solid was collected and dried. The solid was then placed into a 100 mL flask containing 30% sodium hydroxide solution (10 mL) and ethanol (30 mL) and refluxed for 1 h. After cooling to room temperature, the reaction mixture was diluted with water and glacial acetic acid was slowly added until a pH of 7 was obtained. The mixture was then filtered to give a yellow-brown solid (0.586 g, 95.0%). ^{1}H NMR (300 MHz; DMSO-d_6): δ 8.24 (s, 2H, ArH), 8.22 (d, J = 3.3 Hz, 2H, CH), 7.87 (d, J = 5.3 Hz, 2H, CH), 7.24 (t, J = 4.6 Hz, 2H, CH). HRMS (ESI+) calculated for $C_{18}H_{10}N_4O_2S_2$ (M+): 378.0245 found 378.0241.

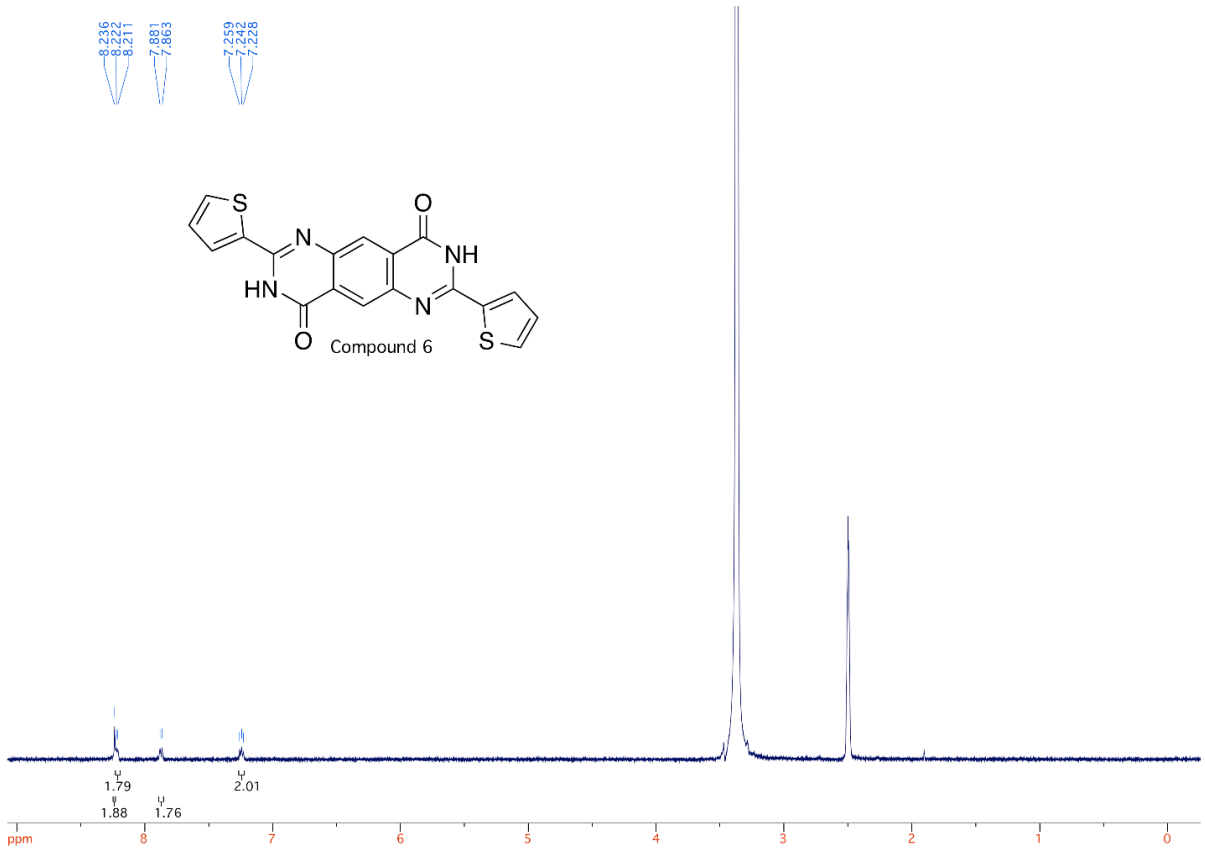

Figure B-14. 300 MHz ^{1}H NMR of 2,7-di(thiophen-2-yl)pyrimido[4,5-*g*]quinazoline-4,9(3*H*,8*H*)-dione (compound **6**) measured in DMSO-d_6.

Synthesis of 3,8-Bis(2-decyltetradecyl)-2,7-di(thiophen-2-yl)-3,8-dihydropyrimido[4,5-*g*]quinazoline-4,9-dione (7)

A 100 mL two-neck round bottom flask was charged with **6** (0.104 g, 0.274 mmol) and potassium carbonate (0.113 g, 0.821 mmol) and purged with argon. *N*,*N*-Dimethylformamide (6 mL) was added and the reaction mixture was heated to 130 °C and stirred for 1 h before 11-(bromomethyl)tricosane (0.343 g, 0.821 mmol) was added. The reaction mixture was stirred at the same temperature for an additional 16 h. After cooling, the reaction mixture was extracted with dichloromethane and the organic phase was washed with water. The combined organic phases were dried and the solvent was removed. The residue was purified by column chromatography using 33% dichloromethane in hexanes to give a yellow liquid, which was treated with isopropanol three times to afford a yellow solid (0.211 g, 73.2%). ^{1}H NMR (300 MHz; $CDCl_3$): δ 8.71 (s, 2H, ArH), 8.14 (d, J = 3.8 Hz, 2H, CH), 7.53 (d, J = 4.1 Hz, 2H, CH), 7.19 (t, J = 4.4 Hz, 2H, CH), 4.65 (d, J = 5.5 Hz, 4H, CH2), 1.99 (br, 2H, CH), 1.54-1.18 (m,

80H, CH_2), 0.86 (m, 12H, CH_3). ^{13}C-NMR (75 MHz; $CDCl_3$): δ 167.49 (C=N), 156.95 (C=O), 147.68 (quat-C), 144.34 (quat-C), 130.50 (=CH), 129.88 (=CH), 128.56 (=CH), 123.06 (quat-C), 120.39 (=CH), 70.68 (CH_2), 38.02 (CH), 32.30 (CH_2), 31.82 (CH_2), 30.39 (CH_2), 30.06 (CH_2), 30.04 (CH_2), 29.74 (CH_2), 27.34 (CH_2), 23.06 (CH_2), 14.50 (CH_3). MS (ESI+) [M+H]+: 1051.

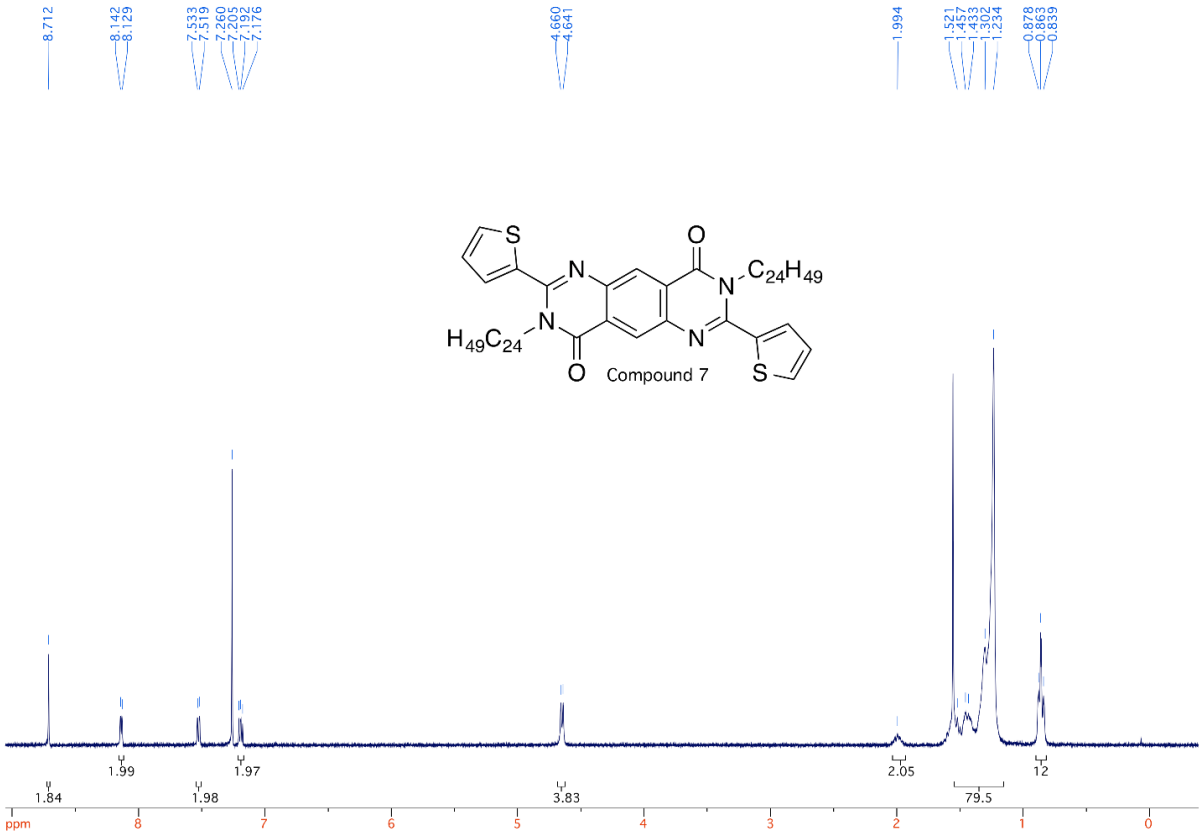

Figure B-15. 300 MHz ^{1}H NMR of 3,8-dis(2-decyltetradecyl)-2,7-di(thiophen-2-yl)-3,8-dihydropyrimido[4,5-*g*]quinazoline-4,9-dione (compound **7**) measured in $CDCl_3$.

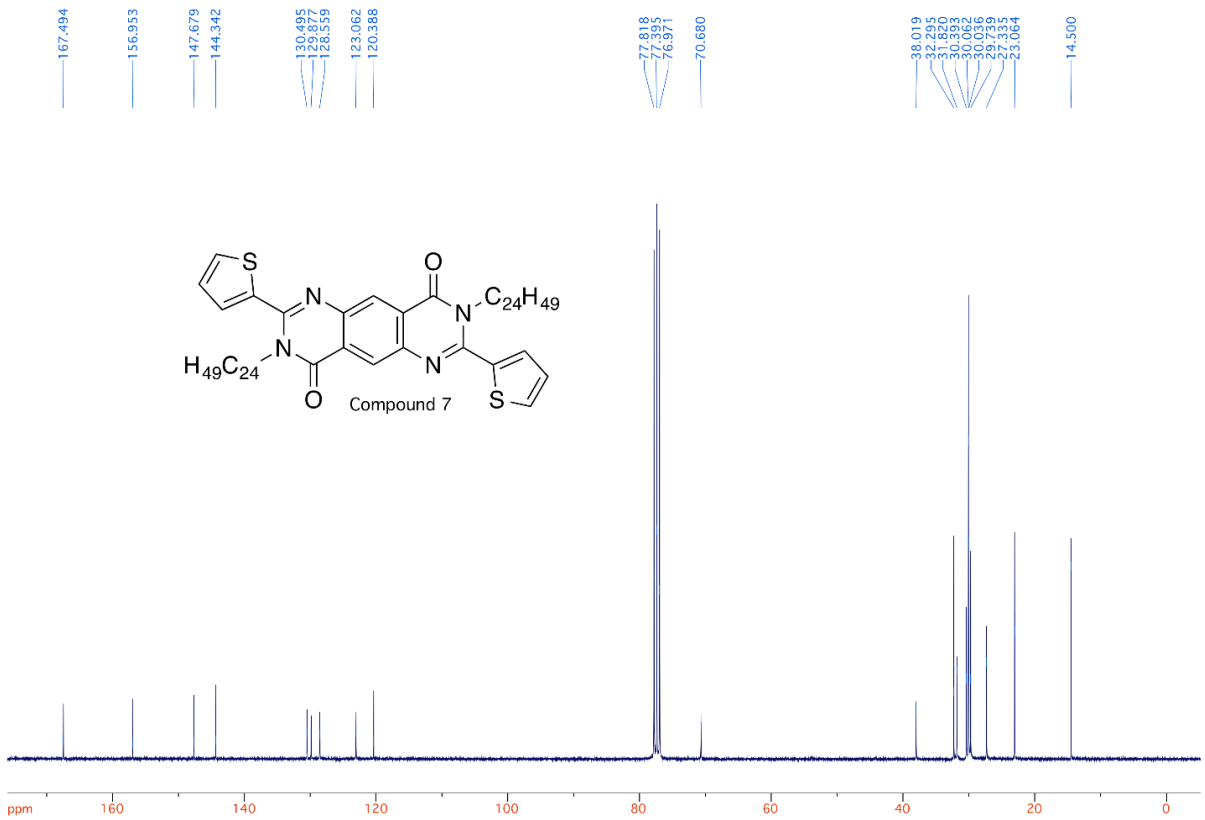

Figure B-16. 75 MHz ^{13}C NMR of 3,8-bis(2-decyltetradecyl)-2,7-di(thiophen-2-yl)-3,8-dihydropyrimido[4,5-*g*]quinazoline-4,9-dione (compound **7**) measured in $CDCl_3$.

Synthesis of 2,7-Bis(5-bromothiophen-2-yl)-3,8-bis(2-decyltetradecyl)-3,8-dihydropyrimido[4,5-*g*]quinazoline-4,9-dione (8)

A 50 mL two-neck flask was charged with **7** (0.210 g, 0.199 mmol), and chloroform (3 mL). The reaction mixture was cooled to 0 °C and *N*-bromosuccinimide (0.094 g, 0.528 mmol) was added. The reaction mixture was gradually warmed to room temperature and left overnight in the absence of light. A catalytic amount of bromine may be used to accelerate bromination. The reaction mixture was washed with a sodium sulfite solution and water, and then dried over sodium sulfate. Purification using column chromatography with a mixture of 2% ethyl acetate in hexanes afforded a brown solid (0.181 g, 75.2%). ^1H NMR (300 MHz; $CDCl_3$): δ 8.66 (s, 2H, ArH), 7.87 (d, J = 4.3 Hz, 2H, CH), 7.15 (d, J = 4.0 Hz, 2H, CH), 4.62 (d, J = 5.7 Hz, 4H, CH_2), 1.99 (br, 2H, CH), 1.43-1.23 (m, 80H, CH_2), 0.84 (m, 12H, CH_3). ^{13}C -NMR (75 MHz; $CDCl_3$): δ 167.24 (C=N), 155.67 (C=O), 147.29 (quat-C), 145.26 (quat-C), 131.40 (=CH), 129.50 (=CH), 122.83 (quat-C), 120.18 (=CH), 117.77 (C-Br), 70.65 (CH_2),

37.76 (CH), 32.08 (CH_2), 31.61 (CH_2), 30.17 (CH_2), 29.85 (CH_2), 29.82 (CH_2), 29.52 (CH_2), 27.12 (CH_2), 27.04 (CH_2), 22.85 (CH_2), 14.28 (CH_3). HRMS (ESI+) calculated for $C_{66}H_{104}Br_2N_4O_2S_2$ (M+H)+: 1207.6046 found 1207.6028.

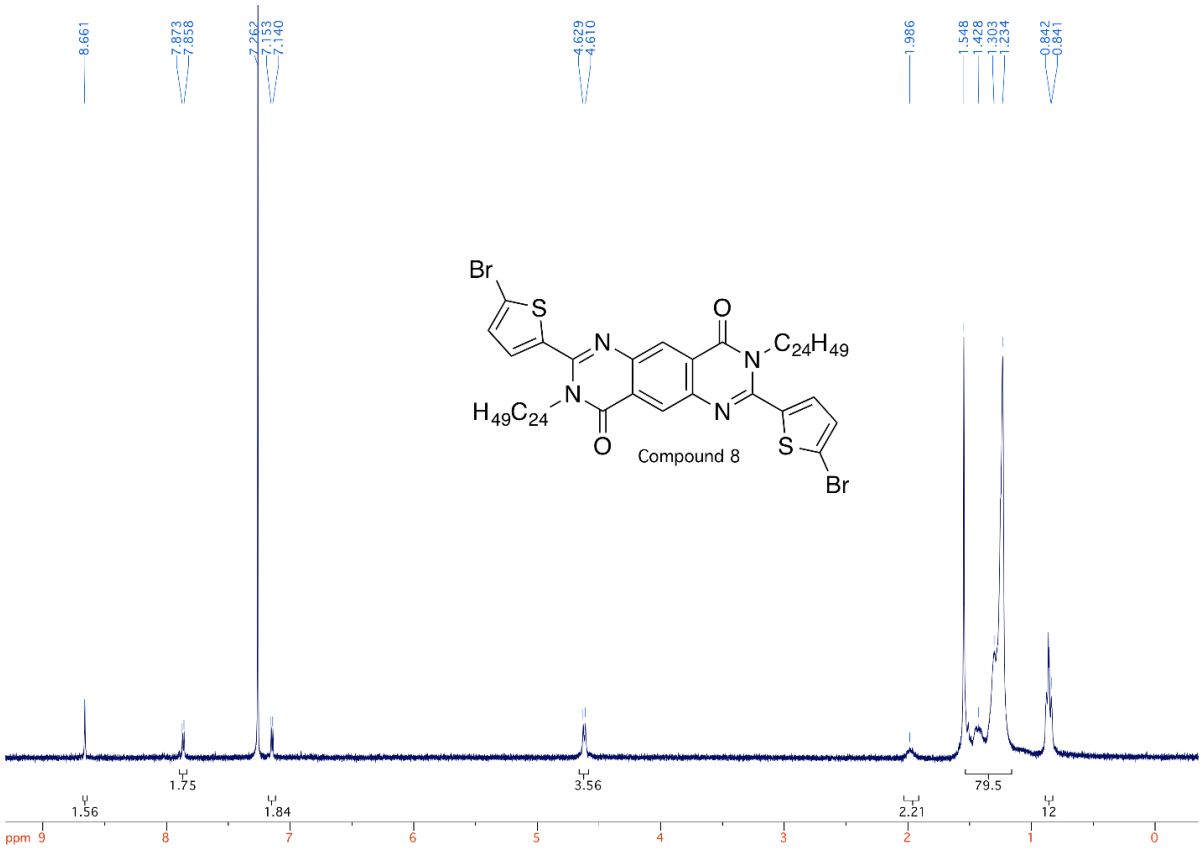

Figure B-17. 300 MHz ^{1}H NMR of 2,7-bis(5-bromothiophen-2-yl)-3,8-bis(2-decyltetradecyl)-3,8-dihydropyrimido[4,5-*g*]quinazoline-4,9-dione (compound **8**) measured in $CDCl_3$.

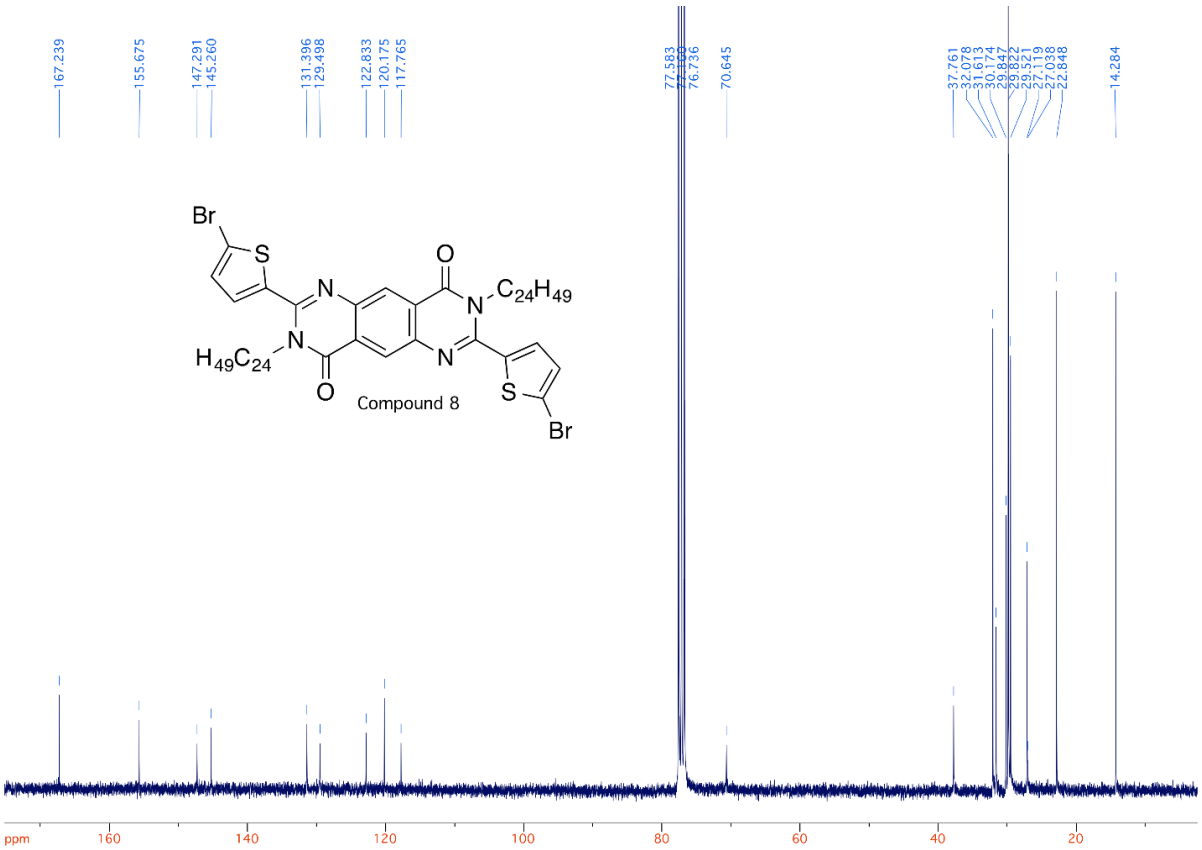

Figure B-18. 75 MHz ^{13}C NMR of 2,7-bis(5-bromothiophen-2-yl)-3,8-bis(2-decyltetradecyl)-3,8-dihydropyrimido[4,5-*g*]quinazoline-4,9-dione (compound **8**) measured in $CDCl_3$.

Synthesis of 3,8-bis(4-octadecyldocosyl)-2,7-di(thiophen-2-yl)-3,8-dihydropyrimido[4,5-g]quinazoline-4,9-dione (PQ2T-40)

A 100 mL two-neck round-bottom flask was charged with **6** (0.11 g, 0.29 mmol) and potassium carbonate (0.12 g, 0.88 mmol) and purged with argon. *N*,*N*-Dimethylformamide (DMF) (6 mL) was added and the reaction mixture was heated to 130 °C and stirred for 1 h before 19-(3-iodopropyl)heptatriacontane (0.60 g, 0.88 mmol) was added. The reaction mixture was stirred at the same temperature for an additional 16 h. After cooling, the reaction mixture was extracted with chloroform and the separated organic phase was washed with water. The combined organic phases were dried and the solvent was removed. The residue was purified by column chromatography using 33% chloroform in hexanes to give a yellow liquid, which was treated with isopropanol three times to afford a yellow solid (0.29 g, 66%). 1H-NMR (300 MHz, CDCl3) δ 8.78 (br, 2H), 8.18 (br, 2H), 7.54 (d, J =

5.1 Hz, 2H), 7.20 (t, J = 4.5 Hz, 2H), 4.72 (t, J = 6.7 Hz, 4H), 1.95 (d, J = 7.8 Hz, 4H), 1.59 – 1.20 (m, 142 H), 0.87 (t, J = 6.5 Hz, 12H). 13C-NMR (75 MHz, CDCl3) δ 167.06, 156.62, 147.43, 144.21, 130.19, 129.54, 128.27, 122.84, 120.08, 68.41, 37.38, 33.78, 32.10, 30.33, 30.07, 29.92, 29.88, 29.53, 26.90, 26.08, 22.86, 14.28. MS (ESI+) [M+H]+: 1500.7.

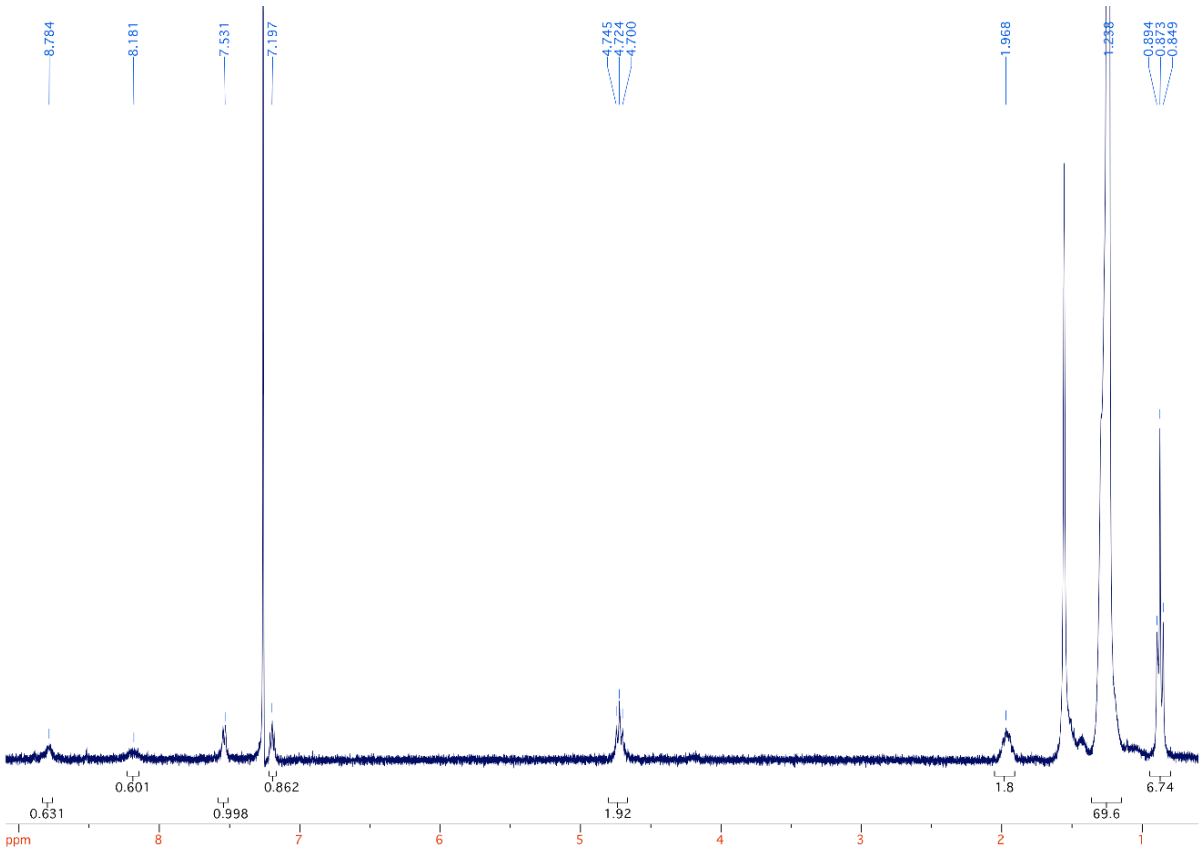

Figure B-19. 300 MHz ^{1}H NMR spectrum for 3,8-bis(4-octadecyldocosyl)-2,7-di(thiophen-2-yl)-3,8-dihydropyrimido[4,5-*g*]quinazoline-4,9-dione (**PQ2T-40**) in $CDCl_3$.

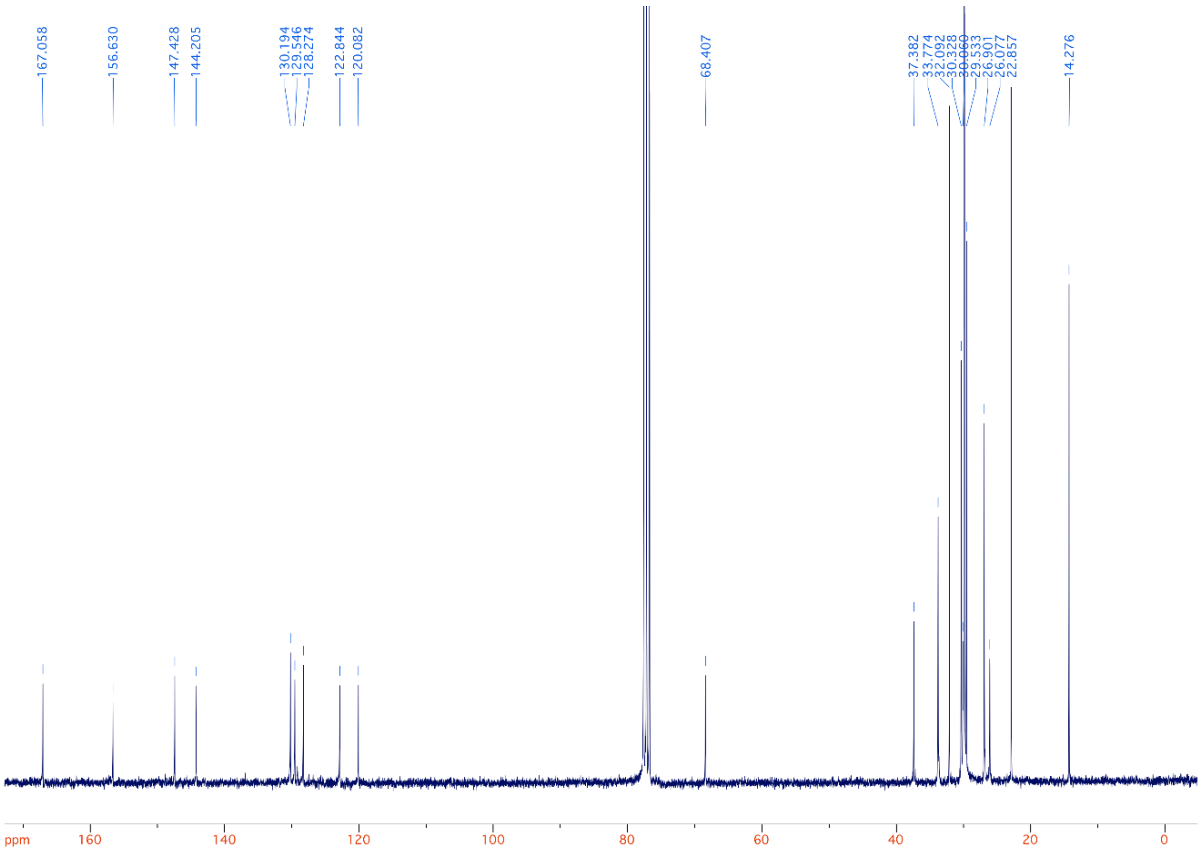

Figure B-20. 75 MHz ^{13}C NMR spectrum for 3,8-bis(4-octadecyldocosyl)-2,7-di(thiophen-2-yl)-3,8-dihydropyrimido[4,5-*g*]quinazoline-4,9-dione (**PQ2T-40**) in $CDCl_3$.

Synthesis of 2,7-bis(5-bromothiophen-2-yl)-3,8-bis(4-octadecyldocosyl)-3,8-dihydropyrimido[4,5-g]quinazoline-4,9-dione (PQ2T-Br-40)

A 100 mL two-neck round-bottom flask was charged with **PQ2T-40** (0.23 g, 0.16 mmol) and chloroform (14 mL). The reaction mixture was cooled to 0 °C and *N*-bromosuccinimide (NBS) (0.072 g, 0.41 mmol) was added. The reaction mixture was gradually warmed to room temperature and a catalytic amount of bromine was used to accelerate bromination. After stirring overnight in the absence of light, the reaction mixture was washed with a sodium sulfite solution and water, and then dried over sodium sulfate. Purification using column chromatography with a mixture of 25% dichloromethane in hexanes afforded a brown solid (0.21 g, 80%). 1H-NMR (300 MHz, CDCl3) δ 8.72 (s, 2H), 7.92 (br, 2H), 7.14 (d, J = 4.0 Hz, 2H), 4.69 (t, J = 6.7 Hz, 4H), 1.96 (d, J = 8.9 Hz, 4H), 1.70 – 0.97 (m, 142H), 0.88 (t, J = 6.2 Hz, 12H). 13C-NMR (75 MHz, CDCl3) δ 166.99, 155.56, 147.21, 145.32, 131.36,

129.42, 122.82, 120.03, 117.72, 68.54, 37.33, 33.74, 32.10, 30.33, 29.90, 29.54, 26.89, 25.99, 22.86, 14.29. HRMS (ESI+) calculated for C98H168Br2N4O2S2 (M+H)+: 1656.1054 found 1656.1036.

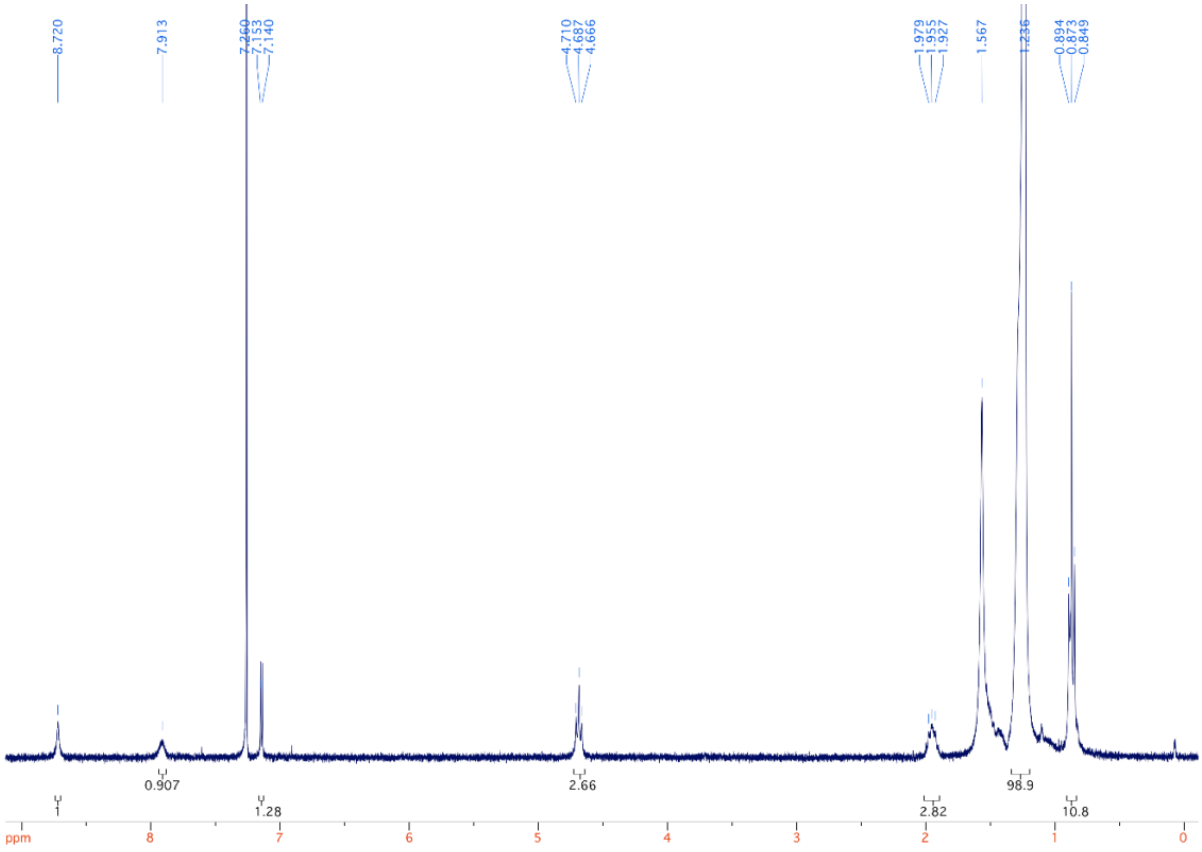

Figure B-21. 300 MHz ^{1}H NMR spectrum for 2,7-bis(5-bromothiophen-2-yl)-3,8-bis(4-octadecyldocosyl)-3,8-dihydropyrimido[4,5-*g*]quinazoline-4,9-dione (**PQ2T-Br-40**) in $CDCl_3$.

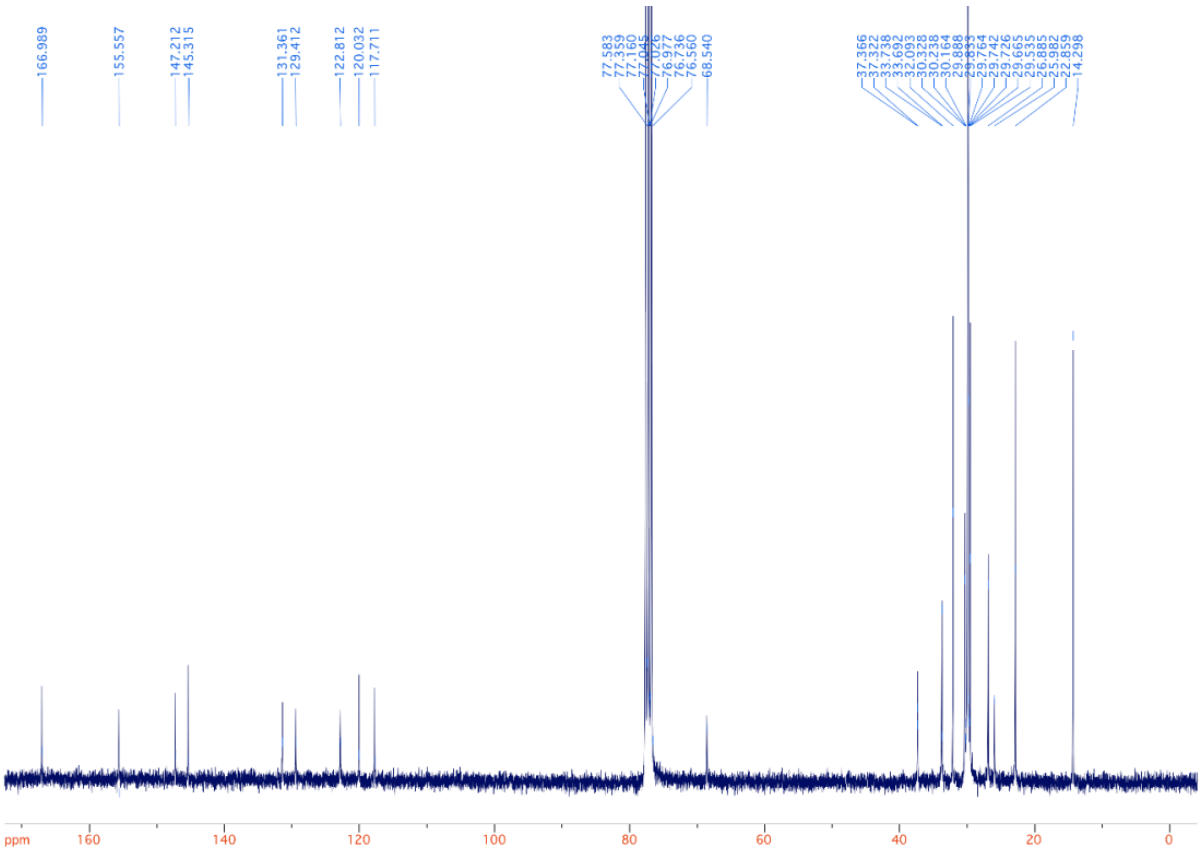

Figure B-22. 75 MHz ^{13}C NMR spectrum for 2,7-bis(5-bromothiophen-2-yl)-3,8-bis(4-octadecyldocosyl)-3,8-dihydropyrimido[4,5-*g*]quinazoline-4,9-dione (**PQ2T-Br-40**) in $CDCl_3$.

Synthesis of PPQ2T-BT-24

To a 25 mL Schlenk flask, **PQ2T-Br-24** (110.0 mg, 0.091 mmol), 5,5'-bis(trimethylstannyl)-2,2'-bithiophene (44.7 mg, 0.091 mmol) and tri(*o*-tolyl)phosphine (P(*o*-tolyl)$_3$) (2.2 mg, 0.007 mmol) were charged. After degassing and refilling argon three times, chlorobenzene (3 mL) and tris(dibenzylideneacetone)-dipalladium ($Pd_2(dba)_3$) (1.7 mg, 0.002 mmol) were added. The reaction mixture was stirred at 130 °C for 72 h. Upon cooling to room temperature, the reaction mixture was poured into methanol (100 mL). The precipitate was collected by filtration and subjected to Soxhlet extraction with acetone, hexanes, and chloroform successively. Further treatment with 1,1,2,2-tetrachloroethane was required to give **PPQ2T-BT-24** upon removal of solvent *in vacuo*. Yield: 105 mg (95%).

Synthesis of PPQ2T-BT-40

To a 25 mL Schlenk flask, **PQ2T-Br-40** (100.7 mg, 0.061 mmol), 5,5'-bis(trimethylstannyl)-2,2'-bithiophene (29.9 mg, 0.061 mmol) and P(*o*-tolyl)$_3$ (1.5 mg, 0.005 mmol) were charged. After degassing and refilling argon three times, chlorobenzene (3 mL) and $Pd_2(dba)_3$ (1.1 mg, 0.001 mmol) were added. The reaction mixture was stirred at 130 °C for 72 h. Upon cooling to room temperature, the reaction mixture was poured into methanol (100 mL). The precipitate was collected by filtration and subject to Soxhlet extraction with acetone and hexanes successively. The residual was dissolved in chloroform to give **PPQ2T-BT-40** upon removal of solvent *in vacuo*. Yield: 75 mg (74%).

Appendix C

Materials Characterization

NMR data were recorded on a Bruker DPX 300 MHz spectrometer with chemical shift relative to the deuterated solvent (2.50 ppm DMSO-d_6 or 7.26 ppm $CDCl_3$) [333]. GPC measurements were performed on a Malvern SEC system using 1,2,4-trichlorobenzene as eluent and polystyrene as standards at 140 °C. TGA measurements were carried out on a TA Instruments Q500 at a temperature ramping rate of 10 °C min^{-1} under nitrogen atmosphere. DSC measurements were carried out on a TA Instruments Q2000 at a temperature ramping rate of 20 °C min^{-1} under nitrogen atmosphere. The UV-Vis-NIR absorption spectra were recorded on a Thermo Scientific GENESYS™ 10S VIS spectrophotometer. CV data were obtained on a CHI600E electrochemical analyser using an Ag/AgCl reference electrode and two Pt disk electrodes as the working and counter electrodes in a 0.1 M tetrabutylammonium hexafluorophosphate solution in anhydrous acetonitrile at a scan rate of 50 mV s^{-1}. Ferrocene was used as the reference, which has a HOMO energy level of −4.8 eV [271]. EIS was performed using an Au/water/OSC/Au or Au/water/Au structure under V_{AC} of 50 mV with varying DC Bias on a CHI760D electrochemical analyser. Data was fitted to a simple equivalent circuit. Reflectance XRD diagrams of polymer thin films (~40 nm) spin-coated on DDTS-modified SiO_2/Si substrates and annealed at various temperatures for 15-20 min in nitrogen were obtained using a Bruker D8 Advance powder diffractometer with Cu Kα radiation (λ = 0.15406 nm). Transmission XRD measurements were carried out on a Bruker Smart 6000 CCD 3-circle D8 diffractometer with a Cu Kα (Rigaku) X-ray source (λ = 0.15406 nm) using polymer flakes stacked between two Mylar film substrates. AFM height images were taken on polymer thin films spin-coated on the DDTS-modified SiO_2/Si substrates with a Dimension 3100 scanning probe microscope.

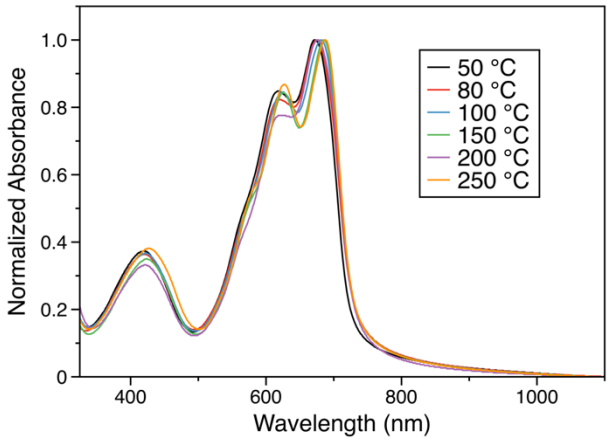

Figure C-1. UV-Vis spectra of a **PFTPDOBT** film spin coated on a glass substrate and annealed in nitrogen at different temperatures.

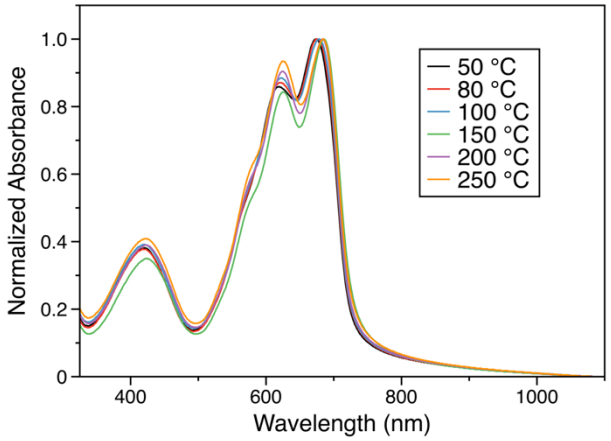

Figure C-2. UV-Vis spectra of a **PFTPDOBT** film spin coated on a glass substrate and annealed in air at different temperatures.

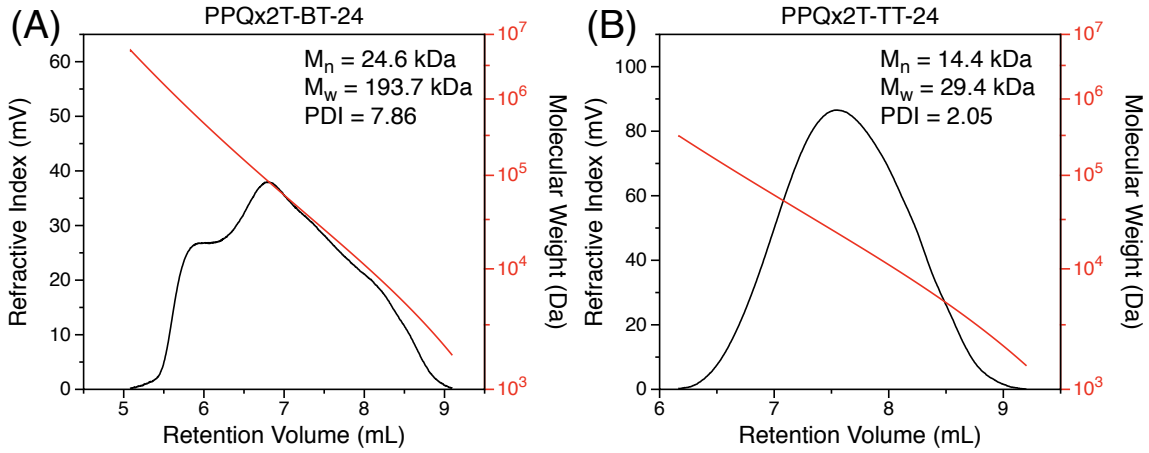

Figure C-3. High temperature GPC traces of **PPQx2T-BT-24** (A), and **PPQx2T-TT-24** (B) with refractive index detector measured at 140 °C.

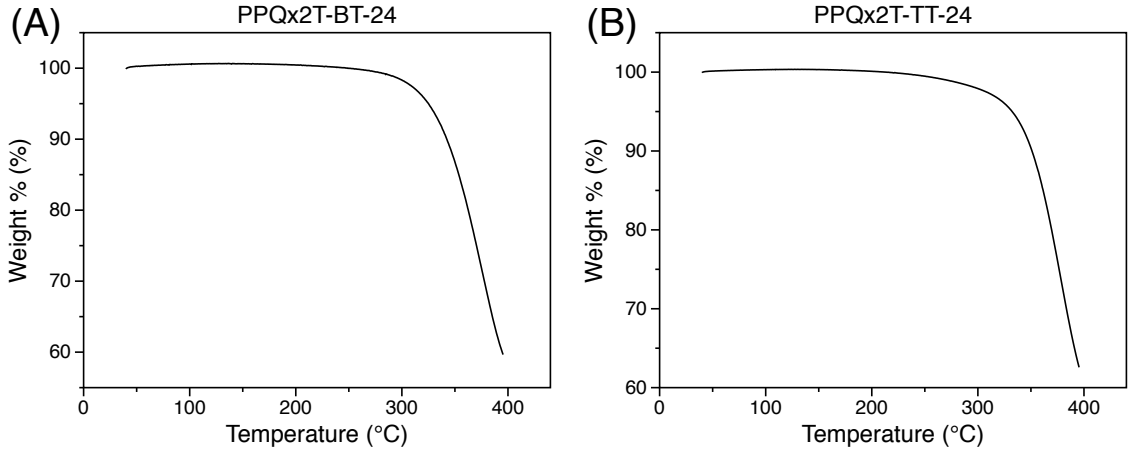

Figure C-4. TGA thermograms of **PPQx2T-BT-24** (A), and **PPQx2T-TT-24** (B) with a heating rate of 10 °C min^{-1} under nitrogen.

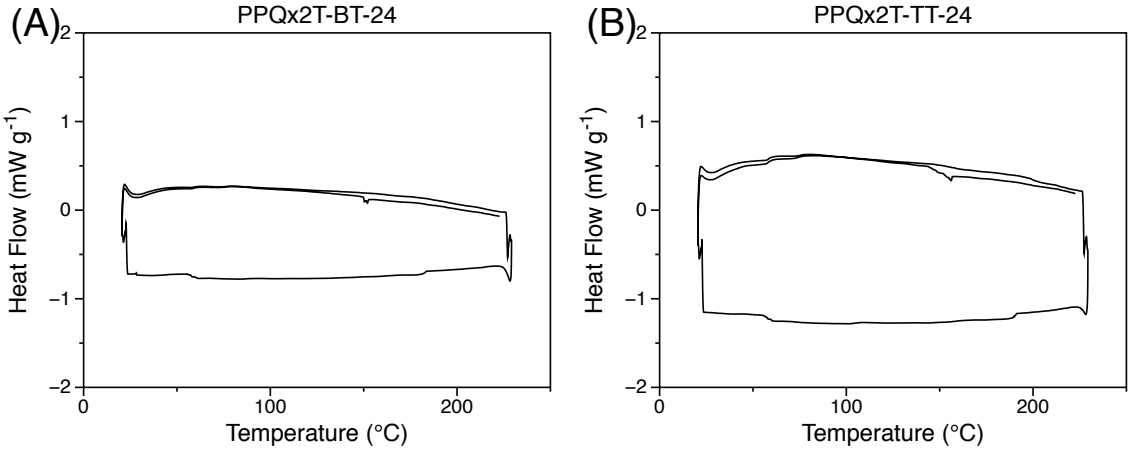

Figure C-5. DSC thermograms of **PPQx2T-BT-24** (A), and **PPQx2T-TT-24** (B) with a temperature ramp of 20 °C min^{-1}. Heating, cooling, and heating cycle was used to remove the memory effect.

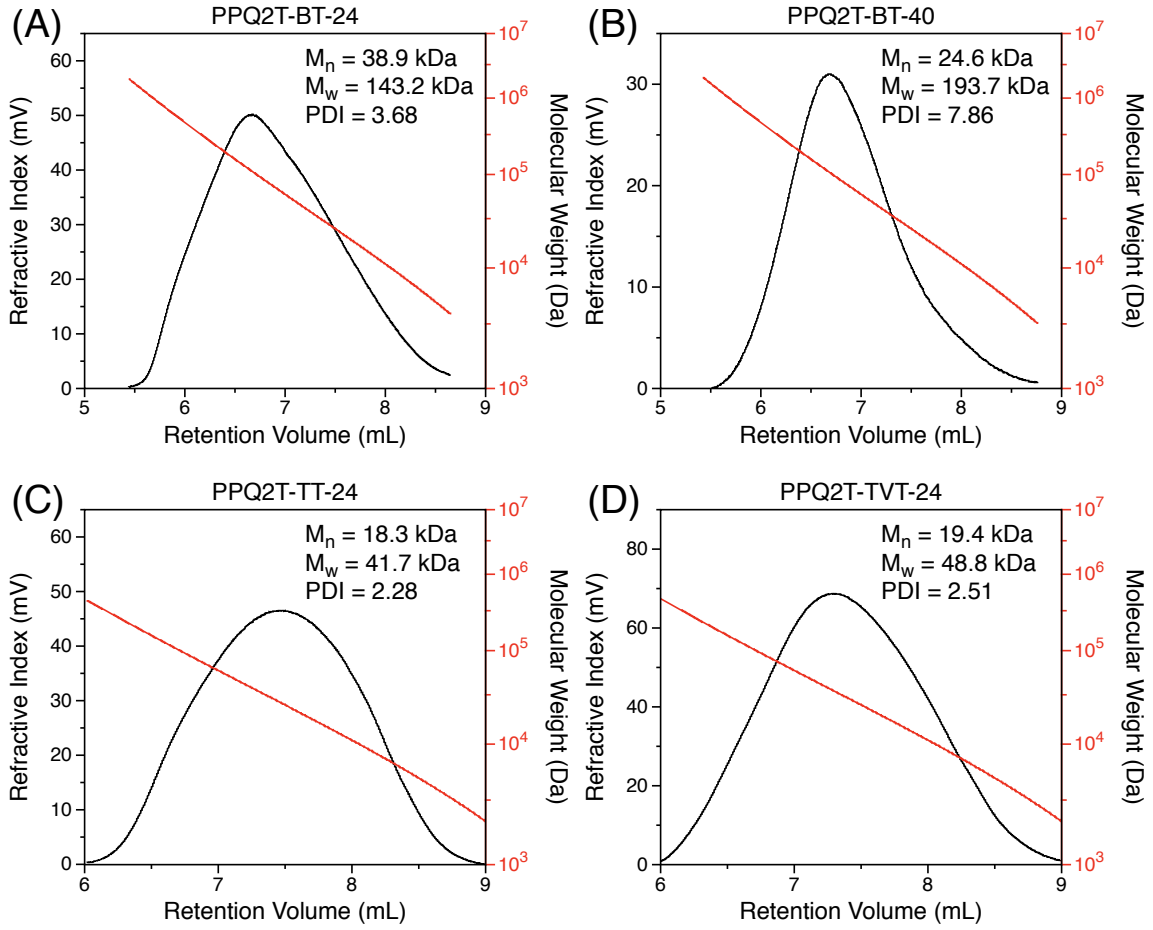

Figure C-6. High temperature GPC traces of polymers with refractive index detector measured at 140 °C.

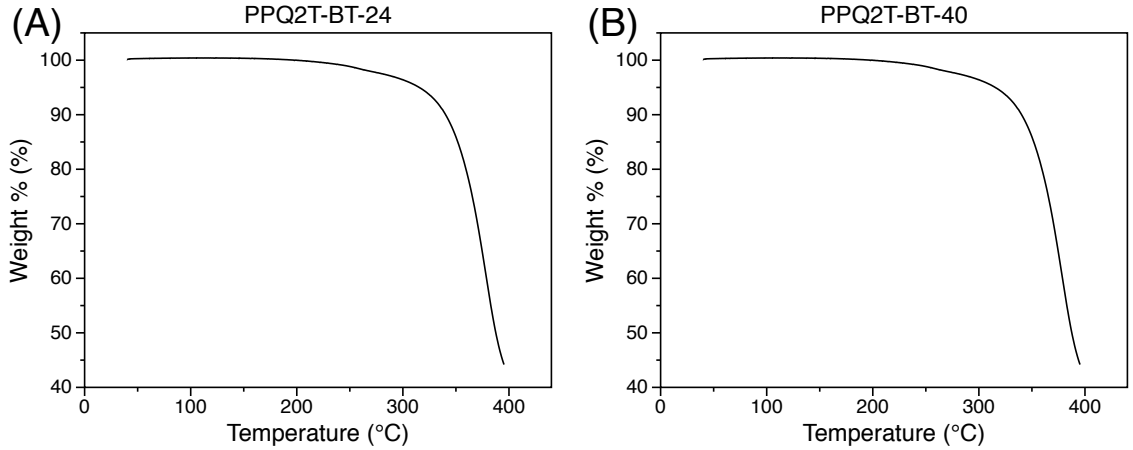

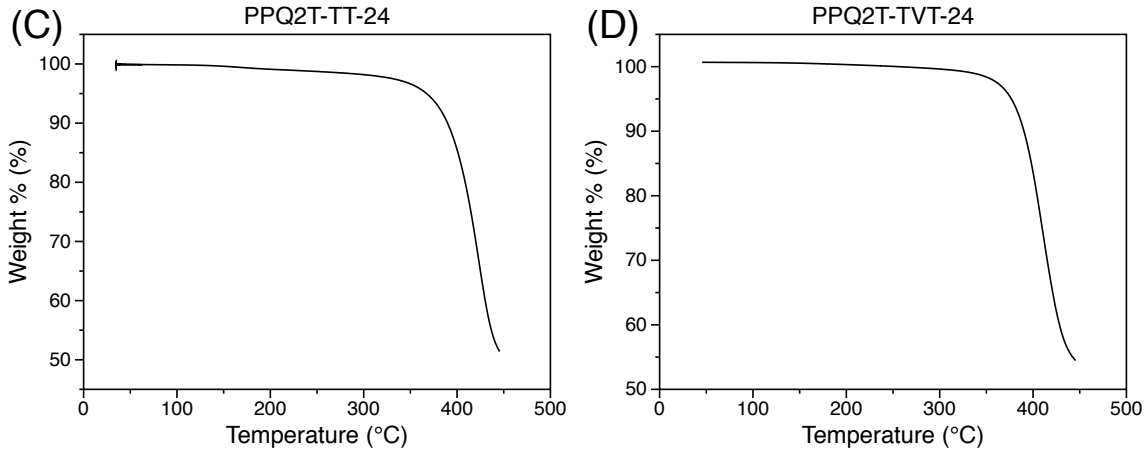

Figure C-7. TGA thermograms of polymers with a heating rate of 10 °C min^{-1} under nitrogen.

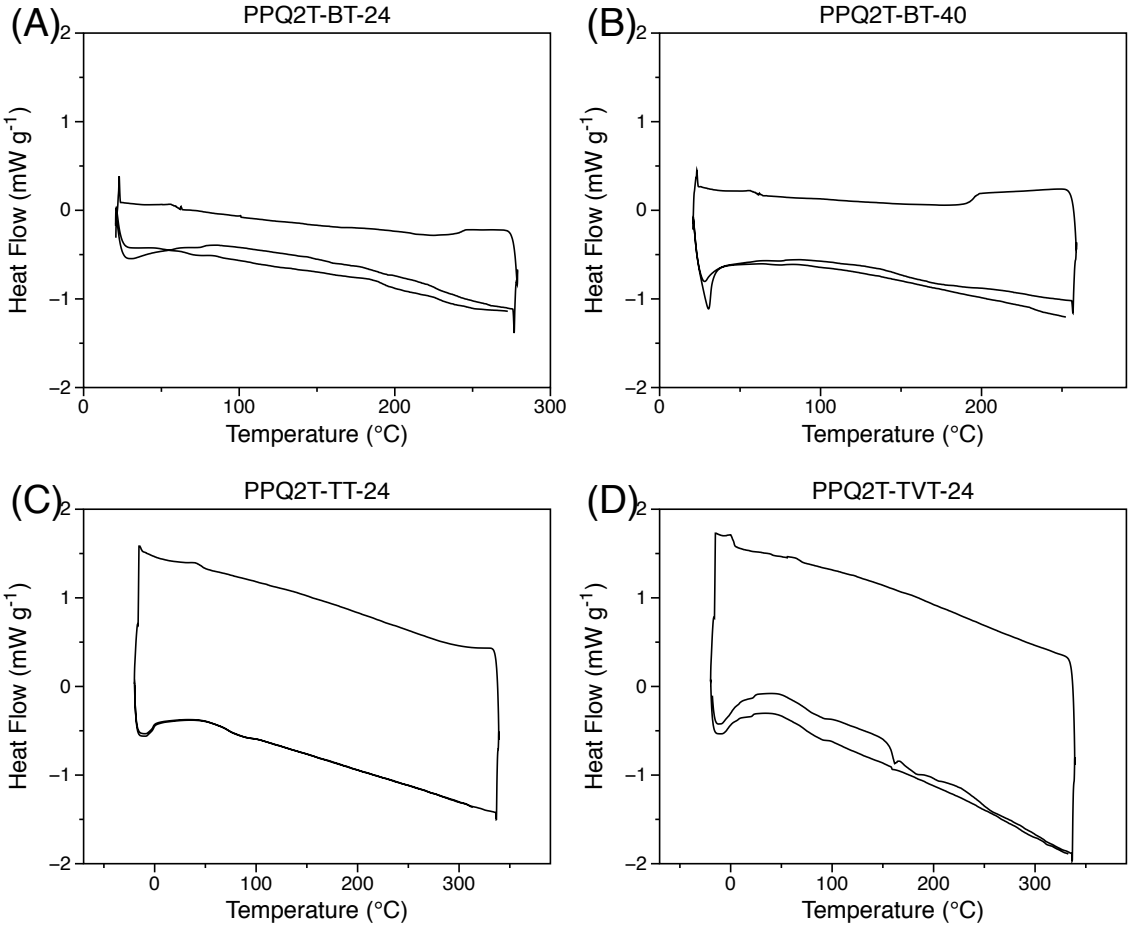

Figure C-8. DSC thermograms of polymers with a temperature ramp of 20 °C min^{-1}. Heating, cooling, and heating cycle was used to remove the memory effect.

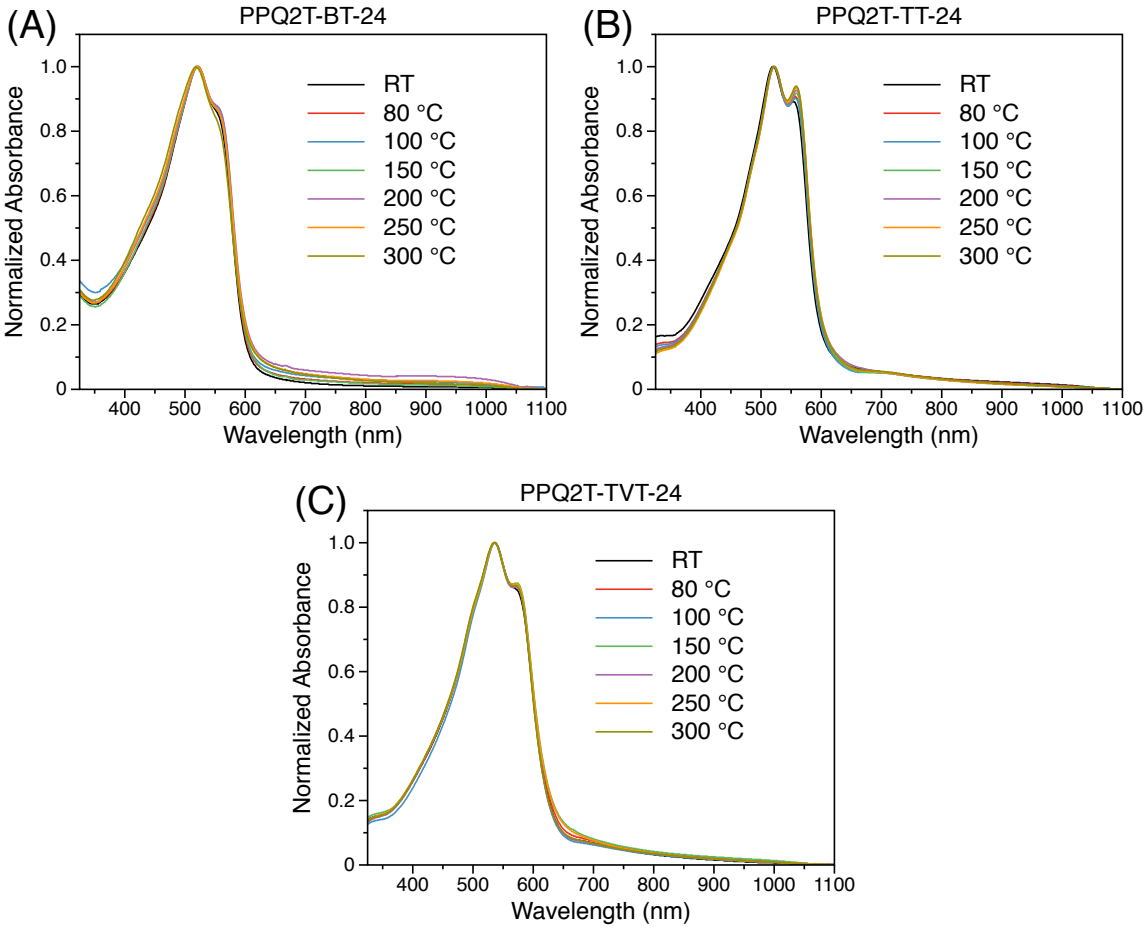

Figure C-9. UV-Vis-NIR absorption spectra of **PPQ2T-BT-24** (A), **PPQ2T-TT-24** (B), and **PPQ2T-TVT-24** (C) thin films annealed at various temperatures under nitrogen atmosphere.

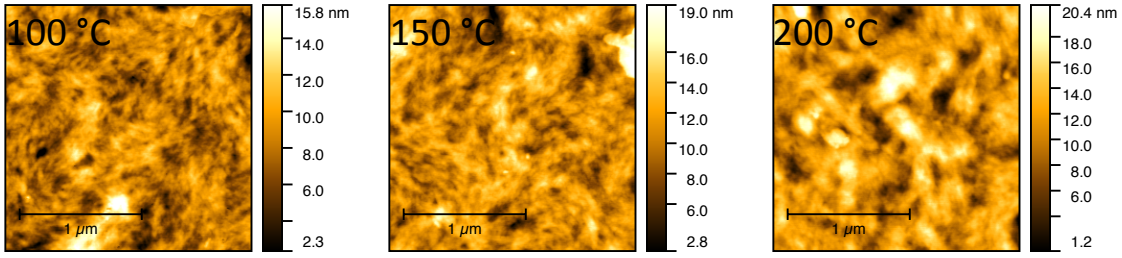

Figure C-10. AFM images (2 μm × 2 μm, 1 μm scale bars) of **PPQ2T-BT-40** thin films after annealing at various temperatures.

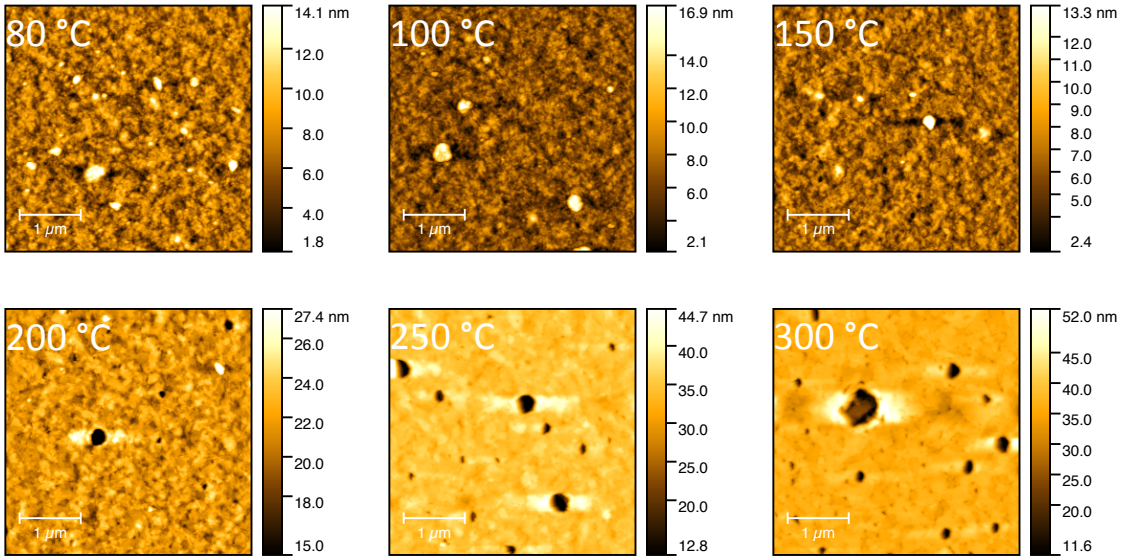

Figure C-11. AFM images (4 μm × 4 μm, 1 μm scale bars) of **PPQ2T-TVT-24** thin films after annealing at various temperatures.

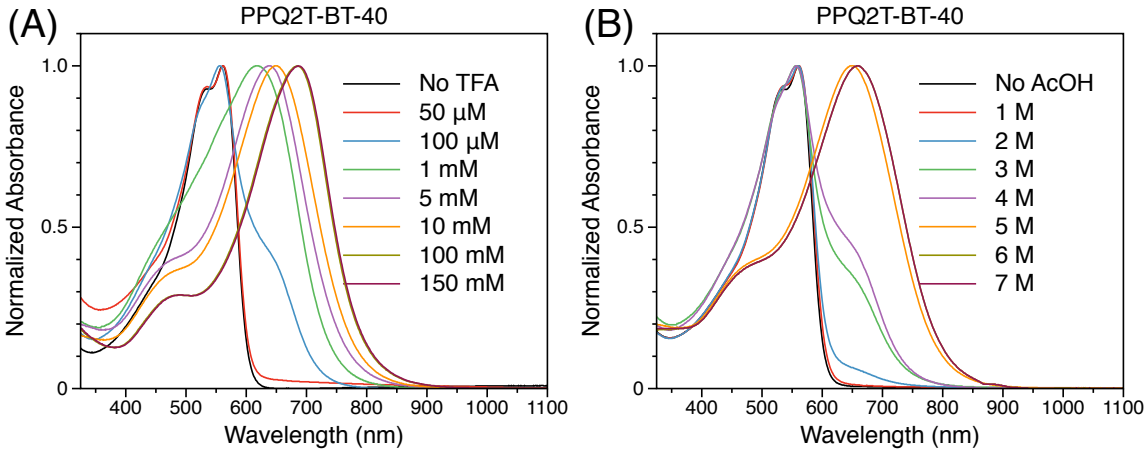

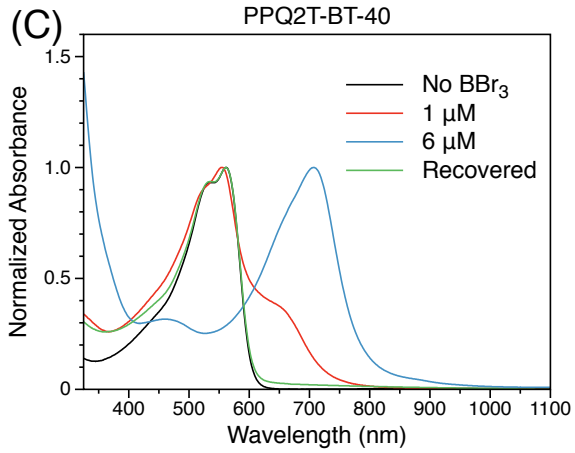

Figure C-12. The UV-Vis-NIR absorption spectra of **PPQ2T-BT-40** in chlorobenzene with various concentrations of TFA (A), AcOH (B), and BBr_3 (C). The measurements were conducted under nitrogen with a molar concentration of the polymer repeat unit at ~1×10^{-5} M.

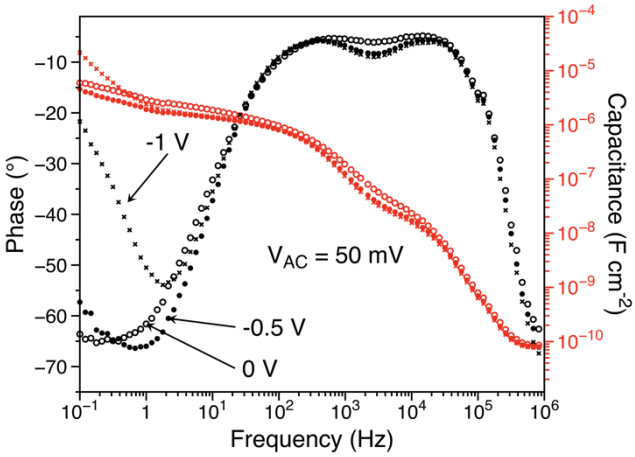

Figure C-13. Phase and capacitance versus frequency for **PPQ2T-BT-24** when used in an equivalent electrical circuit with deionized water at different V_{DC} bias'.

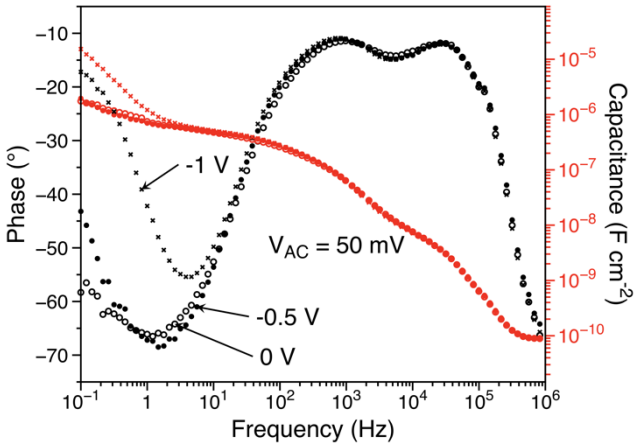

Figure C-14. Phase and capacitance versus frequency for **PPQ2T-TT-24** when used in an equivalent electrical circuit with deionized water at different V_{DC} bias'.

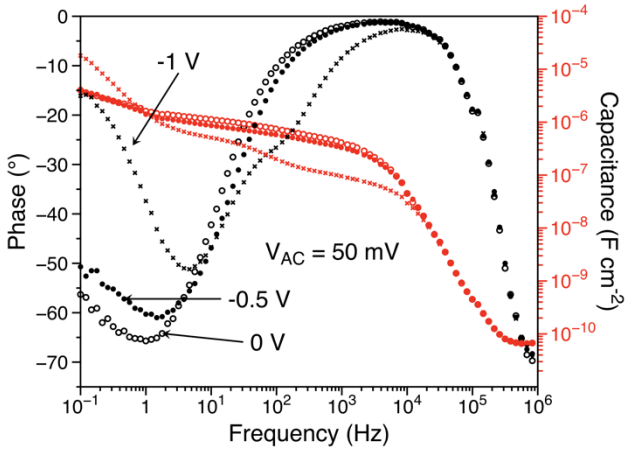

Figure C-15. Phase and capacitance versus frequency for **P3HT** when used in an equivalent electrical circuit with deionized water at different V_{DC} bias'.

Appendix D
I-V Characterization

D.1 Bottom-Gate Bottom-Contact Device Fabrication:

An n^{++}-doped Si wafer with a 300 nm thick SiO_2 layer (dielectric) was used as the substrate. The gold source and drain electrodes (~60 nm thick) were deposited onto the substrate by common photolithography and thermal evaporation methods. The patterned substrate was treated with oxygen plasma, cleaned by ultra-sonication with acetone and isopropanol, flushed with nitrogen, and further dried at 120 °C for 1 min on a hot plate. The substrate was then cooled to room temperature and submerged in a dodecyltrichlorosilane (DDTS) solution (3% in toluene) for 20 min. Subsequently, the substrate was rinsed with toluene and dried under a nitrogen flow. Polymer films with a thickness of ~40 nm were deposited onto the substrate by spin-coating a polymer solution in chloroform (5 mg mL^{-1}) or 1,1,2,2-tetrachloroethane (10 mg mL^{-1}) at 3000 rpm for 80 s and were annealed at the intended temperature for 20 min under nitrogen atmosphere in a glovebox.

D.2 Top-Gate Bottom-Contact Device Fabrication:

An n^{++}-doped Si wafer with a 300 nm thick SiO_2 layer (dielectric) was used as the substrate. The gold source and drain electrodes (~60 nm thick) were deposited onto the substrate by common photolithography and thermal evaporation methods. The patterned substrate was treated with oxygen plasma, cleaned by ultra-sonication with acetone and isopropanol, flushed with nitrogen, and further dried at 120 °C for 1 min on a hot plate. The substrate was then cooled to room temperature. Polymer films with a thickness of ~40 nm were deposited onto the substrate by spin-coating a polymer solution in chloroform (5 mg mL^{-1}) or 1,1,2,2-tetrachloroethane (10 mg mL^{-1}) at 3000 rpm for 80 s and were annealed at the intended temperature for 20 min under nitrogen atmosphere in a glovebox. A Cytop layer (~570 nm with C_i = 3.2 nF cm^{-2}) as the gate dielectric was deposited on the polymer semiconductor layer by spin-coating a Cytop solution at 2000 rpm for 60 s, followed by drying on a hotplate at 100 °C for 30 min in nitrogen. Finally, a ~70 nm thick Al layer was deposited by thermal evaporation as the top gate electrode.

D.3 Device Characterization

The OTFT (in dark), OPT (under illumination), water-gated transistors, and gas sensor devices were characterized in the same glove box where they were fabricated (nitrogen atmosphere), in ambient

conditions, or dry air. The μ and V_{TH} in the saturation regime were calculated by using a slope obtained from the linear fitting of $(I_{DS})^{1/2}$ against V_{GS} according to the following equation [338]:

$$I_{DS} = \left(\frac{W}{2L}\right) C_i \mu (V_{GS} - V_{TH})^2 \qquad (10)$$

where I_{DS} is the drain current, C_i is the insulator capacitance per unit area (~11.6 nF cm^{-2}), and V_{GS} is the gate voltage. Device dimensions were 15,800 μm or 1000 μm in W and 30 μm in L.

Table D-1. Performance of OTFT devices with **PFTPDOBT** films annealed in nitrogen and characterized in nitrogen.

T_{anneal}, °C	Polymer films annealed in N_2/devices measured in N_2			
	μ_{max}, cm^2 V^{-1} s^{-1}	μ_{avg} (std), cm^2 V^{-1} s^{-1}	V_{th}, V	I_{on}/I_{off}
50	8.62×10^{-4}	6.34×10^{-4} (2.35×10^{-4})	-18.40	~10^3
80	7.03×10^{-4}	4.16×10^{-4} (2.43×10^{-4})	-25.40	~10^4
100	1.44×10^{-3}	9.79×10^{-4} (4.37×10^{-4})	-24.89	~10^4
150	3.90×10^{-3}	3.24×10^{-3} (9.61×10^{-4})	-23.79	~10^4
200	5.27×10^{-3}	3.76×10^{-3} (1.22×10^{-3})	-24.92	~10^5
250	1.21×10^{-3}	9.61×10^{-4} (1.85×10^{-4})	-46.48	~10^4

Table D-2. Performance of OTFT devices with **PFTPDOBT** films annealed in nitrogen and characterized in air.

T_{anneal}, °C	Polymer films annealed in N_2/devices measured in air			
	μ_{max}, cm^2 V^{-1} s^{-1}	μ_{avg} (std), cm^2 V^{-1} s^{-1}	V_{th}, V	I_{on}/I_{off}
50	1.69×10^{-3}	1.51×10^{-3} (1.33×10^{-3})	-48.63	~10^4
80	3.70×10^{-3}	3.38×10^{-3} (1.05×10^{-3})	-36.84	~10^4
100	4.69×10^{-3}	5.44×10^{-3} (1.46×10^{-3})	-35.35	~10^5
150	8.19×10^{-3}	1.07×10^{-2} (2.85×10^{-3})	-32.79	~10^5
200	1.44×10^{-2}	1.36×10^{-2} (3.81×10^{-3})	-36.59	~10^5
250	1.02×10^{-3}	5.02×10^{-3} (1.70×10^{-3})	-54.94	~10^4

Table D-3. Performance of OTFT devices with **PFTPDOBT** films annealed in air and characterized in air.

T_{anneal}, °C	Polymer films annealed in air/devices measured inair			
	μ_{max}, $cm^2\ V^{-1}\ s^{-1}$	μ_{avg} (std), $cm^2\ V^{-1}\ s^{-1}$	V_{th}, V	I_{on}/I_{off}
50	3.09×10^{-3}	1.51×10^{-3} (1.33×10^{-3})	-60.51	$\sim 10^4$
80	4.50×10^{-3}	3.38×10^{-3} (1.05×10^{-3})	-53.72	$\sim 10^5$
100	6.75×10^{-3}	5.44×10^{-3} (1.46×10^{-3})	-44.55	$\sim 10^5$
150	1.30×10^{-2}	1.07×10^{-2} (2.85×10^{-3})	-30.60	$\sim 10^5$
200	1.57×10^{-2}	1.36×10^{-2} (3.81×10^{-3})	-37.26	$\sim 10^5$
250	6.60×10^{-3}	5.02×10^{-3} (1.70×10^{-3})	-53.89	$\sim 10^4$

Table D-4. The summary of OTFT performance of **PPQx2T-BT-24** and **PPQx2T-TT-24**.

Polymer	Annealing temperature (°C)	Hole mobility[a] (10^{-3} $cm^2V^{-1}s^{-1}$)	Electron mobility[a] (10^{-3} $cm^2V^{-1}s^{-1}$)	Average V_{th} (V) p-/n-channel	I_{on}/I_{off}[b]
PPQx2T-BT-24	100	0.42 (0.38 ± 0.03)	4.62 (3.99 ± 0.46)	-23.06/44.12	$\sim 10^3$
	150	0.47 (0.48 ± 0.02)	4.47 (3.94 ± 0.40)	-25.63/49.68	$\sim 10^3$
	200	0.52 (0.50 ± 0.02)	4.28 (3.97 ± 0.31)	-30.47/42.42	$\sim 10^3$
	250	0.31 (0.28 ± 0.03)	2.84 (2.62 ± 0.25)	-50.49/43.48	$\sim 10^3$
PPQx2T-TT-24	100	16.20 (12.90 ± 1.89)	0.14 (0.12 ± 0.05)	-23.83/79.48	$\sim 10^5$
	150	42.00 (34.10 ± 5.46)	2.95 (2.81 ± 0.20)	-19.45/66.36	$\sim 10^5$
	200	48.20 (37.90 ± 6.75)	3.95 (3.12 ± 0.98)	-20.29/62.63	$\sim 10^5$

	250	36.60 (27.30 ± 6.53)	2.09 (1.30 ± 0.58)	-22.14/63.11	~10^5

[a] The maximum (average ± standard deviation) mobility was calculated from the saturated regime of at least five devices for each condition. [b] Only dominant channel data are reported.